EFFORTS TO LINK MACHINE PARAMETERS TO VERY HIGH CYCLE FATIGUE LIFE OF ELECTRON BEAM MELTED TI-6AL-4V AND SEAM PRODUCED 4340 STEEL

By

Tyler J. Bauder

A DISSERTATION

Submitted to
Michigan State University
in partial fulfillment of the requirements
for the degree of

Mechanical Engineering – Doctor of Philosophy

2023

ABSTRACT

Electron Beam Melting (EBM) is a relatively new Powder Bed Fusion (PBF) Additive Manufacturing (AM) process. Unlike a very similar laser PBF process, the EBM process occurs in an Ultra-High Vacuum (UHV) and high temperature (~700°C) chamber, reducing residual stress and providing superior protection against oxidation. This makes EMB ideal for processing oxygen sensitive materials like Ti-6Al-4V, whose high strength-to-weight ratio, corrosion resistance, and high temperature performance have drawn the interest of aerospace and other high-performance manufacturing. Due to the nature of these industries, fatigue life is of particular interest. However, the relationship between EBM processing and fatigue life is not well studied and is thus the focus of this dissertation.

First, a L_{16} Taguchi Design of Experiments (DOE) was constructed to investigate the effects of Focus Offset, Line Offset, Speed Function, Hot Isostatic Pressing (HIP) treatment, and surface roughness on the Very High Cycle (VHC) fatigue life of Ti-6Al-4V. Two HIP treatments were 800°C and 200 MPa for 2 hours and 1100°C and 100 MPa for 2 hours with 2.5°C/min quench. Half of the samples were tested in the as-machined condition with an average roughness, R_a, of 0.2 μm and the other half were further polished using Magnetic Assisted Finishing (MAF) to R_a = 0.1 μm. An ultrasonic fatigue testing machine was used to test fatigue life at 500 and 550 MPa loads, with a load ratio of R = -1. Nearly 225 samples were tested with 7 repeats per load condition.

Fatigue results indicated that none of the machine parameters and surface roughness had a statistically significant correlation with fatigue life. However, a statistically significant correlation between HIP treatment and fatigue life was found. The 800°C samples performed as

well as, if not superior, to conventional Ti64 with the average fatigue lives of 8.08E+07 and 3.28E+06 cycles for 500 and 550 MPa, respectively. In contrast, the 1100°C samples had significantly lower fatigue performance with the average fatigue lives of 7.21E+05 and 1.38E+05 cycles for 500 and 550 MPa, respectively. Microstructure and fractography investigations suggest that the poor performance of 1100°C samples can be attributed to coarsening of the prior beta (β) grains during the super-transus HIP treatment leading to the formation of large colonies of similarly orientated alpha (α) grains, allowing for easier dislocation movement across aligned preferential slip directions.

This study concluded that the most important factor controlling fatigue life of EBMed Ti-6Al-4V is post HIP/heat treatment and that fine-tuning of print settings beyond those required to prevent obvious porosity and swelling defects will not have significant effects on the fatigue life of HIPed Ti-6Al-4V.

This thesis is dedicated to Mom and Dad.
Without your support none of this would have been possible.

ACKNOWLEDGEMENTS

I would like to thank my colleagues Hoi Ho Hawke Suen, Guangchao “Jack” Song, Truong Do, Aaron Oneil, Hoa Nguyen, Bibek Poudel, Juan Sandoval, Ryan Khawarizmi, and Beytullah Aydogan for their continued support throughout my time at the Laboratory of Advanced Manufacturing Processes. Special thanks to Jacob Overla and Richard Linn for their contribution to the work presented in this dissertation, I could not have done this without either of you. I know each and every one of you will go on to do great things.

Special thanks to the staff of the Manufacturing Teaching Laboratory, Roy Bailiff and Mike Koschmider, your constant support and tutelage was critical to my success in both undergraduate and graduate studies.

I would like to thank Chad Beamer and Quintus Technologies for their generous donation of time, resources, and technical knowledge for your assistance with HIP treatment. As well as, Rob Rhein, for coordinating this project on behalf of Eaton corporation.

Thank you everyone at Michigan State University and the School of Engineering for providing me with the skills, resources, and environment needed to realize this accomplishment.

Lastly, I would like to thank my committee members Dr. Patrick Kwon, Dr. Thomas Bieler, Dr. Haseung Chung, and Dr. Himanshu Sahasrabudhe. I have learned a great deal from each of you and am thankful to have such great mentors.

TABLE OF CONTENTS

1.0 INTRODUCTION

Additive Manufacturing (AM) has drawn significant attention from a broad range of industries looking to leverage AM's unique processes to challenge the norms of current design and manufacturing. AM itself is a broad term covering a variety of processes characterized by the production of three-dimensional (3D) parts in a layer-by-layer process. In recent years the advent of affordable plastic Fused Deposition Modeling (FDM) printers, such as the MakerBot Replicator, has led to a boom in public knowledge and experience with AM.

Figure 1. MakerBot Replicator desktop Fused Deposition Modeling (FDM) printer. (1)

However, few know that AM has been around much longer, with the first commercialized Stereolithography (SL) system being released by 3D systems in 1987. (2) AM continued to mature with the commercialization of plastic, wax, and even paper lamination printers in subsequent years. However, due to the material limitations of these early printers, AM was limited to rapid prototyping or low load applications. The first step towards high strength AM printers was the release of the EOSINT M250 printer by EOS in 1994. (3) Unlike modern metal printers, the M250 used a low melting point metal as a binder matrix for a blend of additional metal powders. (3) Similarly, Extrude Hone, now ExOne, released its ProMetal RTS-300 in 1998

based on Binder Jet Printing (BJP) technology capable of producing metal components using an ink-jet printer to bind powders together into a “green part” before being de-bound and sintered. (4) It was around this time that the first Selective Laser Sintering (SLS) systems were also being commercialized. Using higher power lasers, these systems were able to heat a bed of metal powder high enough to partially sinter them together into partially sintered parts with higher strengths. They could then be completely sintered in a furnace or infiltrated with another low melting point metal. Although these new metal AM printers could produce parts with significantly higher strengths than their plastic predecessors, their mechanical properties were still limited by their low density or use of low melting point metal infiltration. It would not be until 2003 that the first complete melting metal printer was commercialized by Arcam AB, their S12 EBM printer is also the first commercialized Electron Beam Melting (EBM). (5) In 2004 EOS released their the EOSINT M270 printer, becoming the first commercialized full melting system laser system. (2) The advent of these complete melting AM systems allowed for the production of full (or near full) density, high strength, metal components capable of competing with conventionally produced ones. Unfortunately, the cost of these machines made them extremely cost prohibitive and were primarily restricted to research or extremely high value applications. Nevertheless, metal printers would continue to mature driving down the cost as new printers, companies, and techniques were developed.

Apart from BJP, most of today’s metal AM processes completely melt their feedstock thanks to advancements in Laser and E-Beam technology, which enabled them to achieve superior mechanical properties over sintered or infiltrated parts. These processes can be broken down into two main categories: Powder Bed Fusion (PBF) and Directed Energy Deposition (DED). PBF processes focus their heat source onto a layer of powdered metal feedstock and melt

the desired part cross section by directing the focal point selectively on the powder bed. After completing each layer, the build bed is lowered by an elevator mechanism and fresh powder is deposited atop the previous layer using a raking mechanism. PBF can be further characterized based on their heat source, the two most common being Electron Beam and Laser. Unlike PBF which melts pre-deposited material, DED systems use a material feed system to move print material into the focal point of the heat source. This allows DED systems to deposit material on flat baseplates like PBF or existing three-dimensional (3D) parts. DED machines themselves also feature a wider variety of setups, but typically resemble plastic FDM printers having a deposition head mounted above the deposition area and some mechanism to maneuver the focal point around said area or manipulate the base material. Like PBF, DED printers can be further characterized by the feed system, the most popular being powder or wire feed systems.

1.1 Electron Beam Melting (EBM)

In this section, several common terms and processes associated with EBM will be defined and explained to help with the understanding of later discussion.

MSU currently has an Arcam A2X EBM printer which is a larger, more sophisticated version of Arcam's S12 printer mentioned previously as one of the first commercialized complete melting metal printers. At this time, the EBM PBF machines are exclusively produced and sold by Arcam AB, acquired by GE aviation in 2017. The Arcam A2X is separated into two units, as shown in Figure 2. On the left is the control unit, which handles the machine's power distribution, computer control, and data acquisition. On the right is the build unit which houses the vacuum chamber, vacuum pumps, and electron beam gun assembly. Opening the door on the build unit reveals what is referred to as the build chamber, a depiction of the build chamber is

provided in Figure 3. All aspects of EBM that involve the actual printing of material happen inside the build chamber.

Figure 2. Arcam A2X. (6)

Although EBM machines are typically more expensive and less common than their laser-based counterparts, they have several advantages stemming from their use of an electron beam gun as a primary energy source. The electron beam gun assembly is housed above the build chamber as shown in Figure 3. At the top of the assembly, high voltage (≈60KV) electrical current is passed across a tungsten filament, which produces a "cloud" of free electrons by thermionic emission. (7) These free electrons are then collected, directed, and accelerated down towards the build bed by the grid cup, drift tube, and anode, which make up the remaining parts of the electron beam source assembly. The first major advantage of EBM over other AM processes lies here in the beam generation.

In order to produce an electron beam, there cannot be any gases inside the chamber, Otherwise, the buildup electrons will ionize the air and ground out to a metal surface in the machine, similar to lightning. As a result, EBM cannot use a shielding gas to prevent oxidation like most other AM processes. Instead prior to powering up the E-beam assembly, the build chamber is pumped down to 4E-4 mBar, known as ultra-low vacuum, allowing for electron build up as well as removing any gas that may react with the print material at elevated temperatures. In laser-based systems, which typically use a shielding gas, heat applied to the build bed is quickly removed by the gas through convection. However, residual stresses associated with this rapid cooling can build up over multiple layers resulting in part warping and cracking, a common problem for laser-based systems. By printing in vacuum, the cooling rate of the build bed is significantly reduced, keeping the part temperature between 630 and 730°C throughout the build process and, after completing the printing process, allowing it to slowly cool via radiation as a single part, effectively eliminating residual stresses in the part.

The generated beam passes through a series of electromagnetic coils, which act as a series of lenses to focus and direct the beam around the powder bed. However, unlike traditional glass optical lenses that focus light passing through them, these electromagnetic ‘lenses’ do not directly interact with the electron beam. Instead, they are fitted around the outside of the upper column and generate a magnetic field inside the build chamber. Due to the magnetic nature of electrons, their path through the column is dictated by the magnetic fields produced by the coils, allowing the machine to control the beam path by adjusting the current in the coils. This can be done several thousand times a second making EBM unparalleled in terms of beam speed. Laser systems typically utilize mirrors attached to Galvanometer motors to quickly direct the laser spot around the build bed, but while extremely fast, these motors must overcome the inertia

associated with moving parts thus limiting their speed. An EBM machine is similar in design to a Scanning Electron Microscope (SEM), but the beam power is many orders of magnitude greater and is directed onto a powder bed contained in the vacuum chamber.

Moving further down the machine is the main build chamber, where powder distribution and printing occurs. Powder is stored in two gravity feeding powder hoppers which hang from the ceiling on the left and right sides of the build chamber. In the center of the build chamber is the build tank, which refers to the walls that contain the powder bed, and the elevator which is the device that raises and lowers the powder bed to allow for deposition of new layers. Prior to printing, a build plate is placed on a pad of insulating powder atop the build elevator and leveled to a raking arm. Between each print layer, this raking arm travels back and forth between two "powder dunes", which are continually replenished by powder freely draining from a slot in the powder hoppers. As the rake moves into the dune, it collects a small amount of powder using four fine-toothed, steel combs, called rake blades, mounted under the rake. Next the elevator lowers the build plate by one layer thickness of 50 μm, and the rake brushes the collected powder over the build tank depositing new material for the next print layer. The electron beam then melts through and beyond the whole depth of the currently printing layer, and the processes repeats layer by layer until the build is complete.

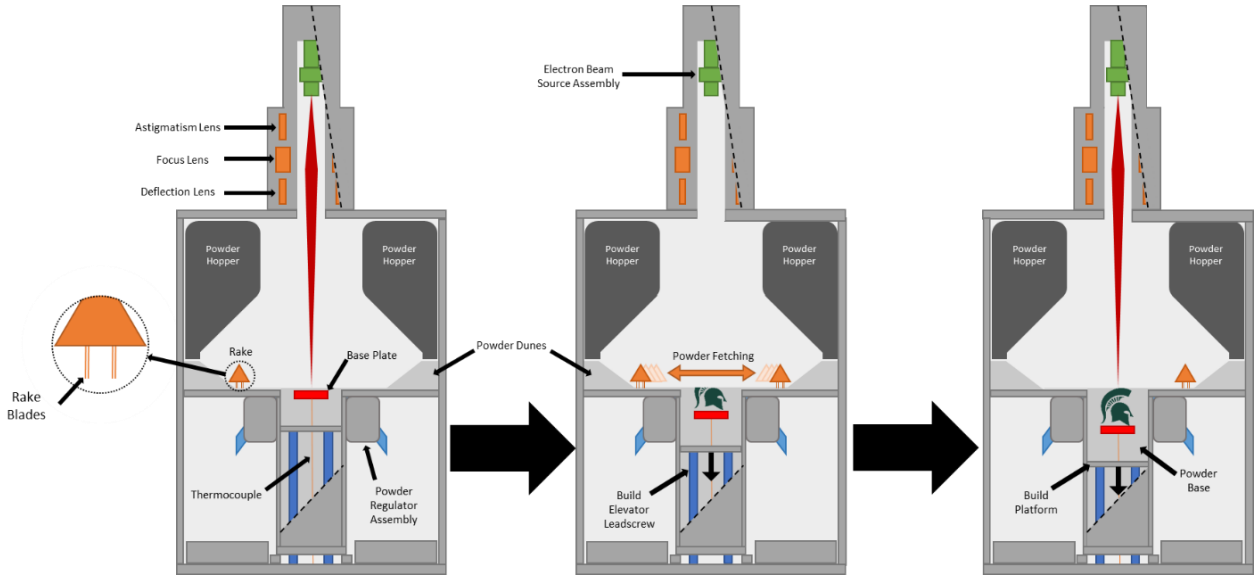

Figure 3. Illustration of EBM printing process. (left) Powder is gathered by a rake from powder "dunes" on ether end o the build chamber and distributed over the build plate. Then the cross section is melted, the build plate is lowered, and powder again distributed (middle). This process repeats layer-by-layer until the part is complete (right).

1.1.1 Primary Melt Parameters

Now that the basic machine operations are covered, the terms associated with melt settings will be examined.

Melt parameters are broken down into two semi-independent types known as contour and hatch. Contour refers to a series of short scan lengths that trace the outside perimeter of a printed part. The contour region typically consists of hundreds of these short scan lengths that combine to create the outer wall of each layer of a part and are typically around two to three scan widths wide. Hatch makes up the bulk of most printed parts and is characterized by a single snaking path that melts the remaining area bounded by the contours. In almost all printing cases, contour is preformed prior to hatching. As long as either contour or hatch printing stays within normal ranges, there may not be much interaction between the two. However, aggressive contouring may cause the outlines to swell blocking powder distribution on subsequent layers, while

excessive heat generated from hatch can bleed through the contour layers causing small bulges of powder to melt or sinter to the outer part surface.

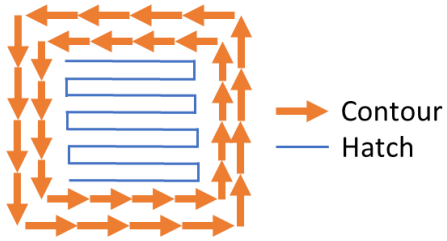

Figure 4. Simplified illustration of Hatch vs. Contour melt strategies. Contour traces the outer perimeter of the part using a series of short scans. This method is known as "multisport" contour and is the machines default contour setting. After the counter is finished the interior is melted using Hatch which is characterized by a single raster or "snaking" path.

With nearly one-hundred different controllable machine parameters there a multitude of ways to fine tune the melting process, however from literature review there is a popular equation used by researchers to estimate the energy density directed into the powder bed which is given by Tammas-Williams et al. (8) as

$$E = \frac{P}{v \cdot h \cdot t} \left(\frac{J}{mm^3}\right) \quad (1)$$

where E is the energy density (Jmm^3), P is the beam power (W), v is the beam velocity, h is the line spacing (mm), and t is the layer thickness (mm). Unfortunately, this equation does not accurately represent the actual energy input, as it does not account for all factors such as beam material interaction (8). Nevertheless, Eq. (1) is still useful for comparing various melt parameters and providing insight into which parameters are commonly used for print optimization. The four most investigated and influential melt parameters are Max Current (MC), Focus Offset (FO), Line offset (LO), and Speed Function (SF) measured in mA, mA, mm, and an integer, respectively. These parameters are of particular interest as they can be varied to control energy density as described in Eq. (1), with MC and FO controlling beam power, LO controlling

line spacing, and SF controlling beam velocity. Layer thickness is typically fixed at 50 μm because of powder and raking characteristics.

As with many aspects of the machine, these parameters have some control over printing, however due to the black box nature of Arcam, it is not entirely clear how much the machine is able to automatically override. For example, MC refers to the maximum allowed power of the electron beam, however there is no setting to control the instantaneous current of the beam during printing as this is handled by the machine. Limiting the MC is the extent of control over the current.

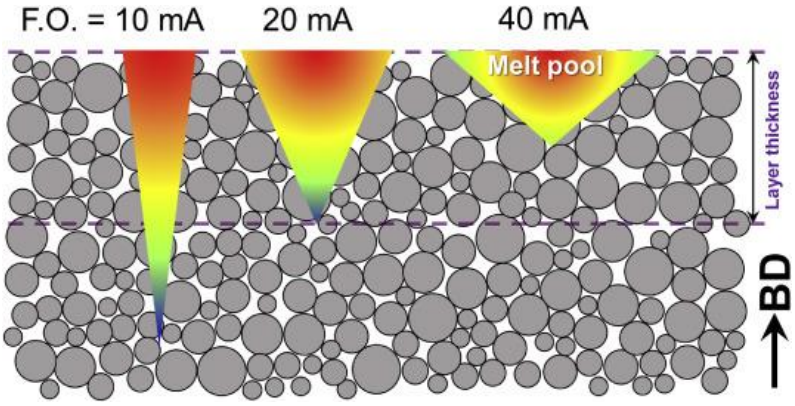

Figure 5. Representation of Focus Offset melt setting for EBM. (9)

FO controls the focal point of the beam as depicted in Figure 5. Although one would expect the height of the focal point to be measured in mm, the mA unit for FO refers to the electrical current of one of the magnetic lenses responsible for setting the beam focal point. Both MC and FO are responsible for controlling the "spot size" of the electron beam, which refers to the diameter of the interaction area between the EB and the print material. Spot size is an important factor for optimizing melt settings as the interaction volume between the beam and material is where all heating occurs and thus has a direct effect on final print quality. However, the spot size and interaction volume can be difficult to calculate or simulate and is typically preformed using a

Monty Carlo simulation, named after the famous casino, which simulates a series of random paths through the material (from which it derives its name), as depicted in Figure 6.

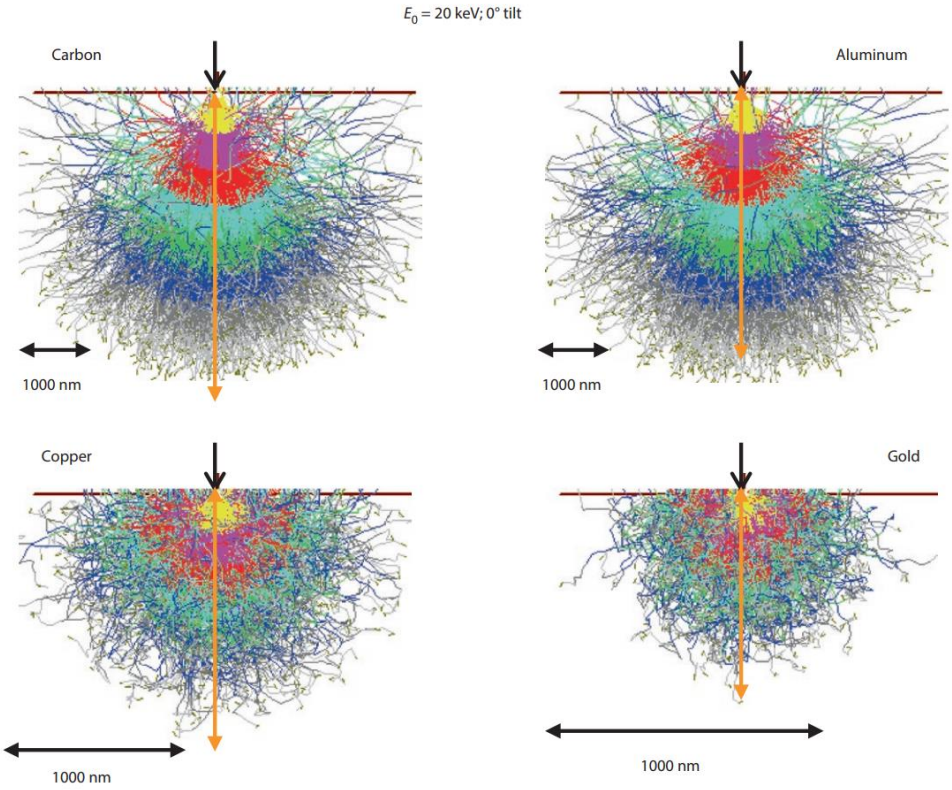

Figure 6. Monte Carlo simulation of electron beam volumetric interaction with carbon, aluminum, copper, and gold. (10)

LO refers to the distance between raster scans, a diagram of the LO is presented in Figure 7.

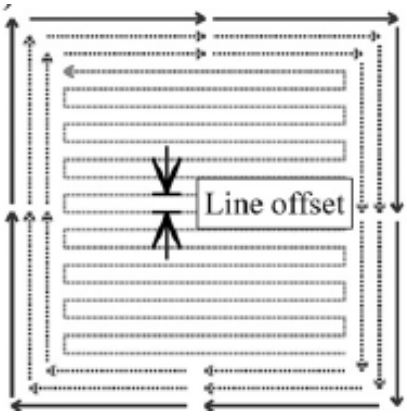

Figure 7. Line Offset refers to the stepover distance between the snaking raster scans. (8)

SF is not as straightforward as the previous melt settings, as it is unitless. SF is a whole number integer corresponding to a single curve among a set of proprietary curves stored in the machine, a representation of these curves with sample data is presented in Figure 8. At the start of any given scan, the EB is not able to achieve full current instantaneously and must ramp up to the desired level. If an optimal beam velocity designed for a given current is used for the whole scan length, then based on Eq. (1), the beginning section would receive a lower energy density and risk being under melted. SF is used to compensate for the beam current ramping by comparing the instantaneous current with the selected SF curve to determine the appropriate instantaneous beam velocity. As the current increases the machine will follow the curve, ramping up beam velocity along with beam current until the desired current is achieved. Unfortunately, to this author's knowledge, no one outside of the machine developers know the exact values of the SF, just that there is a positive correlation between SF and average beam velocity.

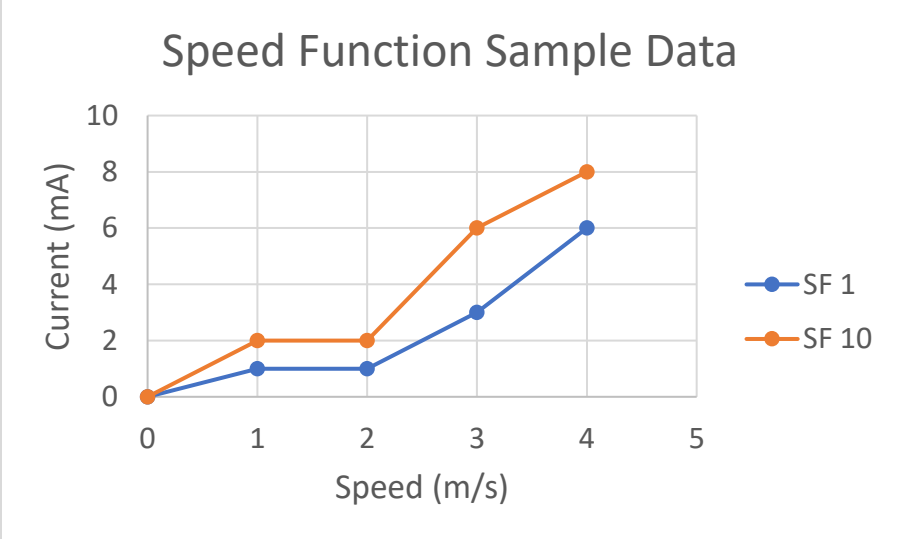

Figure 8. Representation of speed function curves. The curves and unit scales of this figure are not accurate. Sample data was used to illustrate the function of SF. Actual SF curves are proprietary and, to this author's knowledge, unknown to anyone outside of Arcam.

1.2 Porosity

Porosity is an all-encompassing term for a variety of voids and defects found in additive manufactured components and are a constant concern across multiple AM processes. While not unique to additive methods, its layer-by-layer nature makes it particularly susceptible to porosity as any gap or insufficient bonding between deposited materials may result in the formation of internal voids or defects. Some of the most common porosity morphologies include trapped gas, lack of fusion (LOF), and keyhole (KH) porosity. Illustrations of these morphologies can be found in Figure 9, Figure 10 and Figure 11. Origin, prevention, and effect on material properties for each of these three major pore types will be discussed below.

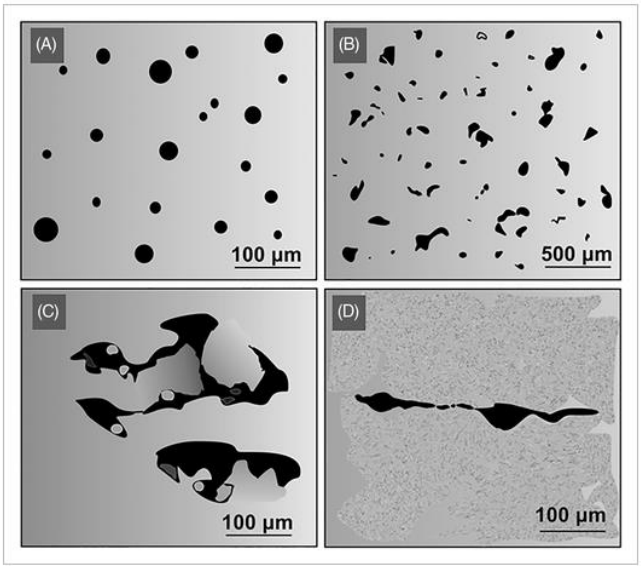

Figure 9. (A) Tapped gas porosity; (B) incomplete melting porosity; (C) lack of fusion porosity, and (d) cracks. (9)

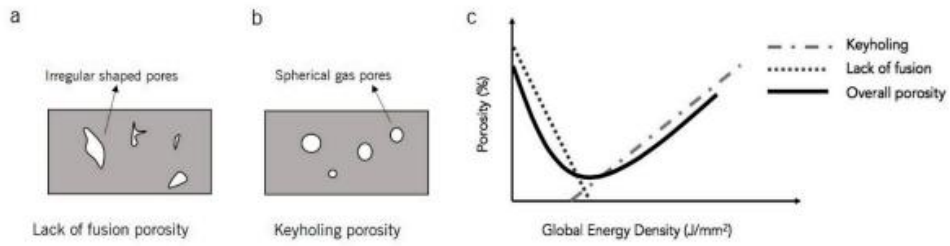

Figure 10. (a) lack of fusion porosity; (b) keyhole porosity; (c) relation between global energy density and porosity percentage. (11)

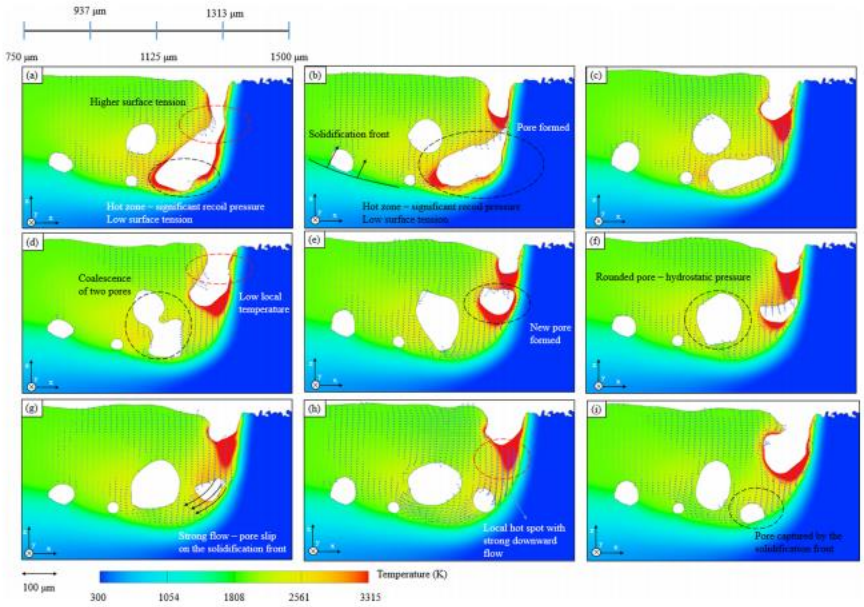

Figure 11. Process of keyhole porosity formation in laser LPBF process. (12)

LOF porosity is perhaps the simplest of the three major pore types, which occurs when a fresh powder layer is incompletely melted, leaving behind large, irregular cavities typically filled with un-melted powders. Typically, these pores are easily eliminated by increasing the energy density applied to the bed to ensure complete melting. However, excessive heating can result in KH porosity.

KH pores form when the beam vaporizes material on the part surface allowing the beam to penetrate further into the layer temporarily forming a deep, narrow hole from which the pore gets its name. As the vaporized material near the surface leaves or condenses, the surrounding

molten material rushes in to close the hole, trapping a bubble of still gaseous metal vapor below the surface. Like an air bubble under water, the metal vapor forms a spherical cavity and prevents the surrounding material from closing the pore. If the bubble survives long enough, the surrounding material solidifies creating a large, spherical void. Since this type of pore is the result of excessive heating, it can be prevented by reducing the applied energy density. (12) Through trial and error or thermal simulations, it is possible to find an energy density that minimizes or completely eliminates the occurrence of both LOF and KH pores, as shown in Figure 10, and is one of the major first steps taken when attempting to print a new material.

The last of the three major pore types is trapped gas (TG) porosity. TG porosity is very similar to LOF porosity, but instead of being caused by printing, TG pores are the result of the metal powder manufacturing process. Most metal AM processes, including EBM, use spherical metal powders because of their superior flowability properties over other available powder types such as irregular or plate like powders. One of the most common ways to produce these spherical powders is known as gas atomization, a diagram of which is provide in Figure 12.

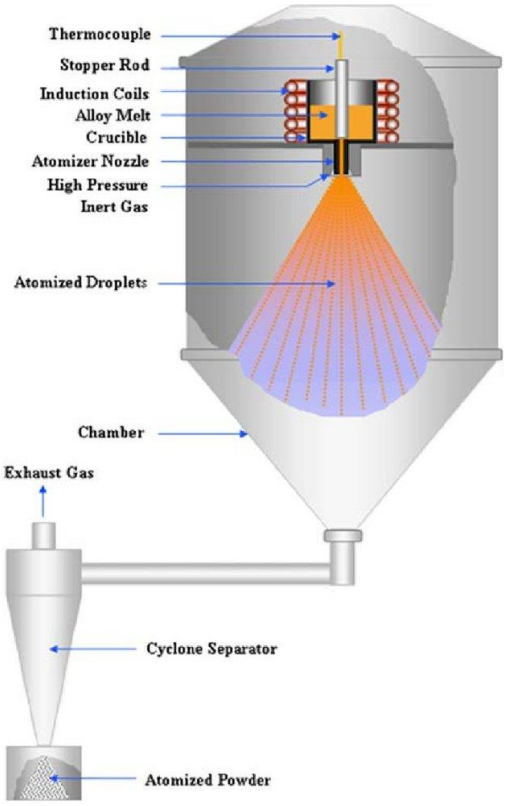

Figure 12. Gas atomization process for producing spherical metal powders. (13)

Powders begin as solid feed stock which is fed into and melted inside a crucible mounted above an atomization nozzle. As the molten metal flows through the nozzle, it is blasted by high pressure inert gas, typically Argon, which disperses the stream of molten metal into individual droplets. Much like water droplets in a rainstorm, these metal droplets take on a spherical shape as they fall and eventually solidify. Similar to LOF pores, this high-pressure Argon can become

trapped inside the solidifying metal, forming spherical voids inside individual powders, as shown in Figure 13. (14)

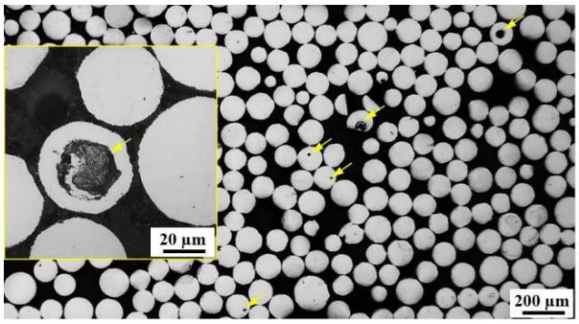

Figure 13. Optical image of sectioned metal powders with trapped gas pores formed during the gas atomization process used to manufacture the spherical powders. (14).

Although AM process like EBM fully melt the powders, they do not remain molten long enough for all the Argon to escape, causing some pores sized between 1 to 100 µm in diameter, which almost always are retained in the final structure. While it is possible to eliminate the aforementioned LOF and KH pores through energy density optimization, the nature and prevalence of TG pores in the powder feedstock makes it nearly impossible to completely eliminate it without post processing. However, it is possible to drastically reduce the amount of TG pores retained in the final part as demonstrated by Tammas-Williams et al. (8) Using X-ray Computed Tomography (XCT), they found that regions of EBMed Ti-6Al-4V parts printed using contours had significantly fewer TG pores, as clearly seen in Figure 14. This reduction in TG porosity was attributed to the higher energy density of the contour theme compared to the bulk melt hatch theme. This higher energy density keeps the recently melted material molten longer and allows for the re-melting of previously deposited layers as new layers are printed. The combination of these two effects gives trapped argon gas more time to work its way out of the part reducing the final number of TG pores. (8)

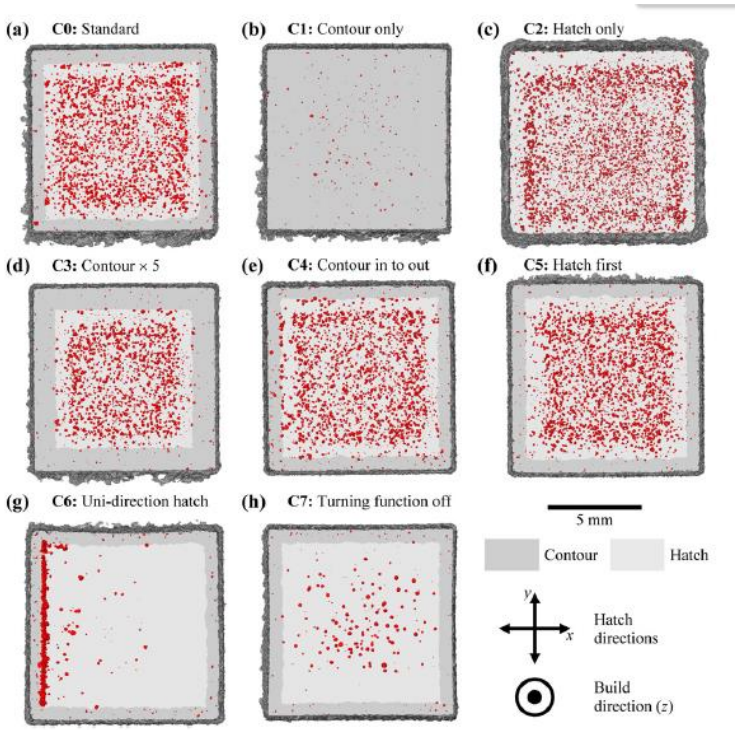

Figure 14. Low resolution 3D XCT scan of EBMed Ti-6Al-4V with detected pores denoted by red points. Approximate melt strategies, hatch (light) and contour (dark), denoted by shading. (8)

1.3 Hot Isostatic Pressing (HIP)

One of the most common post processing steps for nearly all AM applications, especially for those in the VHC fatigue regime, is Hot Isostatic Pressing (HIP). As the name suggests HIP uses a high temperature and pressure inert gas, typically argon, to uniformly compress parts inside a pressure vessel. The combination of the high temperature and pressure helps close the defects like pores and cracks inside the part, while the isostatic or uniform applied pressure prevents the part from losing it shape. A diagram of a typical powder metallurgy HIP chamber is provided in Figure 15.

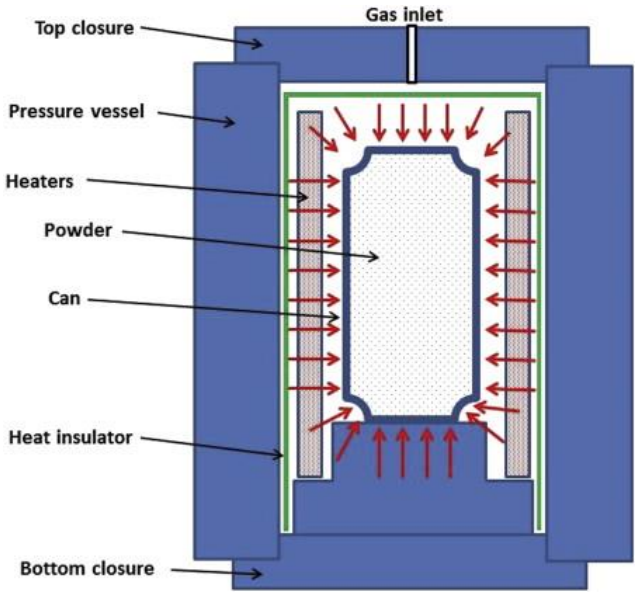

Figure 15. Diagram of powder metallurgy HIP pressure vessel. (15)

Depending on the material and HIP treatment parameters, it is possible to close a wide variety of internal defects of various sizes as demonstrated by Tammas-Williams et al. (8) who used XCT scanning to map defects in EBMed Ti-6Al-4V samples before and after HIP treatment. With a HIP treatment of 920°C at 100 MPa for 2 hours Tammas-Williams et al. demonstrated that HIPing can eliminate gas pores, LOF defects, and large-scale porosity. Before and after treatment images from this study are provided in Figures 16 and 17.

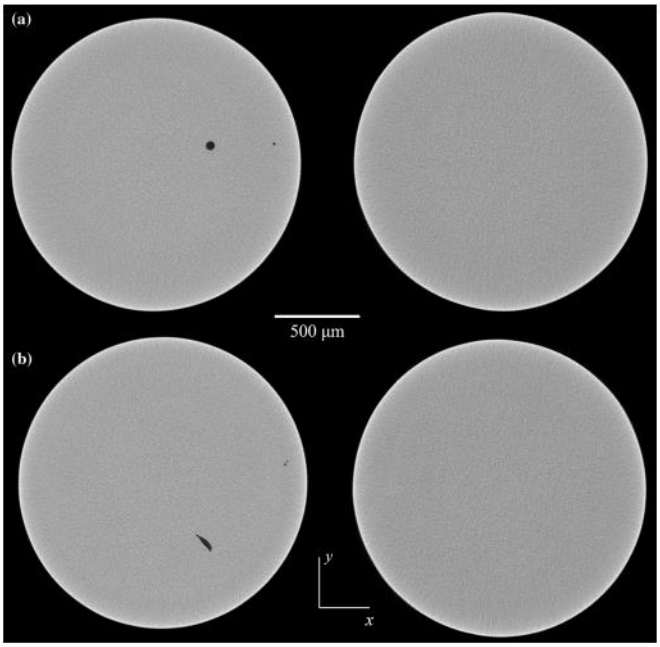

Figure 16. XCT scan on EBMed Ti-6Al-4V before (left) and after (right) HIP treatment. a) Large gas pores. b) Lack of fusion defect. (16)

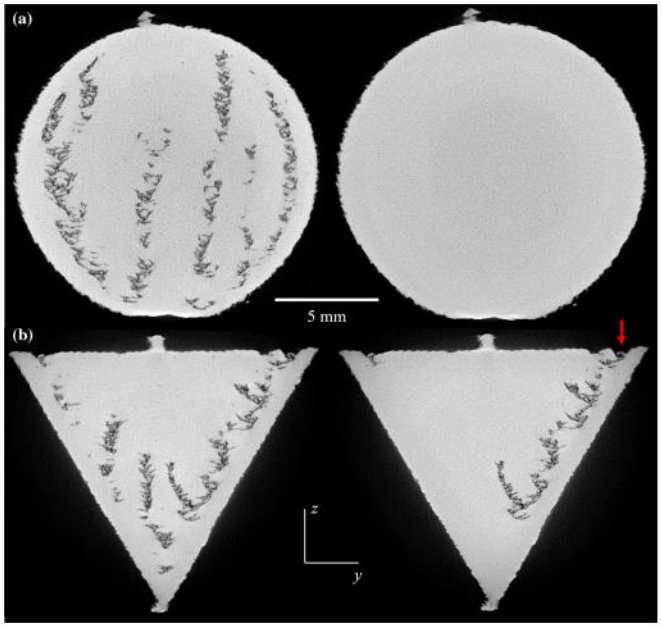

Figure 17. XCT scan on EBMed Ti-6Al-4V before (left) and after (right) HIP treatment with tunneling defects. Note surface connected pore in b (right) was not closed due to infiltration of high-pressure Argon. (16)

In addition, Günther et al. (17) found that defects closed by HIP were not found to reopen, propagate, or initiate cracking in EBMed Ti-6Al-4V fatigue samples. It should also be noted that,

if Argon is able to work its way into cavities near or connected to the surface, it will counter the pressure applied to the outer surface and prevent pore closure, as demonstrated in Figure 17.

Overall, the work presented in these studies have shown to be an effective guide for correcting print defects and persistent trapped gas porosity common in EBM. Additional information on common treatments and their effect on fatigue life of EBMed Ti-6Al-4V parts will be discussed further in the literature review section found below.

1.4 Material Background on Ti-6Al-4V

Titanium in general is known for its high strength, low density, and excellent corrosion resistance. (18) One of its first and most famous applications being the Lockheed SR-71 "Blackbird" produced in 1950's. (18) Although first discovered in 1791 by William Gregor, it proved costly to extract and refine until the invention of the Kroll's processes by William Kroll in the 1940s, who used liquid magnesium to reduce titanium tetrachloride ($TiCl_4$) and form a pure titanium "sponge" that can then be worked into ingots. (19) This newly available material was then studied for armor applications at the Army Research Laboratory in the early 1950s. Here, Stanley Abkowitz invented Ti-6Al-4V (Grade 5), the most commonly used titanium alloy used today for a variety of applications such as landing gear, turbine blades, biomedical and dental implants, golf clubs, eye-glass frames, and much more. (18) (20)

Pure titanium has two primary phases, a body-centered cubic (BCC) or β phase at high temperatures and a hexagonal close-packed (HCP) or α phase at lower temperatures. The transformation point between the two phases is known as the β-transus and occurs at 882°C for pure titanium. Unit cell diagrams for both phases are provided in Figure 18 and Figure 19

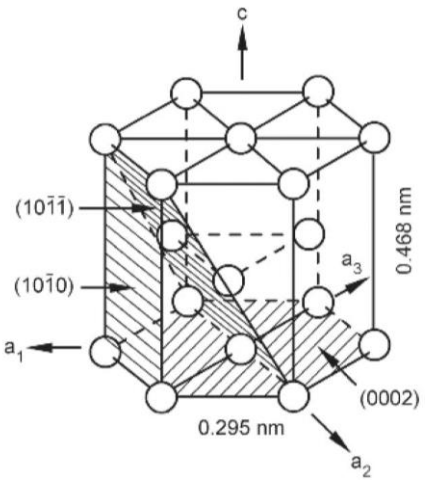

Figure 18. Unit cell of α phase titanium. (18)

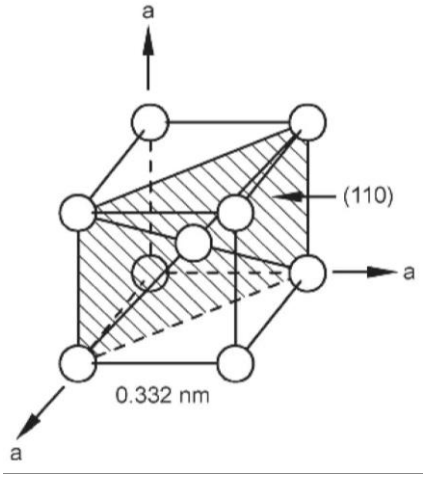

Figure 19. Unit cell of β phase titanium. (18)

The β-transus temperature is largely dependent on the alloying elements. Elements that raise the transus are designated as α stabilizers while elements that lower the transus are designated as β stabilizers. The most commonly used α stabilizers are oxygen, nitrogen, carbon, and aluminum. β stabilizers are further classified into either β isomorphous or β eutectoid stabilizers depending on their effect on the phase diagram. Typical β isomorphous stabilizers include vanadium, molybdenum, and neodymium. Typical β eutectoid stabilizers include chromium, iron, and silicon. The amount of β phase that can be retained in the alloy at room temperature is dependent

on the concentrations of β stabilizers. (18) A diagram of how each of these elements effect the phase titanium phase diagram is provided in Figure 20.

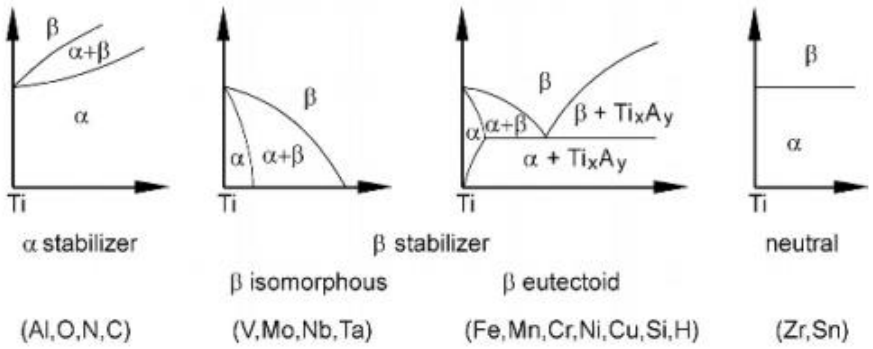

Figure 20. Effect of various alloying elements on the phase diagram of titanium. (18)

Ti-6Al-4V is the primary material used in this study. The alloy gets its name from its alloying elements aluminum (Al) and vanadium (V), and their relative concentrations of 6 wt% and 4 wt%, respectively. The typical composition of Ti-6Al-4V is provided in Table 1.

Table 1. Composition of Ti-6Al-4V (Grade 5) as given by ASTM F1472 – 14. (21)

Element	Composition (wt %)
Nitrogen, max	0.05
Carbon, max	0.08
Hydrogen, max	0.015
Iron, max	0.03
Oxygen, max	0.2
Aluminum	5.5 – 6.75
Vanadium	3.5 – 4.5
Yttrium, max	0.005
Titanium	Balance

Ti-6Al-4V is known as an α – β alloy because the additions of both aluminum and vanadium allow for both phases to be retained in the microstructure at room temperature. Retaining both phases makes the material more versatile and widens the range of properties achievable through processing. Ti-6Al-4V properties are primarily controlled by grain refinement after cooling from β or α + β phase. (22) Examples of mill-annealed Ti-6Al-4V microstructures of cooled by water quenching, air cooling, and furnace cooling from various starting temperatures are presented in

Figure 21.

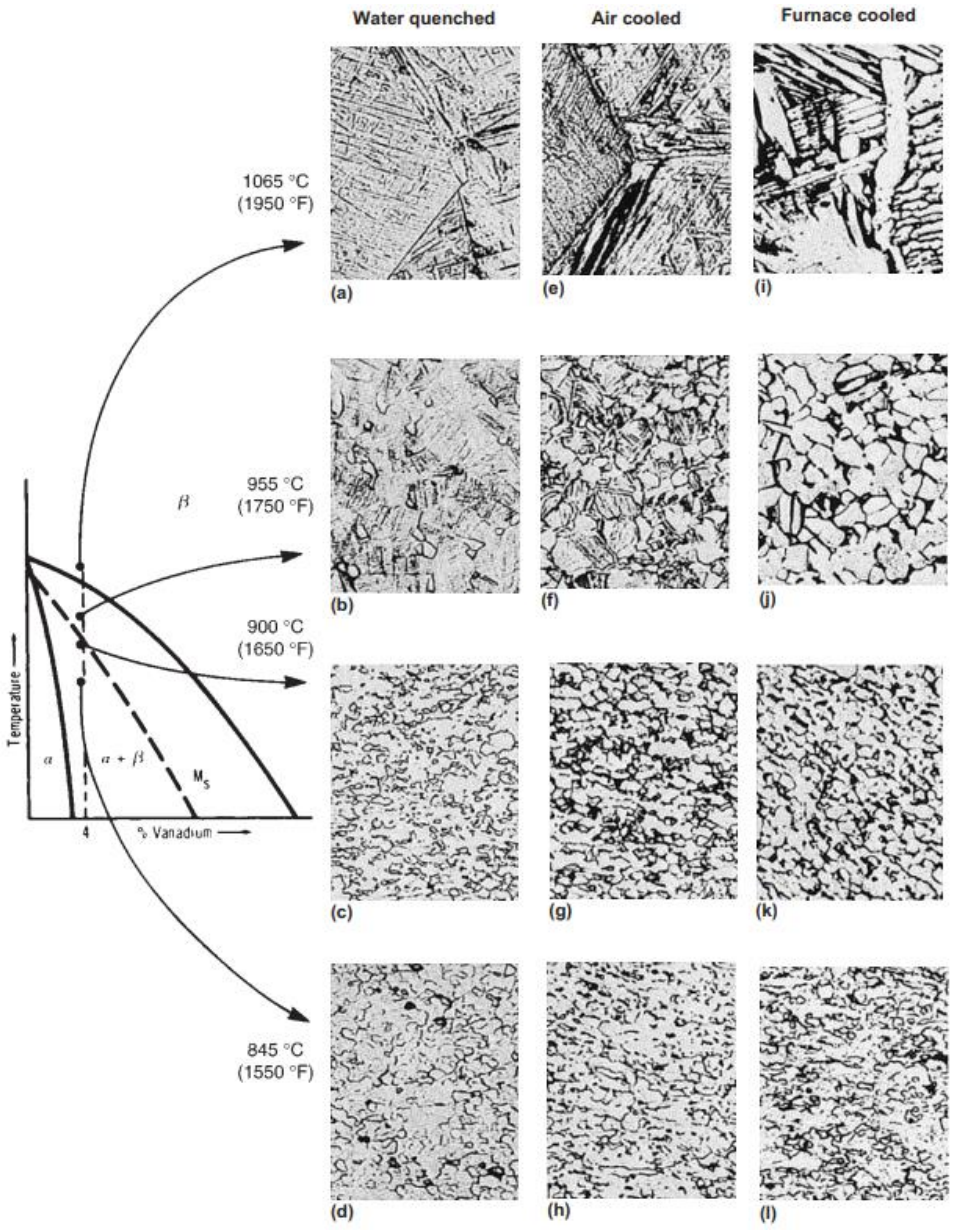

Figure 21. Effect of cooling rate on the microstructure of an alph-beta alloy (Ti-6Al-4V). (a) α′ + β; prior beta grain boundaries. (b) Primary α and α′ + β. (c) Primary α and α′ + β. (d) Primary α and metastable β. (e) Acicular α + β; prior beta grain boundaries. (f) Primary α and acicular α + β. (g) Primary α and acicular α + β. (h) Primary α and β. (i) Plate-like α + β; prior grain boundaries. (j) Equiaxed α and intergranular β. (k) Equiaxed α and intergranular β. (l) Equiaxed α and intergranular β. Etchant: 10 HF, 5 HNO3, 85 H2O. 250x. (22)

Another morphology most similar to image (i) in Figure 21, is known as Widmanstätten or

"basket weave" structure, formed by slow cooling rates from above β-transus. Widmanstätten

structure is characterized by nucleation and slow growth of parallel α plane at β grain boundaries. These plates share a crystallographic relationship with the parent β grain, growing with their densest packed plane (basal plane) parallel to one of the six β, non-parallel growth directions. New α plates that nucleate from existing α plates, do so with aligned crystallographic orientations, forming colonies of parallel α plates sharing a common crystal orientation, separated by β phase. An image of a typical Widmanstätten structure is provided in Figure 22.

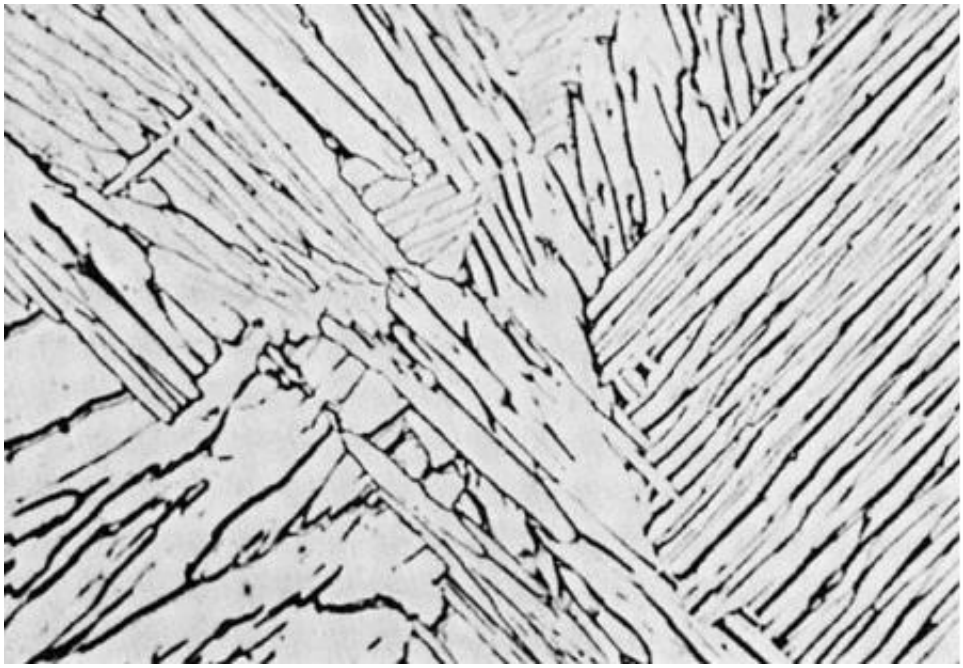

Figure 22. Typical Widmanstätten observed after slow cooling from above the β-transus. Dark regions are β and white regions are α. (22)

The Widmanstätten microstructure is commonly found in as-fabricated Ti-6Al-4V produced by EBM, due to the high build chamber temperature and slow cooling rates. Rapid cooling from the β or α + β fields can cause the β phase to transform into α through a shear type transformation process to produce martensitic alpha (α'). α' appears in two forms, massive martensite (only for pure titanium) and "acicular martensite" characterized as a mixture of needle-like individual α plates with different crystallographic orientations, supersaturated in β stabilizers, and high dislocation density. (18) In titanium, the martensitic $\alpha'$is not as strong as martensite formed in

steels and does not provide the same hardening effects. In steels, hardenability describes the ability to reach a desired hardness by controlling the amount of martensite formed. For titanium alloys, hardenability is a measure of the ability to fully transform β into α or to retain β at room temperature in a strategic morphology. (22) Hardening in Ti-6Al-4V can be done using solution treatment and aging. Solution treating is done at 25 – 85°C below the β-transus and is used to control the ratio between α and β phases. Aging is done between 425 and 650°C and is used to decompose supersaturated β and α' phases formed during quenching. (22) Effects of these treatments on mechanical properties of Ti-6Al-4V are provided in Figure 23.

Solution-treating temperature		Room-temperature tensile properties(a)				
		Tensile strength		Yield strength (b)		Elongation in 4D(c),
°C	°F	MPa	ksi	MPa	ksi	%
845	1550	1025	149	980	142	18
870	1600	1060	154	985	143	17
900	1650	1095	159	995	144	16
925	1700	1110	161	1000	145	16
940	1725	1140	165	1055	153	16

(a) Properties determined on 13 mm (½-in.) bar after solution treating, quenching, and aging. Aging treatment 8 h at 480 °C (900 °F), air cool. (b) At 0.2% offset. (c) D, specimen diam

Figure 23. Effect of solution treating temperature on tensile properties of Ti-6Al-4V bar stock. (22)

The HCP structure of α titanium makes it inherently anisotropic, for example the stiffness of single crystal α grain is dependent on the declination angle between the applied stress and the c-axis of the unit cell. When aligned, the elastic modulus is 145 GPa and falls to just 100 GPa

when the applied stress is perpendicular to the c-axis (declination angle = 90°). (18) A plot of elastic modulus against declination angle of single crystal α grain can be found in Figure 24.

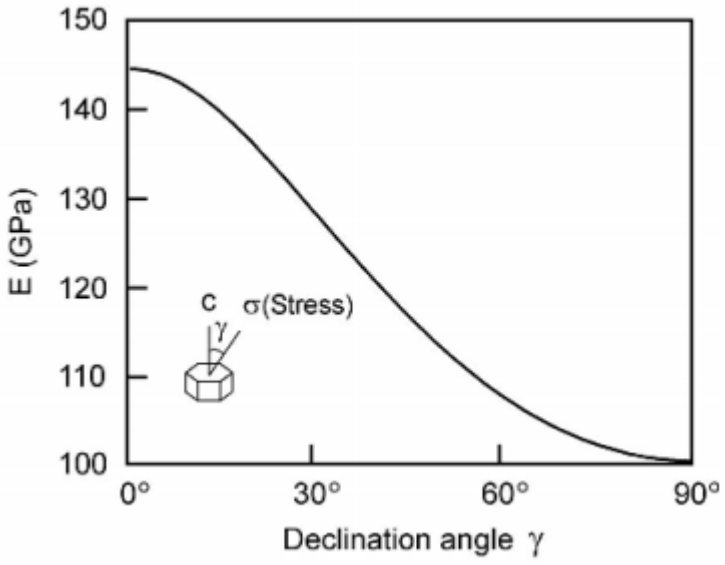

Figure 24. Elastic modulus E of single crystal of α titanium vs declination angle. (18)

This effect is typically less severe in polycrystalline materials but is sensitive to the overall texture (the preferred distribution of particular crystal orientations) of the specimen. Additional material properties such as thermal and electrical conductivity are similarly anisotropic. (18) The superior corrosive resistance properties of titanium result from a thin oxide layer that immediately forms on the surface of titanium in the presence of oxygen. This stable oxide layer does not flake off like iron rust, producing a cohesive ceramic layer that protects the titanium from corrosive environments. However, this affinity for oxygen limits the maximum operating temperature to around 600°C where oxygen will penetrate further into the material, growing the oxide layer and embrittling the surface. (18) This affinity for oxygen makes the ultra-low vacuum chamber of the Arcam ideal for processing titanium alloys.

2.0 EFFECT OF MELT PARAMETERS ON FATIGUE LIFE OF ELECTRON BEAM MELTED TI-6AL-4V

2.1 Project Scope

The objective of this chapter is to investigate the effect of machine melt parameters, surface roughness, and HIP condition on the fatigue life of EBM printed Ti-6Al-4V samples. In the end, we hope to be able to use this data to predict the endurance limit of a part produced by the tested conditions. Samples are to be tested using an ultrasonic fatigue setup presented in Figure 25 with a fully reversed load condition (R = -1).

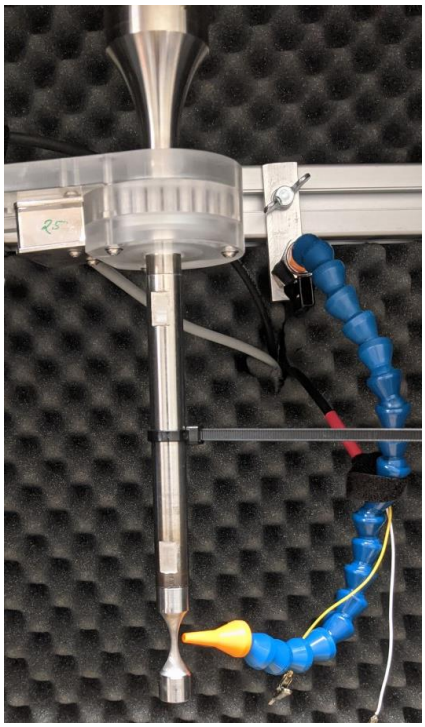

Figure 25. Ultrasonic fatigue testing setup with mounted EBMed Ti-6Al-4V sample. Setup build and tests performed by Eaton Corporation. Machine model is Ultrasonic Fatigue Testing Equipment (UFTE) BOKU Wien, Vienna, Austria.

Samples were machined from Ti-6Al-4V cylindrical blanks printed with EBM to resemble a cylindrical hourglass geometry with threaded end for mounting with the fatigue tester, as shown in Figure 26.

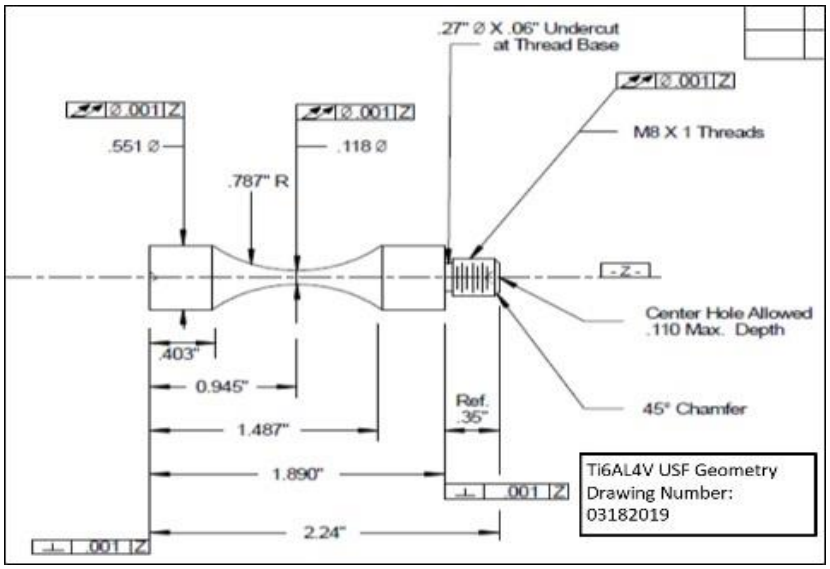

Figure 26. Diagram of EBM Ti-6Al-4V fatigue sample. All dimensions given in inches.

To simplify printing, blanks were printed as a cylinder with a constant cross-section where additional material on all sides must be removed by machining. Blank dimensions are given in Figure 27.

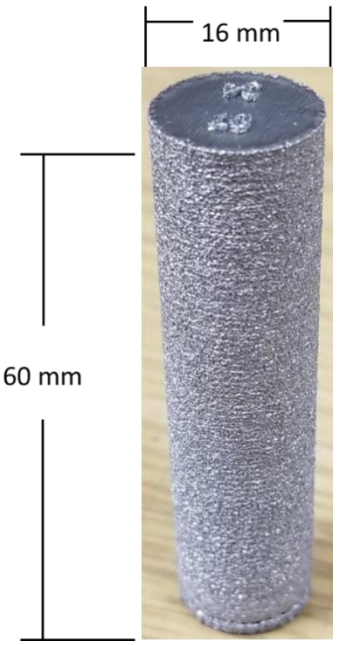

Figure 27. Dimensioned image of EBMed Ti-6Al-4V blank.

As discussed previously with Eq. (1), the most commonly investigated and influential melt parameters are Max Current (MC), Focus Offset (FO), Line offset (LO), and Speed Function (SF) measured in mA, mA, mm, and integer, respectively. With the major parameters to be tested already established, the first step of this project was to conduct further literature review on their effect on defect frequency and fatigue life.

2.2 Literature Review

2.2.1 Melt Parameters

After extensive literature review, it was surprisingly difficult to find any published papers that attempted to directly link EBM print parameters to fatigue life, as similarly stated by Victor et al. (23). The majority of papers published focus on linking melt parameters to porosity or the effect of porosity on fatigue life. For example, Gong et al. (24) used a Taguchi DOE and Archimedes method to establish general trends between melt parameters and pore volume fraction in EBM printed Ti-6Al-4V.

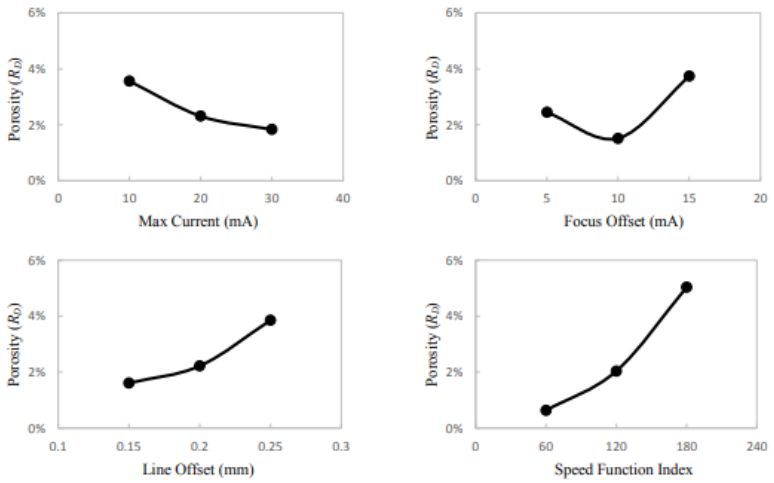

Figure 28. Mean porosity of each melt parameter tested. (24)

Referring back to the energy density in Eq. (1), Figure 28 shows a negative correlation between energy density and pore volume fraction. In fact, Tammas-Williams et al. produced a very similar chart shown in Figure 29.

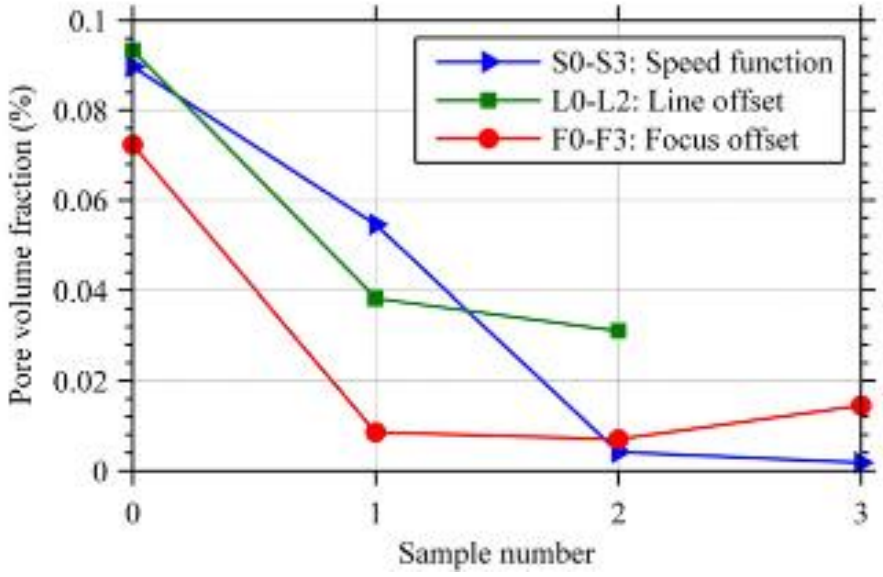

Figure 29. Pore volume fraction versus melt parameter. To clarify, sample number refers to the level of parameter tested. This table represents 11 different samples. (16)

A chart of the print settings used for each sample in Figure 29 is reproduced in Table 2.

Table 2. Melt parameters for samples 0-3 from Tammas-Williams et al. To clarify, sample number refers to the level of parameter tested. This table represents 11 different samples. Sample 3 has no LO as only 3 levels of LO were tested. (16)

Sample	0	1	2	3
Speed Function	36	30	18	12
Line Offset (mm)	0.2	0.15	0.1	N/A
Focus Offset (mA)	19	12	6	0

While the data from both authors support a common hypothesis, neither of them makes any significant attempt to link these findings to fatigue life. Also, it should be noted that, while both trends are consistent, the values tested are significantly different. For example, Gong et al. (24) tested a SF range from 60 to 180 while Tammas-Williams et al. (16) tested SF from only 12 to 36. This suggests that only the general trends are comparable among various machines and quantitative results, or explicit parameter ranges cannot be directly compared.

In addition, while increasing energy density, within a certain range, should reduce the pore volume fractions, the data from both authors show that FO has its own unique interaction with porosity. For the ranges of 5 to 15 mA, the data from both authors show that FO takes on a parabolic shape with respect to pore volume fraction, having an optimal point of minimum porosity around 11 mA, which quickly increases as FO is adjusted towards either extreme. While this parabolic trend is quite apparent in Figure 28, the lower FO values in Figure 29 based on the data by Gong et al. (24) has a much shallower slope than the other side of the parabola. Thus, caution needs to be taken when establishing the testing ranges of FO to ensure the absolute minimum is captured in the future Design of Experiments (DOE) that will be used for the basis of this dissertation.

From this portion of the literature review, it was clear that preliminary testing ranges should be generated around our specific A2X's default melt parameters and biased towards

increasing energy density, as only the trends relating melt parameters and porosity could be compared across various machines and not the explicit values.

2.2.2 Post Processing and Microstructure Effects on Fatigue

Literature review was done to investigate best practices for maximizing fatigue life with post processing and heat treatment. Perhaps the most helpful study was a review paper which consolidated EBMed Ti-6Al-4V fatigue data from a multitude of studies to identify the general effects of common post processing treatments, mainly HIPing and machining, on fatigue life. (25) Because it was a review paper, not all samples were produced, treated, or tested under the same conditions. To account for the differences in testing, each loading condition was normalized to an effective maximum applied stress (σ_{eff}), allowing for tests with different loading conditions to be directly compared. (26) The equation used for normalizing these loads is given by

$$\sigma_{eff} = \sigma_{max}\left(\frac{1-R}{2}\right)^{0.28} \quad (2)$$

where σ_{max} is the maximum applied load and R is the load ratio (R-ratio). After normalization, the collected data were categorized based on the post-treatment and plotted on a series of stress *vs.* number of cycles to failure diagrams (S-N curve) alongside conventionally produced Ti-6Al-4V fatigue samples.

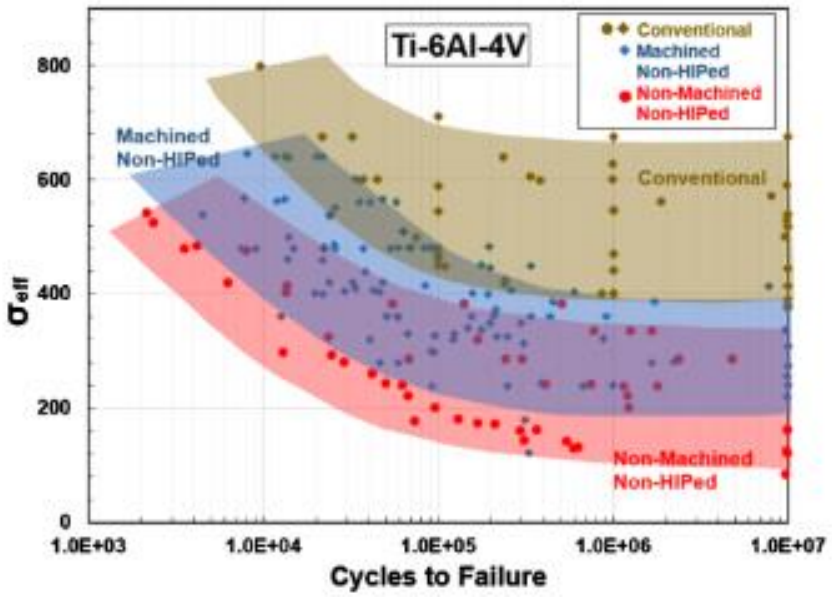

Figure 30. Collection of EBMed Ti-6Al-4V fatigue data from multiple studies alongside conventionally produced reference data. EBMed samples categorized into Non-Machined/Non-HIPed and Machined/Non-HIPed. (26)

Figure 30 shows that non-HIPed and non-machined Ti-6Al-4V samples produced by EBM have a reduced fatigue life compared to conventionally produced Ti-6Al-4V. The figure also shows that fatigue performance is improved for machined but non-HIPed samples. However, the majority of machined and non-HIPed samples performed below conventionally produced material.

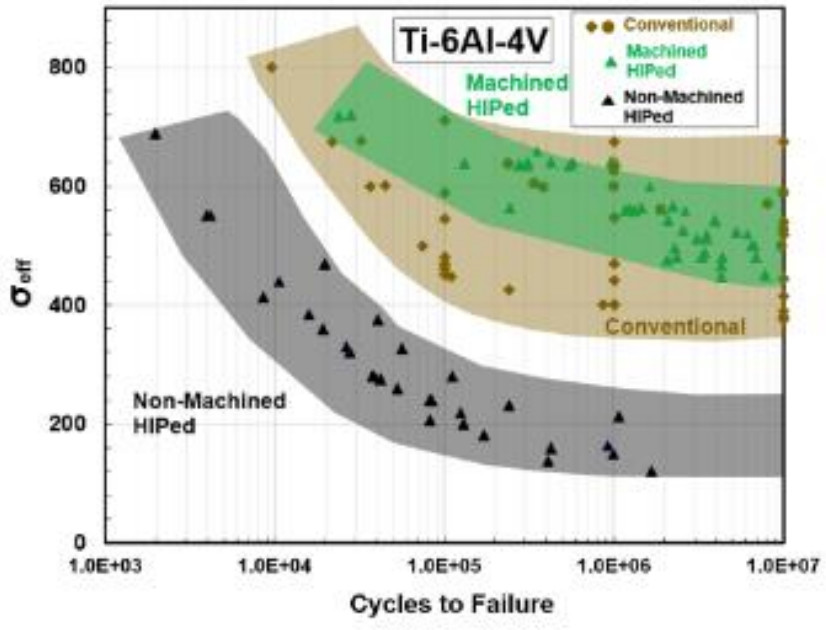

Figure 31. Collection of EBMed Ti-6Al-4V fatigue data from multiple studies alongside conventionally produced reference data. EBMed samples categorized into Non-Machined/HIPed and Non-Machined/Non-HIPed. (26)

Figure 31 Shows that HIPed, non-machined samples also have a reduced fatigue life compared to conventionally produced material. However, a sample treated with both HIP and machining performed as well, or in most cases better, than conventionally produced samples. This is attributed to prevalent internal defects and high surface roughness prevalent, for EBM samples, both of which are known to negatively affect fatigue life. Thus, both closing internal defects and removing external defects are required to significantly improve fatigue life. Interestingly Figure 32 shows that HIPing of non-machined samples only reduces variation in fatigue life without any apparent increase in performance.

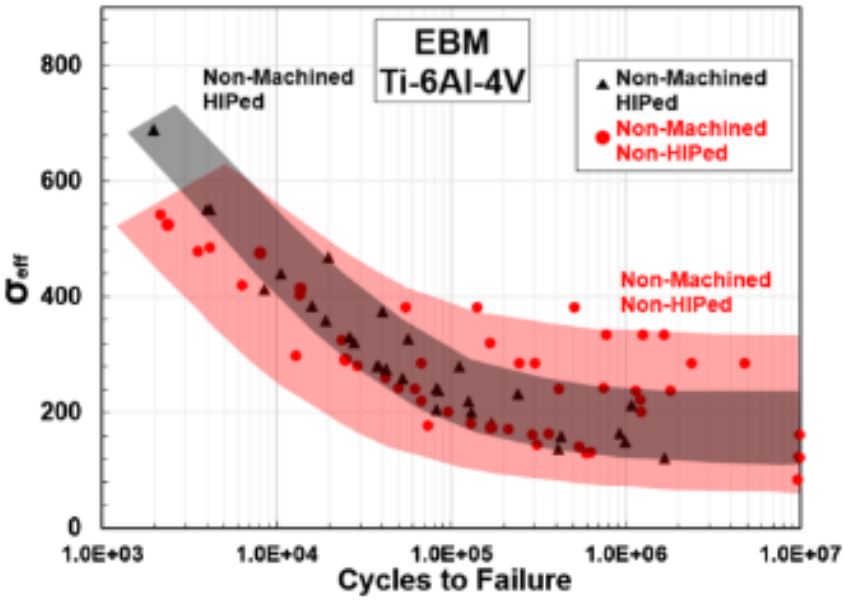

Figure 32. Collection of EBMed Ti-6Al-4V fatigue data from multiple studies. EBMed samples categorized into Non-Machined/HIPed and Non-Machined/Non-HIPed. (26)

Based on Li et al.'s (26) findings, it is clear that our samples would need to be both HIPed and machined to maximize their fatigue life.

The next step was to investigate if additional heat treatment would be required to further improve fatigue performance. One of, if not, the most thorough studies into fatigue performance of Ti-6Al-4V in the VHC range was published by Wu et al. (27), using the data from various publications to populate charts with fatigue properties of three common microstructures: Bi-Modal, lamellar, and Equiaxed structures. Information recorded included: microstructure parameters (lath thickness, grain size, etc.), test frequency, stress ratio, and endurance strength. Microstructure parameters not directly provided in the literature were calculated from SEM images provided in each publication using Nano Measurer 1.2 software. With these data, Wu et al. (27) began analyzing the effects of each microstructure, and their respective parameters, on the fatigue life of Ti-6Al-4V. First trendlines for each microstructure were plotted on the S-N

diagram to compare the effect of microstructure type on fatigue life, as presented in Figure 33. (27)

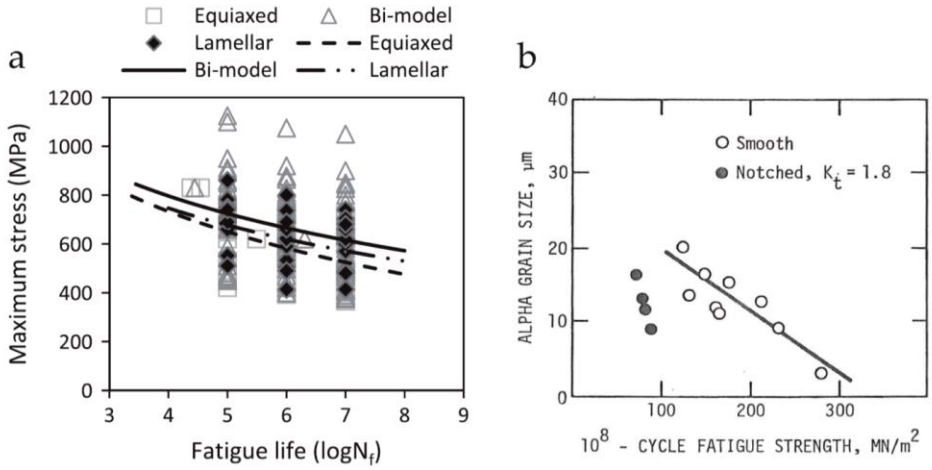

Figure 33. a) S-N diagram for Equiaxed, Bimodal, and lamellar Ti-6Al-4V with fitted exponential curves. b) Effect of α grain size on endurance limit at 10^8 *cycles for smooth and notched fatigue samples. (27)*

Although the bimodal microstructure has superior fatigue performance over Lamellar and Equiaxed grain structures, it is unfortunately not achievable with current AM technology as it requires extensive heat treatment. Of the remaining two, the lamellar microstructure has a slight edge over the equiaxed microstructure at the loads under 700 MPa. (27) Thankfully due to EBM's long cooling rates, the microstructure most typically seen in EBMed Ti-6Al-4V is a type of the lamellar structure called Widmanstätten or basket-weave structure, an example of which is provided in Figure 34. (28)

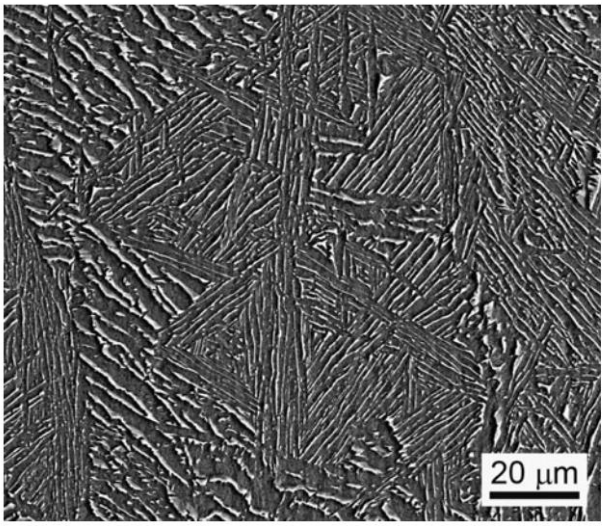

Figure 34. SEM-SE image of Widmanstätten microstructure in EBM produced Ti-6Al-4V. (28)

For the same data in Figure 33, the average α grain size was plotted against the load on the samples which reached 10^8 cycles which showed a clear negative correlation between the α grain size and fatigue strength in the VHC regime. Similar results were found by Everets et al., who studied how α grain size affects fatigue lives of the bimodal Ti-6Al-4V wires. (29)

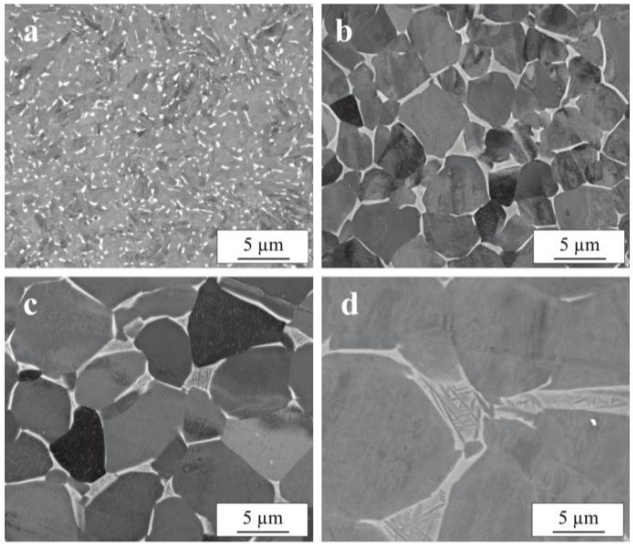

Figure 35. Cross section of Ti-6Al-4V wires. a) Microstructure A. b) Microstructure B. c) Microstructure C. d) Microstructure D. (29)

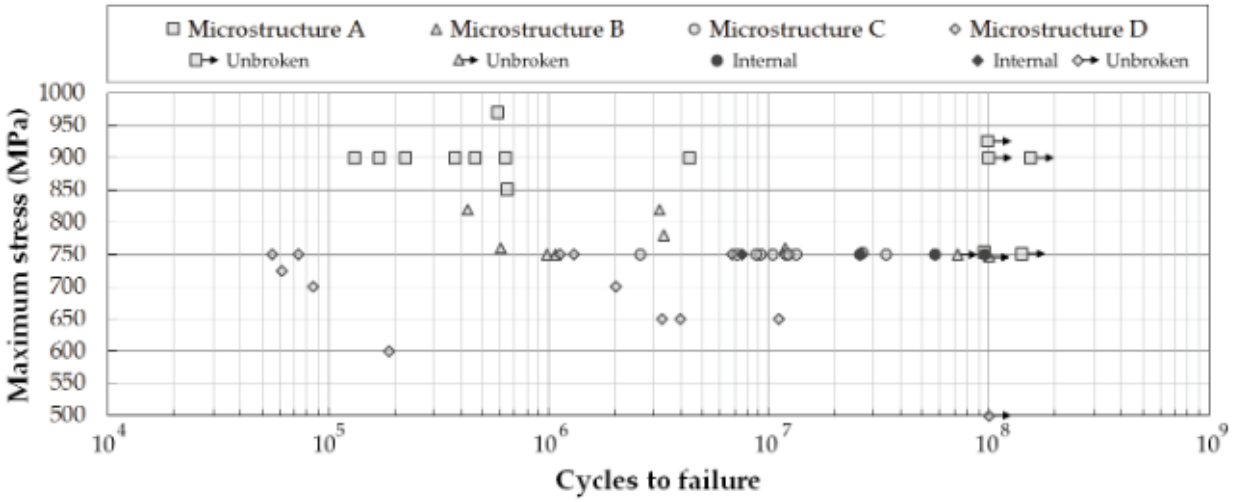

Figure 36. S-N chart for Bimodal Ti-6Al-4V wires of microstructures A, B, C, and D. Symbols with right-facing arrows represent unbroken runouts (7). Darker shaded symbols represent failure from internal crack initiation (4). R = 0.1. (29)

By controlling the grain size of the Ti-6Al-4V wires to produce one of the four microstructures shown in Figure 32, Everates et al. (29) concluded that in general fatigue life increases as average α grain size decreases. Günther et al. (17) came to a similar conclusion, and found that apart from HIP and surface treatment the best way to further improve the fatigue life of EBMed Ti-6Al-4V is to decrease the size of α phase clusters and grain size. (17)

From this information we were able to conclude that the best way to maximize the fatigue life of our samples was to produce the lamellar α + β structure with the smallest α-grain size possible.

2.2.3 Heat Treatment

After determining the ideal microstructure for our material, the next step was to determine the best way to achieve it using heat treatment. To begin, standard HIP treatment for AM produced Ti-6Al-4V, was found to be 900 - 920°C for 2-hours and 100 MPa. (30) However, this treatment was shown to almost double the α-laths thickness. (30) (31) (32) (33) One of our goals was to investigate the effect of HIP treatments on fatigue life. As such, it was decided that

a sub and super-transus HIP treatment would be studied (discussed further below). With the purpose of this study being focused on industrial applications, it was decided that any heat treatment performed would be incorporated into the HIP treatment to reduce the number of required post processing steps. The goal for the sub-transus HIP treatment was to incorporate the information gained by this literature review to try and improve on the standard HIP cycle. The HIP temperature of 800°C which is lower than standard was selected to minimize α-grain growth during HIP treatment while a higher than standard pressure of 200 MPa was selected to compensate for the lower temperature in order to ensure the closure of any large internal porosity. The remaining samples were treated with a super-transus HIP treatment at 1100°C for 2-hours, followed by a -2.5°C/min quench. For most crystalline metals, the best way to minimize grain size is by rapidly cooling from an elevated temperature. However, like steels, titanium forms martensitic phases when rapidly cooled from above the β-transus, forming small needle-like α grains known as alpha prime (α'). (18) Although these α' needles can be very small, they produce unfavorable mechanical properties like reduced ductility, and are not commonly used in industry. (18) A study by Xu et al. (34) demonstrated how SLMed Ti-6Al-4V made primarily of α' displayed inferior fatigue properties compared to an ultrafine $\alpha + \beta$ microstructure and conventional mill-annealed material. (34)

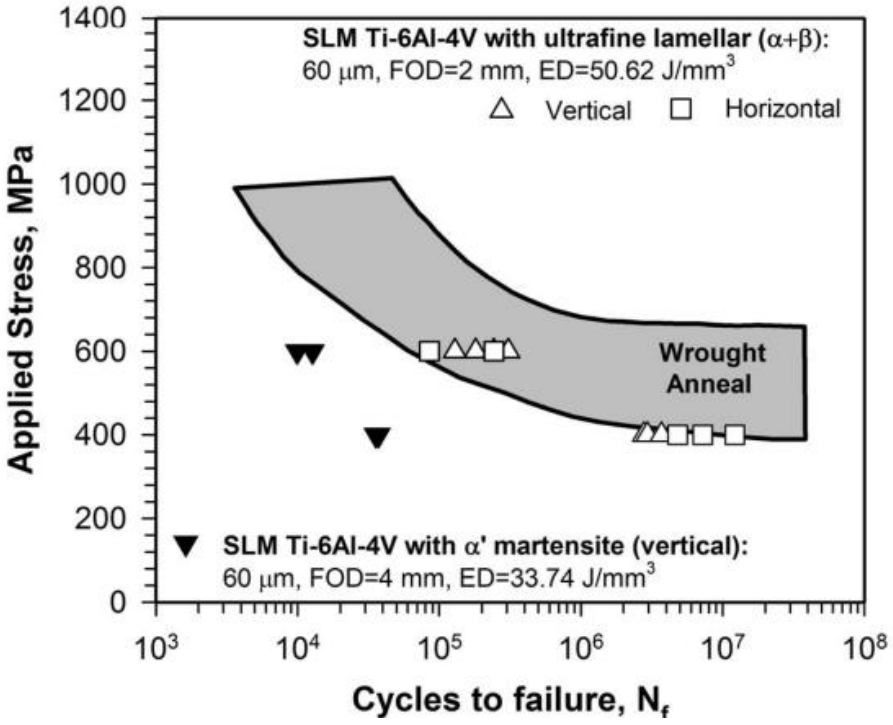

Figure 37. S-N curve for SLM-produced Ti-6Al-4V with ultrafine lamellar, α′, and mill-annealed structures. (34)

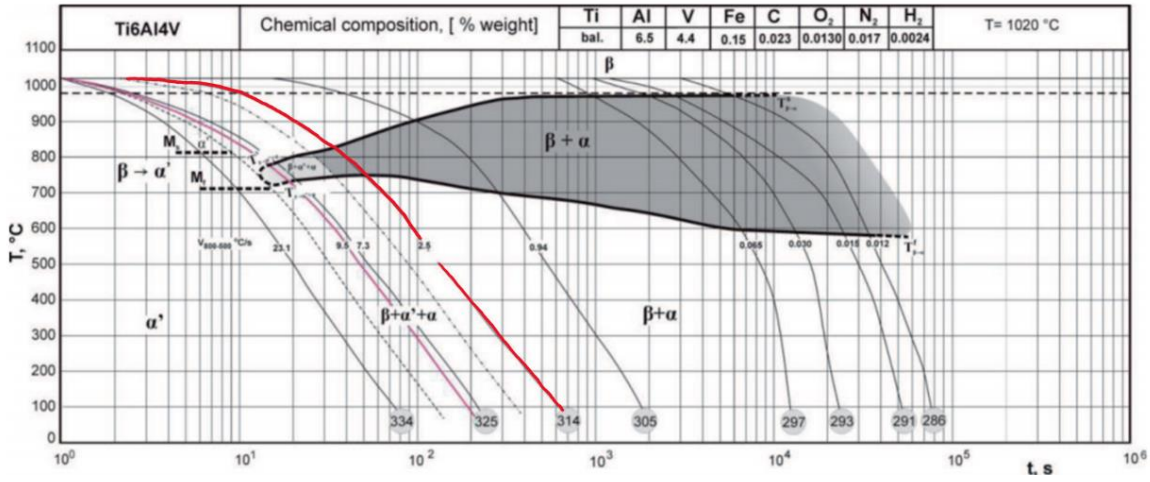

Figure 38. CCT diagram for Ti-6Al-4V with -2.5°C/min traced in red. (35)

The quench rate was selected using a Ti-6Al-4V Constant Cooling Transformation (CCT) diagram, provided in Figure 38. The rate of -2.5°C/s was selected as it is slow enough to prevent

the formation of α', with a small buffer, and fast enough to minimize grain growth. The region where α' begins to form is highlighted in Figure 39.

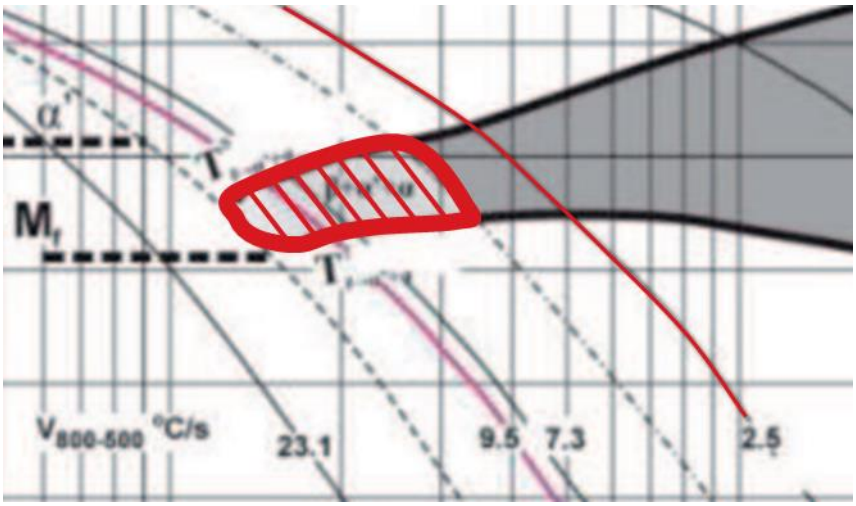

Figure 39. CCT Diagram for Ti-6Al-4V focused on $\beta + \alpha + \alpha'$ region (outlined and shaded in red). -2.5°C/s traced in red. (35)

The cooling rate from the β phase field in Ti-6Al-4V is also associated with yield strength and tensile elongation through control of α colony size. Higher cooling rates result in smaller α colonies and shorter slip lengths as a result. (18) Effects of cooling rate on various titanium alloys can be seen in Figure 40.

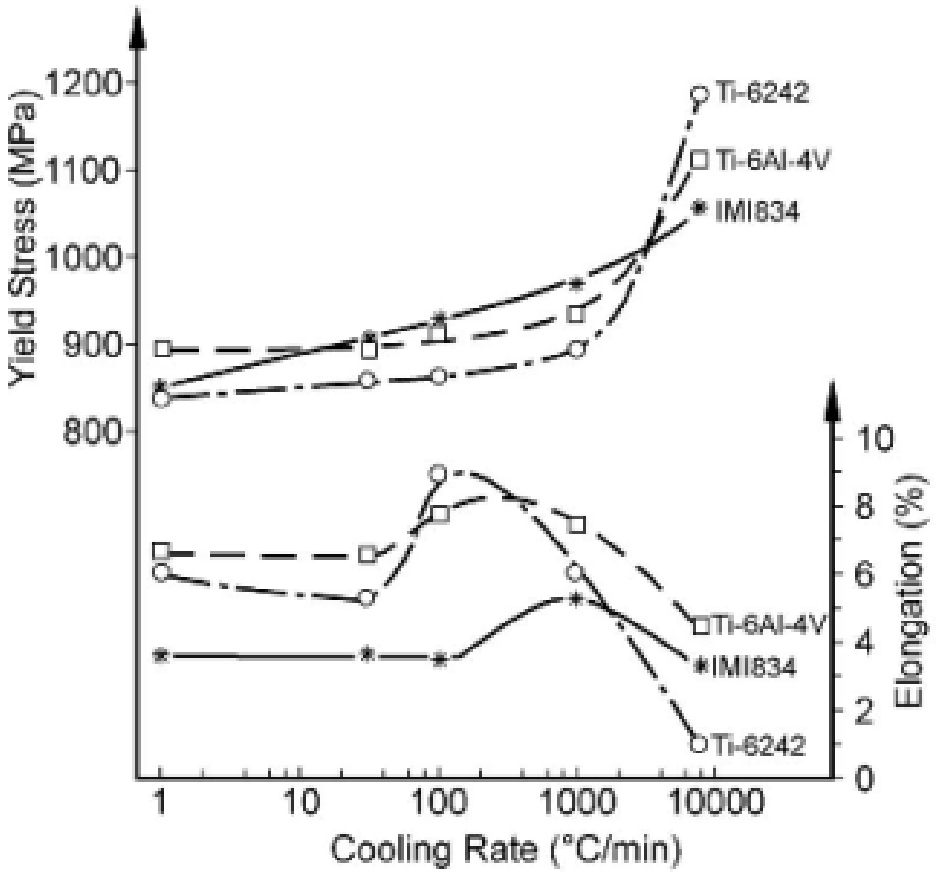

Figure 40. Effect of cooling rate from β phase on yield strength and tensile elongation. (18)

For reference, the proposed quenching rate of 2.5°C/s is equal to 150°C/min. The sharp rise in yield strength and decrease in elongation is associated with the transition to a martensitic dominated microstructure, further illustrating the need to limit the formation of α'.

Quintus Technologies, located outside of Columbus Ohio, was found to be the only company in the U.S. with equipment capable of combining the HIP and quench treatments. To minimize any variability between HIP treatments, both sets of samples were performed HIP treatment at Quintus Technologies.

In addition to the effort of minimizing α lath thickness, the super-transus heat treatment was included in order to investigate if β phase heat treating would eliminate the directionality associated with the as-printed columnar grain structure. Columnar grain structure is common in

as-fabricated Ti-6Al-4V samples produced with AM as a result of solidification in the build bed. As newly melted material solidifies, its structure is influenced by the previous layer aligning the grain boundaries and continuing the grain upwards, depending on the material, this will result in elongated columnar grains that follow the build direction. (36) As expected, these highly elongated grains can cause anisotropy in the material. An example of this columnar grain structure is provided in Figure 41.

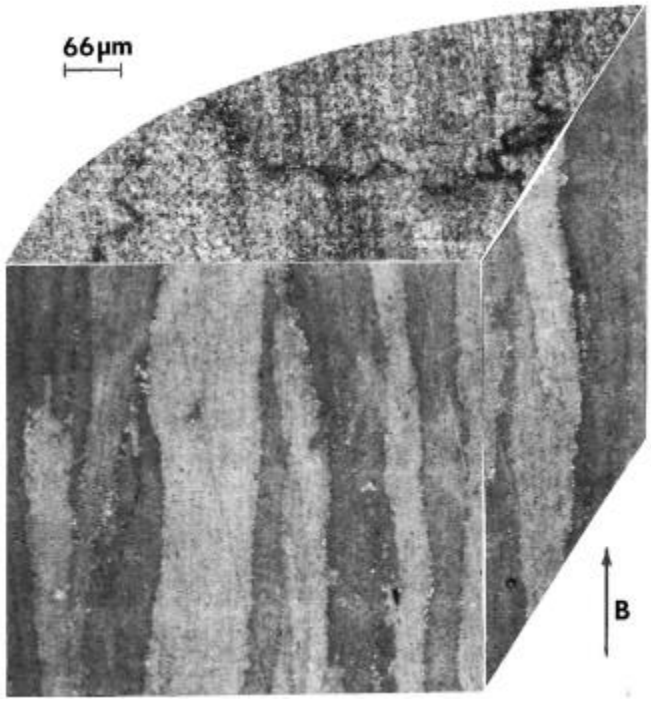

Figure 41. Optical microscopy composition of columnar grain structure of EBM produced Rene 142 Ni-base super alloy. Build direction indicated by B. (36)

The effect of microstructure directionality on fatigue life was not examined in this study, as incorporating it into the DOE would double the number of samples required, as well as introduce additional uncertainties related to how the melt parameters interact with printing different layer profiles. Thus, all samples for this study were printed vertically, additional print details are provided below in Chapter 2.4. However, the effects of the super-transus HIP treatment on columnar grain structure could be examined using metallography and statistically supported by

the fatigue results. Since the columnar grain structure and melt parameter effects are both consequences of thermal history, it is expected that the super-transus HIP treatment cannot affect one without also affecting the other. Statistical results that describe the effect of the super-transus HIP treatment on melt parameters could also be used to support any observed effects of the HIP treatment on columnar grain structure. For example, if correlations between melt parameters and fatigue life hold for both the sub and super-transus HIP conditions and no effects on the as-printed columnar grain structure were observed, then the fatigue results could be used to statistically support claims that the super-transus HIP treatment had no effect on the columnar structure. Conversely, if statistically significant correlations between melt parameters and fatigue life were found for the sub-transus samples, but not the super-transus samples and changes in the columnar grain structure were found, then the fatigue results could be used to statistically support claims that the super-transus HIP treatment had an effect on both melt parameter effects and the columnar grain structure. However, in both cases no claim about the effect of directionality on fatigue life could be made.

After treatment, both sets of samples were sent out for machining into the final hourglass shape and to remove any defects or roughness associated with the printed surface.

2.3 Preliminary Testing

After determining the major melt parameters to be investigated, the next step was to establish a range for each parameter to be varied that would cause minimal defects. To accomplish this, several preliminary test builds were printed. These builds included the same diameter of 16 mm of the final blanks but only 10 mm tall to reduce material use and build time. To mitigate any effects related to build plate leveling or warped build plates, 2 mm of support structure, generated by Materialise software (Materialise NV – Leuven, Belgium), were

incorporated into the blank's stereolithography (STL) file. This was done for all EBM samples presented in this thesis (preliminary and final samples). An example of these support structures can be seen in the bottom of Figure 27.

For the first of these preliminary builds, the default melt parameters pre-installed in the machine were used as a starting point. Based on the theory that increasing energy density generally should result in reduced porosity, each parameter range started with the default values and trended in the direction of increasing energy density. The default values and initial ranges can be found in Table 3, while the values for each parameter can be found in Table 4.

Table 3. Preliminary build 1 parameter ranges. Default values preload on Arcam A2X melt themes highlighted in green.

Parameter	Default	Lower limit	Upper limit
Focus offset (mA)	25	0	30
Line offset (mm)	0.2	0.01	0.2
Speed Function	45	10	45
Max Current (mA)	20	20	32

Table 4. Preliminary build-1 parameter values.

Max Current (mA)	20	22	24	26	28	30	32
Speed Function	10	15	20	25	30	35	40
Line offset (mm)	0.01	0.04	0.07	0.1	0.13	0.16	0.19
Focus offset (mA)	0	5	10	15	20	25	30

A constant risk associated with EBM is part swelling, which, while not unique to EBM, is more prevalent with EBM due to the vacuum atmosphere and high-power energy source. As a result of the high vacuum chamber, there is almost negligible convection, significantly reducing the cooling rate of the powder bed. While reduced cooling rates can benefit by reducing residual stress, it also increases the risk of overheating the print material, resulting in material vaporization and/or swelling. As discussed, the rationale behind increasing energy density is that

melting during later layers can re-melt previously deposited ones allowing trapped gases to escape. This also means that excessive beam power can cause heat to build up between layers to a point where the combined thermal expansion of the material pushes the newest layer out of the build bed far enough to interfere with the rake. In severe cases, no new powder is deposited on the raised areas causing the beam to continue to reheat the previously printed layers again and again in a kind of snowballing effect. Unfortunately, there is no way for the machine to detect this phenomenon and will continue to print until the part swells enough to completely remove the rake blades and eventually block the rake arm, forcing the machine to pause the build, which nearly always results in a complete build loss. The result of excessive runaway swelling can be seen in Figure 42.

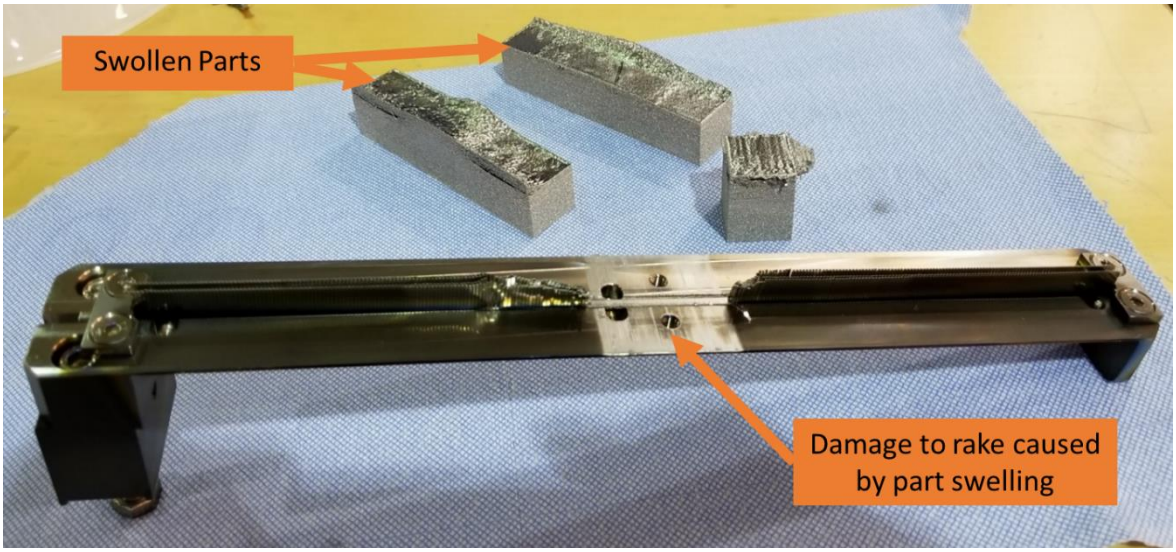

Figure 42. Swelling damage to Arcam A2X rake after failed build.

Not every swelling incident ends with such devastation as some minor swelling around the edges does not significantly affect printing. However, the effects of swelling defects on part performance are unknown and thus should be avoided when possible.

Additional caution was taken with the first preliminary build as it was unclear if the combination of parameters biased towards higher energy density would result in swelling. To

minimize risk of swelling, only a single parameter was adjusted for each sample while the remaining three were kept at the default values to reduce the chances of overheating and to make the effect of a single parameter more apparent. A list of the samples and their respective print settings can be found in Table 5.

Table 5. Preliminary build 1 sample parameters.

Sample	1	2	3	4	5	6	7	8	9	10	11	12	13	14	15	16	17	18	19	20	21	22	23	24	25	26	27	28
Max Current (mA)	20	20	20	20	20	20	20	20	20	20	20	20	20	20	20	20	20	20	20	20	20	20	22	24	26	28	30	32
Speed Fucntion	45	45	45	45	45	45	45	45	45	45	45	45	45	45	10	15	20	25	30	35	40	45	45	45	45	45	45	45
Line Offset (mm)	0.2	0.2	0.2	0.2	0.2	0.2	0.2	0.01	0.04	0.07	0.1	0.13	0.16	0.19	0.2	0.2	0.2	0.2	0.2	0.2	0.2	0.2	0.2	0.2	0.2	0.2	0.2	0.2
Focus Offset (mA)	0	5	10	15	20	25	30	25	25	25	25	25	25	25	25	25	25	25	25	25	25	25	25	25	25	25	25	25

Results of this first preliminary print are presented in Figure 43. Typically, it is possible to print part numbers directly on the surface of parts, however due to the expectation of surface defects that would mask any such markings, special care was taken when removing the build to ensure the parts were left on the plate. Since the print positions for each sample are known they could be labeled using a marker. Following the color convention established in Table 4 and Table 5, the parameter tested for each row, from top to bottom, in Figure 43 is MC, SF, LO, and FO.

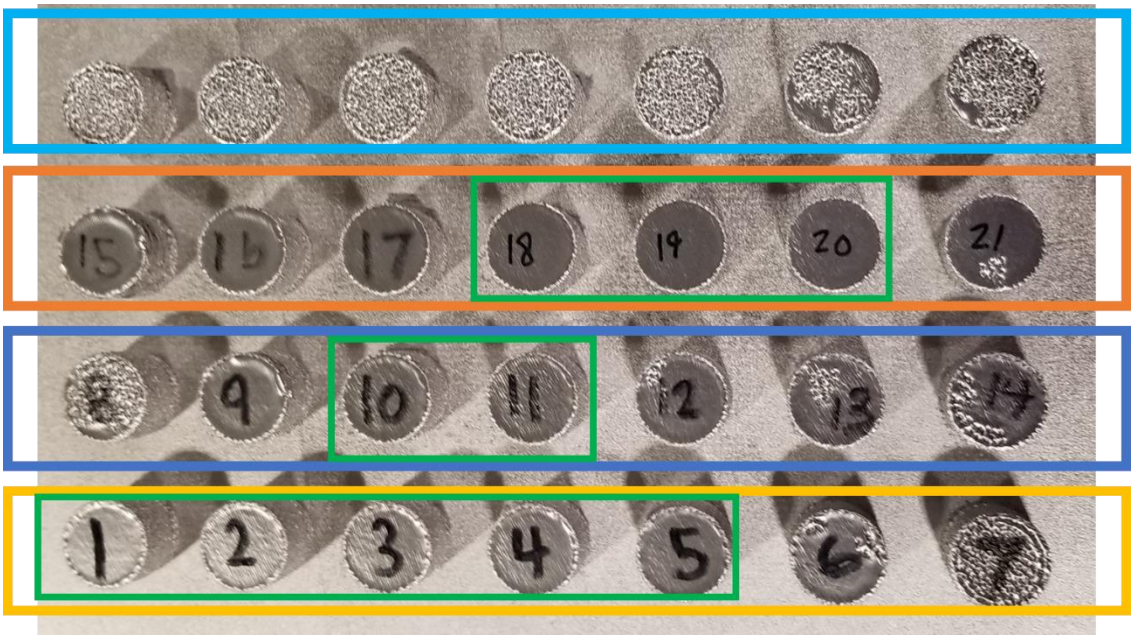

Figure 43. Preliminary build 1 test results. Samples boxed in green did not exhibit significant defects and were used as the new parameter ranges for subsequent preliminary tests. Each row featured a single parameter adjusted while others were left as default, matching the color code from the previous table. From top to bottom: Max Current, Speed Function, Line Offset, Focus Offset.

A significant amount of surface porosity was found on a number of parts, with MC in particular having excessive surface porosity across all samples. Cross-sectional analysis, of sample 22, presented in Figure 43, reveals the surface porosity is not being closed by subsequent melting and is instead forming large, vertically orientated lack of fusion (LOF) pores. The cross-sectional image is provided in Figure 44. From this, it can be concluded that any parameter with significant surface porosity cannot be closed with HIPing and is not viable. As such, these parameters were not considered in future testing. Additional cross-sectional images of remaining samples can be found in Figure 44Figure 47. Although the LOF pores is the indication of insufficient heat input which could be compensated for through adjustment of the remaining parameters, it was decided to only keep values that produced good parts during this test to prevent any instance of a parameter combination resulting in LOF, as such significant defects would have an obvious detrimental effect on fatigue life and thus not be worth the time and

resources for post processing and testing. In addition to severe surface porosity, some samples were eliminated due to the onset of swelling. For example, samples 9, 15 and 6 in Figure 43 show sufficient swelling to potentially interfere with printing if the samples swelled any further. Samples with neither swelling nor excessive surface porosity are boxed in green, and they were used to refine the parameter ranges in the second iteration presented in Table 6.

Table 6. Revised build parameter ranges for preliminary build 2.

Parameter	~~Default~~	Lower limit	Upper limit
Focus offset (mA)	~~25~~	0	25 ← 30
Line offset (mm)	~~0.2~~	0.01 → 0.07	0.13 ← 0.2
Speed Function	~~45~~	10 → 20	40 ← 45
~~Max Current (mA)~~	~~20~~	~~20~~	~~30~~

Figures below provide further insight into the decision making process used to refine the parameter range following this preliminary build.

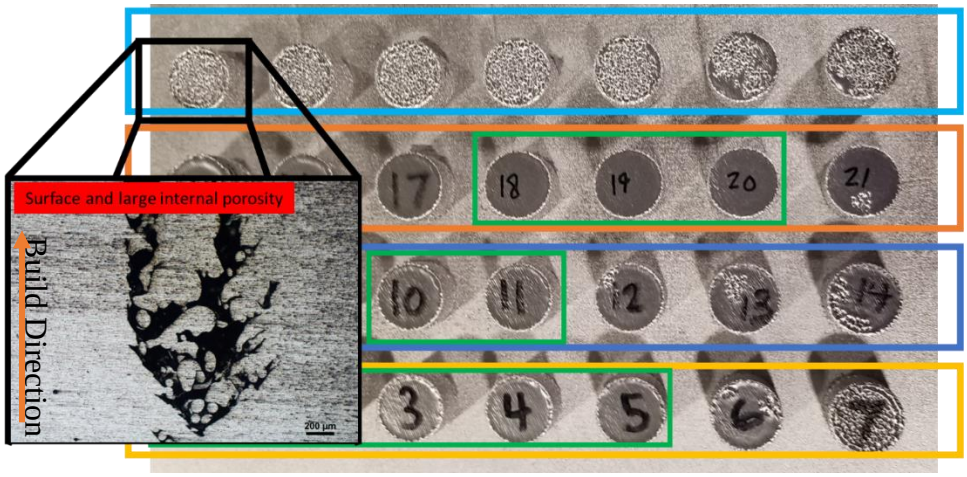

Figure 44. Cross section image of sample 22 from preliminary build 1. Build direction along bottom to top.

The top row of samples had MC increased left to right from 20 to 32 mA. Sample 22, along with the rest of the MC samples (top row) were eliminated due to excessive LOF porosity. Discussions with Arcam technicians suggested that due to how the software controls melting, it

is typically better to leave MC constant and adjust the other melt parameters to achieve the desired energy density.

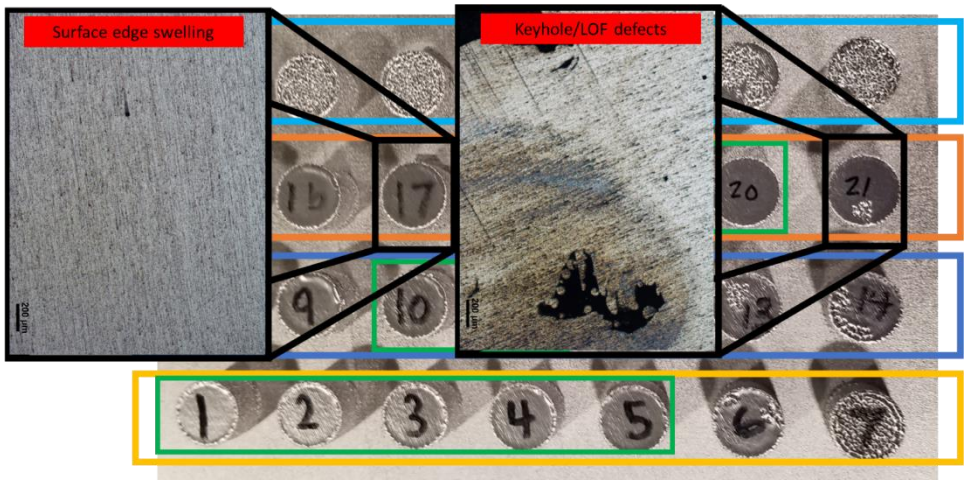

Figure 45. Cross section image of sample 17 (left) and sample 21 (right) from preliminary build 1.

The second row of the samples varied SF, increasing left to right from 10 to 40. Samples 15 – 17 were found to have significant edge swelling. As SF increased, energy density decreased resulting in no swelling for samples 18 – 19. As AF continued to increase, large amounts of LOF porosity were found on the surface of sample 21.

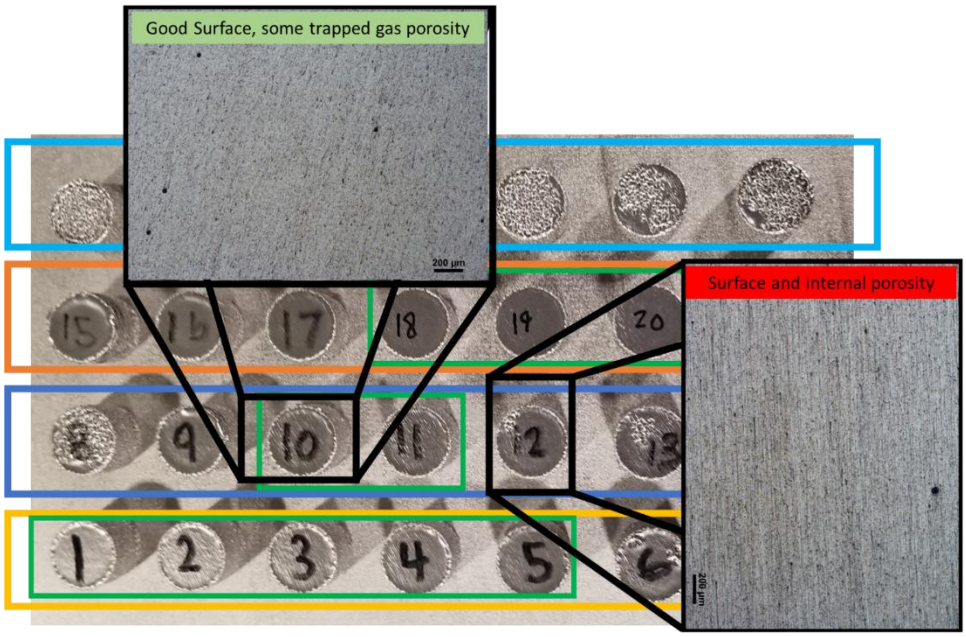

Figure 46. Cross section image of sample 10 (left) and sample 12 (right) from preliminary build 1.

The third row was produced to vary LO, increasing left to right from 0.01 mm to 0.19 mm. Samples 8 and 9 showed signs of swelling, which is expected given that they had the lowest two LOs tested. Surface porosity on the surface of sample 8 is likely keyhole porosity given the presence of swelling and increased energy density from decreasing LO. Samples 10 and 11 were found to have no swelling or any significant surface or internal porosity. As LO increased further, surface porosity, most likely LOF, began to occur on sample 12. Cross-sections of sample 12 revealed additional large internal pores, thus the settings for samples 8 – 9 and 12 – 14 were eliminated.

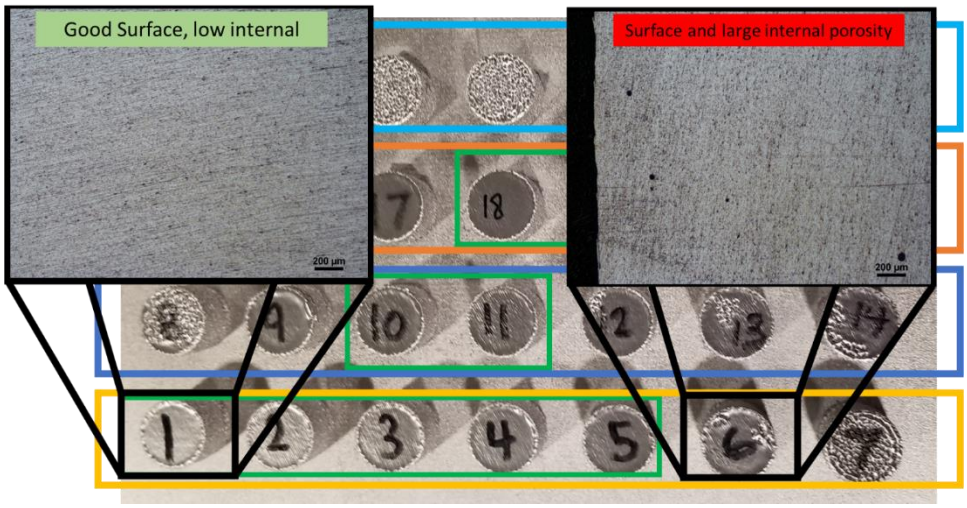

Figure 47. Cross section image of sample 1 (left) and sample 6 (right) from preliminary build 1.

The last row of samples was produced to vary FO, increasing left to right from 0 to 30 mA. Samples 1-5 showed no significant signs of swelling or surface connected porosity. Sectioning of sample 1 revealed no additional large internal porosity. Samples 6 and 7 have large surface and internal porosity, these settings were eliminated. Although FO is not included in the energy density formula Eq. (1), these results indicate that energy density decreases as FO increases. A trend of this kind is expected as FO controls the focal point of beam. Overall, all observations and refinements made during this preliminary test directly followed the trends presented by Gong et al. (24) and Tammas-Williams et al. (8)

With the parameter ranges narrowed down, a 3 factor, 5 level, orthogonal array produced with the Taguchi method was constructed to speed up optimization. Details on the specific sample parameters is provided in Table 7. Unfortunately, the build failed three quarters of the way through printing due to excessive swelling. Examination of the build bed revealed the powder bed surrounding the parts had swollen, forming a square of raised, semi-sintered powder, as seen in Figure 48. Much like part swelling, the powder bed can be similarly overhead and swell enough to interfere with raking. This typically occurs when the preheat power settings are

set too high. At the start each layer, freshly raked powder is prepared for printing by first preheating the entire build bed (preheat I), which is then followed by a second preheat step (preheat II) concentrated on the areas immediately surrounding the print regions, matching the observed swollen region. Further investigation of the build settings revealed that a higher power preheat theme was incorrectly selected, indicating the swelling was caused by incorrect preheat settings and is unrelated to the melt parameter selection. Images of the results are provided below.

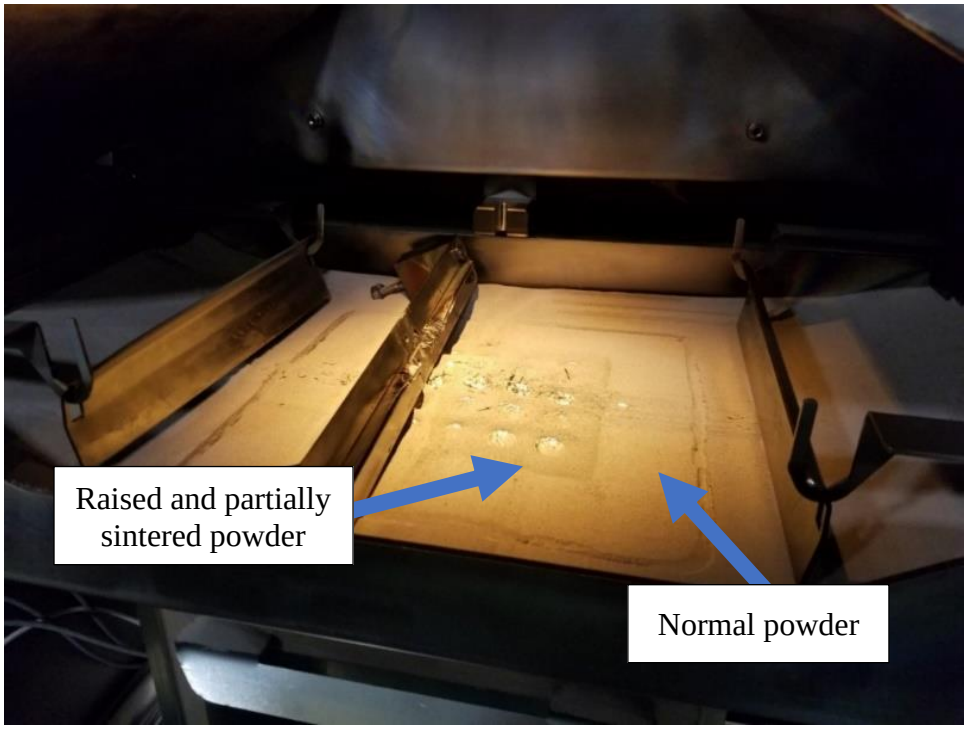

Figure 48. Swelling damage from failed preliminary build 2.

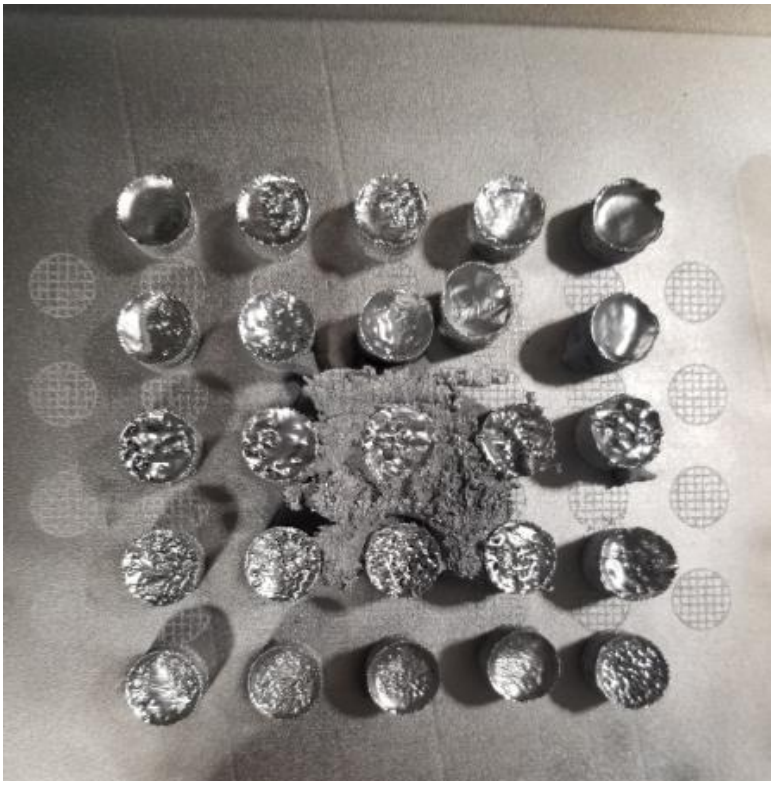

Figure 49. Samples with loose powder removed from failed preliminary build 2.

Further inspection of the samples revealed no evidence of swelling during the first quarter of the build after which a distinct curve on the side of the cylinders was seen, indicating edge swelling. Previous builds where this setting was mistakenly used had similar results where the parts would print normally near the build plate but after passing some critical height would rapidly swell from excessive preheating. Interestingly, a small number of samples had protrusions or bulges on the sides while a majority of samples seemed completely normal with an expected surface texture. These bulges, circled in red in Figure 50, are thought to be the result of excessive heat or beam instability as a result of the melt parameters and not the preheating as they occurred below the clear start of swelling and were not present on all samples as seen in Figure 51.

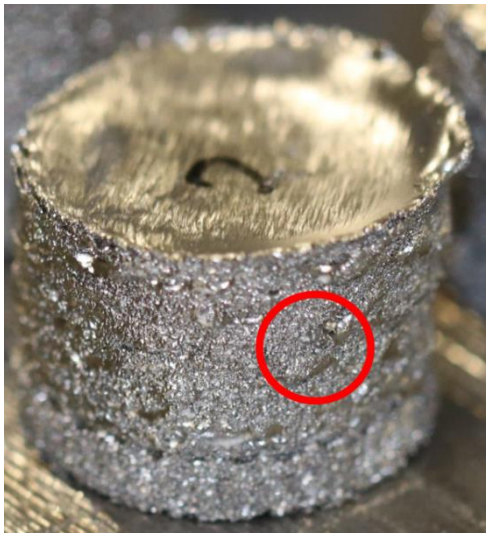

Figure 50. Sample 2 from failed preliminary build 2 with surface protrusions indicating unstable printing.

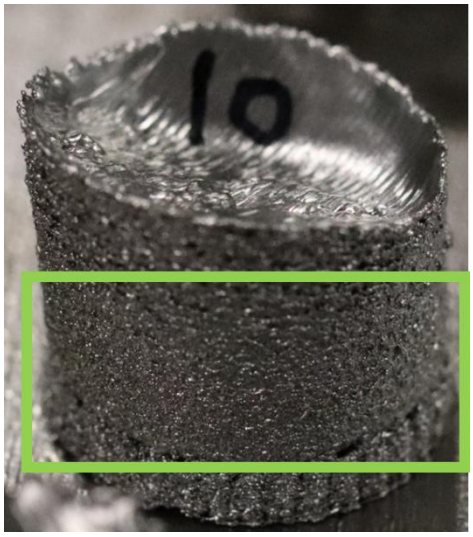

Figure 51. Sample 10 from failed preliminary build 2 with surface clear of protrusions indicating stable printing.

To make the best use of these samples, each one was evaluated using a binary scale, good or bad, to indicate the presence of surface bulges. These results were fed into the DOE and evaluated using MINITAB to search for any correlation between bulges and melt parameters. Melt parameters and evaluation for each sample can be found in Table 7. Table 7, where a “0” indicates the presence of bulges and a “1” indicates the expected surface.

Table 7. Binary good/bad labels for each sample of failed preliminary build 2. Samples labeled bad had surface protrusions below the onset of runaway swelling. Samples labeled good had normal surface free of protrusions.

Sample	Speed Function	Line Offset (mA)	Focus Offset (mA)	Good/Bad
1	20	0.07	0	0
2	20	0.085	6.25	0
3	20	0.1	12.5	0
4	20	0.115	18.75	0
5	20	0.13	25	1
6	25	0.07	6.25	0
7	25	0.085	12.5	0
8	25	0.1	18.75	0
9	25	0.115	25	1
10	25	0.13	0	1
11	30	0.07	12.5	0
12	30	0.085	18.75	0
13	30	0.1	25	1
14	30	0.115	0	1
15	30	0.13	6.25	1
16	35	0.07	18.75	0
17	35	0.085	25	1
18	35	0.1	0	1
19	35	0.115	6.25	1
20	35	0.13	12.5	1
21	40	0.07	25	1
22	40	0.085	0	1
23	40	0.1	6.25	1
24	40	0.115	12.5	1
25	40	0.13	18.75	1

After running the results through MINITAB, there was a very clear correlation between the unstable melt surface and melt parameters. A plot illustrating this correlation is provided in Figure 52, where a lower “Mean of Means” value indicates higher likelihood of the level for

each parameter showing signs of bulges. The horizontal labels of 1 to 5 represent the levels for each parameter, refer to Table 7 for specific values.

Figure 52. Mean of mean plot generated using MINITAB from binary good/bad sample data. A lower mean of means indicates higher likelihood of having a "Bad" label. A, B, and C refer to SF, LO, and FO respectively. 1 to 5 labels on the x-axis refer to respective parameter level.

Due to the clear trends found in Figure 52, the lowest two levels for SF and LO were removed from consideration. Although FO had similar mean of mean values as the removed levels of SF and LO, no FO values were removed as it was not clear how FO was contributing to surface bulges due to the significant inflection point between levels 4 and 5. Refined parameter ranges for the third and final preliminary build can be found in Table 8.

Table 8. Refined parameter ranges for preliminary build 3.

Parameter	Lower limit	Upper limit
Focus offset (mA)	0	25
Line offset (mm)	0.07 → 0.1	0.13
Speed Function	20 → 30	40

Preliminary build 3 finished without significant swelling or surface porosity, as seen in Figure 53. Additional post processing steps were taken to determine if any additional parameter refinement was required. Each sample was sectioned, polished, and inspected with an optical microscope to inspect the porosity morphology. Fortunately, no lack of fusion or keyhole porosity was found and only trapped gas porosity was present. At first glance, some samples appeared to have significantly lower number of these pores. To identify any relationship between melt parameters and trapped gas porosity frequency, the total number of pores, across the entire cross section, larger than 10μm in diameter were tallied for each sample. An optical image of identified pores for sample 15 is provided in Figure 53.

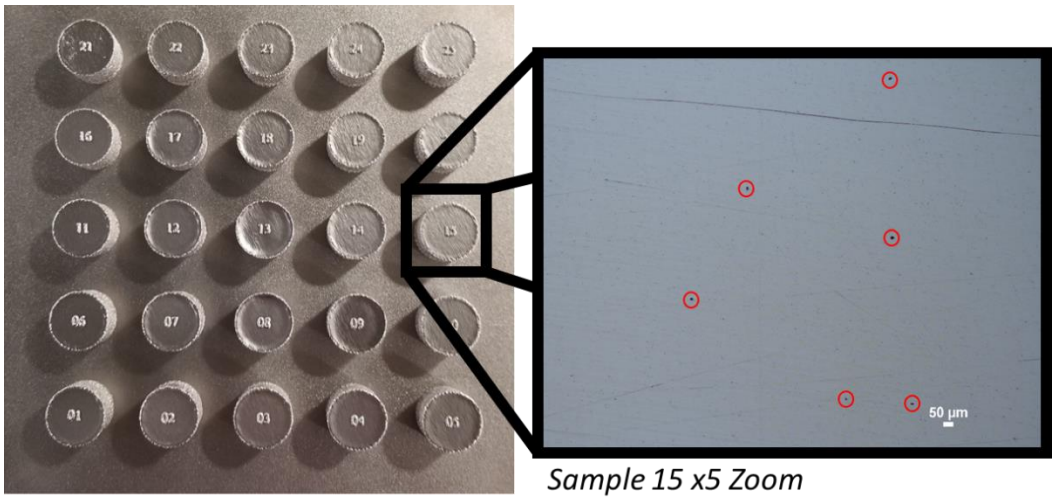

Figure 53. Results of preliminary build 3, featuring cross sectional image of sample 15 with trapped gas pores circled in red.

As described previously, the pore counts for each sample were fed into MINITAB to identify any correlations between melt setting and pores frequency. Results of this analysis are presented in Figure 54, where a larger "Mean of Means" value indicates a higher frequency of porosity.

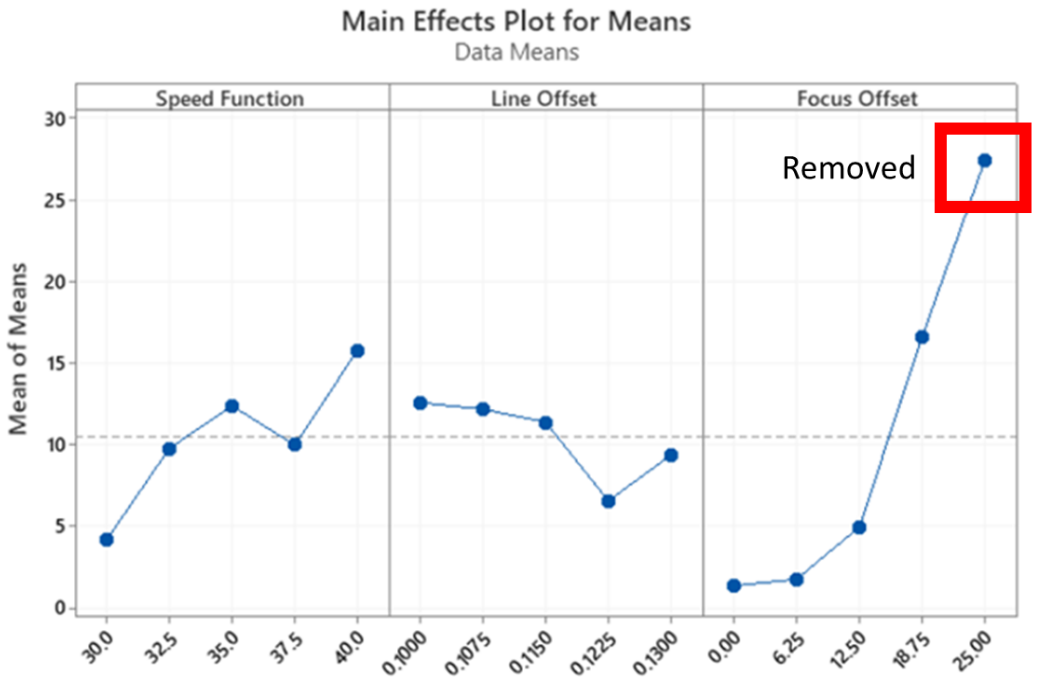

Figure 54. Mean of mean plot generated with MINITAB using trapped gas porosity count data. A larger mean of mean value indicates higher occurrence of large, trapped gas porosity. Parameter level boxed in red was removed due to excessive pore count.

From the analysis, FO of 25mA was associated with the largest number of pores larger than 10µm, and thus eliminated. Although there is a clear trend between increasing FO and porosity frequency, more FO levels were not removed to ensure that enough FO values were tested to identify any effects of FO on fatigue life. A sharp increase in porosity frequency at higher FO values was also observed by Gong et al. (24), as seen in Figure 55.

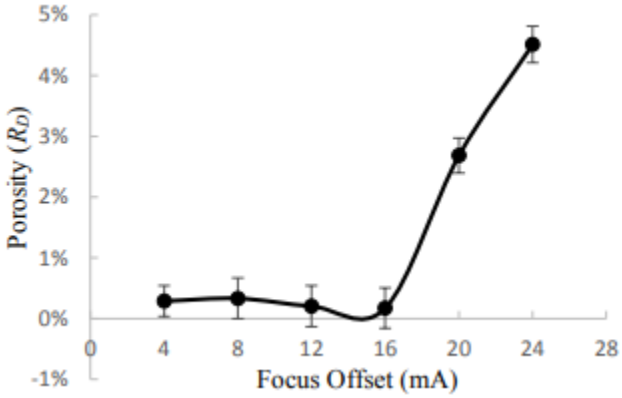

Figure 55. Porosity versus Focus Offset plot showing a large spike in porosity at higher Focus Offset values. (24)

Following this final refinement, the parameter range for the final DOE design was locked in and presented in Table 9.

Table 9. Final parameter ranges for main melt themes determined by preliminary testing.

Parameter	Lower limit	Upper limit
Focus offset (mA)	0	20
Line offset (mm)	0.1	0.13
Speed Function	30	40

2.4 Final Build and Post Processing

In addition to relating melt parameters to fatigue life, another project scope was to investigate the effect of HIP condition and surface roughness on fatigue life bringing the total number of factors studied to five. Again, MINITAB software was used to build an orthogonal Taguchi method array for efficient use of resources and a statistically sound conclusion could be made at the end of the project. A Taguchi method array was selected as it is known for the efficient use of partial factorial design to identify the contribution of selected factors on the process being studied, while also focusing on mitigating process noise. (37). Using MINITAB, a

L16 design was identified as the best candidate, allowing for three 4-level factors and 1-6 2-level factors. The 4-level factors were used for the primary melt conditions SF, FO, and LO allowing the previously established ranges to be explored with a reasonable step size. The remaining 2-level factors were assigned to HIP and average surface roughness. For HIP, two conditions, sub and super β-transus, were selected as discussed above. The selected average surface roughness levels were 0.2 μm and 0.1 μm corresponding to the as-received ground surface and the surface achievable in a one-hour, single-step MAF treatment. 250 samples were prepared to produce an S-N curve with sufficient detail and repeats for engineering applications. With 16 unique variants, 16 builds would be required to meet the 250-sample quota. However, in the interest of time and resources, the 16 builds were consolidated into 8 builds with 2 sets of 16 samples per build. Samples were designated by a pair of numbers in the form x-y, where x represents the build number and y is the sample number. For example, sample 32 from build 1 is designated as 1-32. These identifying labels were printed directly atop each sample to ensure accurate sample tracking.

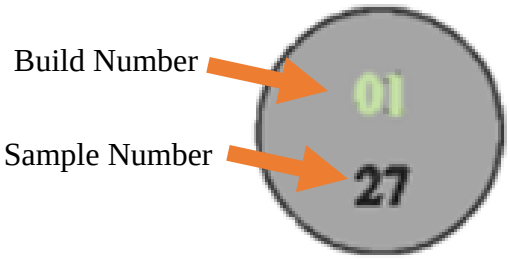

Figure 56. Depiction of sample identification labels printed directly atop each sample. Where the top and bottom numbers refer to build number and sample number respectively, designating this sample as 1-27.

Based on this numbering convention, samples 1-01 and 1-17 are identical apart from build plate location. Samples 1-27 and 2-27 also have identical factor levels with the only difference being the build number. The print settings for each sample are provided below in Table 10.

Table 10. Final DOE for EBMed Ti-6Al-4V samples constructed from a L16 Taguchi orthogonal array using MINITAB software.

Sample	Speed Function	Line Offset (mm)	Focus Offset (mA)	HIP (°C)	Roughness (µm)
1	30	0.1	0	800	0.1
2	30	0.11	7	800	0.1
3	30	0.12	13	1100	0.2
4	30	0.13	20	1100	0.2
5	33	0.1	7	1100	0.2
6	33	0.11	0	1100	0.2
7	33	0.12	20	800	0.1
8	33	0.13	13	800	0.1
9	37	0.1	13	800	0.2
10	37	0.11	20	800	0.2
11	37	0.12	0	1100	0.1
12	37	0.13	7	1100	0.1
13	40	0.1	20	1100	0.1
14	40	0.11	13	1100	0.1
15	40	0.12	7	800	0.2
16	40	0.13	0	800	0.2
17	30	0.1	0	800	0.1
18	30	0.11	7	800	0.1
19	30	0.12	13	1100	0.2
20	30	0.13	20	1100	0.2
21	33	0.1	7	1100	0.2
22	33	0.11	0	1100	0.2
23	33	0.12	20	800	0.1
24	33	0.13	13	800	0.1
25	37	0.1	13	800	0.2
26	37	0.11	20	800	0.2
27	37	0.12	0	1100	0.1
28	37	0.13	7	1100	0.1
29	40	0.1	20	1100	0.1
30	40	0.11	13	1100	0.1
31	40	0.12	7	800	0.2
32	40	0.13	0	800	0.2

As depicted in Figure 57, samples were printed in a 6x6 grid centered on the plate, 9 mm apart edge-to-edge between neighboring samples to prevent thermal bleeding. Blanks had a total height of 63 mm with the first 2 mm being support structure and final 1 mm producing forming the sample labels. Although the effect of build plate positions on mechanical properties is thought to be small, the location of each sample in the grid was randomized for each build in hopes of balancing out any effects of build location. (38) (39).

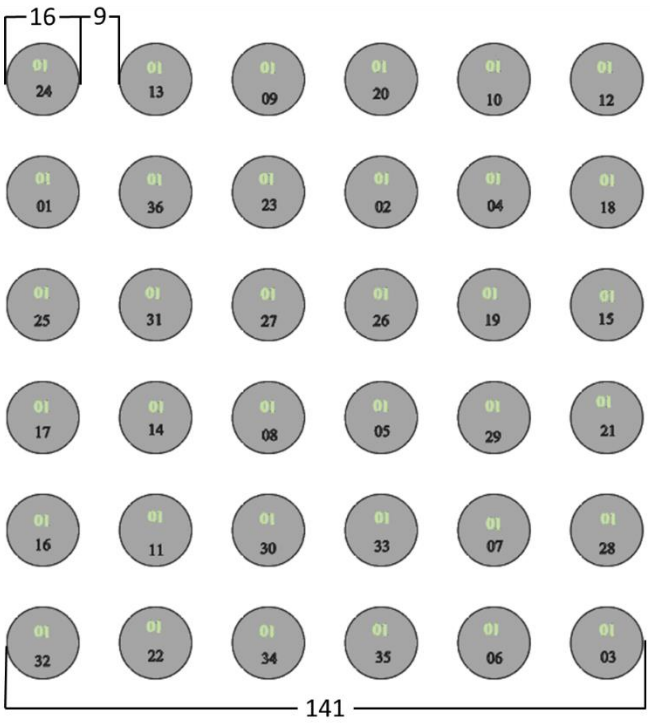

Figure 57. Build layout for build 1 with randomized sample locations. All measurements featured are given in mm.

Samples 33, 34, 35, and 16 are additional "dummy" samples included to fill out the 6x6 grid. These samples were printed using the settings centered in the middle of each range as presented in Table 9. No additional post processing was planned for most of these samples, as their primary purpose was to balance the thermal load during printing. However, samples 2-34 and 5-34 were included with the 800°C samples to be HIPed. This way, any of the remining dummy sample left in the as-printed condition could be used to analyze the effects of HIPing on a sample with identical melt parameters. An image of the completed samples for the first build can be found in Figure 58.

Figure 58. Build 1 blanks after printing and removal from build plate.

After completing all eight builds, samples were shipped to Quintus Technologies, located outside of Columbus, Ohio, for HIP treatment. After reaching out to multiple facilities, Quintus was the only company with equipment capable of preforming the 1100ºC HIP treatment with immediate quenching under pressure, eliminating the need for an addition heat treatment step to achieve the desired microstructure discussed above. Typically, the quench rate for such a system refers to the chamber gas temperature and not the cooling rate experienced by the material. Therefore, the treatment was first calibrated to ensure the samples experienced the desired 150ºC/min quench and eliminate any ambiguity related to heat transfer kinetics across the gas-metal interface. To accomplish this, a high temperature thermocouple was placed inside a drilled-out Ti-6Al-4V dummy sample, allowing for recording of the sample's centerline temperature throughout the calibration cycle. An equivalent thermal mass of stainless-steel blocks was also added to the HIP chamber to simulate the Ti-6Al-4V samples which would be present in HIP treatment for the main sample set. After adjusting the shielding gas quench rate based on Quintus' previous experience, the cycle was run and, using the thermocouple data, the quench rate for the Ti-6Al-4V dummy sample was calculated to be 150ºC/min. With the calibration completed, the two HIP treatments of 800ºC at 200 MPa for two hours and 1100ºC at

100 MPa for two hours and 150ºC quench were run. Like the calibration run, the high temperature thermocouple placed inside the same dummy sample, as shown in Figure 59, to record the metal temperature throughout both HIP treatments and has been plotted in Figure 60.

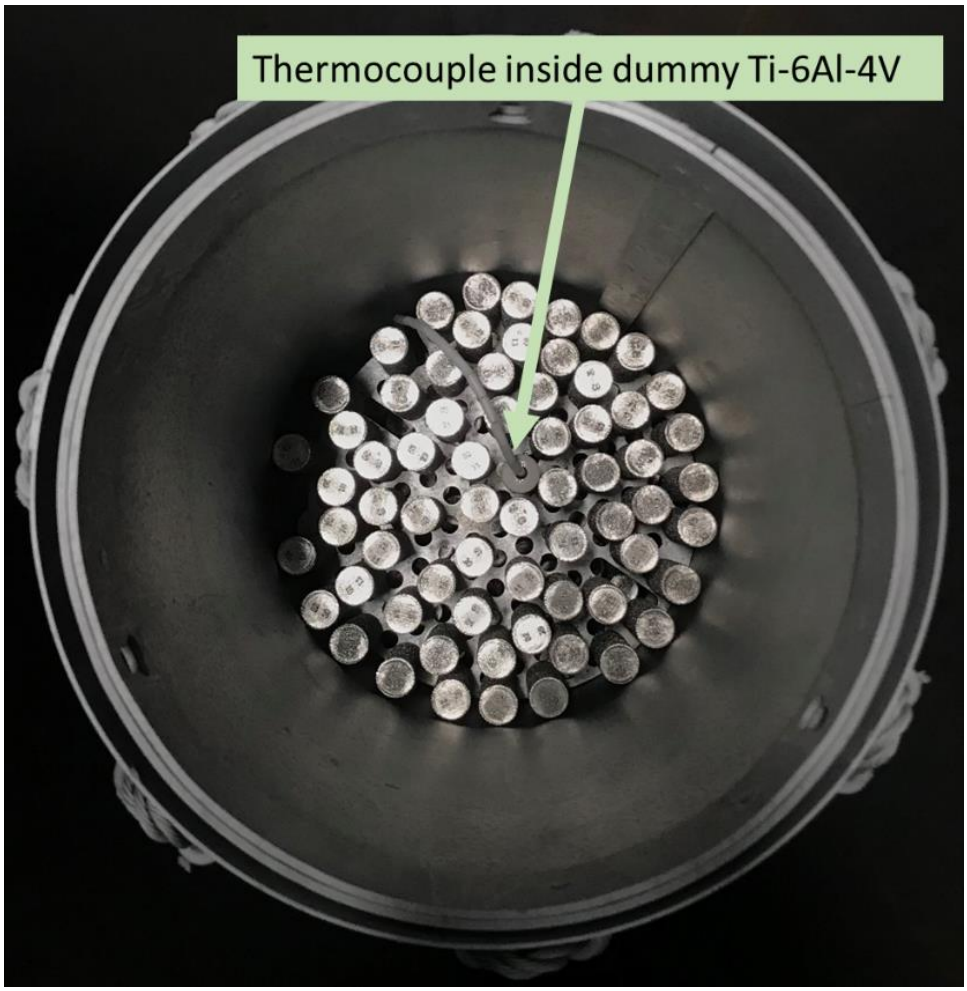

Figure 59. 1100°C samples in HIP chamber just prior to treatment at Quintus Technologies in Columbus Ohio. Additional dummy sample with higher temperature thermocouple installed for measuring centerline temperature during treatment.

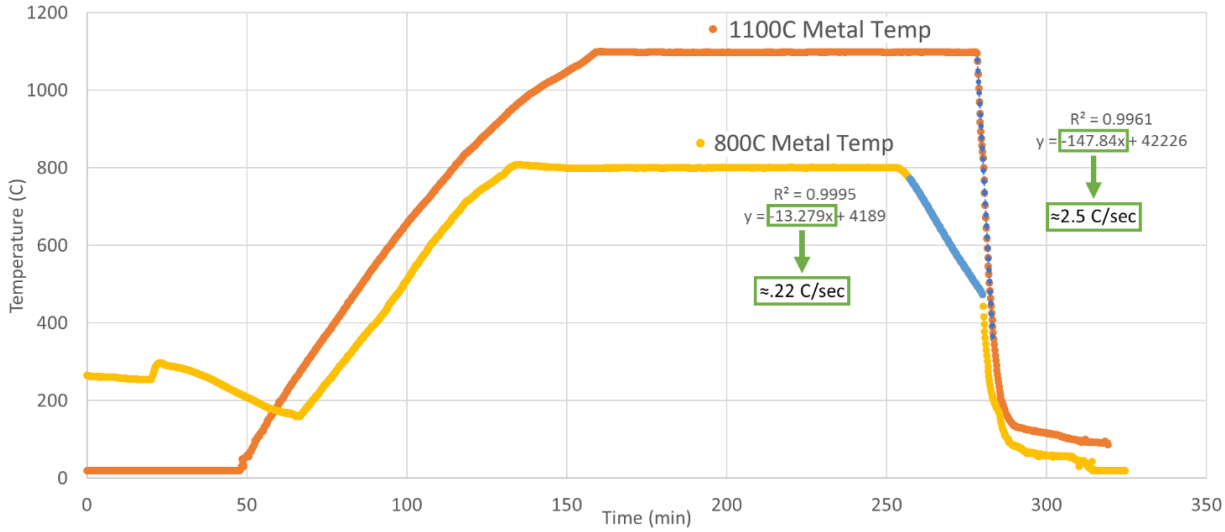

Figure 60. Centerline temperature history measured using high temperature thermocouple installed in dummy sample for both 1100°C and 800°C HIP treatments. Cooling rate curve fits overlayed along with R^2 values and equation for line of best fit.

Using the time and temperature data, the quench rate for the 1100ºC HIP treatment was calculated to be just under 150°C/min (2.5°C/sec) at a rate around 148ºC/min. It should be noted that the HIP machines at Quintus were large enough that only a single run was required to treat all the samples for each condition, eliminating another possible source of variability.

Following the successful HIP treatments samples were sent to a machine shop for turning down to the final geometry. The final dimensions of the turned fatigue samples can be found in Figure 26 and a picture of the finished sample can be found in Figure 61.

Figure 61. Machined Ti-6Al-4V hourglass fatigue sample.

Each sample was turned using a Computer Numerical Control (CNC) lathe and were center drilled on both ends to ensure concentricity during subsequent grinding and polishing procedures. At this time, the sample number was engraved on the non-threaded end of the samples and could be accurately identified after the printed number labels were removed. To remove any machining defects, each sample was then ground with silicon carbide emery cloth using a custom lathe sanding setup. Once returned, samples designated for testing in the as-received surface condition were separated out and shipped to Eaton Corporation to begin ultrasonic fatigue testing. The remaining samples were first measured using a surface profilometer to determine the as-received arithmetic average roughness parameter. Ra is a commonly used surface roughness parameter, all further references to surface roughness in this dissertation will be given in terms of Ra. Roughness of the as-received fatigue samples was found to be 0.203 μm. Using Magnetic Assisted Finishing (MAF), the samples were polished to a roughness of approximately 0.100 μm. Additional details about the MAF process are discussed in the next chapter of this dissertation. After all samples were polished, they were also sent for fatigue testing.

2.5 Ultrasonic Fatigue Testing

All samples in this study were tested using the ultrasonic fatigue testing machine (Ultrasonic Fatigue Testing Equipment (UFTE) BOKU Wien, Vienna, Austria) at Eaton Corporation. An image of their setup can be found in Figure 25. All samples were tested using fully reversed load condition with a load ratio of R = -1 and a runout of 1E8 cycles. Samples were designed to have a resonant testing frequency of around 20 KHz, the actual frequency during testing was found to be 19.2 KHz. This resonant frequency is maintained throughout the test while the applied stress is controlled by adjusting the vibration amplitude. As cracks grow

the resonant frequency of the sample decreases, so after the frequency decreases below a preset threshold the test stops and the sample is considered to have failed. (40) In some cases, a complete fracture separating the sample into two or more pieces and the sample remains remained in one piece, without any visible indication of internal crack growth.

The stress level was not originally incorporated in the DOE as the effects of higher applied stress on the fatigue life of a material is already well understood. However, Eaton requested that at least two stresses be tested so that even a limited SN curve could be produced. Only two stresses were tested, minimizing the number of additional conditions, and maximizing the number of repeats for each condition. Ideally, the lower stress should require a larger number of cycles to failure and yield more unfailed samples, but not be below the endurance limit of a material in order to obtain statistical data relating the effects of build conditions on fatigue life. Similarly, the higher tested load should not be so high that samples fail very early regardless of the processing conditions. To determine the stresses to be tested, all of build 2 was removed from the study and used as test samples. Starting with a conservative stress of 300 MPa, samples were tested until runout and then increased in stress by 50 MPa increments until 500 MPa when failure occurred. Results of this testing are presented in Table 11. It should be noted that all samples in this preliminary stress testing were 800°C HIP condition.

Table 11. Preliminary stress testing date used to determine stress to be used for main study.

Sample	Stress (MPa)	Cycles
2-16	300	1.0E+08
2-16	400	1.0E+08
2-16	450	1.0E+08
2-16	500	7.98E+07
2-10	400	1.0E+08
2-10	450	1.0E+08
2-10	500	6.5E+07
2-25	500	1.0E+08
2-25	550	6.40E+06
2-31	400	1.0E+08
2-31	450	1.0E+08
2-31	500	9.7E+07
2-32	550	1.20E+06
3-34	550	8.40E+04
5-34	500	1.0E+08
5-34	550	5.90E+07

The stress was increased again to 550 MPa where a significant reduction in fatigue performance was observed. From this testing, it was determined that the best stresses to use were 500 and 550 MPa. Stresses were assigned to samples so that identical samples from each build were given different loads. For example, samples 1-01 and 1-17, which have identical processing conditions, were assigned different test stresses. Splitting the samples in this way ensured that each of the 16-processing parameters had seven repeats at each stress level. This also ensured that each build was equally represented at both stress levels to mitigate any effect a particular build would have on study results.

2.6 Metallography and Mechanical Characterization

While samples were being fatigue tested at Eaton Corporation, metallography and additional mechanical characterization were performed on the tested samples, including microhardness testing, density analysis, tensile testing, and microstructure imaging.

First, previously cycled samples were sectioned at the wide unthreaded end of the hourglass sample using a diamond wafering saw, an illustration of the sectioning location is provided in Figure 62.

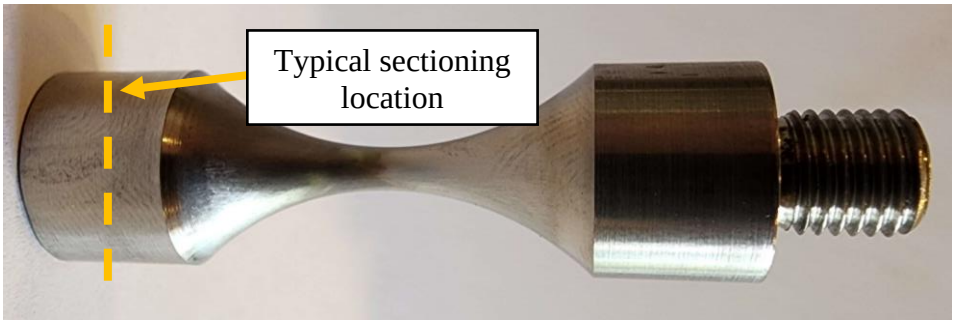

Figure 62. Typical sectioning location for producing metallography samples.

In some cases, the sectioned sample was cut again down the center to produce two samples providing views along and perpendicular to the build direction, as depicted in Figure 63.

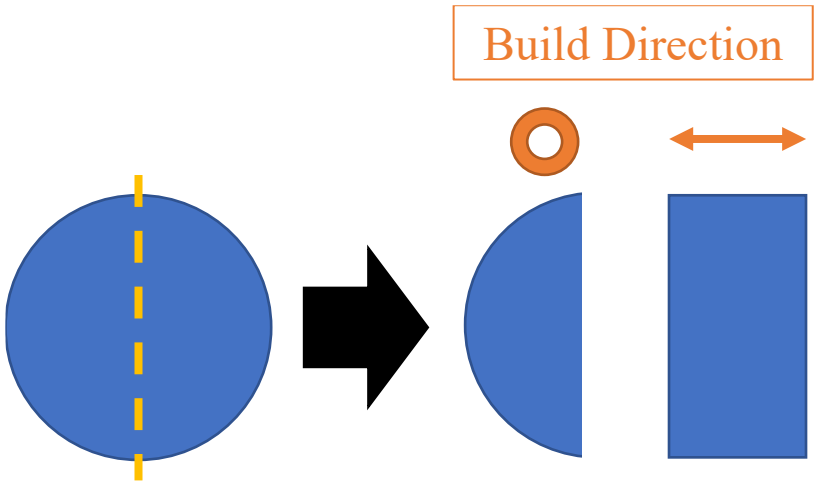

Figure 63. Depiction of how section samples were section a second time to provide views along and perpendicular to the build direction.

Unfortunately, the build direction (i.e., printed threaded to non-threaded side or vice versa) was not recorded when the sample was machined, so the sample's orientation with respect to the base plate is unknown. However, because of the blank geometry, the build direction must be aligned with the longitudinal axis of the part. Depending on how the blank was machined, the

approximate ranges a sample could have been sectioned is between 10-15 mm or 45-50 mm from the build plate. With the initial blank size of 60 mm and final machined length of 57 mm the gauge section of the fatigue sample could only vary by between 10 to 13 mm depending on how the fatigue sample was machined relative to the blank and the amount of material removed from each end.

After sectioning, samples were hot mounted in epoxy resin and labeled using an engraving tool. If a sample was sectioned twice, both parts were mounted together so that the microstructures of both orientations were visible. Samples were ground and polished using a Buehler Ecomet 4 Grinder Polisher with equipped Automet 2 Power Head. Samples were mounted in the power head's mounting platen and not removed until grinding and polishing were complete. Grinding was performed in a stepwise fashion in the following order: 60-grit, 120-grit, 240-grit, 600-grit, and finally 1200-grit. Each grinding paper was run for 2 minutes with some steps requiring use of multiple grinding papers to complete. The final polishing step was performed on the same machine using METLAB 0.06 μm colloidal silica and chem pad, for anywhere between 10 and 60 minutes depending on the samples.

First, density was measured on each sample using a combination of optical imagining and image processing. This method was selected over more traditional Archimedes' method as the section samples had already been mounted and polished. In addition, there were concerns about air bubbles being trapped in threaded and center drilled sections when submerged, slightly altering the measurements. 10x optical images of the polished cross sections were taken using a Nikon ECLIPSE LV100ND (Nikon – Tokyo, Japan). Four images were taken of each sample in random locations, but away from the less polished edges, to ensure accurate unbiased measurements. The calculated densities from each image were then averaged to find the overall

density of the sample. At least one sample per build condition was measured. Dummy samples that were not machined into fatigue specimens, in the as-printed condition, as well as those included with the 800°C HIP treatment were also imaged and are labeled as melt parameter 17. Example images for each HIP condition are provided below.

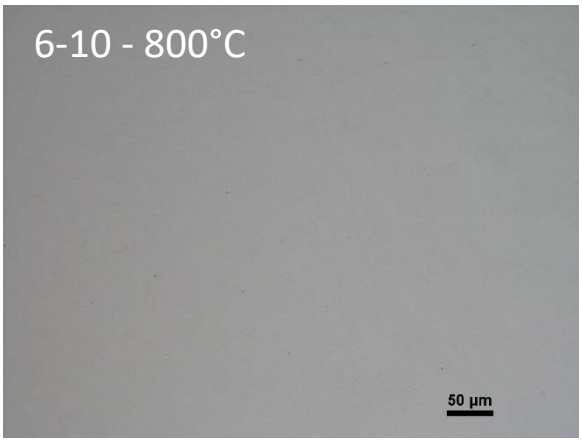

Figure 64. 10x optical image of cut, mount, and polished section of sample 6-10 HIPed at 800°C.

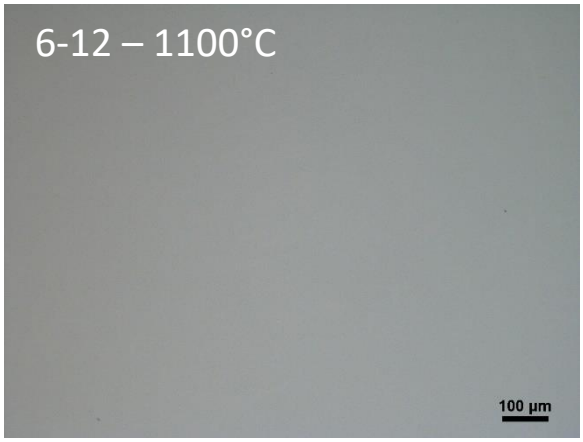

Figure 65. 10x optical image of cut, mount, and polished section of sample 6-12 HIPed at 1100°C.

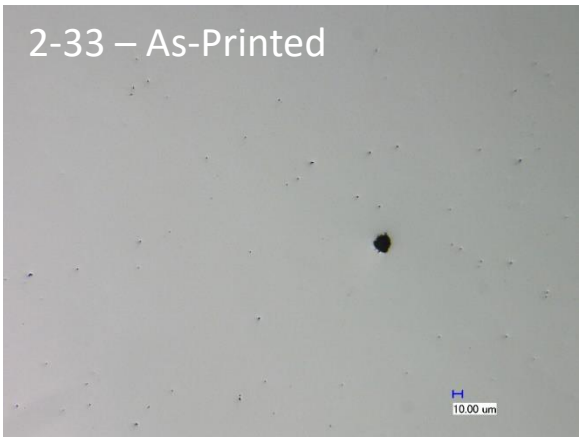

Figure 66. 10x optical image of cut, mount, and polished section of sample 2-33 (aka 2-17) still in the as-printed (non-HIPed) condition.

Across all the images taken, no evidence of Lack-of-Fusion (LOF) or Keyhole porosity was found in any of the samples, even in the as-printed (non-HIPed) condition. This was expected as no such defects were found during the late stages of the preliminary testing. Small Trapped Gas (TG) pores less than 10 μm in diameter were found in all samples, as expected. However, any pore larger than 10 μm, like that presented in Figure 66, were only found in the as-printed condition. Pores of this size were not found during preliminary testing and raises questions about their frequency throughout the samples. Although extensive sectioning and imaging was performed, it is not possible to find every pore in a sample without utilizing a volumetric scanning technique like X-ray Computed Tomography (XCT) like that performed by Tammas-Williams et al. (8) Unfortunately, due to limited resources, no machine powerful enough to scan the entire sample were available.

To determine the pore volume fraction, each of the images taken were analyzed with the custom porosity detection and measuring MATLAB script written for this project. The script first converted the image to gray scale, using an adaptive threshold to eliminate any lighting gradients. Next the image was converted into a binary mapping using simple thresholding to isolate the dark porosity from the brighter bulk material, after which several binary image

processes, like imfill, are used to clean up the binary image. Finally, information about individual pores characteristics like size and aspect ratio were recorded, before the total number of identified pore pixels was divided by the image size to determine the percent porosity. A copy of the script used for this analysis is provided in Appendix B. Results of this analysis in recorded in Figure 67.

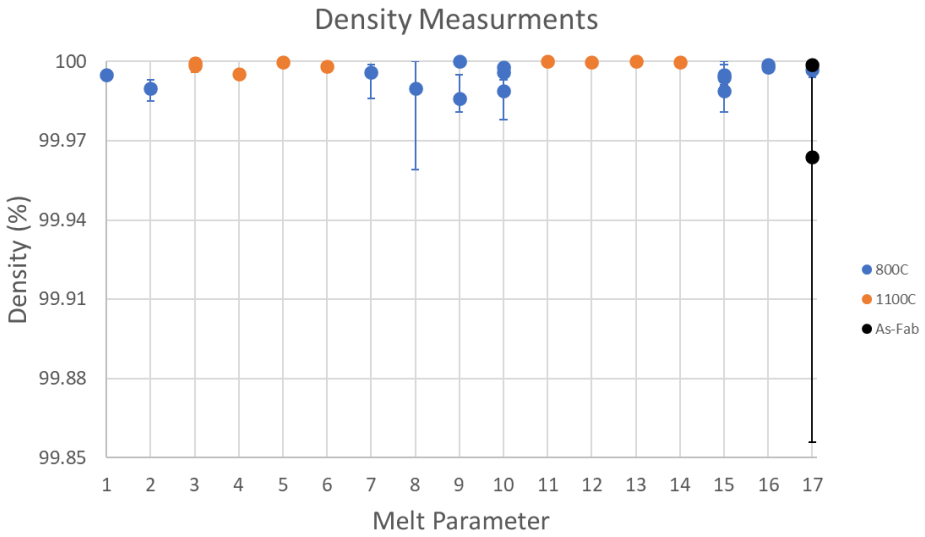

Figure 67. Density measurements of EBM printed Ti-6Al-4V fatigue samples measured using combination of optical measuring and image processing using a custom MATLAB script.

It should be noted that error bars, representing the range of densities calculated, are plotted for all samples. The variation for the 1100°C samples is so small that the marker used to designate the average calculated density covers the error bars. This alone is enough to conclude that 1100°C was more effective at reducing the amount of TG pores than the 800°C. This makes sense as the increased temperature should further decrease the strength of the material, increasing the capability of pore closing due to the applied isostatic pressure. However, the absence of any large pores and densities all over 99.87% indicates that both HIP conditions were effective at closing large TG porosity. This is especially important for the 800°C HIP condition, as it is a non-standard HIP condition designed to minimize grain growth during processing.

Next, Vickers microhardness was measured using a Phase II hardness tester (Phase II - Upper Saddle River, New Jersey). The testing used a 1 Kg load and 15 second load time. A standard test block with a known hardness of 759 HV_1 and evenness (term listed in the gauge qualification) of 1.4% was measured before, during, and after testing to confirm the accuracy of the measurements. The results of these calibration tests are provided in Table 11.

Table 12. Calibration measurements taken before (1 & 2), during (3 & 4), and after (4 & 6) hardness measuring to ensure accuracy. Measurements were taken on a Mitutoyo calibration samples with known hardness of 759 HV_1 and 1.4% evenness.

Known Standard		Calibration Measurements (HV_1)							
Hardness (HV_1)	Evenness (%)	1	2	3	4	5	6	Avg.	SD
759	1.40%	758.4	758.1	754.1	758.4	759.9	764	758.8	2.9

A single sample was hardness tested for each of the 16 build conditions. Dummy samples in the as-printed and 800°C HIPed condition were also included and labeled as melt parameter 17. Six measurements were taken for each sample and were evenly spaced with approximately 0.25 mm spacing to ensure statistically meaningful measurements were taken from several colonies. All measurements were taken from horizontal cross-sections (perpendicular to the build direction). Results of hardness testing are provided in Figure 68.

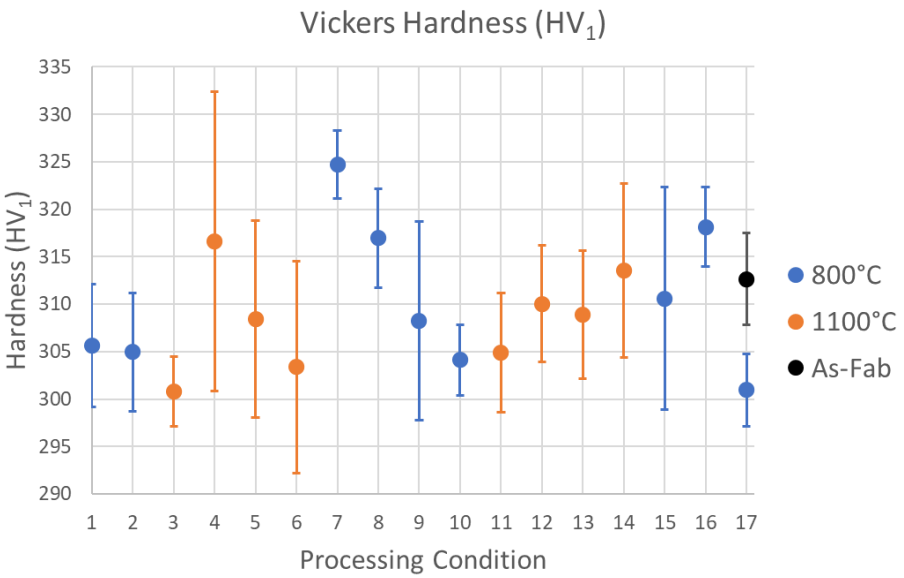

Figure 68. Vickers hardness measurements for 800°C and 1100°C fatigue samples. Measured on cut, mount, and polished samples. Single sample tested per condition. Six measurements per sample spaced in a line approximately 0.25 mm apart. Error bars represent ± 1 standard deviation from the average.

All the measurements are relatively similar, with all samples having an average hardness between 300 and 325 HV_1. This is relatively low for annealed Ti-6Al-4V, which is typically listed between 310 – 350 HV with some sources closer to 350 HV (41) (22). One-tailed T-tests were performed using MINITAB to identify if any relevant parameters had a statistically significant impact on the hardness. The surface roughness condition was not tested as it should have no effect on hardness. Results of these tests are listed in Table 13, where P-value is a measure of the likelihood of each parameter having a statistically significant impact on hardness. In general, when performing this type of analysis, a significance level of 0.05 is selected, meaning that, with P-value less than 0.05, there is only a 5% risk the detected impact is the result of random chance. (42)

Table 13. One-tailed T-test for hardness results of each relevant design parameter. Only melt parameters 1-16 (main DOE) were included.

Source	P-Value
Speed Function	0.017
Line Offset	0.034
Focus Offset	0.360
HIP	0.009

From these results, it can be concluded that the difference between the mean hardness for each level of Speed Function (SF), Line Offset (LO) and HIP condition are statistically significant. In other words, SF, LO, and HIP have a statistically supported impact on the measured hardness. This data alone is not enough to understand the magnitude of each parameter's effect on hardness. To better visualize this, impact plots were also generated as shown in Figure 69.

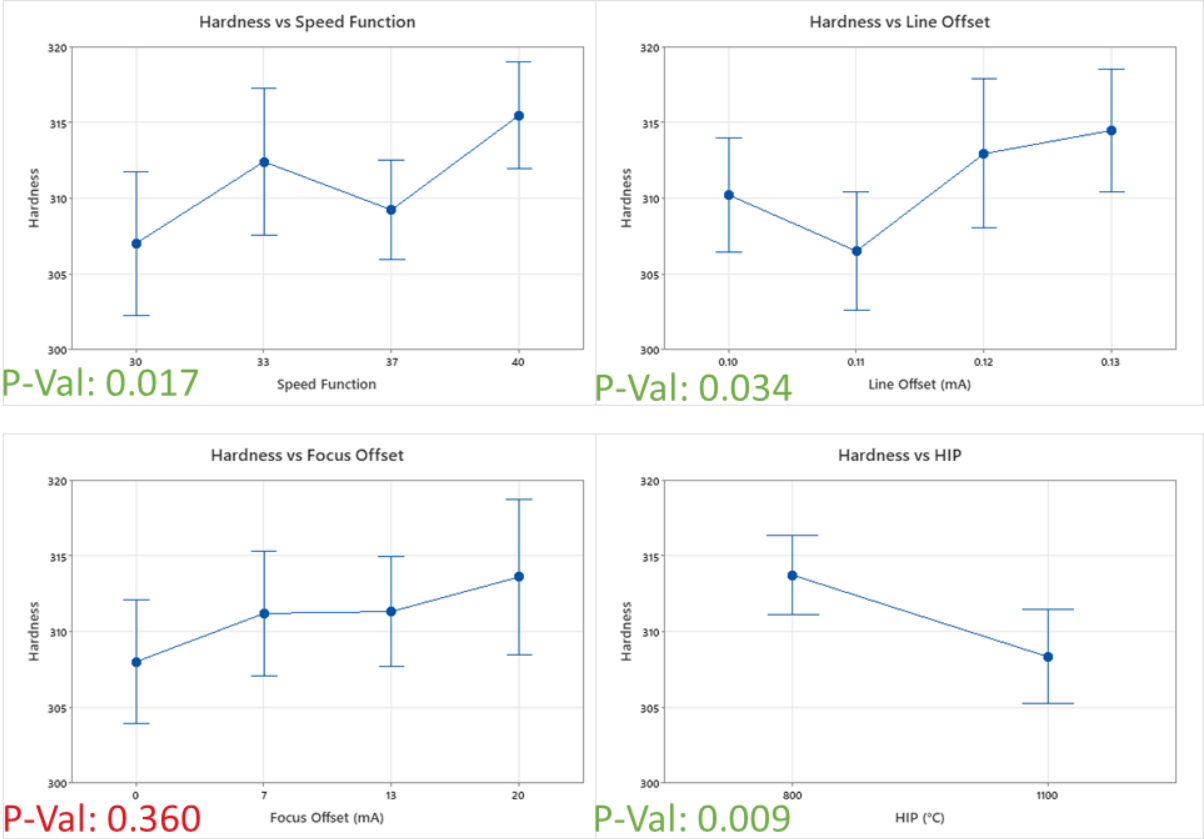

Figure 69. Impact plots representing the average hardness for each level of parameter. Plots are generated using MINITAB.

From these plots, it can be seen that increasing SF and LO increased sample hardness. Although a similar trend can be seen for Focus Offset (FO), the averages for each level are contained within the error bars of one another, thus no statistically significant difference between means was found. Finally, it can be seen that the HIP treatment had the largest impact in hardness. However, while samples treated with the 800°C HIP condition were found to be harder with an average of 313.7 HV_1 as compared to 308.4 HV_1, a difference of only 5.3 HV_1. An additional

correlation test between hardness and relevant processing parameters was also performed to further confirm the results as shown in Table 14.

Table 14. Correlation data between hardness and major processing parameters.

Factor 1	Factor 2	N	Correlation	P-Value
Hardness	Speed Function	96	0.232	0.023
Hardness	Line Offset	96	0.212	0.038
Hardness	Focus Offset	96	0.188	0.067
Hardness	HIP	96	-0.265	0.009

Here SF, LO, and HIP were found to have statistically significant correlations with hardness, just as found with the T-test. HIP was found to have the highest correlation magnitude of 0.265, similarity observed in the impact plots. While this data does provide meaningful insight into the relationship between the processing parameters and hardness, the magnitude of the impact is still quite small. It should also be noted that despite extensive statistical investigation, various plotting methods, and data representations, no explanation could be found for the apparent linear relationships observed in Figure 68 for processing parameters 3-6, 7-10, and 11-14.

Anisotropy and large colonies in titanium alloys can make measurements on the micro scale inconsistent and highly dependent on locations measured. While large spacing between measurement locations was used to mitigate this effect, tensile testing should give a better understanding of the bulk material characteristics. Unfortunately, during project planning, no plan for tensile testing were made to produce proper tensile samples. Instead, untested fatigue samples were milled into flats to produce non-standard tensile samples. An image of one of these samples is shown in Figure 70.

Figure 70. Ti-6Al-4V fatigue sample reworked into tensile sample.

Due to the sample's tapered cross section, it lacks a constant length gauge section that is found in typical tensile sample geometries. Without this, it would be difficult, if not impossible, to make accurate strain measurements using typical methods like extensometer or Digital Image Correlation. Instead, the crosshead extension was used. Tensile tests were performed on an MTS insight 300 KN (MTS – Cypress, Texas), using 1" wedge grips and 300 KN load cell. Samples were mounted in the grips as deep as possible to ensure enough a tight grip was maintained during the test. All samples were tested at a rate of 0.3 mm/min derived from the ASTM E8 standard and an assumed 30 mm gauge section (distance between grips). (43) Due to the limited number of available untested samples, only four samples for each HIP condition were tested. Stress vs Extension curve for each of the samples tested is provided in Figure 71.

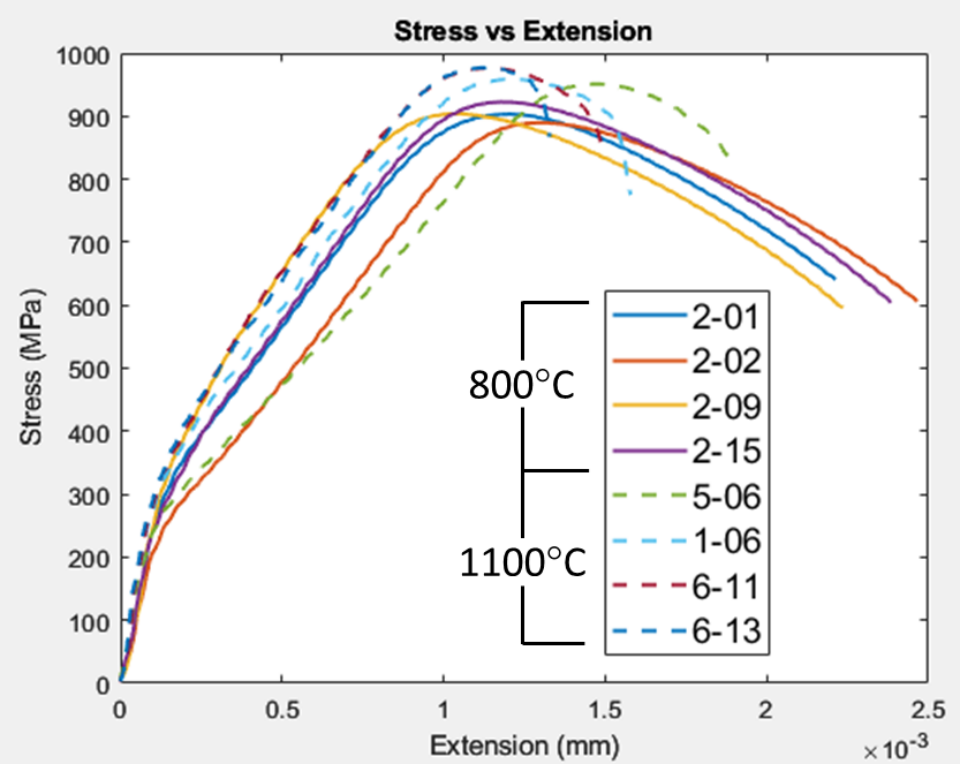

Figure 71. Stress vs Extension of reworked tensile sample. 800°C and 1100°C samples are represented by solid line and dashed lines, respectively.

Crosshead extension is not typically used for tensile strain measurements as it lumps the deformation of the sample together along with any compliance in the machine or fixturing setup (slack or deformation), making it impossible to isolate the sample deformation. This issue is normally avoided by using an Extensometer or Digital Image Correlation (DIC) to directly measure sample deformation. Unfortunately, the hourglass gauge section of the reworked fatigue samples made it difficult to use either method. However, since all tests were conducted using the same setup, the relative extension at failure can be used to qualitatively compare the ductility between samples. Figure 71 shows clearly that the 800°C samples had a higher ductility, and thus toughness, as compared to the 1100°C samples.

The curves presented in Figure 71 have an abnormal shape unlike standard tensile tests, with much lower apparent yield stress, yet higher ultimate tensile stress values consistent with

reported Ti-6Al-4V mechanical properties. (22) (41) An image of a typical stress vs. strain diagram is included in Figure 72.

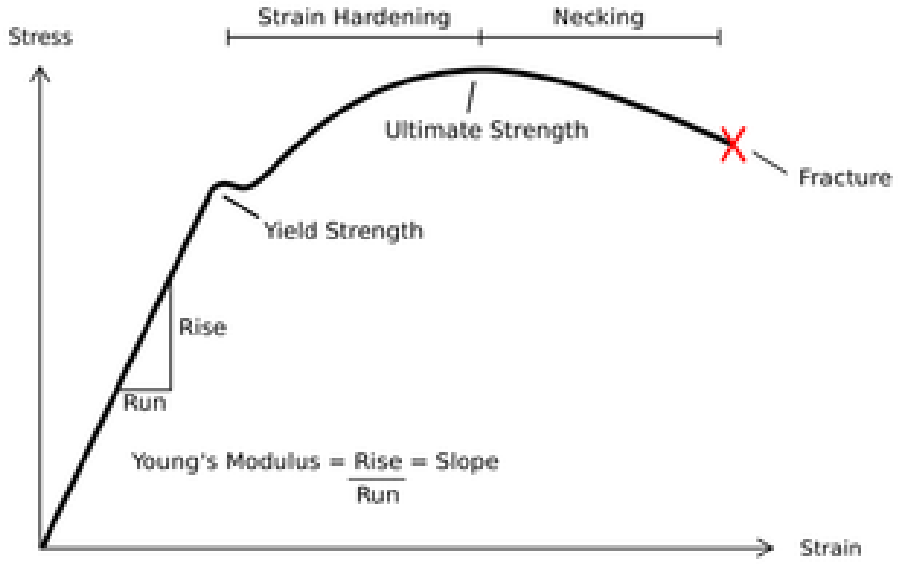

Figure 72. Typical stress vs strain diagram. (44)

The much greater degree of hardening results from the sample's tapered geometry, which is akin to a mild notch that enhances the local stress at the center of the gauge section where the cross section is narrowest. As yielding hardens the deforming center, the adjacent unyielded material deforms gradually with increasing load along the tapered gauge section, increasing faster near the shoulder. When the stress at the narrowest section reaches the UTS, a necking instability occurs. While the 1100°C samples have a higher UTS, the neck developed is less stable.

Due to the early onset of yielding, the yield strength was not extracted based upon the typical 0.2% offset method. Instead, two lines were drawn following the nearly linear sections near the apparent yield around 250 MPa and 0.2 mm extension, as illustrated in Figure 73. Yield and UTS strengths for each sample are provided in Figure 74.

The average yield strengths for 800°C and 1100°C samples are 305 MPa and 325 MPa, respectively. The averages UTS are 911 MPa and 972 MPa, respectively. Yield strength was

found to be much lower than expected and is a direct result of the sample geometry. Based on elongation and UTS data it is clear that the 1100°C samples have a lower toughness compared to the 800°C samples. The difference in ductility becomes even more apparent when looking at the fracture surfaces of the tensile samples, provided side by side in Figure 75. All 800°C samples exhibited a uniform and similar cup and cone ductile fracture, while all the 1100°C samples exhibited a more jagged fracture surface where heterogeneous deformation led to a more significant plastic instability, and failure at a smaller displacement. The potential causes of this difference in ductility will be discussed in a later section.

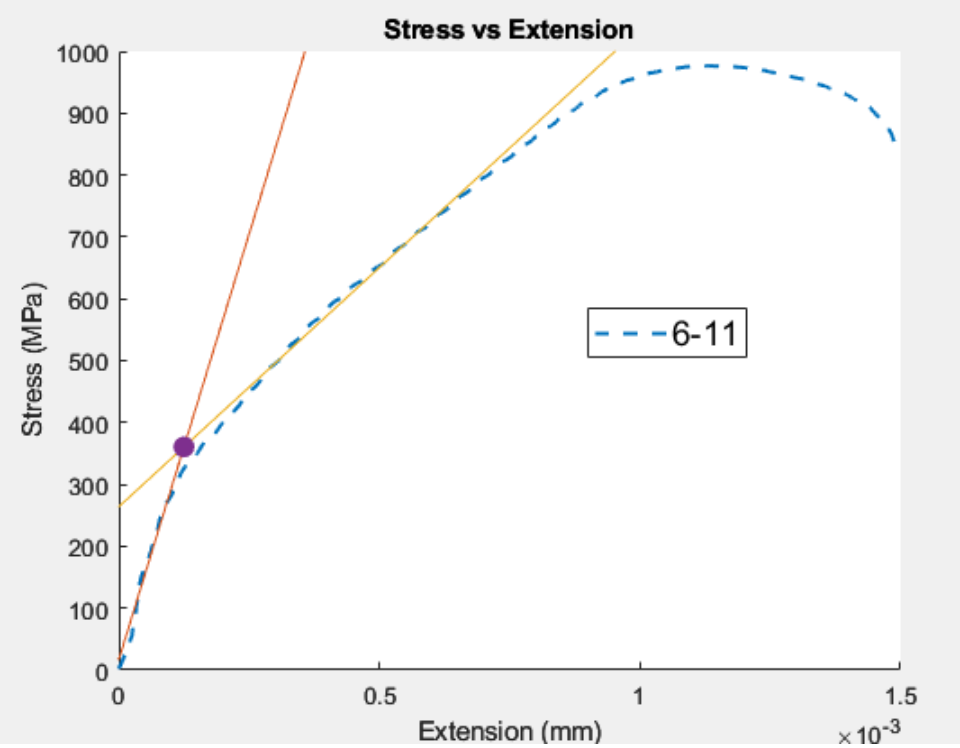

Figure 73. Stress vs Extension curve for reworded tensile sample 6-11 illustrating how the yield strength was calculated. The intersection between the best fit lines for each linear section is marked with a purple dot.

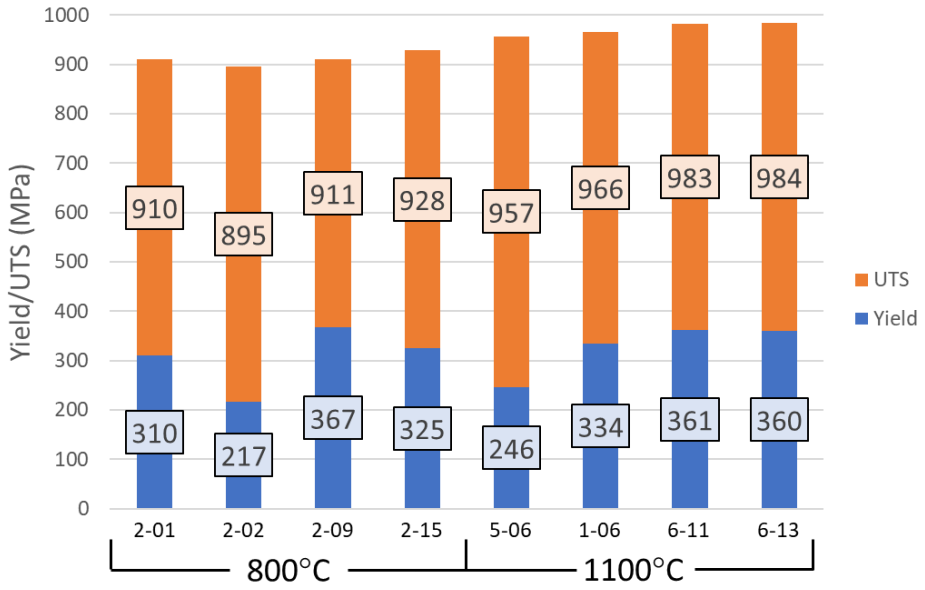

Figure 74. Yield and ultimate tensile strengths of reworked fatigue samples.

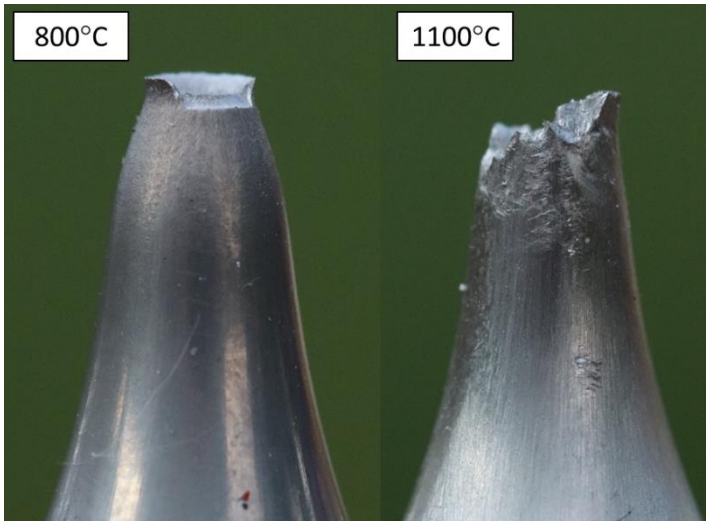

Figure 75. Profile images of fracture surfaces of reworked fatigue samples after tensile testing.

This testing clearly indicates that samples exhibit significantly different bulk material properties depending on the HIP treatment and any differences stemming from melt parameters are quite small in comparison.

2.7 Fatigue Results

Fatigue results were first separated by HIP condition and checked for outliers using Grubbs' test in MINITAB software. No outliers were found in the 800°C samples, however one

outlier was found for the 1100°C samples. The outlier identified was sample 8-21 and was the only 1100°C sample to survive until runout. A chart containing all fatigue results can be found in Appendix B. An outlier plot, generated by MINITAB software, is included in Figure 76 to illustrate the extent of which sample 8-21 (orange square symbol) is detached from the rest of the data set (blue symbols). Grubbs' test is designed to detect only a single outlier in a data set. (45) As such, the test was rerun after the outlier was eliminated from the data set. No additional outliers were detected on this subsequent run. After confirming all outliers were eliminated, fatigue results were plotted as an SN curve, which can be found in Figure 77.

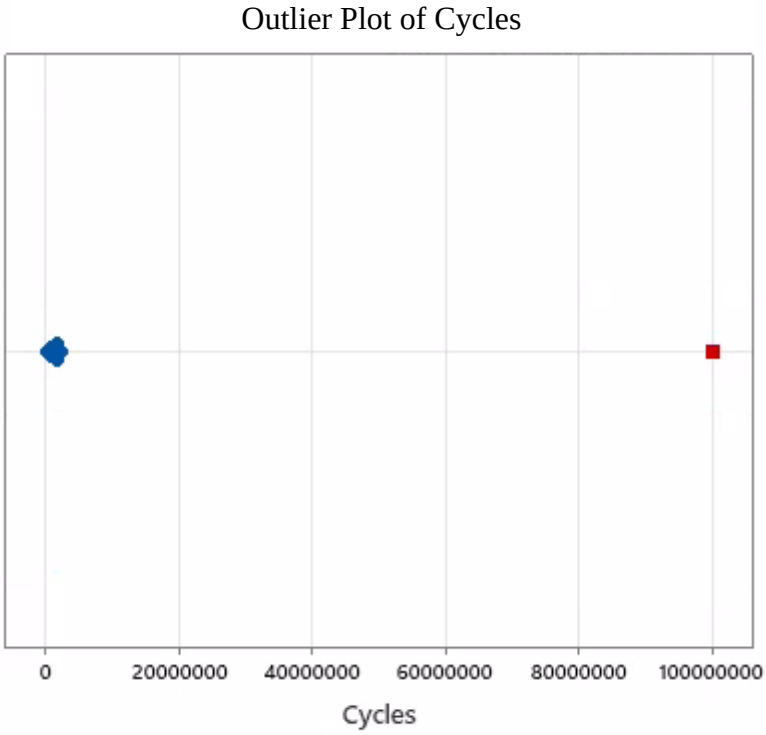

Figure 76. Outlier Plot of Cycles using Grubb's Test.

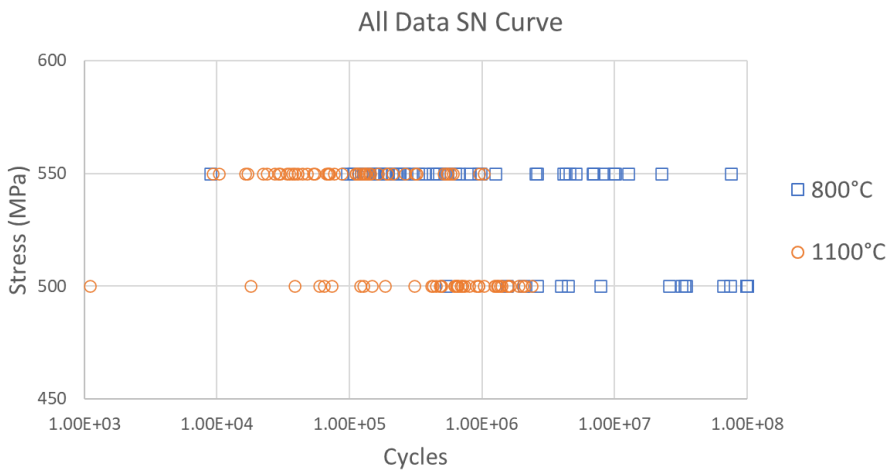

Figure 77. SN curve for all fatigue samples tested.

The SN curves clearly indicate that 800°C HIP condition outperformed the 1100°C HIP condition at both stress levels. With the 800°C samples having an average fatigue life of 8.08E+07 and 3.28E+06 cycles for 500 and 550 MPa, respectively. While the 1100°C samples exhibited a significantly reduced fatigue performance with the average fatigue lives of 7.21E+05 and 1.38E+05 cycles for 500 and 550 MPa, respectively. In fact, for the 500 MPa condition, twenty-three 800°C samples achieved runout (1E8 cycles). No samples achieved runout for the 550 MPa condition, and no 1100°C samples made it to runout at either stress level. The relationship between the processing parameters and fatigue life was calculated using MINITAB. Correlation results using all fatigue data are presented in Table 15.

Table 15. Correlation results for fatigue data using all samples. Where N is the number of included samples and Correlation refers to the calculated correlation coefficient.

Factor 1	Factor 2	N	Correlation	P-Value
Cycles	Build	204	0.02	0.776
Cycles	Speed Function	204	0.021	0.762
Cycles	Line Offset	204	0.023	0.746
Cycles	Focus Offset	204	-0.007	0.925
Cycles	HIP (°C)	204	-0.51	0.0
Cycles	Roughness (μm)	204	0.009	0.895
Cycles	Stress	204	-0.499	0.0

Here again, P-values less than 0.05 mean that the corresponding correlation coefficient is considered statistically significant. Correlation coefficient for factors with P-values larger than 0.05 are also reported, but not considered statistically significant. These calculations indicate that no processing condition apart from HIP condition had a statistically significant correlation with fatigue life. Only the HIP condition and Stress level had statistically significant correlations. It might be obvious that stress level would correlate with fatigue life, but if both selected loads were too low or too high, then many samples at both levels would run out or fail prematurely at both levels thus appearing to have no effect on fatigue life. For this reason, the stress level was included in correlation analysis as a sanity check. The existence of the statistically significant correlation between stress level and cycles indicates everything is as expected and the stress levels were selected appropriately. The correlation between each sample's build number and cycles is another important sanity check, because a statistically significant correlation between the two would indicate that something had changed over the course of producing the samples and effected performance. For example, oxygen pickup of powder during recycling or metallization

build up could be possible causes of decreased fatigue performance over time. Thankfully no such trend was found. Interestingly, surface roughness was also found to have not statistically significant correlation with fatigue life. The relationship between surface roughness and fatigue life is well known and found in most basic engineering textbooks. In this case, the roughness improvement from 0.2 µm to 0.1 µm is not enough to make meaningful impact on fatigue life and whatever minor effect the improvement had was drown out by noise or another untested factor. Impact plots for each processing condition were again generated using MINITAB to illustrate the impact of each condition on fatigue life as shown in Figure 78. This plot clearly shows how only HIP and stress level were found to have a statistically significant impact on fatigue life.

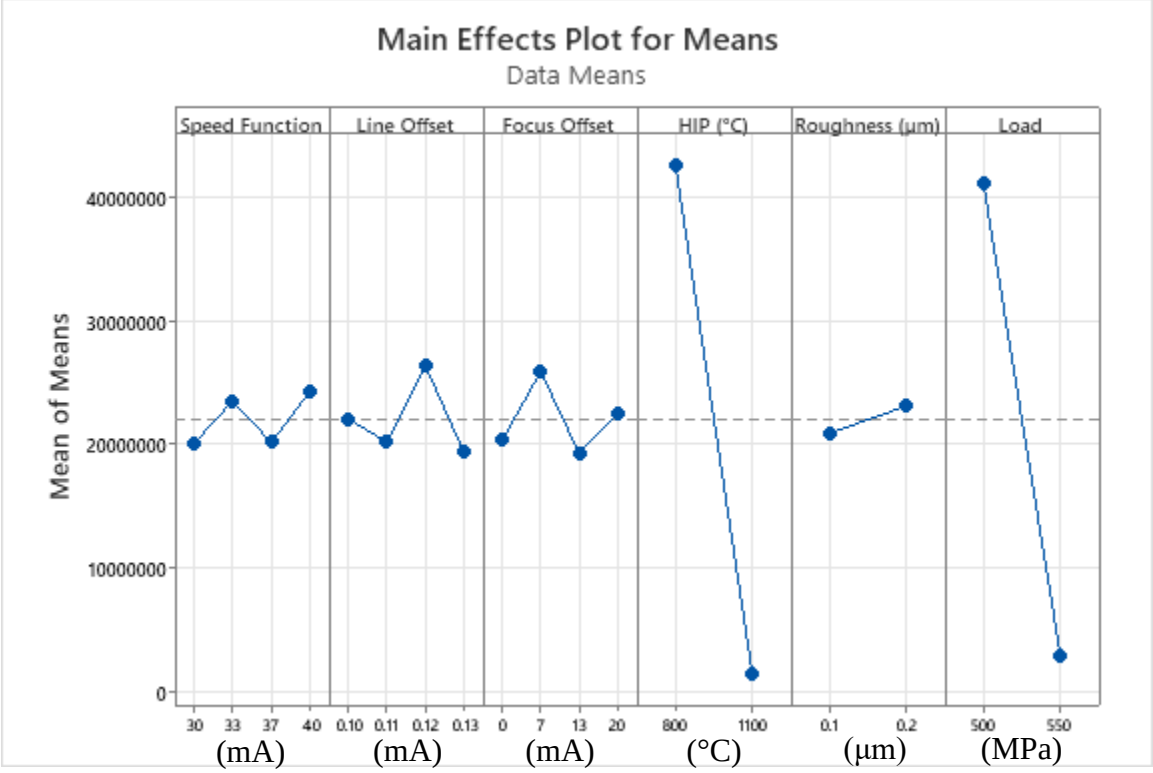

Figure 78. Taguchi method Mean of Mean plots impact plots for all fatigue samples. Generated using MINITAB software.

To ensure that the effect of melt parameters was not being masked by the difference in HIP conditions, the same analysis was redone by examining each HIP condition individually. SN plots of 800°C HIPed samples only can be found in Figure 79. In this plot, each build condition was separately plotted and given its own unique marker. Although condition 8 stands out as the lowest performer in both load conditions, it also had several runs near the highest life, averaging out with all the others. Correlation between each processing conditions and fatigue life for just the 800°C was done using MINITAB and recorded in Table 16. As previously found, no processing condition other than stress level was found to have a statistically significant correlation with fatigue life among the 800°C samples.

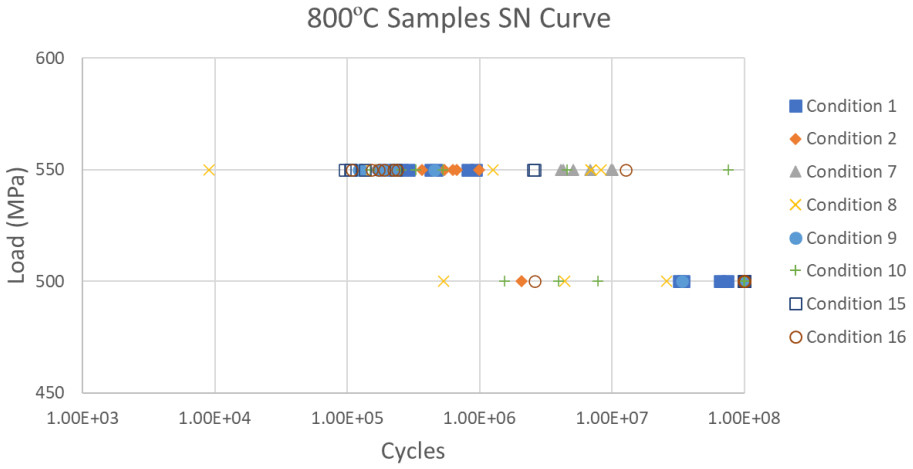

Figure 79. SN curve for 800°C fatigue sample data only.

Table 16. 800°C fatigue sample correlation results only. Where N is the number of included samples and Correlation refers to the calculated correlation coefficient.

Factor 1	Factor 2	N	Correlation	P-Value
Cycles	Build	106	0.002	0.984
Cycles	Speed Function	106	-0.063	0.523
Cycles	Line Offset	106	0.074	0.451
Cycles	Focus Offset	106	0.082	0.403
Cycles	Roughness (µm)	106	-0.113	0.248
Cycles	Stress	106	-0.812	0.000

The SN curve for only the 1100°C samples is provided in Figure 80. Again, each of the conditions was plotted separately and given their own makers with no condition in particular standing out. Correlation between each processing conditions and fatigue life for just the 1100°C was done using MINITAB and recorded in Table 16.

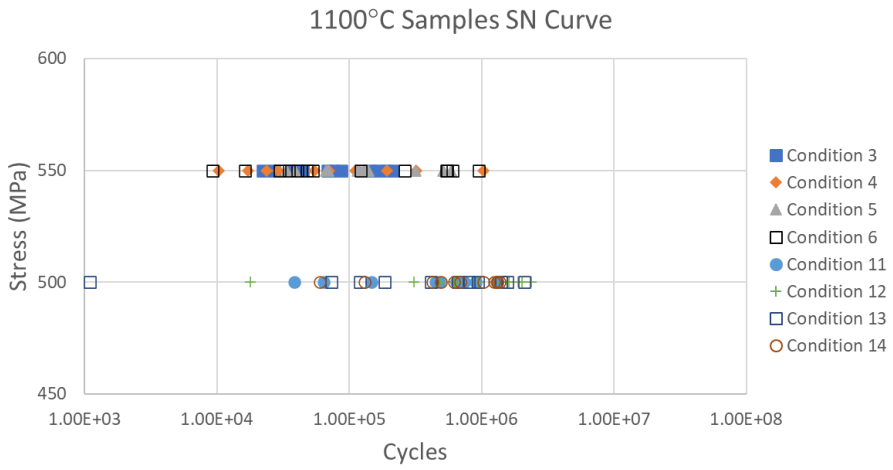

Figure 80. SN curve for 1100C fatigue sample data only.

Table 17. 1100C fatigue sample correlation data. Where N is the number of included samples and Correlation refers to the calculated correlation coefficient.

Factor 1	Factor 2	N	Correlation	P-Value
Cycles	Build	98	0.146	0.151
Cycles	Speed Function	98	-0.051	0.618
Cycles	Line Offset	98	-0.139	0.172
Cycles	Focus Offset	98	-0.043	0.676
Cycles	Roughness (µm)	98	0.099	0.33
Cycles	Stress	98	0.067	0.51

The 1100°C samples show that none of the processing paramaters had a statistically significant correlation with fatigue life, not even stress level. This information along with the lack of the 1100°C sample runouts indicate both of the loads tested were far above the endurance limit of the material and demonstrates the poor fatigue performance of the 1100°C samples compared to the 800°C samples. In Figure 81 all the fatigue sample results from this study are plotted over the ORNL review paper data gathered by Li et al. (26) from a varity of EBM Ti-6Al-4V fatigue studies. (26) It can be seen here that the 800°C samples performed as well if not better than both the conventionally produced and AM produced Ti-6Al-4V. This is very important for the 800°C samples as it shows that the HIP treatment with lower temperature and higher pressure was successful. Surprisingly many of the 1100°C samples still fall within the conventionally

produced region. However, the lower performing samples, especially those tested at 550 MPa, are right on the edge.

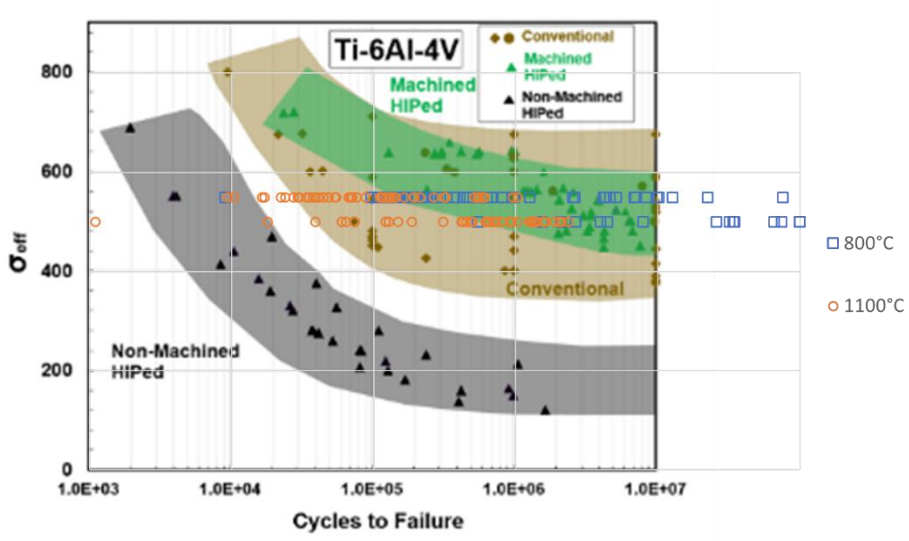

Figure 81. All fatigue sample data plotted over ORNL review paper results. (26)

It should be noted that splitting up the samples by stress level and analyzing each level independently did not result in any different conclusion. An additional effort to link fatigue life to energy density was also attempted using a parameter coding system. Parameter levels for SF and LO were coded from 1 to 4 based on increasing energy density given by Eq. (1). Next these factors were multiplied giving a "meta score" related to energy density. For example, the combination of the hottest SF and LO would result in a score of 16, while the coldest settings would result in a score of 1. These meta scores calculated for each of the samples tested were assessed using MINITAB to correlate against fatigue life. Again, no statistically significant correlation between these energy density meta scores and fatigue life were found.

One may be quick to conclude that the main melt parameters had no effect on the sample performance since there is no correlation with fatigue life. However, the statistical testing only failed to prove with 95% confidence that a trend was not caused by random chance, it did not conclude there was zero effect. Mechanical properties of any specimen are completely controlled

by its thermal history, and changing processing parameters absolutely changed the thermal history of a part. Therefore, it would be more accurate to conclude that the effect of these parameters was indiscernible from random chance or might have been drowned out by other factors that may not have been accounted for. In addition, the apparent lack of impact of melt parameters on fatigue life could be the result of parameter refinement preformed during the preliminary testing. During this testing, parameter ranges were refined to avoid processing defects like obvious swelling and lack of fusion porosity. It is expected that if the ranges were not pruned, more significant correlations would be observed. However, these correlations would likely be between fatigue life and pore characteristics, like the porosity eliminated during preliminary parameter refinement, and not from direct effects of the melt parameters on the microstructure. Hopefully the conclusions made in this study will allow others to save time by reducing the required parameter refinement to that preformed in preliminary testing, eliminating the need for such extensive fine-tuning. More significantly, the lack of discernable effect of processing parameters essentially defines the acceptable processing window to achieve good properties, which is very important for manufacturing.

It has been suggested that perhaps the HIP treatment mitigated the effect of different melt conditions on fatigue life. Unfortunately, because of how the study was designed, a conclusion on this cannot be made. Including un-HIPed condition seems reasonable from an academic/scientific point of view, as it may reveal some interaction with fatigue life that is masked by the HIP treatment. However, when looking at this project with a design for manufacturing point of view, the effect of processing conditions on the un-HIPed condition means very little. Li et al. (26) showed that HIP and machining are both required to achieve fatigue results in EBM that are comparable to traditional manufactured Ti-6Al-4V. In addition,

to this author's knowledge, most, if not all, AM parts designed for high cycle applications are HIPed. With this design for manufacturing mindset, it becomes clear that only HIPed samples should be studied for high cycle fatigue studies of this type as any industrial application of EBM for a high cycle application will almost certainly require HIP treatment. Perhaps this will not always be the case as the EBM process becomes more sophisticated, at which point this study may need to be reperformed.

While it was surprising to find no clear relationship between melt parameters and fatigue life, the conclusion is still relevant. Overall, these results show that the time and resource intensive process of fine-tuning melt parameters does not yield meaningful improvements in fatigue life of Ti-6Al-4V. Instead, a rough optimization like that preformed in the preliminary testing is sufficient while the primary focus should be on HIP and heat treatment.

Although the main question of this study had been answered, additional testing was done to understand the cause of the poor performance of the 1100°C samples. With density, hardness, and tensile testing not providing a definitive answer, the next step was to investigate the microstructure.

2.7.1 Microstructure Analysis

Following fatigue testing samples were cut, mounted, polished, and etched for microstructural analysis. Etching was done using Kroll's reagent, with a composition of 95% water, 4% nitric acid and 1% hydrofluoric acid. Due to the danger associated with handling hydrofluoric acid, etching was performed at Eaton Corporation. After etching, samples were imaged using a combination of Scanning Electron Microscopy (SEM) and optical microscopy. SEM images were taken on a Joel 6610 LV SEM (Joel – Peabody, Massachusetts). Optical

images were taken using a Nikon ECLIPSE LV100ND (Nikon – Tokyo, Japan). The sectioning terminology is illustrated in Figure 82.

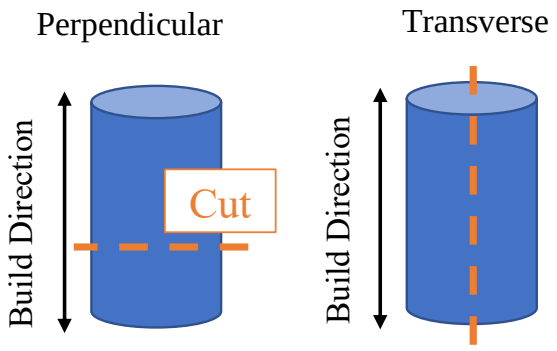

Figure 82. Diagram for sectioning terminology.

Optical images of both sectioning alignments for an 800°C and 1100°C sample were taken and provided in Figure 83 and Figure 84, respectively. A clear columnar grain structure can be seen in Figure 83 for the 800°C HIPed sample. This structure is expected in as-fabricated Ti-6Al-4V samples produced with AM and is a result of solidification mechanics in the build bed. As newly melted material solidifies, its structure is influenced by the previous layer by aligning the grain orientation and following the grain boundaries that continue as the grain grows upwards. Depending on the material, this will result in elongated columnar grains that follow the build direction. (36) As expected, these highly elongated grains can cause anisotropy in the material. The presence of columnar grains in the 800°C samples show that much of the as-fabricated microstructure is preserved after treatment. This is not the case for the 1100°C treatment. Figure 84 clearly shows the significant difference in overall macrostructure and grain texture. Most noticeably, the columnar microstructure found in the transverse 800°C samples has been replaced with a much courser microstructure resembling an equiaxed grain structure in the 1000°C samples. However, these large regions with clearly defined boundaries are not the actual grains of this structure, or at least not at this temperature. The boundaries highlighted in Figure

85 are known as the “ghost structure” and are the remnants of the prior β-grains that existed above the β-tranus. For Ti-6Al-4V, the β-transus occurs at 995°C, above this temperature the entire microstructure is in β-phase. As the material cools below the transus, α-phase first nucleates at the β-grain boundary and grows into the β-grain either along the β-grain boundary or along a β {110} plane that is the interface with an α {0001} plane. These newly formed α-grains share similar crystallographic orientation as the seed α-grains, forming a continuous field of parallel plates known as an α colony. This process is known as sympathetic nucleation and growth. Colonies will continue to grow until they encounter another β-grain boundary or another α colony with a different orientation. This means that the α colony size is dependent on and smaller than the prior β-grain size. Due to the β stabilizing vanadium, a portion of the β matrix is retained between the α-grains forming the α-β structure, known as α-β lamellae. (18) As a result of this nucleation and growth process the boundaries of the original β-gains are visually preserved while the actual “grains” of the microstructure have the smaller α-β lamellae structure seen in the superimposed 50x optical image found in Figure 85. Although harder to see, the 800°C perpendicular section also has prior β-grains boundaries. However, they are much smaller and difficult to see since the material did not remain above the β-tranus for long enough to allow for significant β-grain coarsening like that occurred to the 1100°C sample. In fact, the large columnar grains are also the remnants of prior β-grains that were built up little by little from multiple solidification pools, rather than grain coarsening. The role these colonies play in fatigue life will be discussed further after additional characterization is presented.

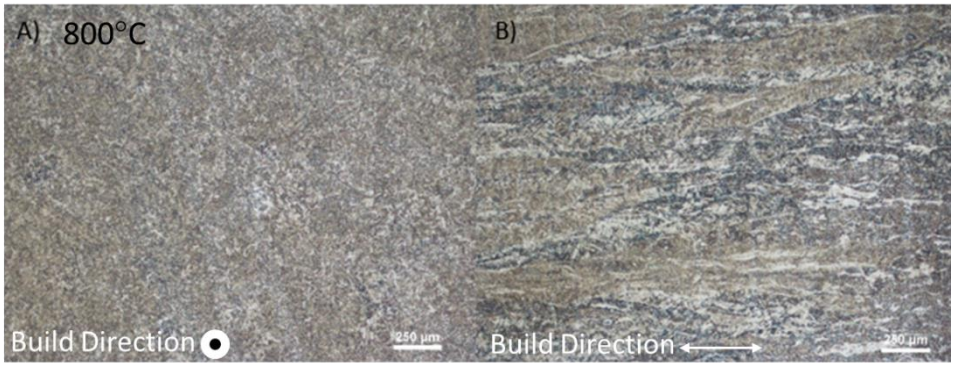

Figure 83. 10x optical image of 800C etched sample. A) Perpendicular and B) Transverse.

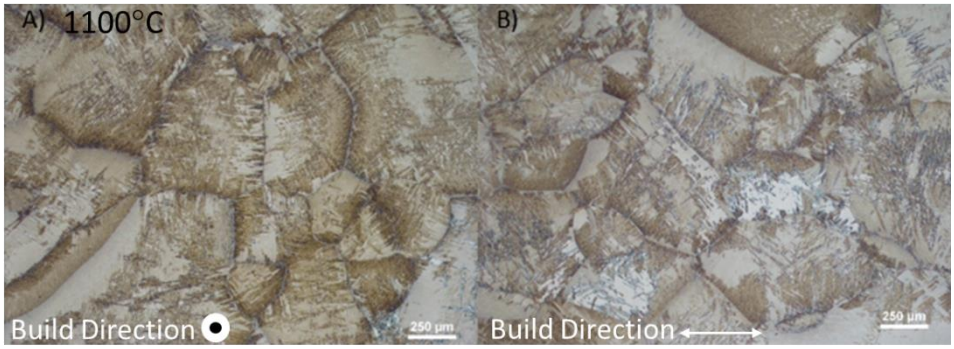

Figure 84. 10x optical image of 1100°C etched sample. A) Perpendicular and B) Transverse

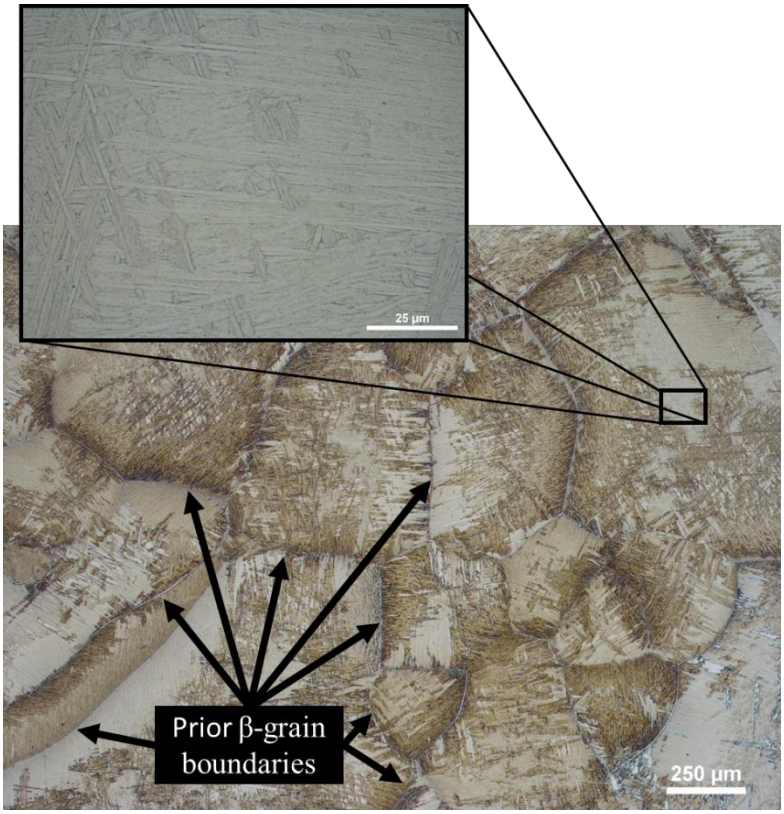

Figure 85. 10x optical image (background) of 1100°C microstructure highlighting prior β-grain boundaries and superimposed 50x optical image highlighting the α-β lamellar grain structure.

The optical images alone show a significant difference in the macrostructure and grain texture between the 800°C and 1100°C HIP samples. SEM micrographs were taken to further investigate the difference in microstructure between samples. To analyze the effects of processing conditions on the microstructure further, a method of measuring the α-lath thickness was developed using a combination of automatic image processing and manual point selection. With these measurements, it became possible to quantitatively evaluate the effects of processing conditions on a major microstructure characteristic. First, MATLAB's adaptive thresholding and Imbinarize functions are applied to a 1000x SEM micrograph to enable further processing steps. The threshold value is determined by comparing single β-grains (white sections) from the original image to the processed version, ensuring the processed image accurately represents the original image. An example of this proccess is provided in Figure 86.

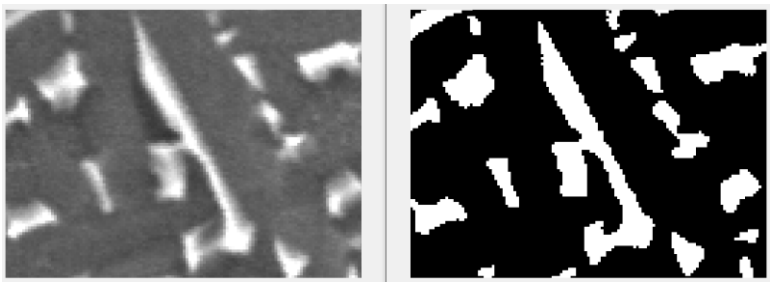

Figure 86. Comparison of 5-34 beta grain in original SEM image (left) and binorized image (right).

As seen in Figure 86, an accurate binary representation of the original image can be easily produced using simple thresholding. Following binarizing, lines were drawn across areas of parallel β-laths by manually selecting and entering the start and end pixel coordinates. These lines represent the measurement locations where lath thickness measurements would be taken. Special care was taken to ensure the lines were as perpendicular as possible to the aligned α/β orientation within the grains. An illustration of these lines is provided in Figure 87.

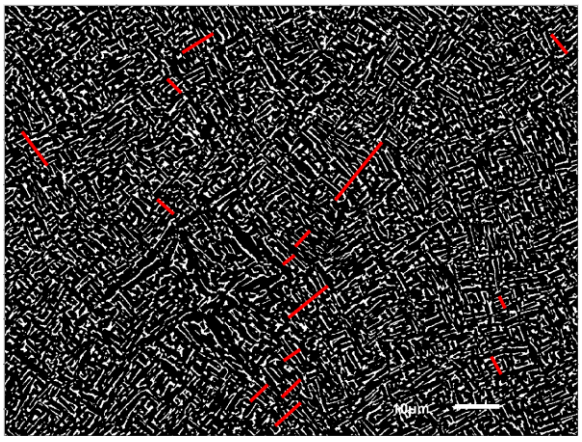

Figure 87. Sample 5-34 binarized with measurement locations highlighted in red.

Next, pixel intensities along the line profile were extracted from the binary image using the MATLAB function “improfile”. A plot of the extracted pixel intensities is provided in Figure 88. The α-grain widths were determined by measuring the widths of the zero intensity regions (start of black pixel to end of black pixel) along the pixel intensity profile.

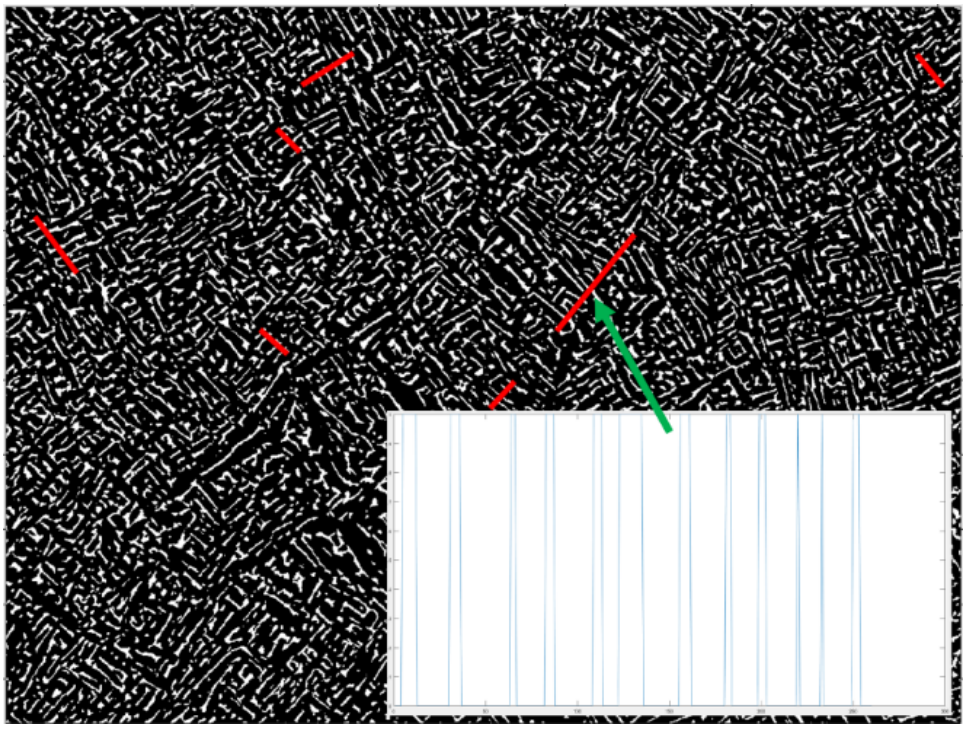

Figure 88. Same binarized image of 5-34 with pixel intensities extracted along the manually designated line.

A binary test image of known pixel dimensions (100 x 100 pixels) and alternating intensity band widths (10 pixels) was used to confirm that improfile and the script correctly accounted for real life vectors rather than the pixel approximation when measuring diagonal lines within the bitmap (binary image). This test image is provided in Figure 89. The script was used to measure the width of the dark bands in the test image at various angles and compared to known values determined by hand. These measurements were in good accordance, confirming the script was able to accurately measure the black bar widths at a variety of angles. This testing method should not be confused with the process of measuring the samples. During microstructure analysis, lines were selected to be as perpendicular as possible to the repeating laths. The script used to measure the a-lath thickness of both the 800°C and 1100°C samples can be found in Appendix B.

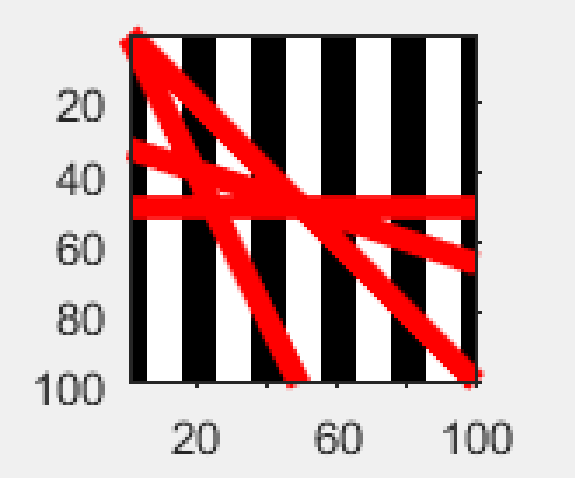

Figure 89. Test image used to confirm code was measuring code correctly.

To further confirm the accuracy of this method, the measured α-lath widths were plotted on a histogram to ensure they followed an expected normal distribution.

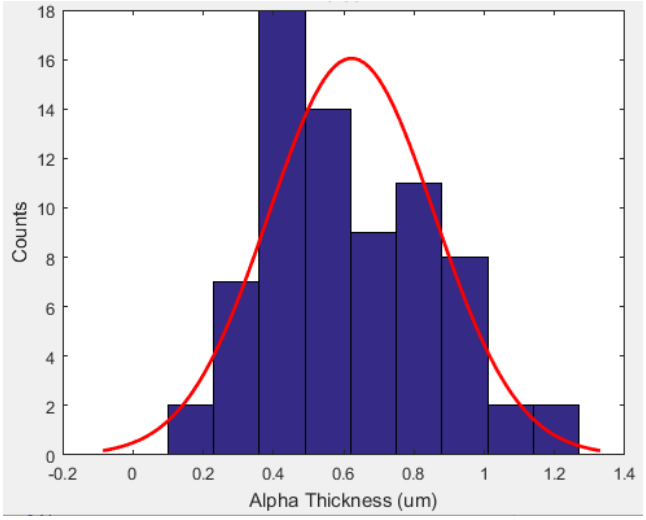

Figure 90. Histogram of sample 5-34 alpha lathe thickness measurements with normal distribution curve plotted overtop in red.

Unfortunately, due to timing, difficulty of safely etching samples, and technical issues with the 1100°C testing (see Chapter 3.3 for details), only a small number of samples could be etched and measured using this method. Although not every condition was measured, an adequate number of samples were measured to understand the effect of processing conditions on the α-lath thickness. Measurements for each sample measured are provided in Table 18.

Table 18. Table of average measured α-lath thicknesses.

Processing Condition	HIP (°C)	Avg. Lath Thickness (μm)
5-33	As-Fab	0.622 ± 0.24
2-33	As-Fab	0.713 ± 0.30
5-34	800	0.906 ± 0.27
3-34	800	0.942 ± 0.36
4-01	800	1.095 ± 0.55
7-04	1100	0.946 ± 0.40
3-06	1100	0.898 ± 0.31
4-06	1100	0.689 ± 0.22
6-07	800	1.230 ± 0.67
2-09	800	1.436 ± 0.76
7-09	800	0.916 ± 0.32
2-10	800	1.492 ± 0.82
6-10	800	1.050 ± 0.47
6-10	800	1.144 ± 0.45
1-15	800	1.146 ± 0.69
2-15	800	1.001 ± 0.41
5-15	800	0.884 ± 0.26
2-16	800	1.204 ± 0.64
8-16	800	1.137 ± 0.50

Average lath thickness for a sample was calculated by averaging all lath thicknesses extracted from around 10+ designated lines using a single 1000x SEM micrograph of each sample. Images were taken near the center of the sample. In most cases, 100+ laths were measured and averaged for each sample. It should be noted that although 6-10 is actually samples 6-10 and 6-26 which have identical print conditions. To better visualize the data, these results were then plotted in Figure 91.

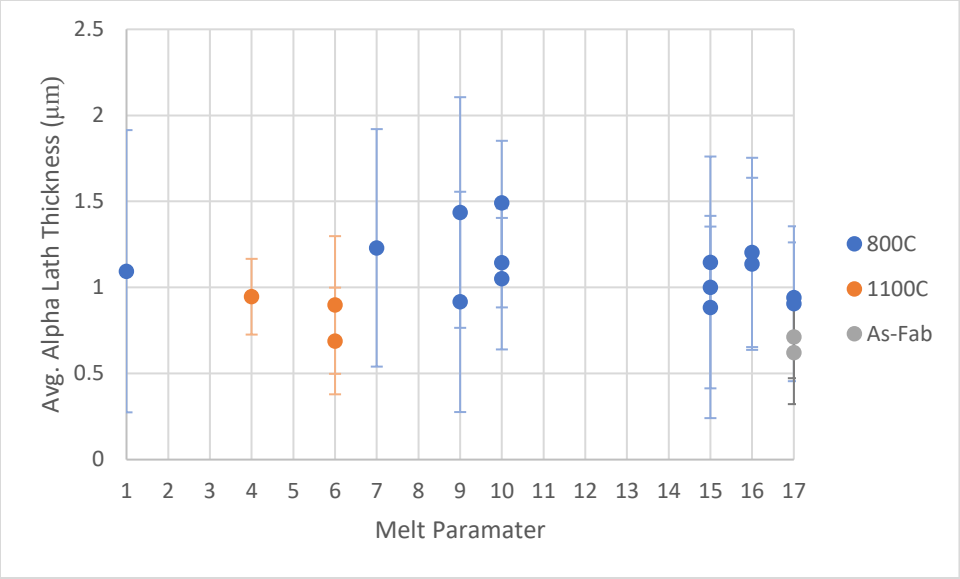

Figure 91. Plot of measured α-lath thicknesses. Processing Parameter 17 refers to dummy samples used as test/control samples for much of this study. Error bars represent ± 1 SD.

Variance in measurements between samples with the melt parameters is attributed to un-accounted parameters like powder bed conditions, natural noise of the system, and difference in measurement height with respect to the build plate. As previously mentioned, the distance of a sectioning to the build plate is unknown. Depending on how the blank was machined, the approximate ranges a sample could have been sectioned is between 10-15 mm or 45-50 mm from the build plate. There are conflicting reports regarding the relationship between α-lath thickness and height relative to the build plate. Author Wanjara et al. (46) found an increase in α-lath thickness with increasing distance from the build plate. While Hrabe and Quinn (47) suggest any changes in α-lath thickness are a statistical aberration as no similar changes in UTS or yield strength were found. Interestingly Galarragga et al. (48) found that α-lath thickness decreased with height. A summary of α-lath thickness *vs.* height relative to build bed for as-fabricated EBMed Ti-6Al-4V is provided in Table 19. In most cases the largest increases in α-lath thickness with increasing build height is reported in tall samples with shorter samples exhibiting lower gradients, with exception of Murr et al. (49). However, in their study only two samples were

examined. The cause of the gradient α-lath thickness with increasing distance from the build plate is thought to be related to cooling rates. Locations near the bottom of the build are able to conduct heat into the build plate, resulting in higher cooling rates and smaller α-lath thicknesses. Locations higher in the build are only able to dissipate heat through less direct means such as radiation from the top surface, conduction into the surrounding powder bed, and down through the printed part to the build plate, resulting in lower cooling rates and larger α-lath thicknesses. (50)

Table 19. Summary of studies that reported α-lath vs. distance from build plate for EBMed Ti-6Al-4V. Different melt parameters, machines, and machine models were used. All samples were analyzed in the as-fabricated (As-Fab) condition.

Author	α-lath thickness (μm)	Distance from build plate (mm)	Condition	Citation
Wanjara et al.	1.21 ± 0.08	20	As-Fab	(46)
	1.68 ± 0.09	360		
	1.06 ± 0.06	20	As-Fab	
	1.63 ±0.08	360		
Murr et al.	1.6*	10	As-Fab	(49)
	3.2*	58		
	1.4*	10	As-Fab	
	2.1*	58		
Lu et al.	0.74 ± 0.06	11	As-Fab	(51)
	0.92 ± 0.02	150		
	1.06 ± 0.05	290		
Tan et al.	0.58 ± 0.11	7.5	As-Fab	(50)
	0.77 ± 0.2	30		
Shama et al.	0.96 ± 0.45	16	As-Fab	(52)
	1.10 ± 0.49	107		
Galarragga et al.	0.61 ± 0.06	5	As-Fab	(48)
	0.32 ± 0.08	120		
Hrabe and Quinn	No significant difference	28 (max sample height)	As-Fab	(47)

* No standard deviation reported

Given the number of contradicting reports and unknown sectioning location for this study, the change in α-lath thickness as a function of distance from the build bed could not be estimated or accounted for. Additionally, the SD of α-lath thickness measured from individual samples

examined in this dissertation (all laths at same height) are approximately equal to the reported differences in measured thickness between top *vs.* bottom measurement locations. With the relatively short samples produced for this dissertation (60 mm) the change in α-lath thickness as a function of distance from the build bed is expected to be small, especially in comparison to the large SD already found for individual sample measurements. After computing the average lath thickness of each sample, MINITAB statistical software was used to determine if there were any statistically significant correlations between the processing conditions, fatigue life, and lath thickness. Similar correlation analysis was performed between the SD of each measurement and appropriate factors, however no statistically significant correlations were found. After completing this analysis, it was then possible to compare the effects of the processing on the resulting microstructure both visually and quantitatively.

Table 20. Correlation coefficients and P-values for image processed samples. Generated using MINITAB software.

Factor 1	Factor 2	N	Correlation	P-Value
Speed Function	Avg. Lath Thickness	17	0.251	0.331
Line Offset	Avg. Lath Thickness	17	0.048	0.856
Focus Offset	Avg. Lath Thickness	17	0.347	0.172
HIP	Avg. Lath Thickness	17	-0.504	0.039
Cycles	Avg. Lath Thickness	11	0.592	0.055

To start, two as-fabricated dummy samples with identical melt parameters, but different build numbers were compared to see if variations between builds had any obvious effect on the microstructure. These micrographs are presented in Figure 92.

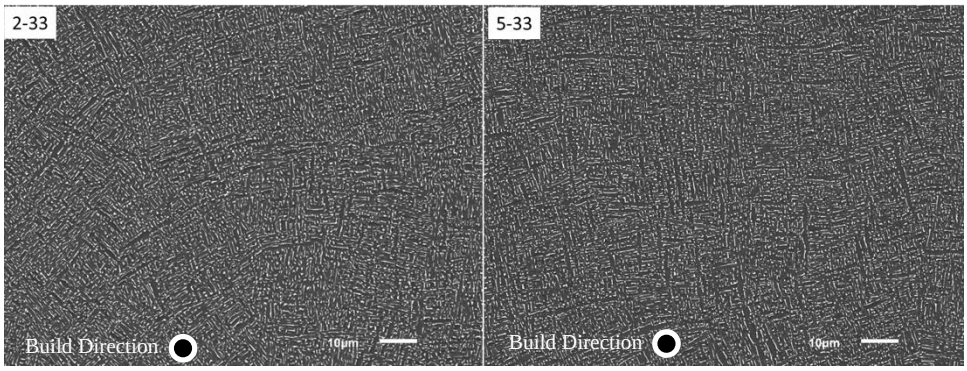

Figure 92. Comparison between two 1000x SEM micrographs of as-fabricated samples 2-33 and 5-33. Both samples have the same melt parameters.

Visually there are no striking differences between the microstructures of sample 2-33 and 5-33. Average lath thickness for these samples were also very similar, being measured as 0.713 and 0.622 μm, respectively. Measurements between different builds for melt parameters 6, 9, 10, 15, and 16 were also found to have similar sized α-laths when SD was taken into account. This is expected as these samples were produced with the same melt parameters and build number was not found to have a statistically significant correlation with fatigue life. Build number was not included in the α-lath thickness correlation analysis because many of the samples imaged for this analysis were from build 2, since they were the first samples available after being used to determine testing stress levels for the other samples. As a result, it would not be correct to present build and lath thickness data as a statistically backed conclusion while a biased samples set was used. However, based on the results of the fatigue study, visual observations, and α-lath measurements, it is assumed that average α-lath thickness did not vary significantly between builds. Using this assumption the effect of HIP condition on microstructure can be investigated by comparing samples with identical melt parameters but different build numbers and HIP conditions.

Although a lower than standard HIP temperature of 800°C was used to minimize grain coarsening, some amount of coarsening is expected. To evaluate the degree of coarsening from

the HIP treatment, dummy samples 2-33 and 3-34 were compared. Both samples were printed with identical melt settings. While sample 2-33 remained in the as-fabricated condition, sample 3-34 was treated with the 800°C HIP treatment. A side-by-side comparison of the two samples is presented in Figure 93.

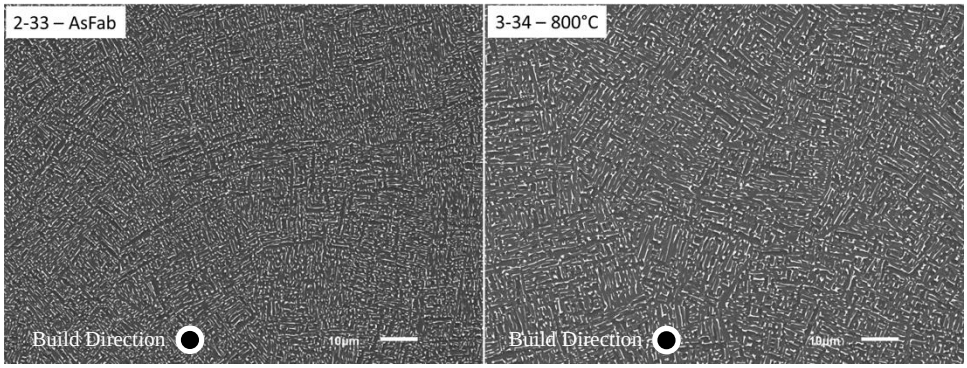

Figure 93. Comparison between two 1000x SEM micrographs of as-fabricated sample 2-33 and 800°C HIP treated sample 3-34. Both samples have the same melt parameters.

Figure 93 shows that the structures are fundamentally similar. Both have a large number of small, narrow sections of parallel α/β laths, with the HIPed sample showing obvious signs of coarsening. Lath measurements indicated a 40% increase in average α-lath thickness from 0.668 µm for the as-printed samples to 0.924 µm for the 800°C HIPed dummy samples. The overall average α-lath thickness for the 800°C HIP condition was found to be 1.15 µm. To illustrate the similarity in microstructures between samples with different melt conditions, a select number of additional micrographs of 800°C HIPed samples have been included in Figure 94.

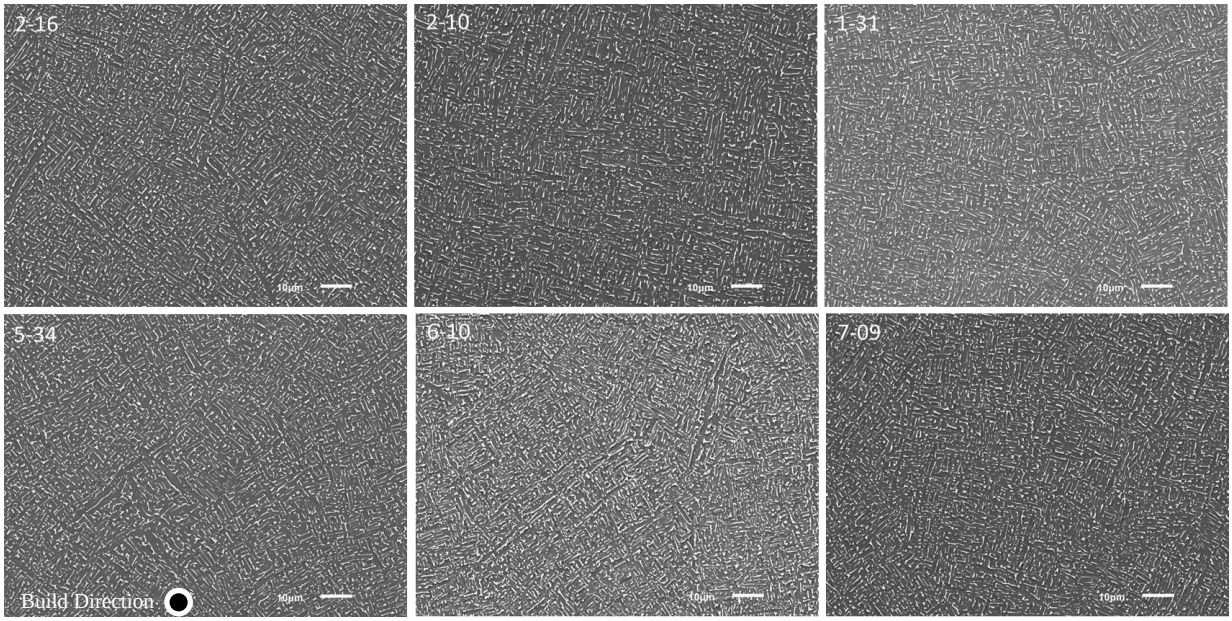

Figure 94. 1000x SEM micrographs of multiple main study fatigue samples treated with 800°C HIP treatment. All images share the same sectioning orientation with the build direction being in or out of the page.

From these micrographs and the statistical analysis performed on the α-lath data, no significant difference exists between samples with different melt conditions. This is in good accordance with the previous fatigue data statistical analysis which found no statistically significant correlations between fatigue life and melt conditions SF, FO, or LO.

The overall microstructure was already shown by optical imaging to vary significantly based on HIP treatment. Micrographs of 1100°C HIPed samples were taken in order to understand the effect of HIP condition in the microstructure. No dummy samples were included with the 1100°C HIP treatment so the effect on identical melt parameters could not be analyzed. Fortunately, it has already been shown that the melt parameters studied and build have an insignificant effect on the microstructure. A comparison between sample 2-10 and 3-22 can be found in Figure 95.

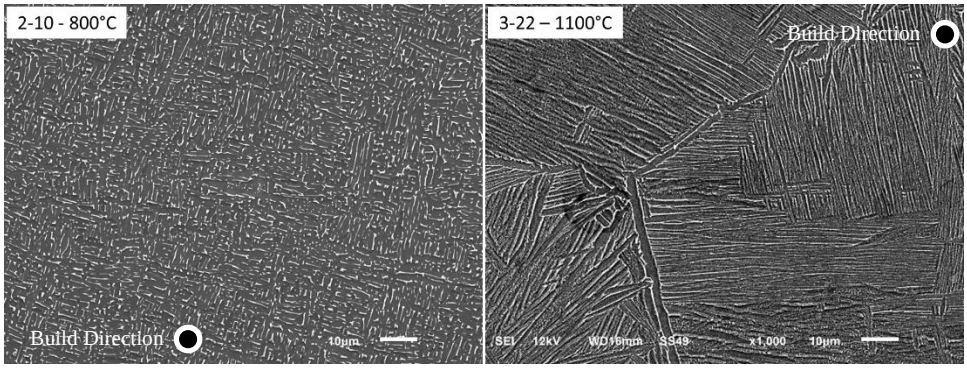

Figure 95. Comparison between two 1000x SEM micrographs of main study sample 2-10 treated with the 800°C HIP treatment and sample 3-22 treated with the 1100°C HIP treatment.

While the 800°C was shown to thicken the α-laths, but preserve the overall structure, the 1100°C exhibits an entirely different macro and microstructures. Large colonies of parallel α laths can be found throughout the micrography of sample 3-22. These colonies are orders of magnitude larger than any structure found in the 800°C micrographs. A select number of additional micrographs of the 1100°C samples are included in Figure 96 to illustrate the size and distribution of colonies across the samples.

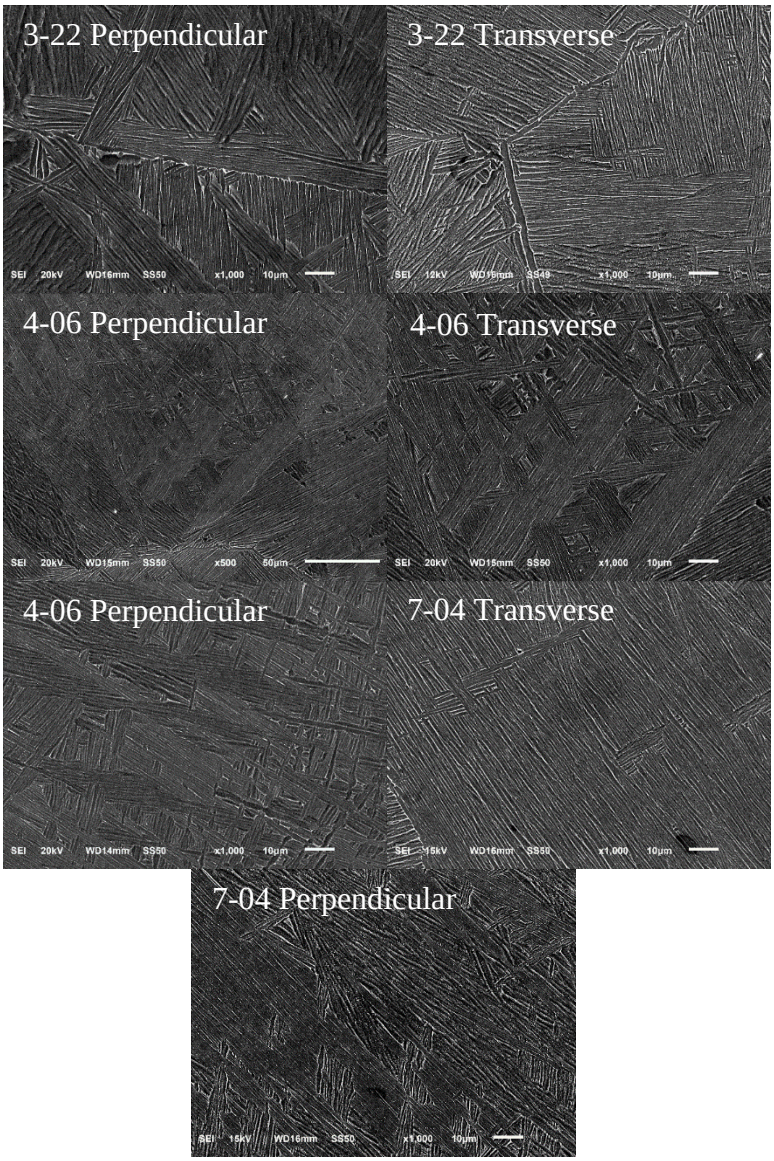

Figure 96. 1000x SEM micrographs of multiple main study fatigue samples treated with 1100°C HIP treatment and 2.5°C/s quench.

The average α-lath thickness for all 1100°C samples was found to be 0.844 μm, indicating the 1100°C HIP treatment with quench did achieve the original goal of producing fine α-laths. However, the correlation between lathe thickness and fatigue life was not found to be statistically significant. This relationship between decreasing α-lath thickness and increasing fatigue life is well studied in literature (29) (27) (53). This statement shows the need for further investigation and is not meant to contradict previously published conclusions. Although the P-value between

these factors is right on the edge of the significance threshold having a value of 0.055, the calculated correlation coefficient of 0.592 suggests that increasing lath thickness increases fatigue strength, which is contrary to what is found in literature. Looking closer at the data, the 800°C samples do, in fact, have a higher average α-lath thickness and fatigue life, as compared to the 1100°C samples. Thus, another, more impactful and systemic characteristic is skewing the α-lath analysis by reducing the fatigue performance of the 1100°C samples. The most likely culprit is β-grain coarsening, and subsequent formation of large α colonies, that occurred during the super-transus, 1100°C HIP treatment.

Optical and SEM imaging showed clear prior β-grain coarsening. During nucleation, α-grains continue to grow until they encounter a β-grain boundary or another α-grain, meaning that larger prior β-grains produce larger α colonies. (18) Everaerts et al. (29) and Zhang et al. (54) refer to these large α colonies as macrozones, due to their large size and tendency to function similar to a single large grain. Their work has shown how the interaction between large macrozones can result in a phenomenon known as internal crack initiation (ICI). Typically, fatigue cracks are initiated at the surface from residual stresses or defects, as the name suggests, ICIs originate inside the material and are associated with longer fatigue lives. (55) (56) As a result, ICIs are more likely to occur in VHCF testing because the higher runout limit allows samples that did not fail from defects, to cycle long enough to fail from slower progressing ICI cracks. Although ICIs are observed in other materials like high-strength steel, these cracks are the result of inclusions. (57) Inclusions are rare in titanium thanks to the Kroll's process used to chemically extract the material from Titanium rich ores. (18) Instead, ICI cracks in titanium are the result of the anisotropic α phase HCP structure and its tendency to form macrozones. (29) ICI sites are found at the interface of two macrozones where at least one zone's c-axis is significantly

misaligned with the load axis. The c-axis of an α-grain's hexagonally close packed (HCP) structure is aligned with the c-axis of the crystal as depicted in Figure 97. Once such ICI site investigated by Zhang et al. (18) is presented in Figure 98.

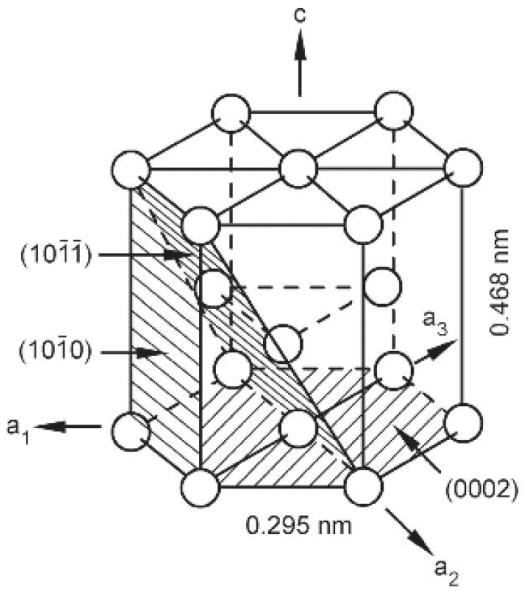

Figure 97. Representation of α-phase titanium's Hexagonal Close Packed (HCP) crystallographic structure. (18)

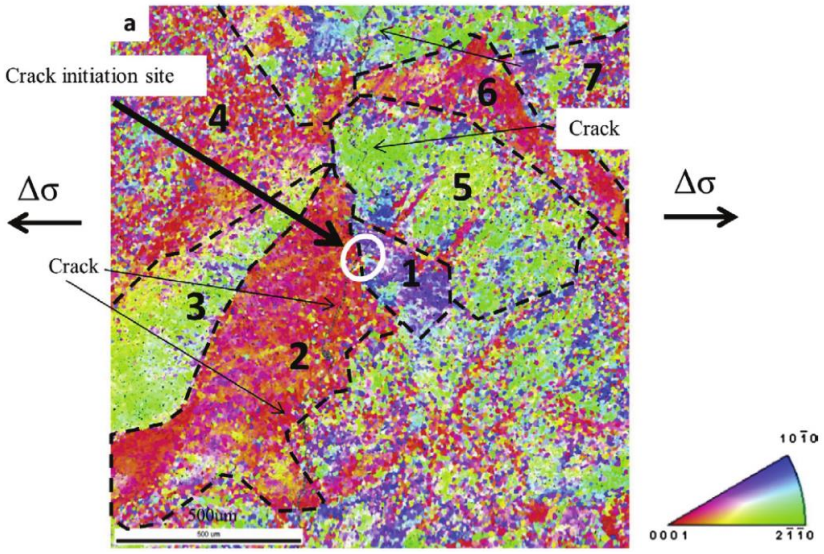

Figure 98. Illustration of crack initiation in macrozones in forged Ti-6Al-4V. Image is EBSD scan representing grain alignment. (54)

This EBSD scan shows that the two macrozones located at the crack initiation site have significantly different orientations with respect to one another. Alignment of slip systems with respect to the load axis is represented by Schmid's Law described by Eq. (3).

$$\tau_C = \sigma_y \cos(\varphi) \cos(\gamma) \tag{3}$$

Schmid's Law is used to calculate the resolved shear stress on a given slip system to determine if it reaches the critical resolved shear stress where yielding occurs, τ_C. σ_y is the yield strength of the material, φ is the angle between the slip plane normal and applied force and γ is the angle between the slip direction and applied force. (58) Together these angles form the Schmid factor given as

$$Schmid\ Factor = \cos(\varphi) \cos(\gamma) \tag{4}$$

An illustration of these angles, applied force, and slip planes is provided in Figure 99.

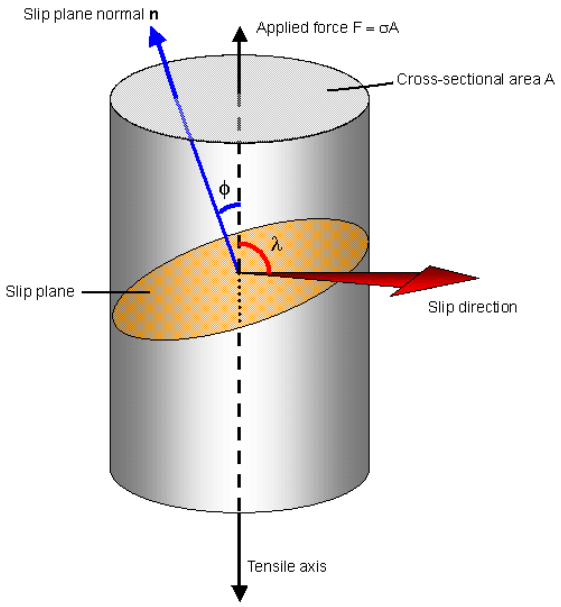

Figure 99. Illustration of applied forces on a single crystal to illustrate the how a tensile stress is translated to a shear stress along the crystal's slip direction as described by Schmid's Law. (58)

Macrozones with sufficiently high Schmid Factors (SF) for slip systems with low τ_C are called 'soft' grains as their alignment allows for easier plastic deformation. (29) Similarly grains with

their c-axis aligned with the load axis have high SF and are called ‘hard’ grains, as their orientation better resists plastic deformation. (54) (29) As the load is applied, these soft grains are the first to plastically deform, which is most commonly caused by the movement of dislocations in the crystal lattice. (59) Dislocations are able to easily travel large distances through these macrozone due to the aligned slip systems, where they pile up at the interface with another macrozone that has a high misorientation with the soft grain. This pile up occurs because a large amount of energy is required for the dislocations to propagate into the misaligned slip system at the interface creating an area of high dislocation density at the interface. Larger macrozones have larger slip distances, increasing the number of trapped dislocations at the interfaces. (54) As more dislocation conglomerate, the stress on the basal plane of the neighboring grain increases until it fractures along the plane, initiating a crack. (29) Fractures of this kind produce a large smooth surface on the fracture surfaces known as facets which are found at or near ICI sites. Most facets are reported to be the basal plane or near-basel plane (10 - 15°). (29)

It is believed that ICI is the cause of the poor fatigue performance found in the 1100°C samples. Holding the material above the super-transus heating during the HIP treatment coarsened the prior β-grains, resulting in large α colonies/macrozones as the material was cooled below the β-tansus. Larger macrozones are more likely to have ICI due to larger interfaces between zones and longer slip lengths resulting in higher dislocation densities at these interfaces. In general, the authors who have studied this phenomenon recommend minimizing macrozone size to prevent this type of crack initiation. (29) (18) (54) (55) This same mechanism is less likely to occur in the 800°C samples as the refined prior β-grains, and subsequent colony sizes, significantly increases the energy required for dislocation movement by requiring dislocations to

transfer between multiple slip systems when traveling a comparable distance in a 1100°C sample. In addition, smaller colonies have smaller slip distances reducing the shear stresses associated with dislocation pileup at zone interfaces. This hypothesis is supported by further analysis conducted on the fracture surfaces of the fatigue samples from both HIP conditions tested in this study.

Before proceeding further, it should be noted that super-transus treatment is not inherently associated with decreased fatigue performance. High heating and cooling rates combined with annealing treatment have been shown to increase fatigue performance, as presented in Figure 100. (18)

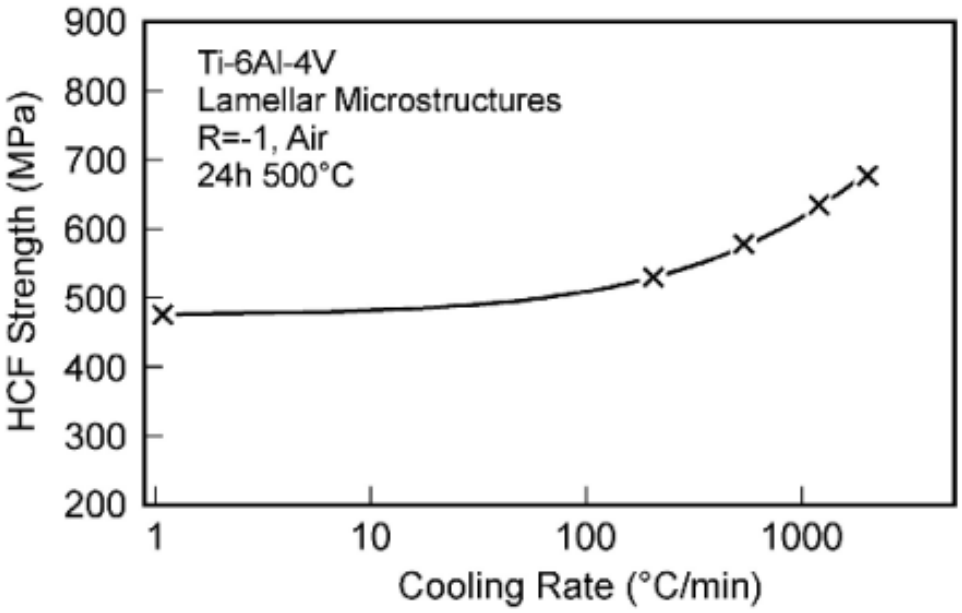

Figure 100. High cycle fatigue strength (10^7 cycle runout and R = -1) vs cooling rate from β phase (above β-transus) field of Ti-6Al-4V lamella microstructure. Following cooling, samples were annealed at 500°C for 24 hours. (18)

For reference, the cooling rate used during the 1100°C HIP treatment was found to be approximately 150°C/min. The increase in fatigue life is attributed to higher cooling rates minimizing α colony size while the subsequent aging treatment transforms any α' into fine α – β

laths. However, in order to minimize the time and number processing steps, lengthy annealing steps as featured in Figure 100 were not considered for this study.

2.7.2 Fractography

Fracture surfaces of fatigue samples were imaged to further differentiate the fracture mechanics exhibited by each HIP condition as well as look for evidence of facet crack initiation. All seven of the 800°C samples that fractured were imaged. A total of # 1100°C samples fractured, but to minimize the analysis, an effort was made to select the three best and worst performing samples for each stress level, but too few samples matching these descriptions were available. It should be noted that these 1100°C samples were selected before all testing was complete and are not the true best and worst performers. In addition, only samples that completely fractured could be analyzed. In some instances, the fatigue machine would detect a sufficient reduction in natural frequency due to crack growth and end the test before actual separation of the two halves could occur. Efforts were made to separate the halves along the crack by the subsequent tensile testing mentioned earlier. However, nothing resembling the fatigue fracture surfaces could be found in the tensile fracture surface, so no further attempts were made.

ICI with facets present in the initiation site were found in nearly every sample. Each instance could be categorized into one of three categories commonly found in literature as illustrated in Figure 101 by Liu et al. (56)

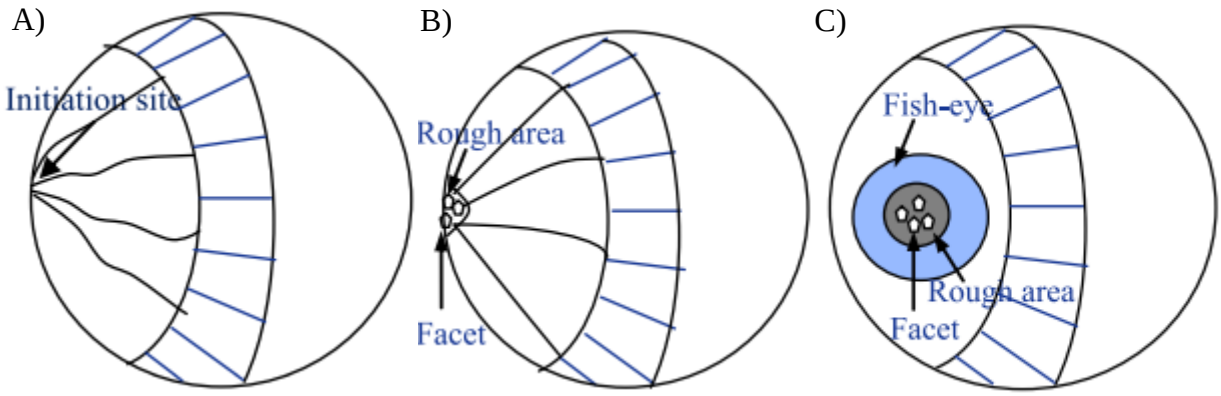

Figure 101. Three common fracture surfaces found in VHCF Ti-6Al-4V as illustrated by Liu et al. A) Surface cracking no facets. B) Near-surface initiation with facets. C) Fish-eye initiation far from surface. (56)

The first is traditional surface-initiated cracking. The next is near-surface ICI with a rough patch containing facets. This rough area is the result of short crack growth, where a crack will propagate through a single α-grain or only a few grains, together initiation and short crack growth take up more than 90% of the sample's fatigue life. (29) (60) After propagating to sufficient size, the short crack growth transitions into long crack growth, characterized by a significantly higher propagation rates and smoother appearance. If the ICI point and subsequent short crack growth region is close enough to the surface, it is said to behave like a surface crack. (29) If sufficiently far enough from the surface, the long crack growth will continue until the effective cross-section is reduced to the point the sample can no longer support the applied load, causing it to fail suddenly from overload fracture. (29) There are disagreements in literature regarding the correlation between ICI depth and fatigue life. For example, Heinz et al. found clear correlation between ICI depth and fatigue life as seen in Figure 102. (61)

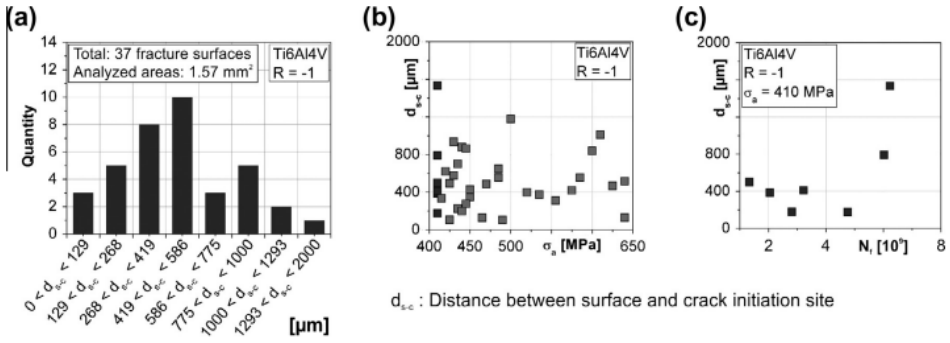

Figure 102. (a) Quantity of occurrence for defined locations of the crack initiation site, (b) location of the crack initiation site versus σ_a and (c) correlation between the location of the crack initiation site and Nf for σ_a = 410 MPa. (61)

However, Yokoyama et al. (62) found no correlation between ICI depth and fatigue life when studying Ti-6Al-4V and Ti-Fe-O alloys. They also found no correlation between the peak load and the ICI location as shown in Figure 103.

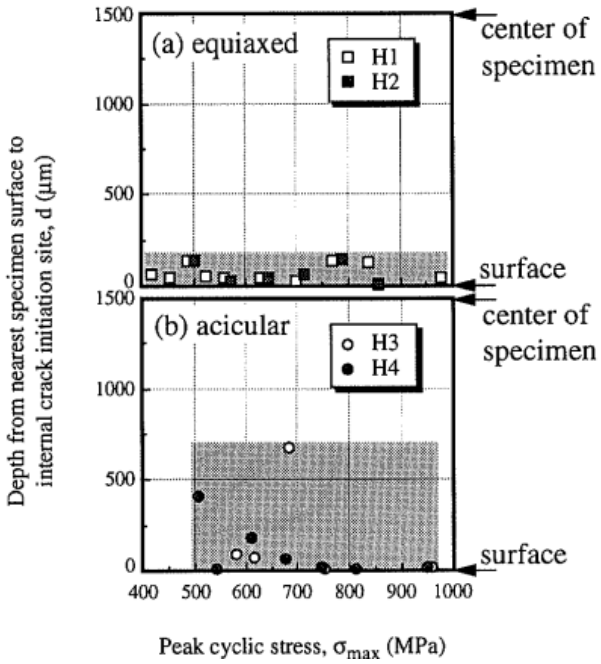

Figure 103. Location of the internal crack initiation site of Ti-6Al-4V alloy. (62)

Everaerts et al. (29) makes the argument that since initiation and short crack growth can take up more than 90% of the samples' fatigue life, as long as the initiation point and short crack growth

regions are not close enough to the surface to act as surface cracks and it would make sense that depth would not have a significant impact on fatigue life. The last category of fracture commonly observed is known as a “Fish-eye” fracture. This occurs when the initiation point is much further from the surface, allowing the short and long growth regions to form concentric rings that resemble the eye of a fish. Typically, these types of fracture are associated with longer fatigue lives, even more than so near-surface ICI. (29) Details of each sample imaged are recorded in Table 21.

Table 21. Sample details of on which fractography was performed. Where Surface, Near and Fish-eye refer to surface initiated crack, near-surface ICI crack, and far from surface ICI crack, respectively.

Sample	Facet	Type	HIP (°C)	Load (MPa)	Cycles
5-30	**Yes**	Near	1100	550	1.64E+04
4-21	**Yes**	Near	1100	550	1.71E+04
7-03	**Yes**	Near	1100	550	2.22E+04
5-22	No	Surface	1100	550	2.39E+04
3-22	No	Surface	1100	550	2.54E+04
4-04	**Yes**	Near	1100	550	3.72E+04
7-04	**Yes**	Near	1100	500	6.40E+04
4-06	**Yes**	Near	1100	550	7.08E+04
3-15	**Yes**	Near	800	550	9.59E+04
1-31	**Yes**	Near	800	550	1.07E+05
8-16	**Yes**	Near	800	550	1.08E+05
7-09	No	Surface	800	550	1.23E+05
7-15	No	Surface	800	550	1.37E+05
6-12	**Yes**	Near	1100	550	3.15E+05
1-03	**Yes**	Near	1100	500	4.49E+05
5-04	**Yes**	Near	1100	500	7.37E+05
7-21	**Yes**	Fish-eye	1100	500	9.45E+05
5-15	**Yes**	Near	800	550	2.25E+07
6-24	**Yes**	Fish-eye	800	500	2.59E+07

Surface-initiated cracking was found in both 800°C and 1100°C HIP conditions. One instance is presented in Figure 104.

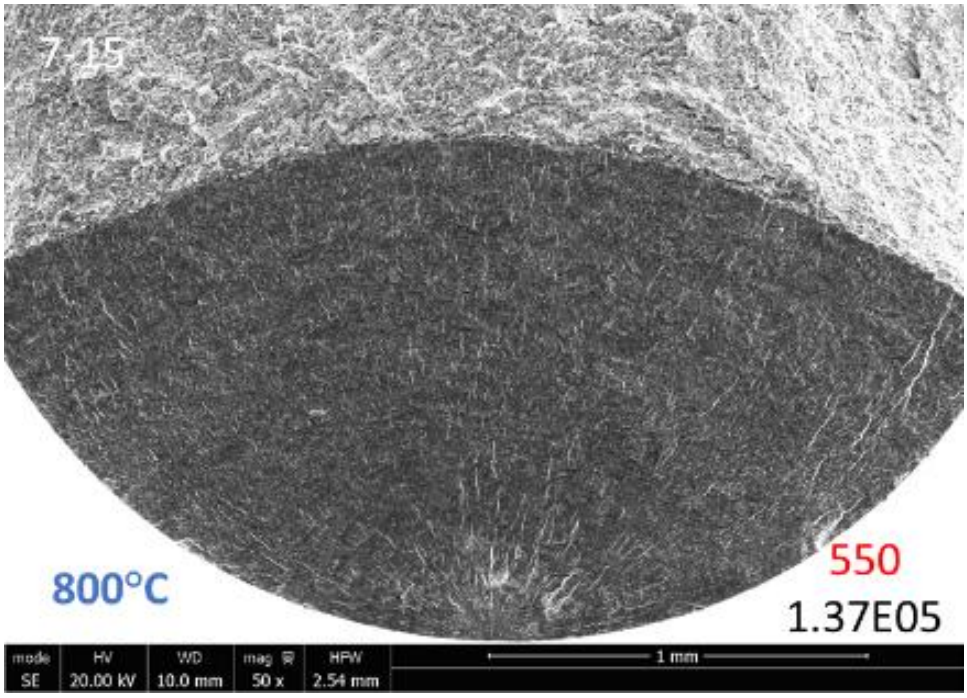

Figure 104. 50x SEM image of sample 7-15.

A higher magnification of the initiation point is presented in Figure 105.

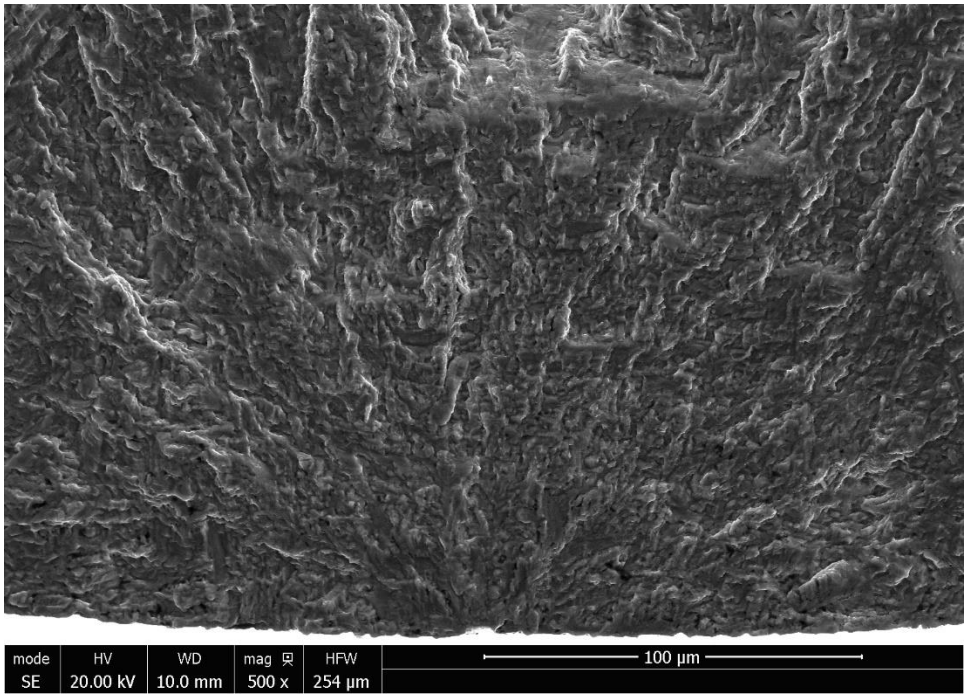

Figure 105. 500x SEM image of sample 7-15 initiation point.

Although the lower magnification image looks like the near-surface ICI and a facet can be seen near the top of Figure 105, further investigation and tracing of the white river marks, which follow the direction of crack growth, indicate the crack in sample 7-15 initiated at the surface. This was similarly observed in sample 3-22, which was one of only two 1100°C HIPed samples whose crack origins did not appear to be directly related to ICI. The other was sample 5-22.

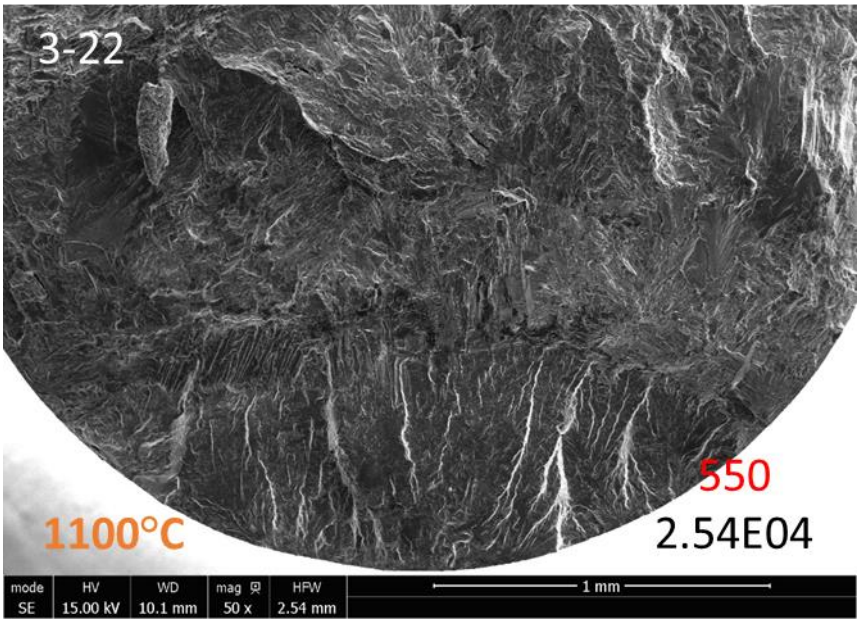

Figure 106. Fracture surface of sample 3-22.

A higher magnification image of the fracture surface of sample 3-22 is presented in Figure 107, where large flat surfaces thought to be facets are circled in red.

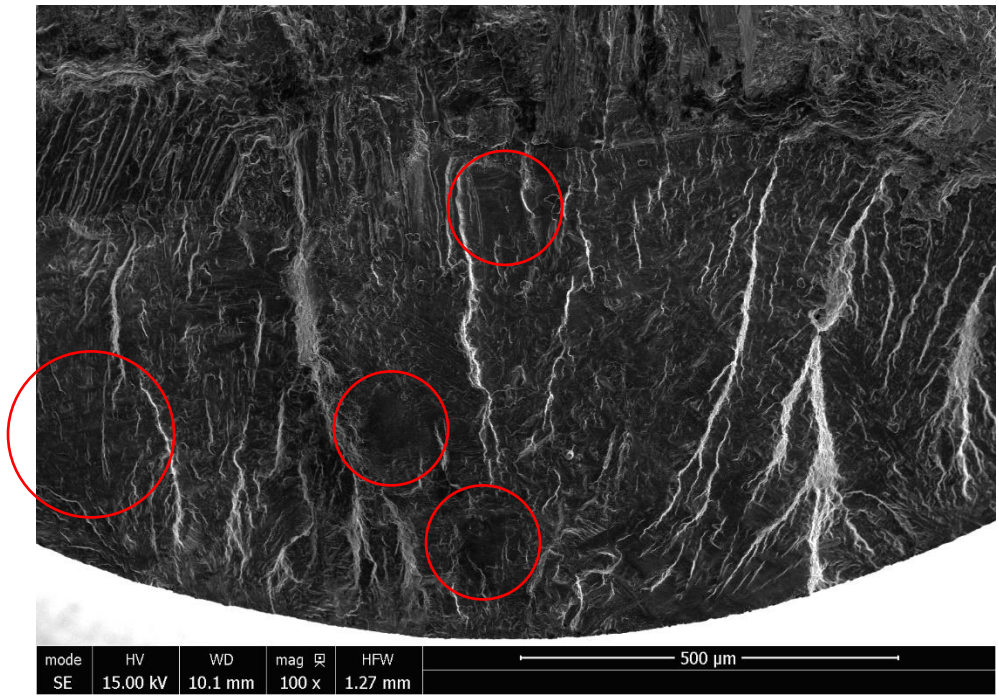

Figure 107. 100x SEM image of sample 3-22 fracture surface. Large flat areas though to be facets are circled in red.

Like sample 7-15, facets were found in the fracture surface of sample 3-22. However, the river marks flow around these regions, but do not emanate from them indicating they did not initiate the crack. By following the river marks, it appears that crack initiation for this sample occurred at the surface. Facets formed in 7-15 and 3-22 do not appear to be the crack initiators, and likely formed during crack propagation. It is possible this speeds up crack growth, particularly in sample 3-22, by allowing the crack to quickly shear much like how dislocations can move easier through an α colonies' aligned slip system.

One instance of fish-eye fractures was observed in both 800°C and 1100°C HIP conditions. An SEM image of the 800°C sample fracture surface is provided in Figure 108, and a higher magnification of the initiation point is included in Figure 109.

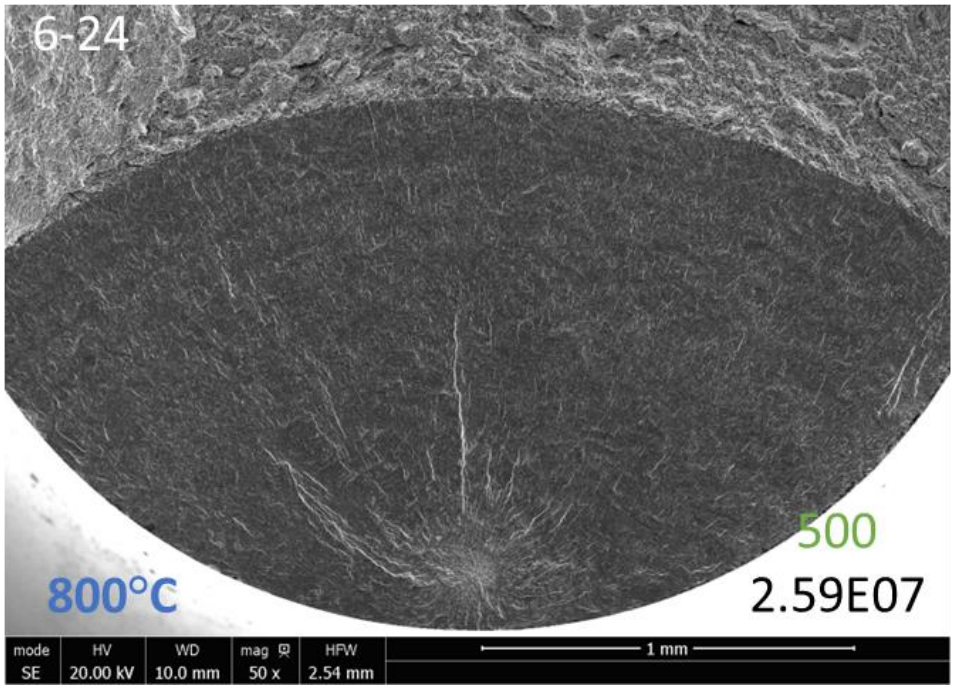

Figure 108. Fracture surface of sample 6-24.

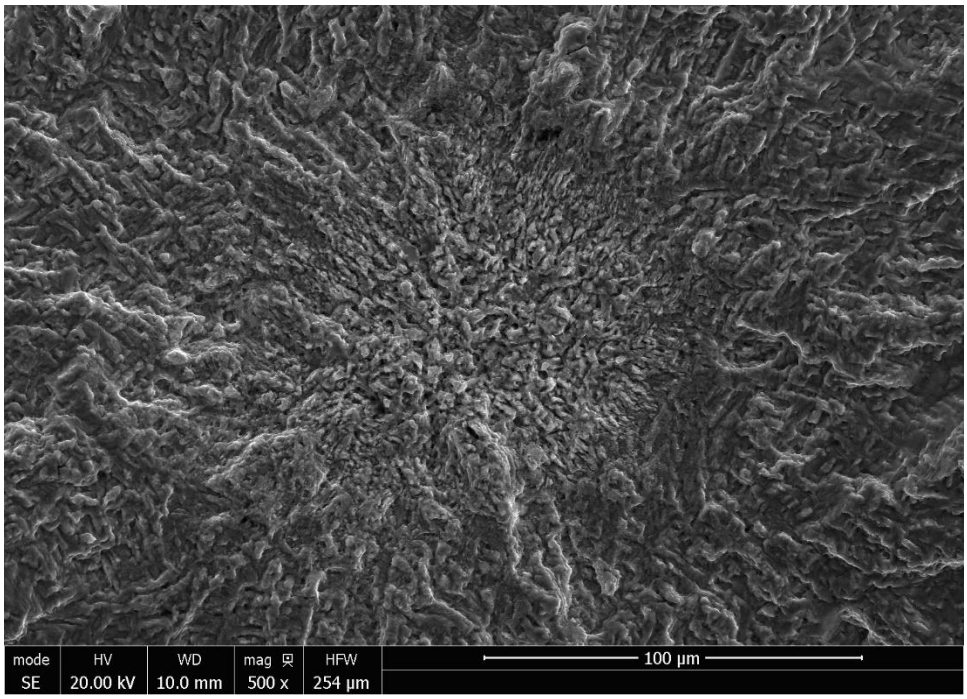

Figure 109. 500x SEM image of sample 6-24.

Interestingly, sample 6-24 does not have appear to have the expected large flat facets in the rough section, however, the appearance of the overall fracture surface is in good accordance with fish-eye fractures presented in literature. The smaller than expected facets are due to the small α colony size found in the 800°C samples during microstructure analysis. As such, the facet found in sample 7-21, as well as the other 1100°C samples, are significantly larger in comparison. A SEM image of sample 7-21 can be found in Figure 110, with an additional higher magnification image of the initiation point included in Figure 111.

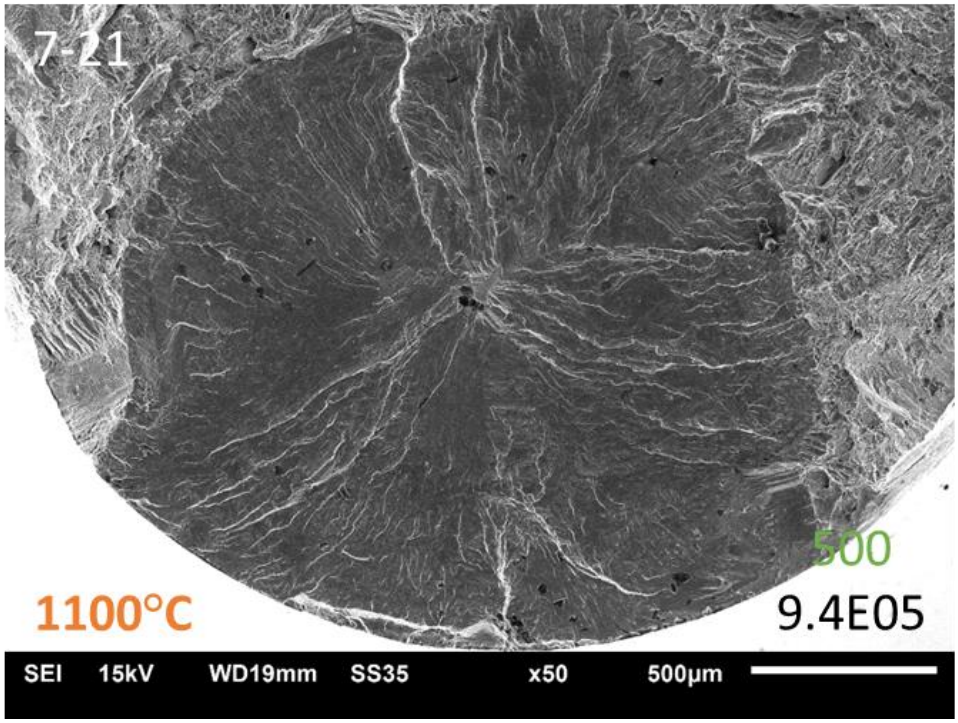

Figure 110. SEM image of sample 7-21 fracture surface which exhibits a Fish-eye fracture.

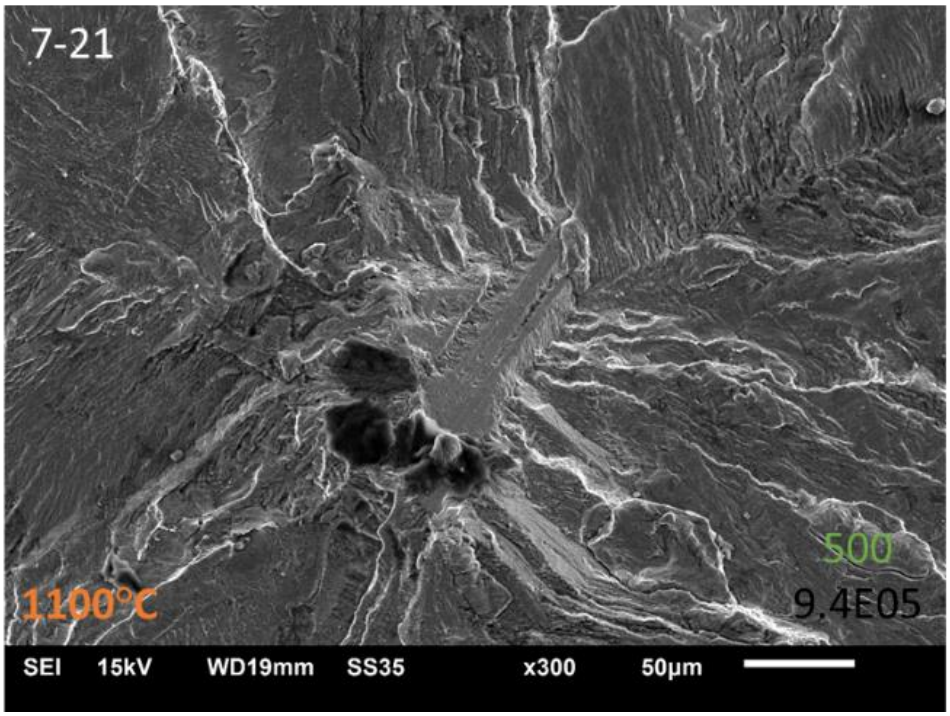

Figure 111. 300x SEM image of ICI point in fracture surface of sample 7-21.

Figure 110 and Figure 111 are not part of the sample and are low density contaminates left over from when the sample was sectioned in preparation for density, hardness, and microstructure analysis. It is not surprising that samples 7-21 and 6-24 presented with fish-eye fractures as they are the longest-lived fractured samples for each of their respective HIP conditions, supporting the idea that fish-eye fractures are associated with higher fatigue lives. It is likely that additional 800°C have similar fish-eye fractures growing inside, but reached runout before the short crack growth could transition to long crack growth. Although 1E08 cycles would be considered infinite

life for most industrial applications, the slow growing ICI cracks brings into question whether titanium alloys have true endurance limits.

Most of the remaining samples failed from near-surface facet ICI. A selection of 800°C samples are provided in Figure 112.

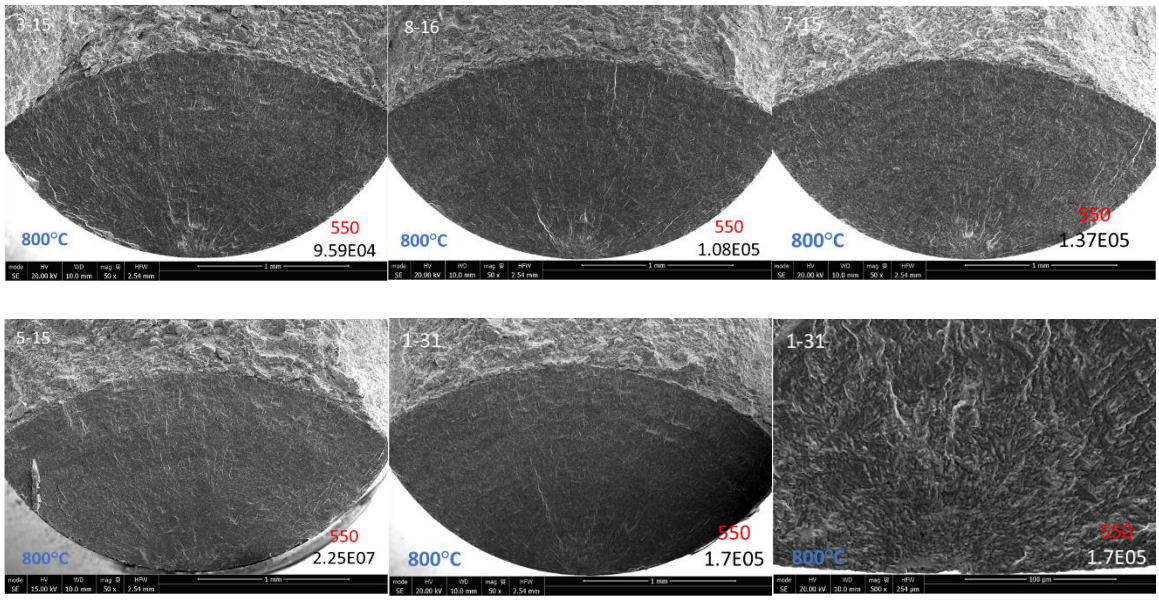

Figure 112. Select fractography images of 800°C HIP treated samples.

Additional 1100°C samples are provided in Figure 113.

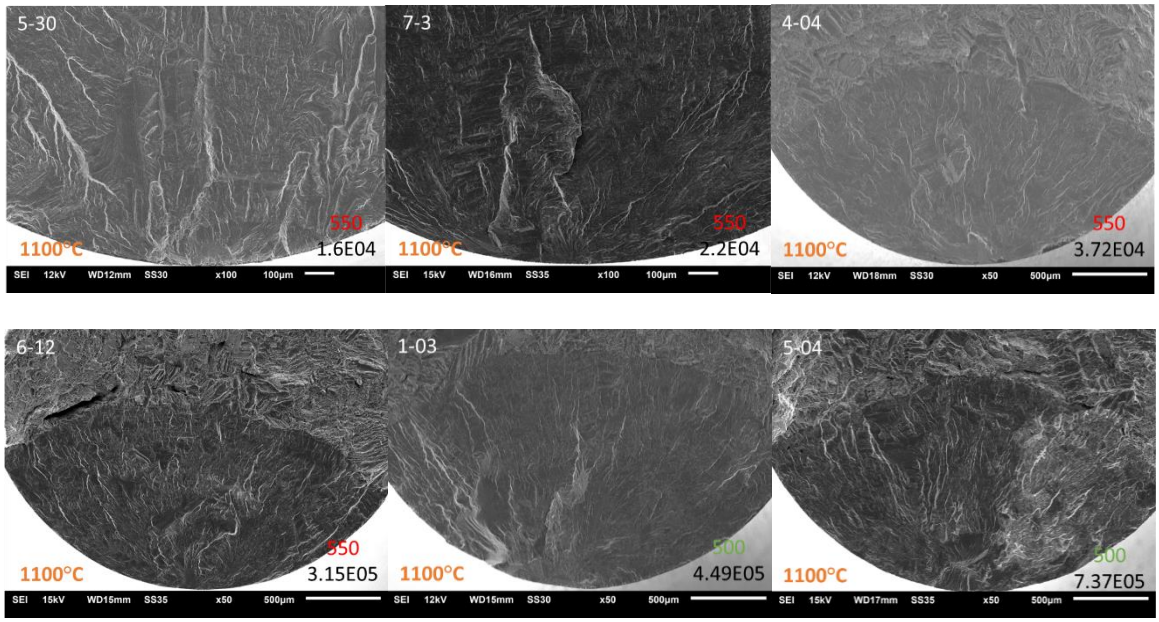

Figure 113. Select fractography images of 1100°C HIP treated samples.

Two of the most noticeable near surface ICI were samples 7-04 and 4-06, as shown in Figure 114.

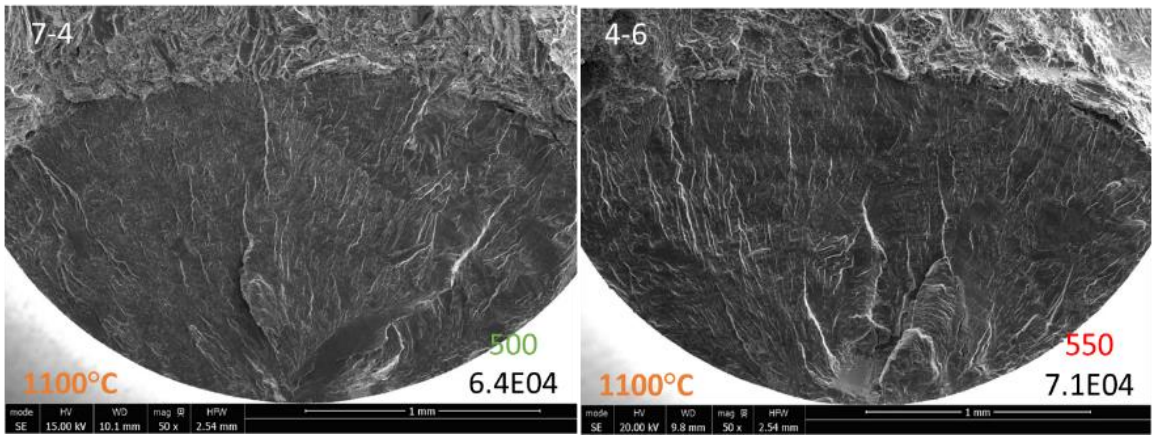

Figure 114. 1100°C HIP treated samples 7-04 (left) and 4-06 (right) with clear evidence of large facet initiated crack formation.

Higher magnification images of these fracture surfaces are provided in Figure 115, Figure 116, and Figure 117.

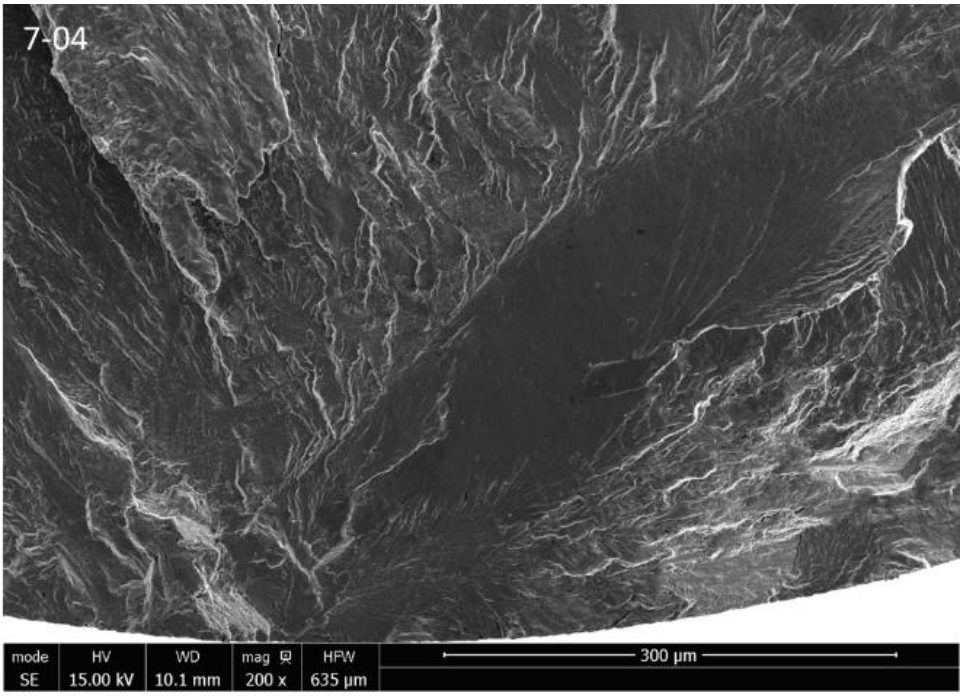

Figure 115. Higher magnification SEM image of facet-initiated fatigue crack in sample 7-04.

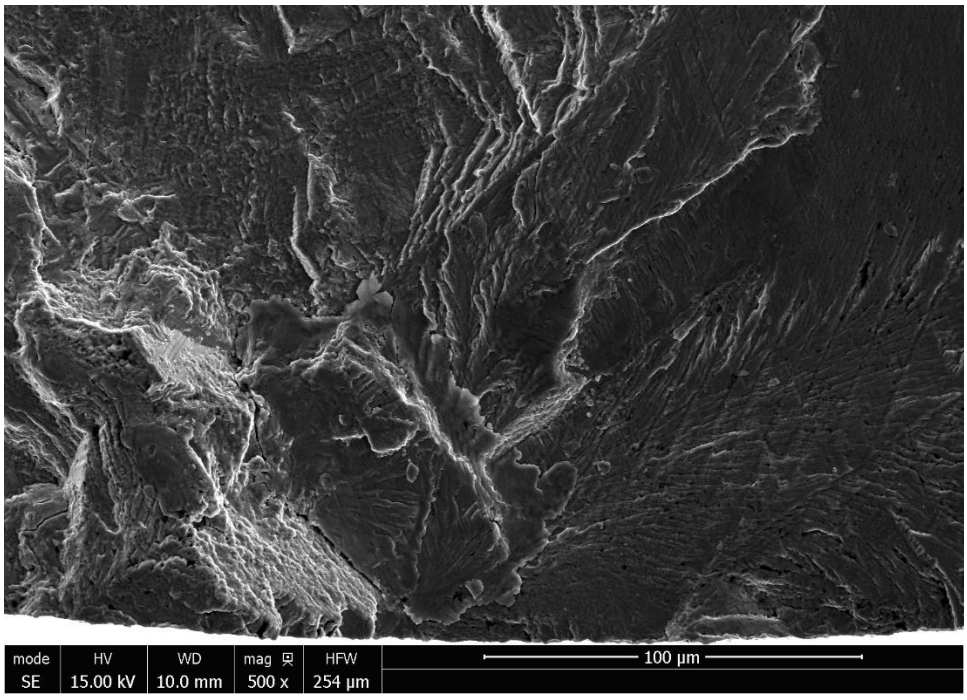

Figure 116. 500x SEM image of facet-initiated fatigue crack in sample 7-04.

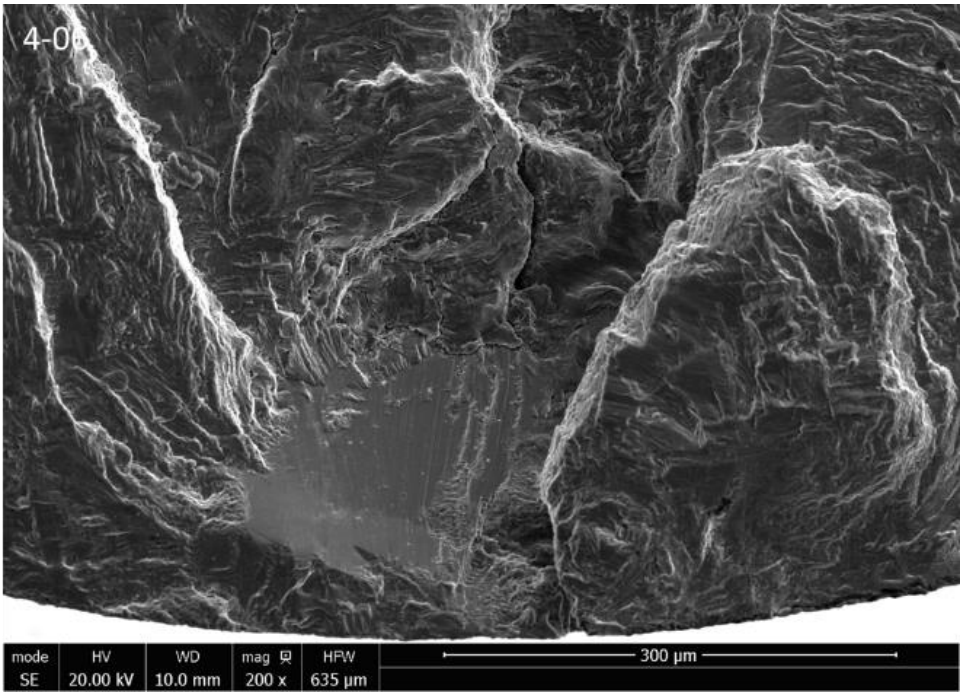

Figure 117. Higher magnification SEM image of facet-initiated fatigue crack in sample 4-06.

Samples 7-04 and 4-06 provide the clearest evidence of facet ICI, having the largest and most pronounced facets of any sample imaged.

It is clear from the images presented that although all three types of fractures were found for both HIP conditions, the fracture surfaces for each treatment are distinct. Any facet found in the 800°C samples was small in comparison to those found in the 1100°C samples. This directly links back to the differences in the microstructure discussed earlier. The larger α colonies of the 1100°C samples produced larger, more dramatic facets as well as a rougher more three-dimensional fracture surface. This dimensionality is most likely the result of long crack growth propagation along the α colony borders. In comparison, the long crack growth section of the 800°C samples are quite smooth. Interestingly, no evidence of porosity induced crack formation was observed in any sample imaged. These observations further reinforce the conclusion that the

cause of the 1100°C samples' poor fatigue performance is formation of large α colonies as the result of prior β-grain coarsening during the super-transus heat treatment.

2.7.3 EBSD

In addition to minimizing α lath thickness, the super-transus heat treatment was selected to eliminate the directionality associated with the columnar grain structure by transforming the structure back to pure β phase. Unfortunately, directionality was not directly tested in this study as it introduced significant complexity to an already complex DOE. Originally, the plan was to compare the fatigue correlations between the two HIP treatments. If correlations between melt parameters and fatigue life were found in the 800°C HIP, but not the 1100°C, then it would be reasonable to conclude that the super-transus treatment was effective at removing the effect of the melt parameters. Conversely, if the same correlations were found to hold for both HIP treatments, then the super-transus treatment did not remove the effect of melt parameters. Since both directionality and effect of melt parameters are the effects of build conditions, it is reasonable to assume that if the treatment had enough impact on the structure to eliminate some of the thermal history, then it stands to reason other effects of the thermal history, like directionality, would be similarly affected and could be confirmed using additional metallography analysis. Unfortunately, no statistically significant correlations between any melt parameter and fatigue life were found for either HIP condition, limiting our ability to conclude how effective the super-transus treatment was at eliminating the build history. Optical microscopy of the etched 1100°C sample showed that the columnar grain structure was eliminated and presented with a more equiaxed prior β-grain structure. However, it is possible some remnants of the build direction still persist in the microstructure through process induced preferential grain orientation. With the lack of supporting fatigue data, optical microscopy alone

was deemed insufficient, and electron backscatter diffraction (EBSD) was performed. EBSD is used to identify the crystallographic orientation across the surface of a polished sample by analyzing the diffraction pattern produced by electrons after being fired at the sample and redirected by the materials crystal lattice. Using this technique, it should be possible to identify any lingering traces of directionality in the super-transus samples, by comparing the distribution and frequency of different orientations that appear for each HIP condition.

EBSD testing was performed on three samples, as-printed, 800°C, and 1100°C. The sample numbers for each of these conditions are 5-33, 5-34, and 3-22, respectively. It should be reiterated that samples 5-33 and 5-34 have the same melt parameters and were both dummy samples used to balance the build bed to 36 samples to create an even 6x6 print pattern. The melt parameters used for these samples were the exact center of the DOE ranges selected. The only difference between these samples is that 5-33 remains in the as-printed condition, while 5-34 was included in the 800°C HIP treatment used on the other main study samples. Neither sample was machined into the hourglass fatigue sample geometry. Although fatigue data result already showed that melt parameters did not significantly impact the fatigue results, it was still thought best to scan two samples with identical melt parameters. Scans were performed on a Tescan Mira scanning electron microscope (SEM) (Tescan Mira – Kohoutovice, Czech Republic) with an accelerating voltage of 25 KeV and working distance of 15 mm. To better analyze the overall texture, eight, 100x, 5-minute scans were taken at multiple locations to ensure that multiple colonies were measured. Orientation mapping was investigated using an Ametek (TSL) orientation imaging microscopy (OIM) system on the TescanMira with a step size of 5 μm. Indents were made in the sample surface using a hardness tester in order to identify locations of

the individual scans and merge them into a single composite image. An illustration of the scans performed on each sample are provided in Figure 118, Figure 119 and Figure 120.

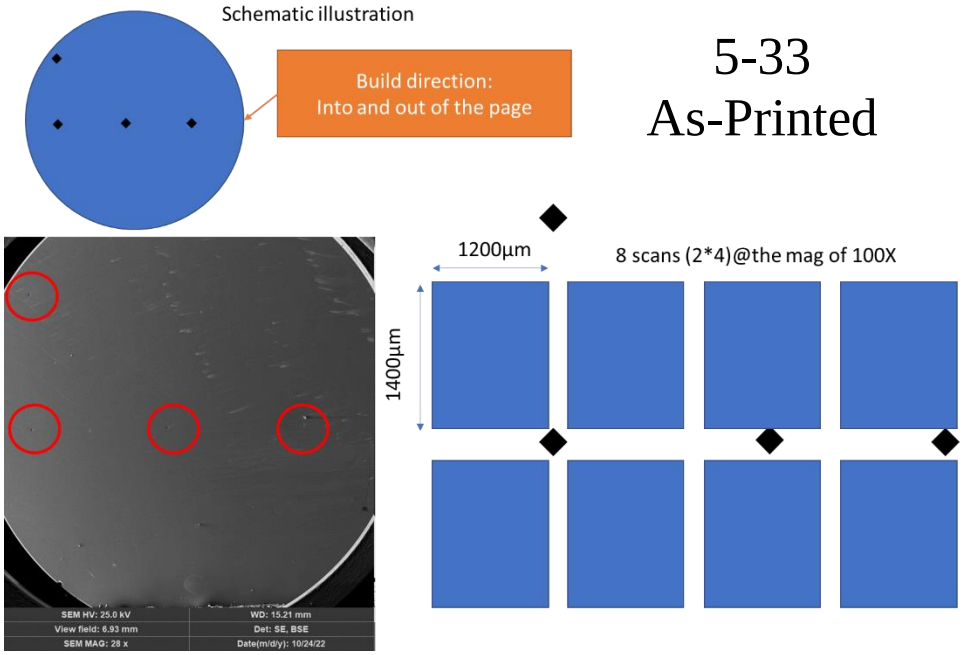

Figure 118. EBSD scan layout for sample 5-33. Still in the as-printed condition and sectioned so build direction is into or out of the page.

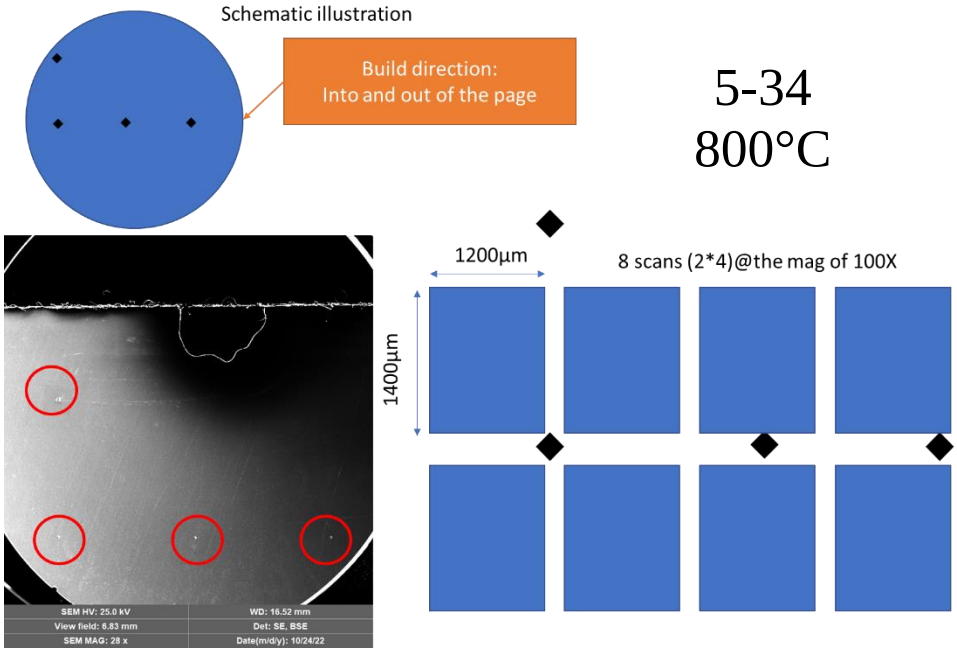

Figure 119. EBSD scan layout for sample 5-34. Sample was HIPed at 800°C and sectioned so build direction is into or out of the page.

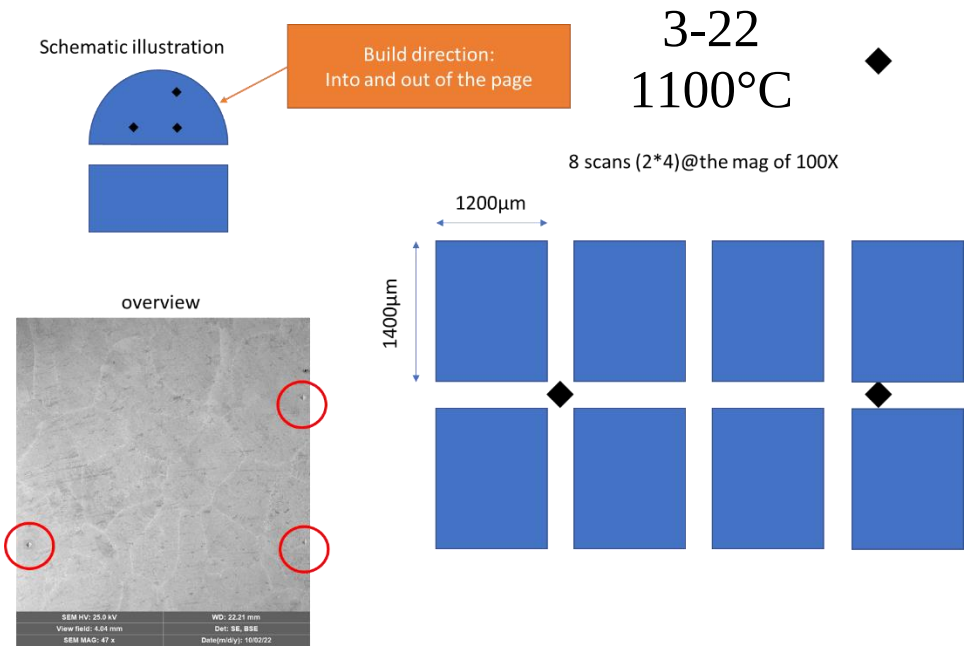

Figure 120. Scan layout schematic for EBSD scan of sample 3-22. Sample was HIPed at 1100°C, sectioned and, tested so build direction is into or out of the page.

To confirm that a large number of colonies were scanned, SEM images for each scan location were then reconstructed using the indentation marks. These composites are provided in Figure 121, Figure 122, Figure 123.

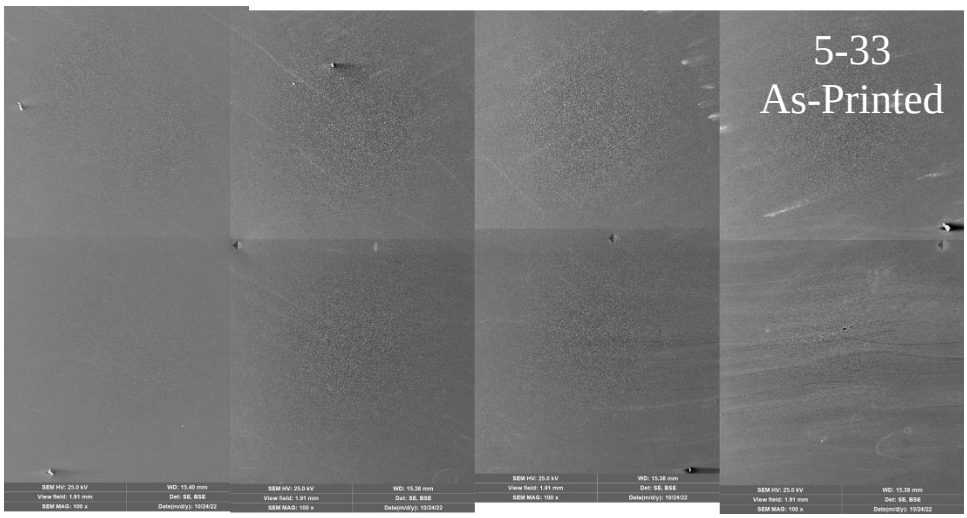

Figure 121. SEM image of 5-33 EBSD scan area. Overall scan area is reconstructed from series of individual SEM images.

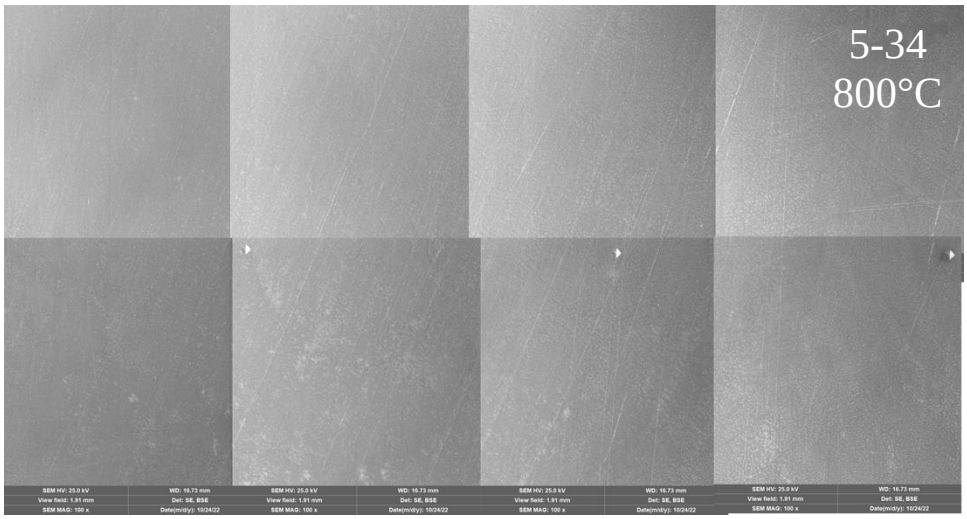

Figure 122. SEM image of EBSD scan area for sample 5-34. Overall scan area is reconstructed from series of individual SEM images.

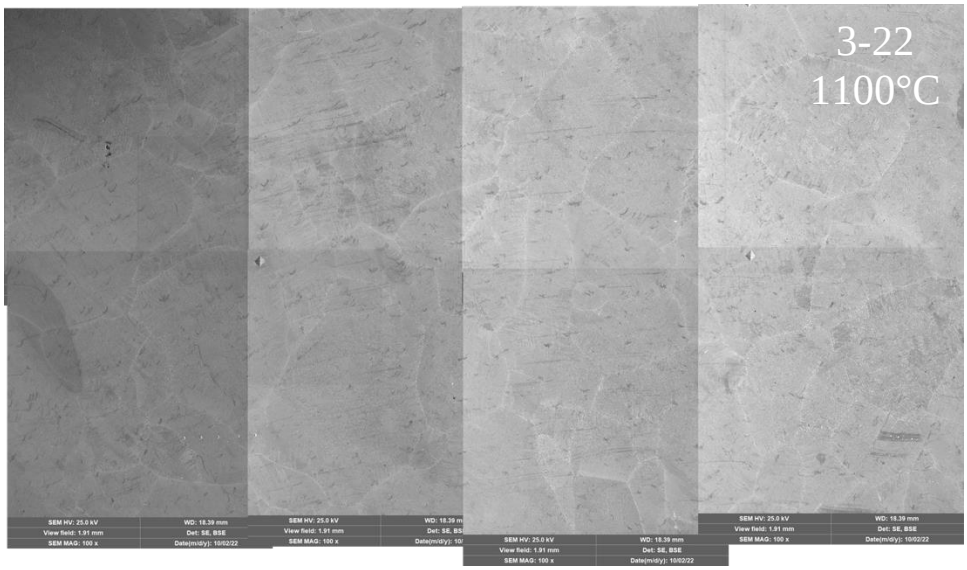

Figure 123. SEM images of EBSD scan area of sample 3-22. Overall scan area is reconstructed from series of individual SEM images.

Grain orientation maps were similarly reconstructed to form a composite image of the scan area. Analysis and cleanup of EBSD data (including one iteration of neighbor confidence index (CI) correlation followed by grain CI standardization clean-up) was conducted using OIM Analysis software v.8.5.0. A CI > 0.1 was chosen to create maps and pole figures (PF). The colors indicate

the crystal direction pointing out of the sample surface (normal direction inverse pole figures maps). These reconstructions are provided in Figure 124, Figure 125, and Figure 126.

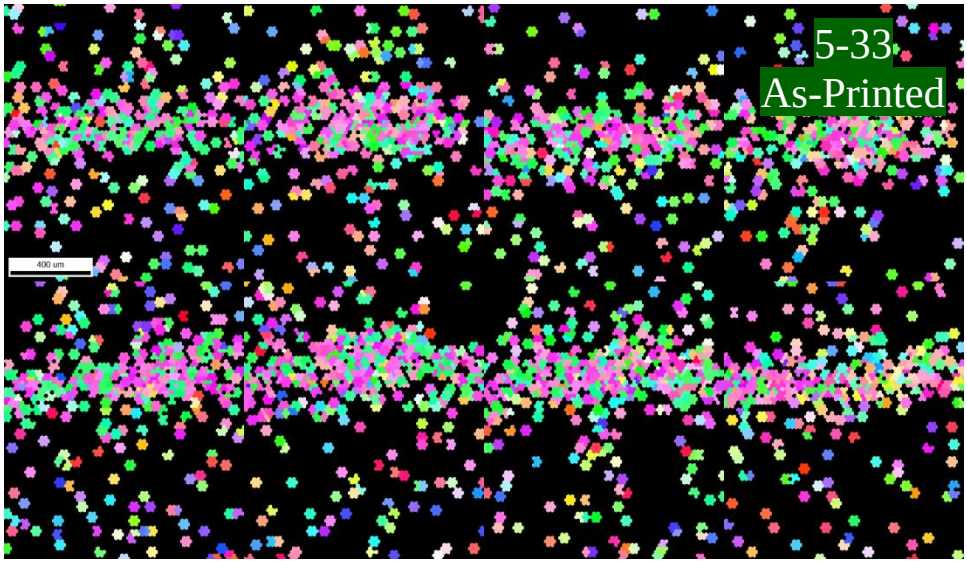

Figure 124. Visualization of EBSD scan for sample 5-33.

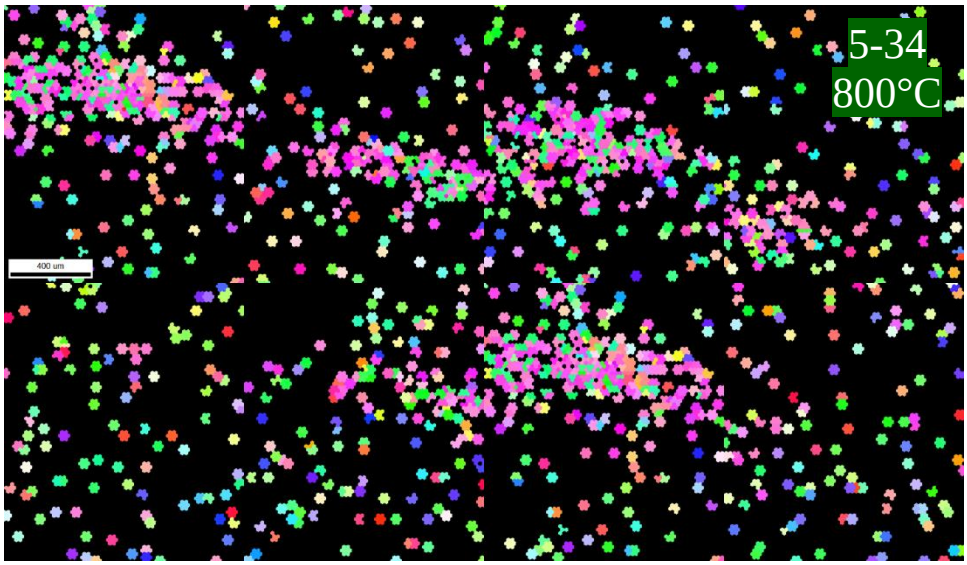

Figure 125. EBSD visualization for sample 5-34.

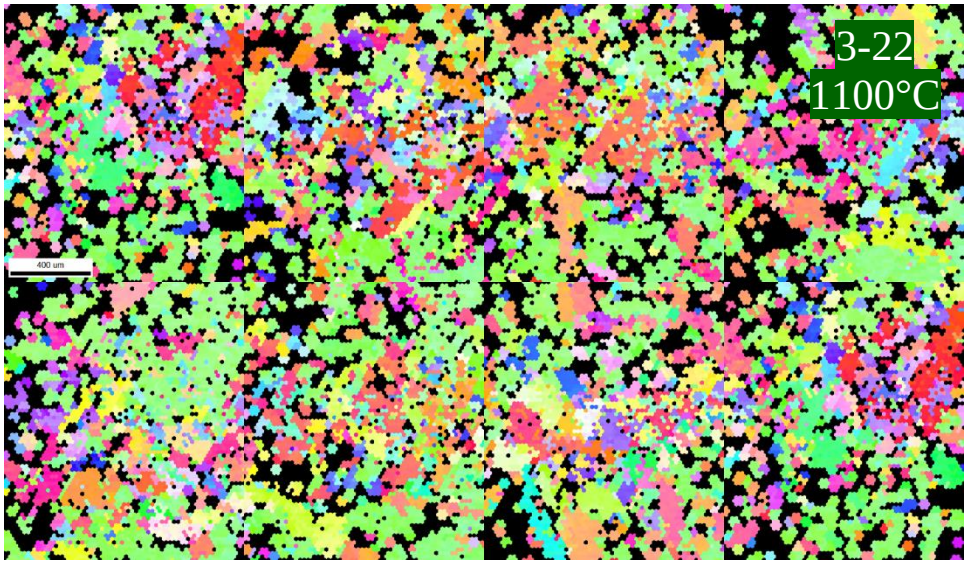

Figure 126. Visualization of EBSD scan for sample 3-22

Finally, pole figures were created to better visualize the distribution of grain orientations using a 5° gaussian smoothing for the orientation of each measured orientation (pixel) in Figure 127, Figure 128, and Figure 129.

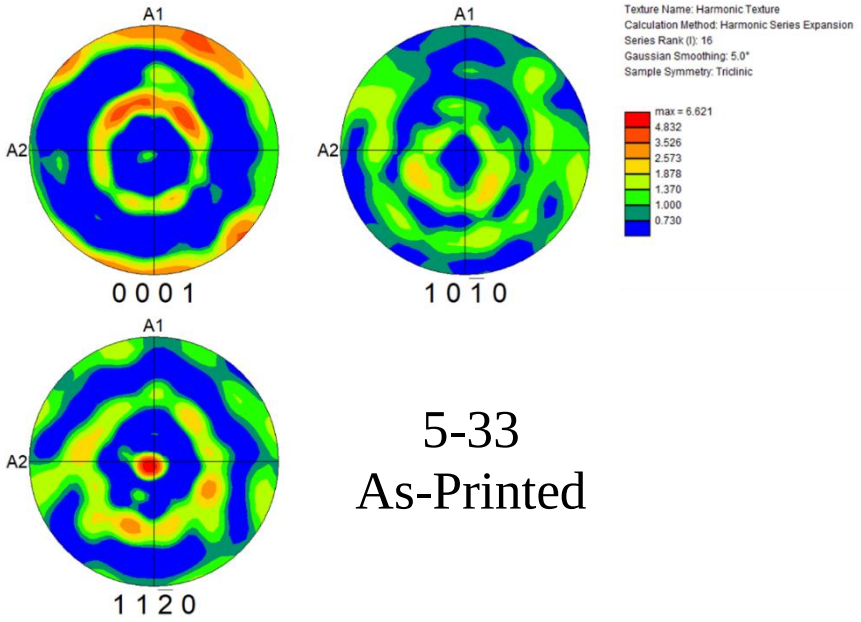

Figure 127. EBSD pole diagram of sample 5-33. Made using results from all eight scans.

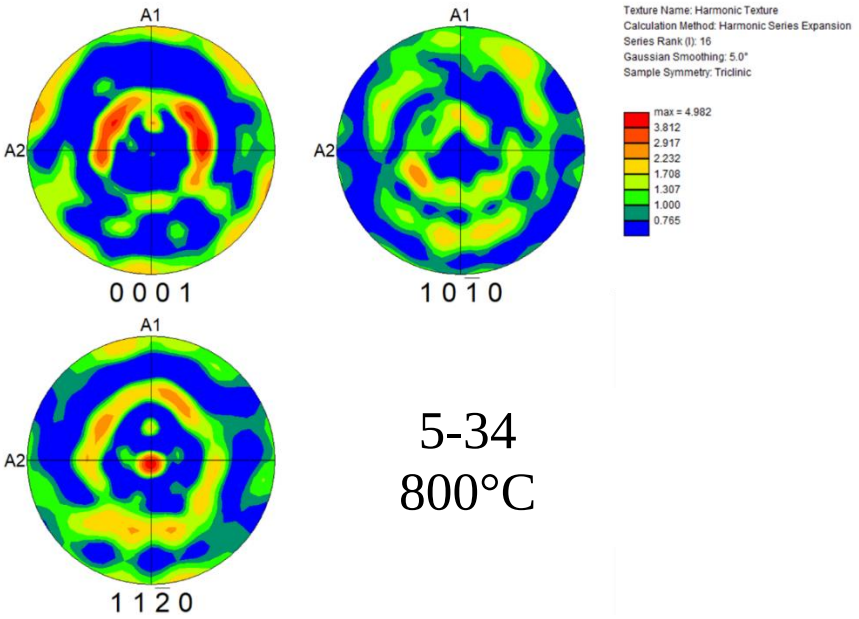

Figure 128. EBSD pole diagram of sample 5-34. Made using results from all eight scans.

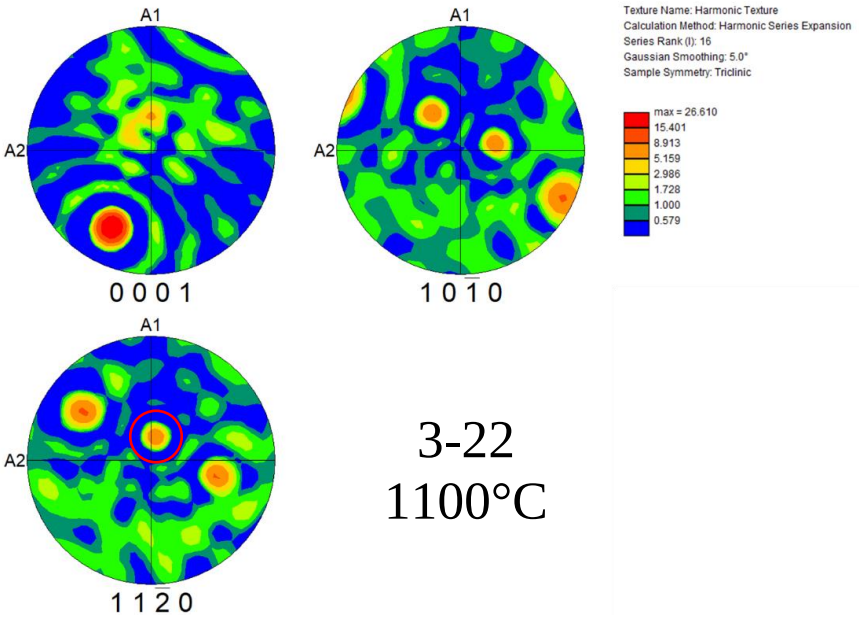

Figure 129. EBSD pole diagram of sample 3-22. Made using results from all eight scans. Peak near $[11\bar{2}0]$ *direction* $[11\bar{2}0]$ *pole figure indicates residual influence of build orientation and is circled in red.*

Starting with Figure 127, it is clear that a large concentration of grains is aligned with the $[11\bar{2}0]$ crystal direction perpendicular to the surface, i.e. a $[11\bar{2}0]$ fiber texture, (aligned with the tensile

axis of fatigue specimens). The ring features indicate that nearly random rotations of the crystal about this axis are presented in the sample with no other significant types of crystal orientations. Looking at Figure 128, the same concentration of grains orientated with the $[11\bar{2}0]$ direction is preserved after HIPing the 800°C samples. In fact, scans for both the as-printed and 800°C samples look strikingly similar. These results coincide with previous microstructure analysis that found the 800°C sample did not significantly change the overall microstructure from the as-printed condition. This is not the case for the 1100°C pole figure in Figure 129, where there is no longer a single dense concentration of $[11\bar{2}0]$ crystal directions aligned with the sample normal directions (tensile axis). Instead, there is a strong $[0001]$ peak (red) near the bottom of the pole figure and a secondary peak (yellow) above the center, and three correlated peaks for the $[11\bar{2}0]$ and $[10\bar{1}0]$ directions that are perpendicular to the $[0001]$ peak crystal direction, indicating a highly preferred crystal orientation. However, on of the three $[11\bar{2}0]$ directions associated with the strong (red) $[0001]$ peak is close to the center of the pole figure. It is possible that one of the original β orientations grew very large and then transformed preferentially to one dominate α orientation. Though speculative, it is clear that the 1100°C samples had a significant change in the overall macrostructure and texture. Although the 1100°C HIP treatment had a significant impact on texture, these findings show that some amount of directionality and/or remnants of the previous thermal history may still be preserved even after significant prior β-grain coarsening. For the initial directionality to be completely wiped out there would need to be no $[11\bar{2}0]$ peaks near the center of the $[11\bar{2}0]$ pole figure, as seen in Figure 129 circled in red. Due to the limitations of examination of only three samples, and the structure of this experiment, no conclusion can be made on how significant an impact the retention of this directionality nor directionality in general has on the fatigue life of the tested samples.

2.8 Conclusion

In this study, 256 Ti-6Al-4V ultrasonic fatigue specimens were additively manufactured (AM) using electron beam melting (EBM) for the purpose of relating melt parameters, HIP condition, and surface roughness to very high cycle fatigue (VHCF) life. A Taguichi L_{16} design of experiments (DOE) was constructed to minimize the number of combinations tested. Samples were tested at a stress level of 500 or 550 MPa with a stress ratio of R = -1 (fully reversed). In total, 5-7 samples were tested for each combination of processing conditions at both stress levels. In addition to fatigue testing, metallography, hardness testing, tensile testing, and electron backscatter diffraction (EBSD) scans were performed to further characterize the material performance. Important findings include:

- All HIPed samples were found to have densities over 99.97%, with only small Trapped Gas (TG) pores (<10μm) identified. Slightly higher densities were observed for the 1100°C HIPed samples, mostly likely due to the higher HIP temperature.
- A statistically significant correlation between microhardness and SF, LO, and HIP condition were identified. The HIP condition was found to have the most impact on hardness with an average hardness of 313.7 HV_1 for the 800°C samples and 308.4 HV_1 for the 1100°C samples.
- No statistically significant correlation was found between fatigue life and Speed Function (SF), Line Offset (LO), Focus Offset (FO), or surface roughness for the ranges tested in which porosity was known to be minimized. A statistically significant correlation between HIP treatment (800°C *vs.* 1100°C) and fatigue life was found, with the 800°C HIP treatment exhibiting superior fatigue properties.

- The 800°C HIP samples had an average fatigue life of 8.08E+07 and 3.28E+06 cycles for 500 and 550 MPa, respectively, performing as well as, if not superior to conventionally produced Ti-6Al-4V as reported by Li et al. (26). The 1100°C samples had an average fatigue life of 7.21E+05 and 1.38E+05 cycles for 500 and 550 MPa, respectively. Despite the reduced performance in comparison to the 800°C HIP samples, a majority of the 1100°C samples still performed as well as conventionally produced Ti-6Al-4V. These results show that the design freedom of EBM can be utilized without sacrificing mechanical performance. Further investigation attributes the poor fatigue performance of the 1100°C to prior β-grain coarsening, which occurred during the super-transus HIP treatment, leading to internal crack initiation (ICI) at cleavage facets. Evidence of this failure mechanism was found in both 800°C and 1100°C treated samples, with larger and more severe instances of ICI found in the 1100°C samples.
- 1100°C samples displayed a higher average ultimate tensile strength (UTS) of 973 MPa, lower extension past the UTS, and a rougher fractur surface morphology reflecting the coarser microstructure. In comparison, the 800°C samples had an average UTS of 911 MPa and a uniform cup-and-cone ductile fracture surface.
- No statistically significant correlations between α-lath thickness and melt parameters were found. A statistically significant correlation between HIP condition and α-lath thickness was found. The average as-printed α-lath thickness was measured as 0.668 μm and found to coarsen by 72% after the 800°C HIP treatment having an average width of 1.15 μm. The average α-lath thickness of the 1100°C HIPed samples was found to be 0.844 μm. Although decreased α-lath

thickness is typically associated with increased fatigue performance, prior β-grain coarsening and resulting increased α colony size ultimately reduced the fatigue performance of the 1100°C samples.

- The columnar grain structure, observed in the as-fabricated and 800°C samples, appeared to be completely transformed into an equiaxed prior β-grain structure by the 1100°C HIP treatment. However, electron backscatter diffraction (EBSD) analysis revealed that some remnants of the build direction persist in the microstructure as a preferential grain orientation in the $[11\bar{2}0]$ crystal direction, even after significant microstructure transformation. Further study is needed to determine the impact of this retained directionality on mechanical properties to better guide part design and build orientation selection.

From this study it can be concluded the most important factor controlling fatigue life of EBMed Ti-6Al-4V is HIP condition and heat treatment. In addition, fine-tuning of print settings, beyond those required to prevent obvious porosity and swelling defects, will not have significant effects on the fatigue life of HIPed Ti-6Al-4V. More importantly, the lack of discernable effect of processing parameters indicates that good fatigue properties can be achieved using a wide processing window, reducing the need for time consuming and expensive DOEs focused on minor parameter adjustments and allowing researchers to concentrate future efforts on the most impactful aspects of the AM process.

3.0 MAGNETIC ASSISTED FINISHING (MAF) OF TI-6AL-4V FATIGUE SAMPLES

3.1 Magnetic Assisted Finishing (MAF)

Magnetic Assisted Finishing (MAF) was selected as the polishing method for improving the surface roughness of the as-machined Ti-6Al-4V fatigue samples discussed previously. This was the perfect opportunity to demonstrate the potential of MAF's as a low-cost, but effective method of polishing a variety of materials and geometries, while simultaneously studying the effect of the improved roughness on the fatigue life of the EBMed Ti-6Al-4V samples. A major advantage of MAF is the flexibility of the magnetic brush, which conforms to the work piece without separating from the polishing device, allowing for continuous use on complex surfaces with minimal risk of collisions or the need for expensive process control systems. For this application, a custom MAF polishing machine was built with the primary goal of polishing the Ti-6Al-4V fatigue samples. This could also be used as a test platform for a variety of different polishing applications. A simple diagram of the MAF process is provided in Figure 130.

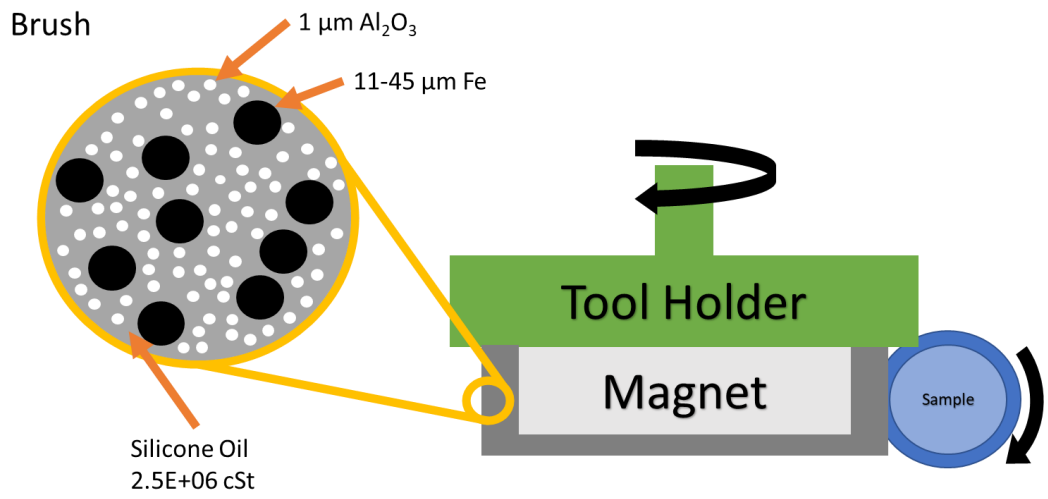

Figure 130. Diagram of Magnetic Assisted Finishing (MAF) setup used for polishing ultrasonic fatigue samples.

The MAF device was built around a simple variable speed benchtop drill press, found at most hardware stores. The specific model used for this project is a WEN 4212T (WEN – West Dundee, Illinois) and costs about $200. An image of the MAF setup can be found in Figure 131.

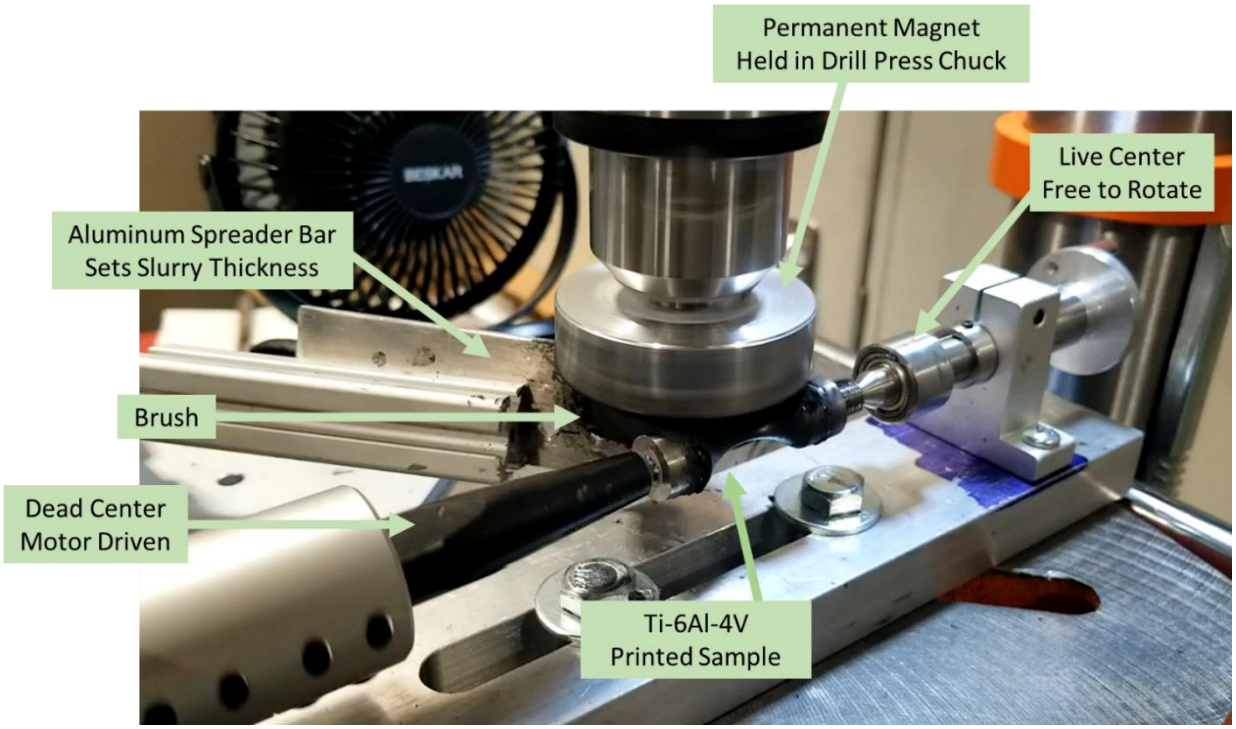

Figure 131. MAF setup for polishing ultrasonic fatigue samples.

When the EBMed Ti-6Al-4V blanks were sent out for bulk machining, center holes were machined into both ends of each sample in preparation for polishing. These center holes are common in turning to ensure concentricity between operations that require unmounting and remounting. Two centers were mounted to the drill press table to hold the sample during polishing akin to a turning-between-centers lathe setup. The dead center is made of a center punch attached to a small brushless motor via a coupling while a miniature tailstock acts as an adjustable live center. After extending and tightening the tailstock, friction alone is enough for the motorized dead center to drive the sample, eliminating the need for a lathe dog. A permanent, cylindrical, neodymium magnet is glued to a custom machined aluminum tool holder and

mounted in the drill press chuck, allowing the height and magnet RPM to be easily adjusted. An adjustable aluminum arm with "L-shaped" end-of-arm attachment, dubbed the "spreader bar", is used to continuously redistribute the magnetic brush across the magnet's surface, resetting its shape and thickness. Otherwise, the sample would push the brush out of the way on the first pass, creating a negative in the brush that conforms to the sample geometry and results in minimal contact between the brush and sample. An illustration of how the spreader bar resets the brush thickness is provided in Figure 132.

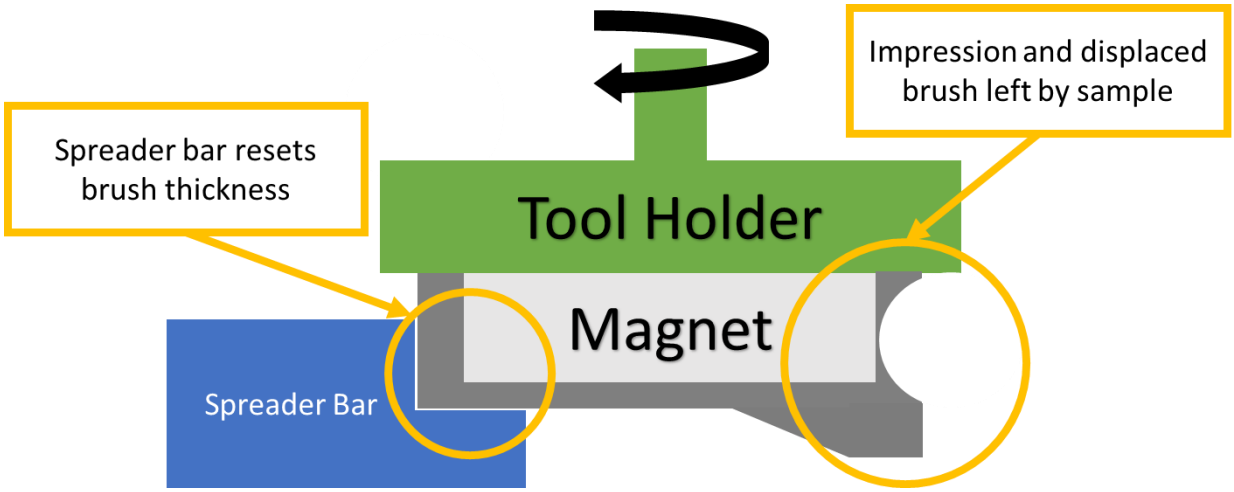

Figure 132. Diagram of spreader bar resetting brush thickness.

3.2 MAF Design Refinement

Before the main test samples were polished, dummy fatigue samples were used as test samples to refine the machine design and establish ideal processing conditions. Polishing is typically a stepwise process where finer abrasive media is used to progressively improve surface finish. However, due to the number of samples requiring polishing in this study, the MAF process was to be limited to a single 1-hour treatment per sample. At this time, it was not possible to estimate how much the surface could be improved in a single hour, making the goal of this preliminary testing to improve the surface roughness as much as possible in the allotted time.

In the interest of time, accessibility, and cost, a surface profilometer was used for all surface roughness measurements in this study. The device used is a Zeiss SURFCOM TOUCH Series profilometer (Zeiss – Oberkochen, Germany). However, due to nature of this measurement process, roughness measurements had to be taken axially, as depicted in Figure 133, requiring multiple measurement locations on each sample to capture the true roughness.

Figure 133. Setup used for measuring surface roughness of machined Ti-6Al-4V ultrasonic fatigue samples using surface profilometer.

Due to the sample geometry, most fatigue failures should occur at the very center of the sample where it is thinnest, making this region the focus of measuring and polishing. A measurement length of 5 mm, centered at the sample's center, was selected. Fortunately, this model came equipped with a software tool called "R-value fitting", which automatically compensated for sample curvature, allowing for the roughness to be measured along the sample curvature. To ensure the accuracy of the profilometer, the roughness of sample 5-34 was measured using a Zygo NewView^{tm} optical profilometer (Zygo – Middlefield, Connecticut) in the as received

condition. The results of the optical scan are provided in Figure 134 and were found to be in good accordance with the profilometer measurements.

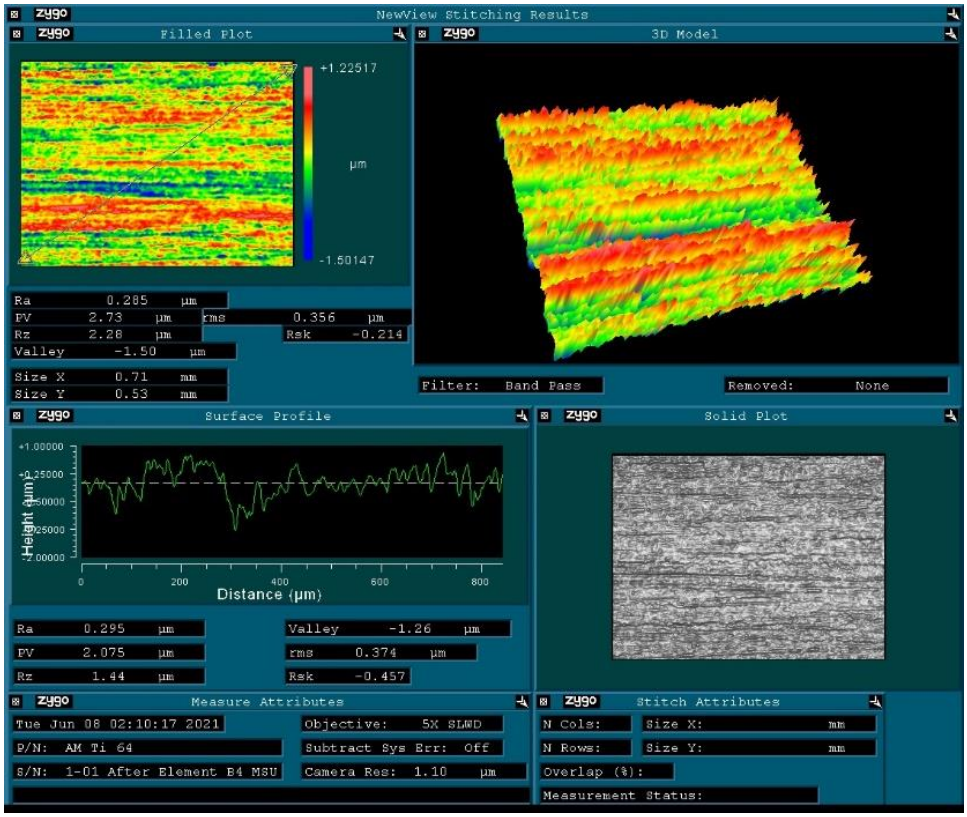

Figure 134. Confocal scan of EBMed Ti-6Al-4V fatigue sample as received from machine shop. Average surface roughness (Ra) across the diagonal of the scan (bottom left to top right) was measured as 0.285µm.

After confirming the accuracy of the profilometer, preliminary testing of the MAF treatment could proceed. A variety of machine configurations and slurry combinations were tested to refine the design and improve its performance. Shortly after testing started, issues with the original straight spreader bar concept became evident. An image of the straight spreader bar can be found in Figure 135 and illustrated in Figure 134 . While the straight wall spreader bar was effective at creating an even brush layer on the magnet, it was very sensitive to placement and angle. This led to dramatic changes in polishing effectiveness between runs depending on the spreader setup.

In addition, this design was found to primarily polish the leading side of the sample leaving the center and tailing sides under-polished.

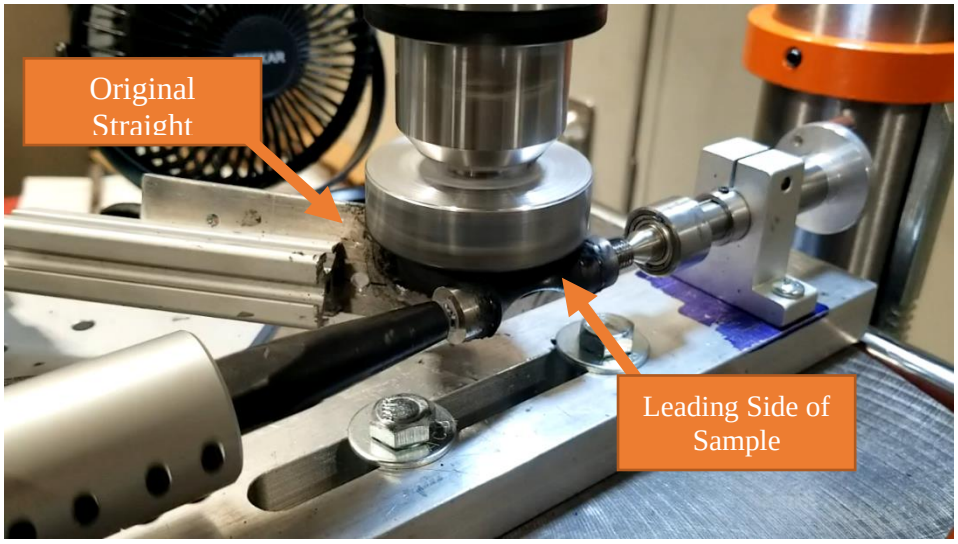

Figure 135. MAF setup with straight wall style spreader bar.

To fix the polishing and consistency issues, a new style of spreader bar was made by bending a piece of sheet steel to create a kind of "C" shaped wedge. Material displaced by the sample is guided by the ends or "wings" of the wedge towards the middle-bent section. As the material converges, the brush is reshaped by the spreader into annular bulge, as shown in Figures 136 and 137. A simplified illustration of Figure 137 is provided in Figure 138. In addition to reshaping the brush, excess brush is retained inside the wedge where it constantly mixes with incoming brush, forming as a sort of "material reservoir" as seen in Figure 137. This reservoir ensures there is always enough material present to reshape the brush into the desired shape. As the Annular bulge reaches the sample, excess brush material is forced above and below the gauge section, significantly increasing the contact area on the sample surface interacting with the brush, as shown in Figure 139. This new style of spreader bar significantly increased the consistency of the setup while focusing the majority of the polishing to the center of the gauge section.

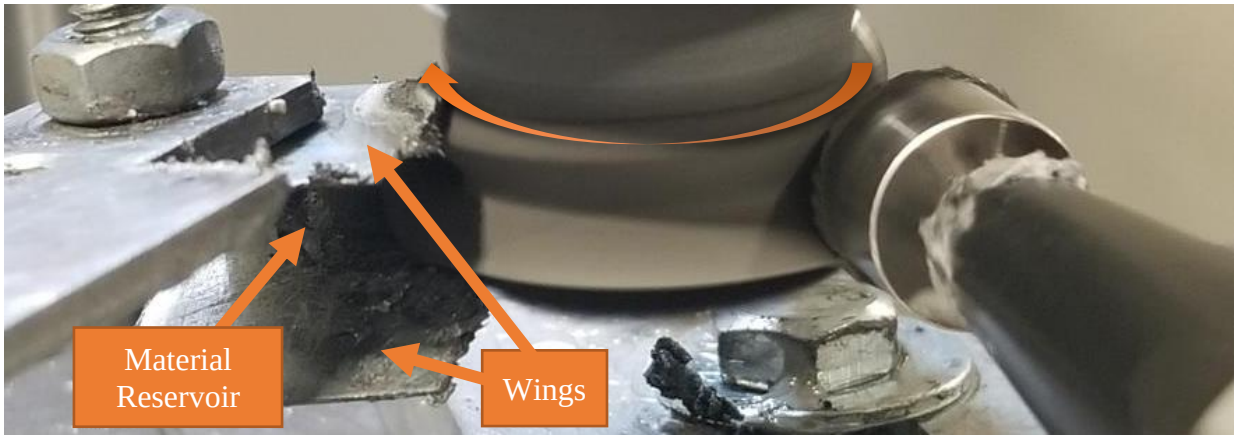

Figure 136. Splayed ends of spreader bar recombining displaced brush back into a fresh hemisphere. The magnet spins in the direction of the arrows (clockwise).

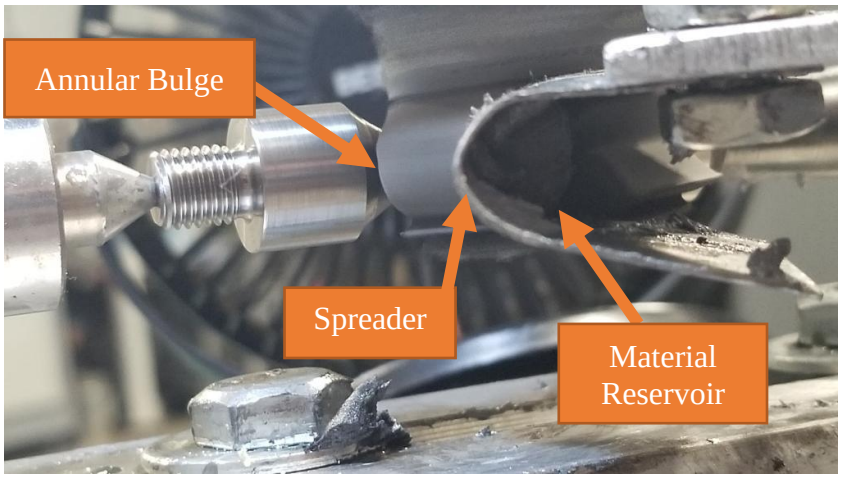

Figure 137. New folded sheet metal spreader design. Magnet spins clockwise.

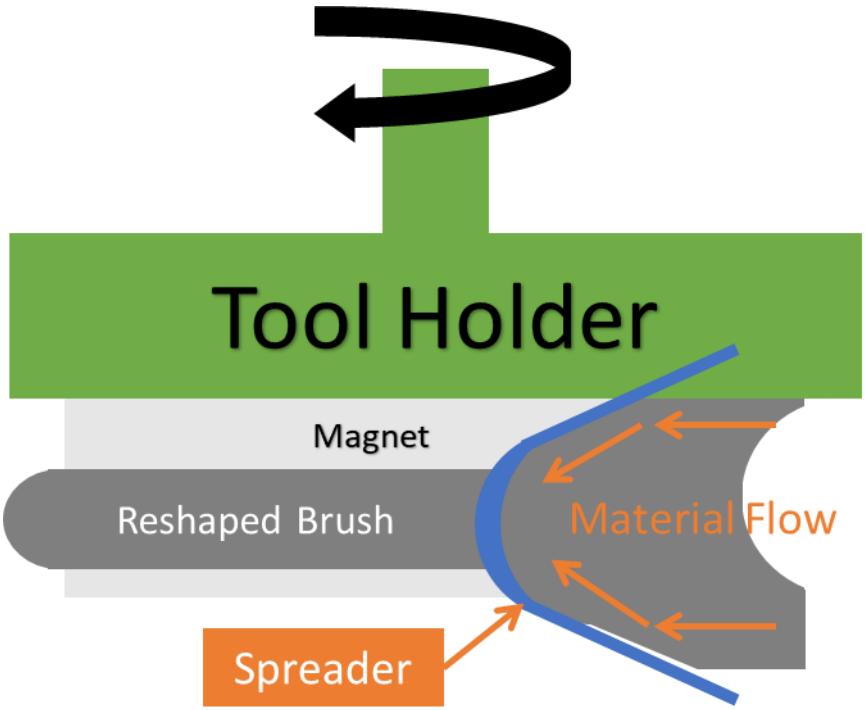

Figure 138. Simplified illustration of the slurry reshaping process.

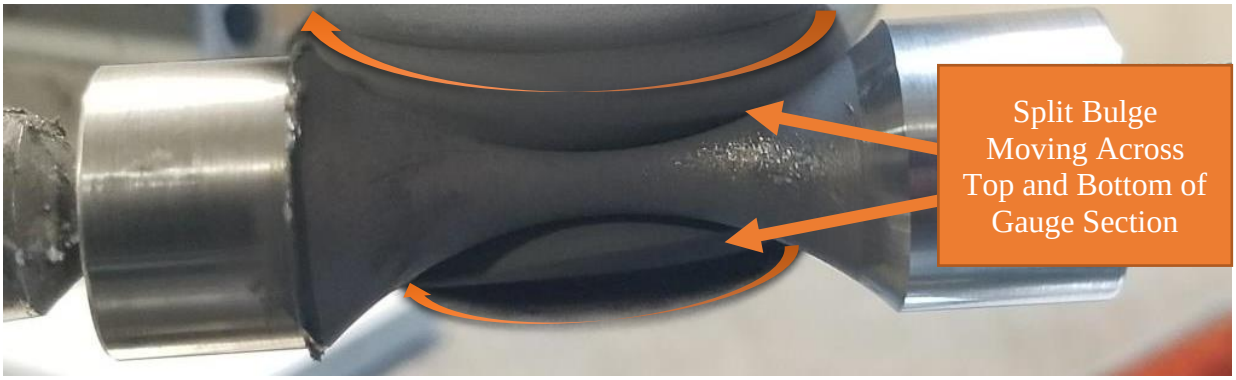

Figure 139. Sample diverting hemisphere of slurry above and below the sample. Increasing interaction between the brush and sample while also focusing polishing to the center of the gauge section. Magnet spins clockwise.

Preliminary testing revealed that grinding performed after machining left considerable variation in roughness across the surface. As-machined measurements of samples 5-34 and 3-34 are plotted as blue circles in Figure 140 and Figure 141. The sample was rotated approximately 50° between measurements so that 6 evenly spaced radial measurements were taken.

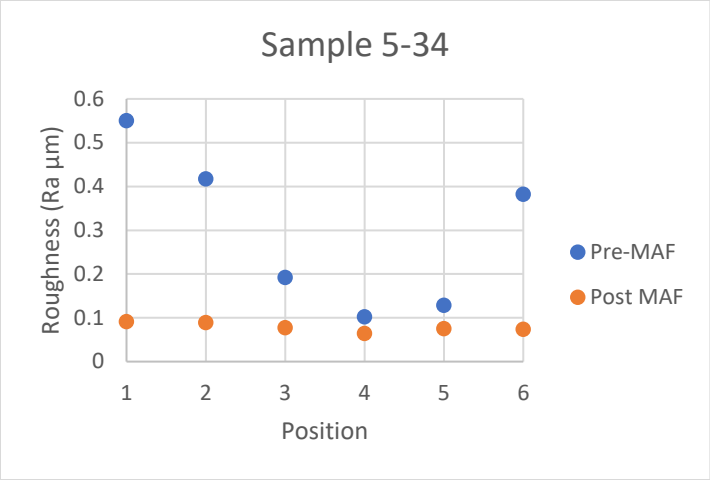

Figure 140. Surface roughness of sample 5-34 measured in 6, 5mm long, locations before and after 1-hour MAF treatment.

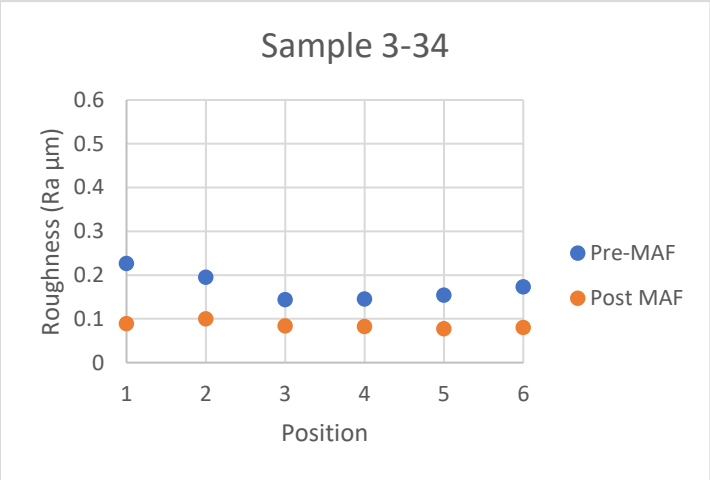

Figure 141. Surface roughness of sample 5-34 measured in 6, 5mm long, locations before and after 1-hour MAF.

With such a large variation in roughness depending on measurement location, division lines were engraved in the sample grip section, as seen in Figure 142. With the addition of these markings, it became possible to measure the same location before and after MAF treatments allowing for accurate roughness tracking as well as overall uniformity of surface roughness. Post MAF roughness measurements of samples 5-34 and 3-34 are plotted as orange circles in Figure 140 and Figure 141. Without these markings, the combination of radial variability and random

measurement location selection made the effectiveness of the MAF treatment appear to vary significantly and at times even appear to increase surface roughness.

Figure 142. Grip section of Ti-6Al-4V ultrasonic fatigue sample with engraving marks to assist with measurement repeatability.

These new measuring practices made it possible to start narrowing down the best performing brush composition and machine settings that gave the best finish. The best settings found are recorded in Table 22.

Table 22. Best MAF setup and slurry composition found during preliminary testing.

Drill Press Speed (rpm)	1000
Dead Center Speed (rpm)	≈ 6
Silicone Oil Viscosity (cSt)	≈ 250000
Oil to Powder Percent (wt%)	20.9
Abrasive Size (μm)	1
Abrasive Type	Alumina
Iron Size (μm)	45-150
Iron Powder Type	Iron Silica
Iron to Abrasive Ratio	4:1
Time (min)	60

Figure 140 and 141 that MAF is effective in not only improving the average surface roughness but also reducing the radial variation in roughness between measurement locations. Sample 5-34 had an average starting roughness of 0.295nm and standard deviation of 0.165 nm and improved to an average roughness of 0.078nm and standard deviation of 0.012nm after the 1-hour MAF treatment. Images of the gage section of sample 5-34 can be found in Figure 143.

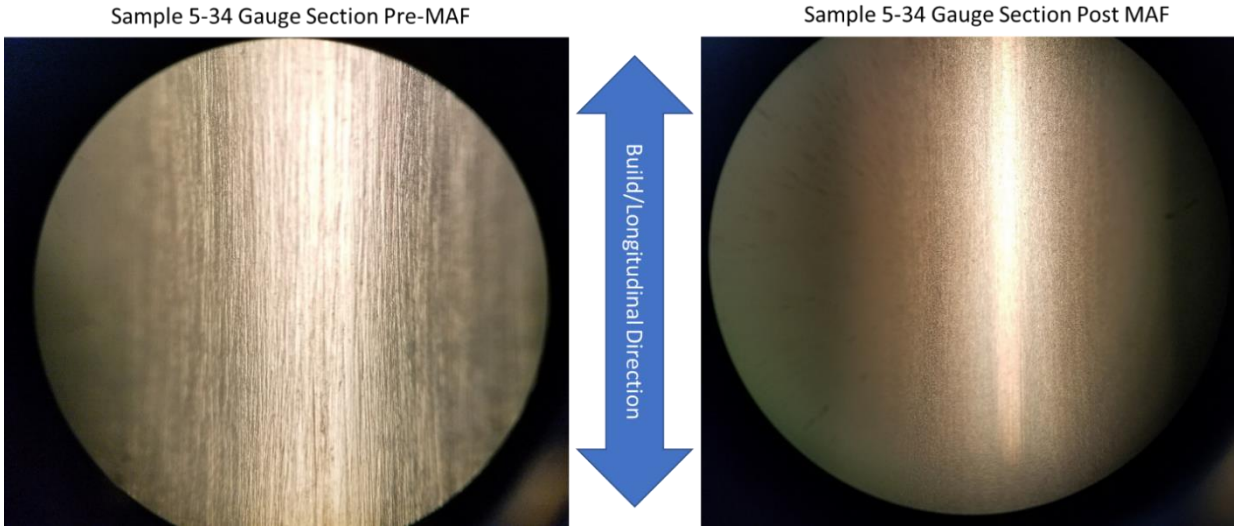

Figure 143. Comparison of gauge section for as received (left) and polished (right) Ti-6Al-4V ultrasonic fatigue samples. These 5x images are taken from eye piece of microscope using a cellphone as microscope software interfered with lighting and focus.

3.3 Results

After establishing best practices for MAF and surface roughness measurement, half of the main DOE samples slated for polishing were measured in preparation for polishing and subsequent post treatment comparison. Like the preliminary testing, four marks were engraved into the ends of each sample to designate locations for samples measurement. Samples were measured twice per location for a total of 8 measurements per sample. Since the HIP condition was expected to be the largest driver of fatigue performance for the main fatigue study, the samples were split into two groups based on HIP condition. Each sample was given the same 1-

hour treatment using the parameters recorded in Table 22. Surface roughness measurements before and after MAF treatment for 800°C samples are presented in Figure 144.

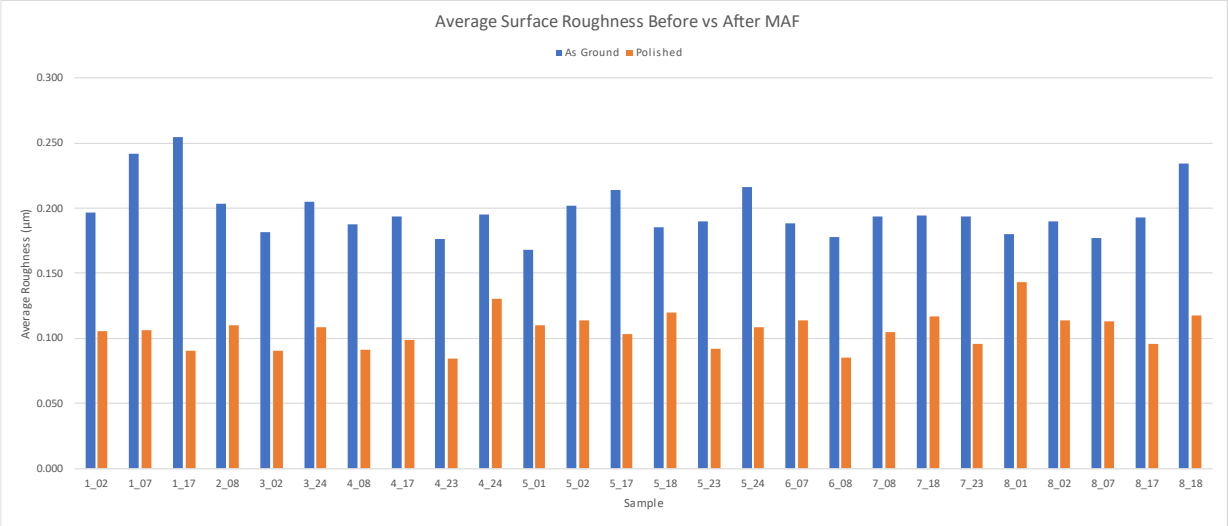

Figure 144. Average surface roughness before vs after MAF for 800°C HIPed samples.

From these results, the 800°C samples had an as-received roughness of 0.197 µm with a standard deviation of 0.035µm. After the MAF treatment, the average roughness for the 800°C samples was 0.106 µm with a standard deviation of 0.018 µm. Surface roughness measurements before and after MAF treatment for 1100°C samples are presented in Figure 145.

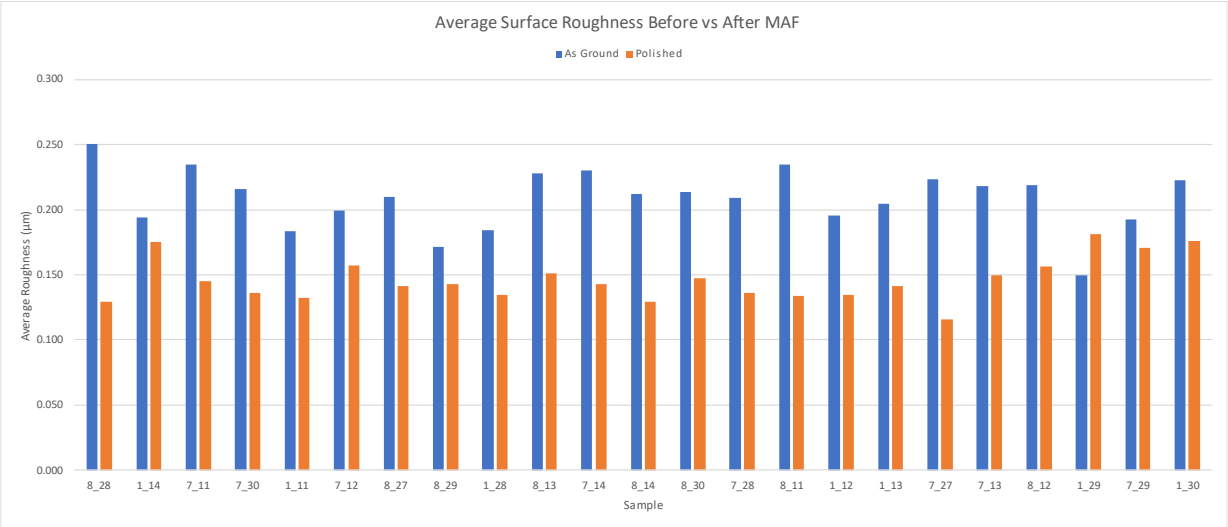

Figure 145.Average surface roughness before vs after MAF for 1100°C HIPed samples.

From these results, the 1100°C samples had an as-received roughness of 0.209 μm with a standard deviation of 0.039 μm. After the MAF treatment, the average roughness for the 1100°C samples was 0.146 μm with a standard deviation of 0.024 μm.

It is clear that the MAF treatment of the 800°C samples was effective in reducing not only the average surface roughness from 0.197 μm to 0.106 μm but also the variability between samples nearly in half from 0.035 μm to 0.018 μm. However, the treatment did not appear to be as effective on the 1100°C samples, only improving the overall average roughness from 0.209 μm to 0.146 μm, an improvement of only 0.063 μm as opposed to an improvement of 0.091 μm for the 800°C samples. The variability among the 1100° samples only improved from 0.039 μm to 0.024 μm, having not only an overall higher variability among the samples but also a smaller improvement of only 0.015 μm as compared to an improvement of 0.017 μm for the 800°C samples. Looking closer at the 1100°C data, it can be seen that for sample 1-20 the surface roughness actually increased from 0.150 μm to 0.182 μm before and after the MAF treatment. This phenomenon was observed during preliminary testing before incorporating the radial markings into the measurement process, after which it was never observed indicating the surface may have been damaged during polishing. Upon further investigation into the surface of the polished 1100°C samples, revealed several raised bumps scattered across the surface. An image of these bumps is provided in Figure 146. It should be noted that these bumps were only found on the 1100°C samples, nothing of this sort was found on any 800°C or un-HIPed sample.

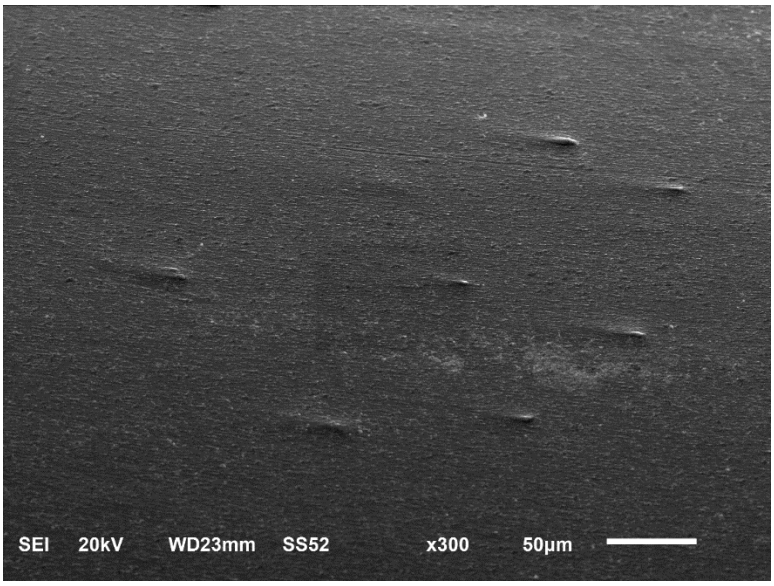

Figure 146. Surface of 1100°C HIPed sample featuring several raised surface defects.

Running the same surface profilometer through a region with large numbers of these particles resulted in large spikes in the profile measurements, as seen in Figure 147.

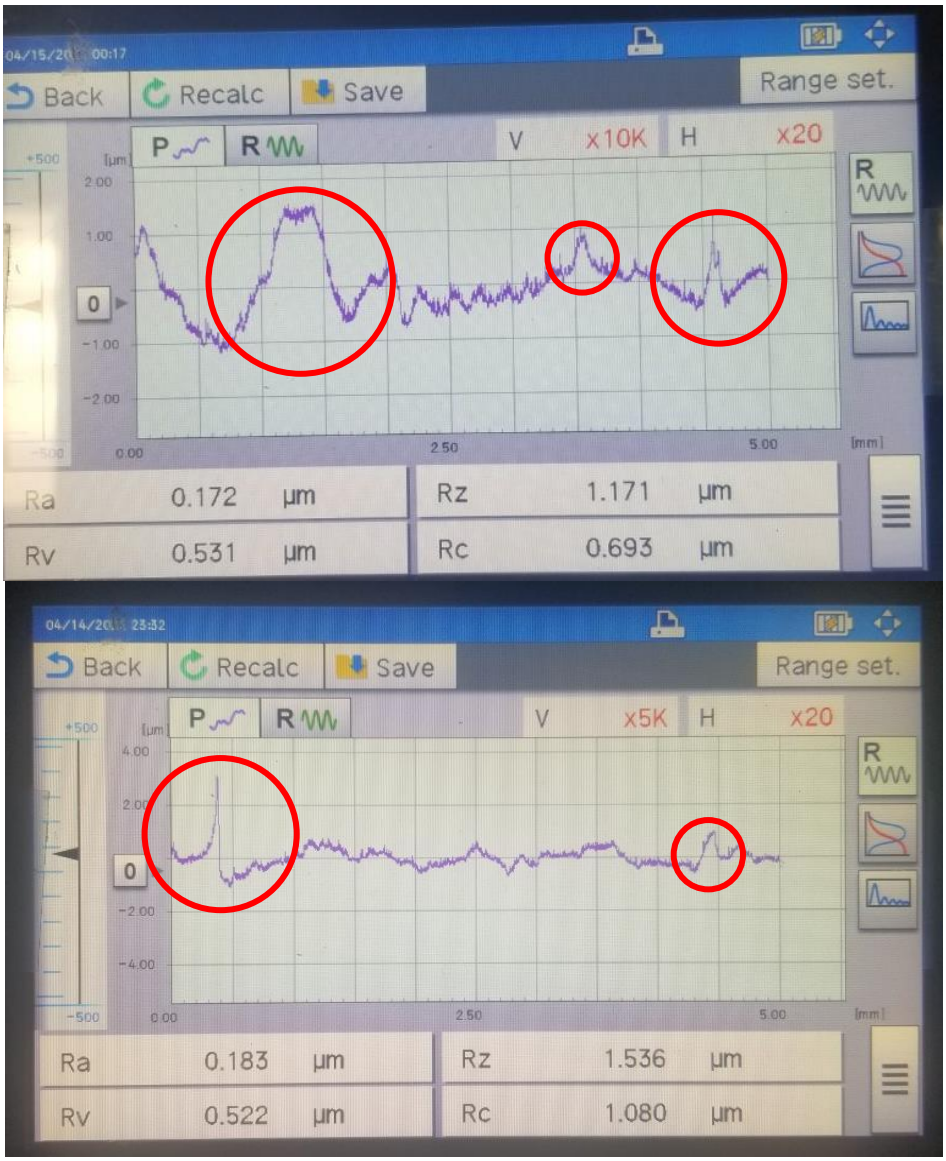

Figure 147. Surface profilometer measurement profile of 1100C sample through a section with several raised surface defects. Large spikes in roughness evidence of raised surface defects interfering with roughness measurements.

It is believed that these spikes in the profile measurement are the result of the profilometer stylus running over and being lifted by one of these particles. Although the remaining surface appears to be as smooth as expected, the spikes from the particles raise the average roughness, making it appear that the treatment was less effective. Further investigation into these particles using Energy-dispersive X-ray spectroscopy (EDX) elemental mapping revealed a large concentration

of Silicon which coincides with a clear lack of titanium and vanadium. Elemental mappings of these scans are provided in Figure 148.

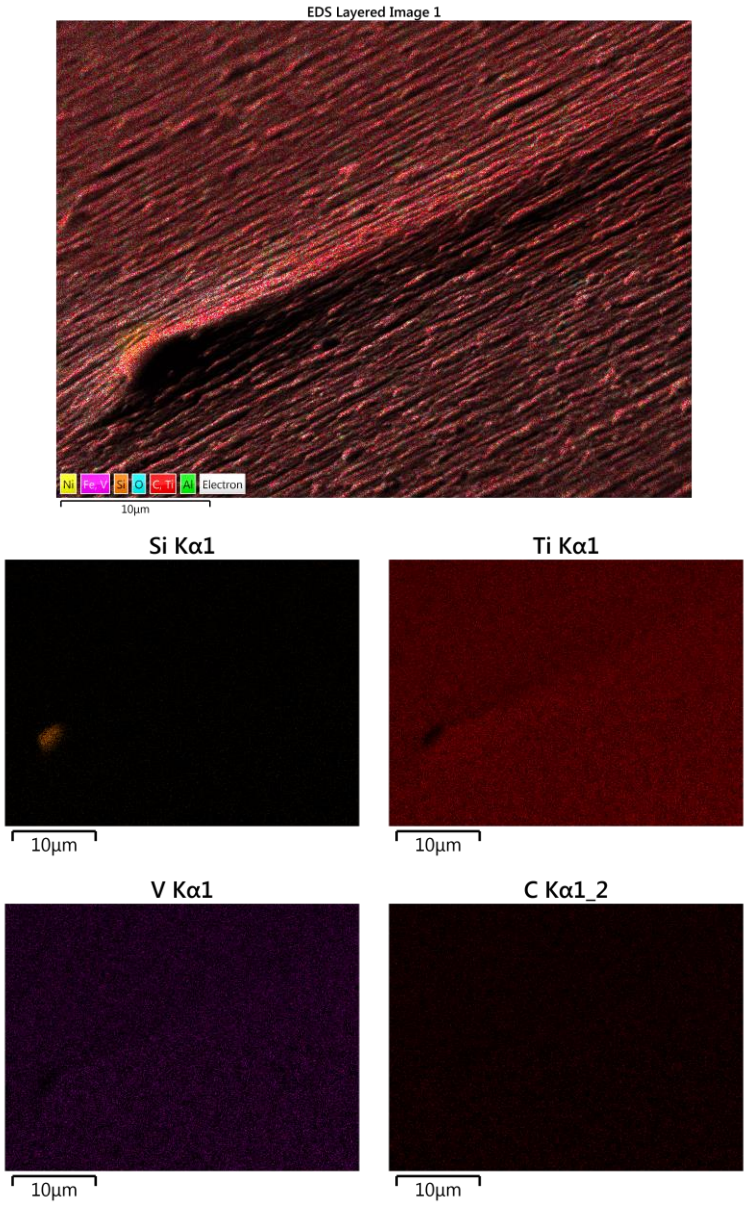

Figure 148. EDX mappings of surface defect on 1100°C HIPed fatigue sample, polished using MAF.

At first, it appeared as if these bumps only appeared on the surface of the polished samples indicating it could somehow be the result of the MAF process even though no source of silicon on these defects could be identified. Similar EDX scans were then performed on fatigue samples in the as-received condition from the machining shop that had yet to be polished using any MAF

treatment. Although much harder to find due to the unpolished machining marks, similar particles were identified, an SEM image and results of the EDX scan is provided in Figure 149.

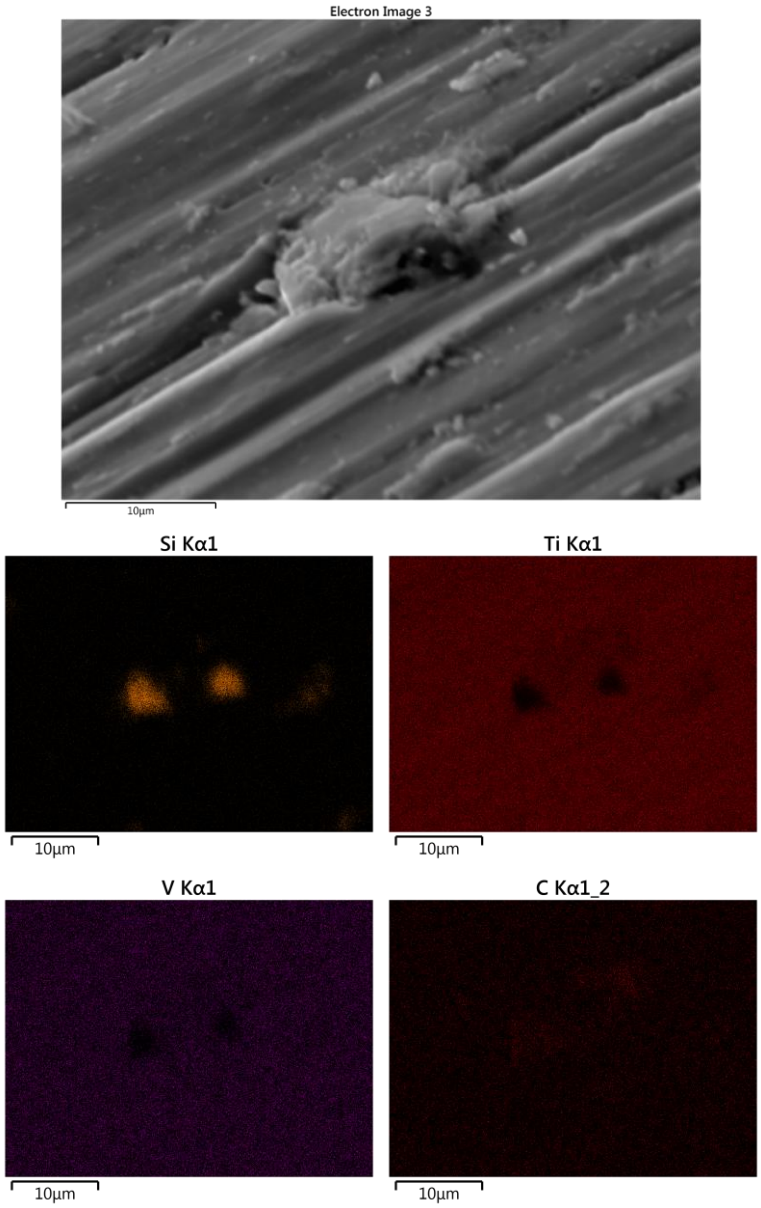

Figure 149. EDX mappings of 1100C fatigue sample in as received condition prior to MAF.

EDX scans of the particle again revealed silicon rich regions that coincided with the regions lacking titanium and vanadium. Unlike the previous EDX scan, this scan showed that the silicon rich regions coincided with a higher concentration of carbon that clearly stood out from the evenly distributed “background carbon” commonly observed in EDX scans. The distinct

similarities between the two measurements confirm that not only the presence of some kind of silicon or silicon carbide (SiC) particles embedded in the surface but also the presence prior to any MAF treatment. Removal of the machining marks after MAF made it easier to identify the particles, rather than being the cause. The most likely source of these embedded particles is the Silicon Carbide abrasive paper used to finish the fatigue samples after bulk machining. An image of the setup used by Element Materials Technology to finish the samples after bulk machining can be found in Figure 150.

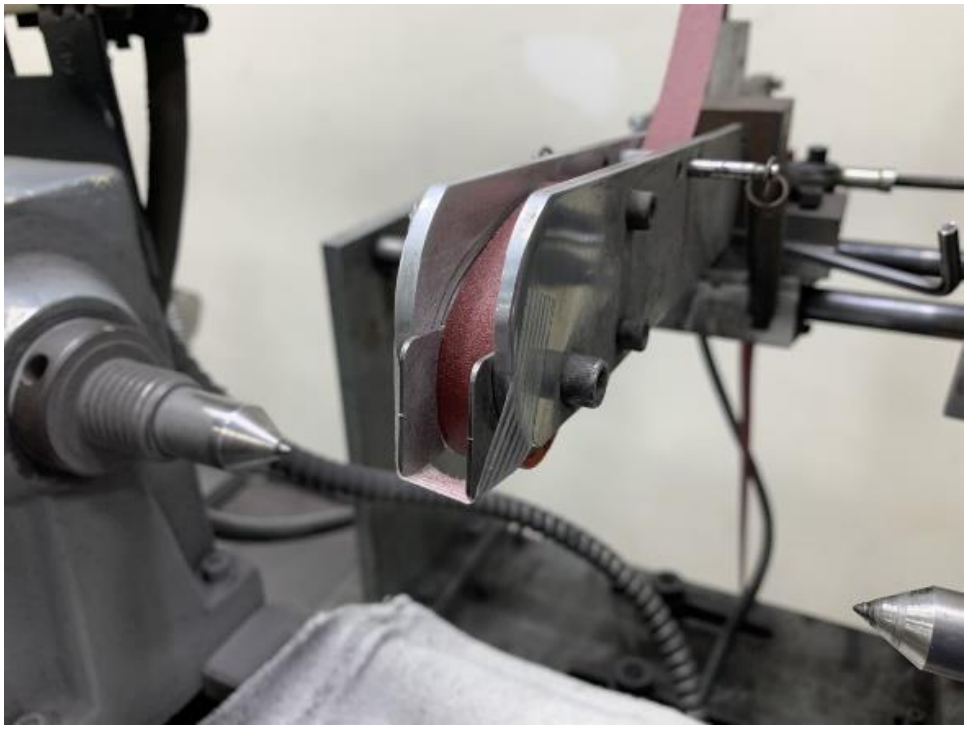

Figure 150. Finishing setup used by Element Materials Technology to grind fatigue samples after turning the hourglass shape. A fatigue sample (not depicted) would be mounted between the two lathe centers (left and right sides).

It was confirmed that both 800°C and 1100°C samples went through the same finishing process. This phenomenon was later reproduced while attempting to rework samples. After removing most of the particles with a combination of scotch-brite and MAF, SiC emery cloth was then used to hand polish the surface resulting in the reintroduction of embedded particles identical to

those observed on the as-received samples. While the source of the particles was identified, it was unclear why it occurred only for the 1100°C samples. After considerable literature review as well as conversations with multiple titanium experts and machinists no information regarding this phenomenon could be found.

At first, the best explanation was the difference in hardness resulting from the different heat treatments. However, as discussed previously and presented in Table 13, despite of the statistically significant effect of HIP condition on hardness, the difference in hardness was not enough to meaningfully change how the silicon carbide emery cloth interacts with the surface. After examining the results of the hardness test, the next most likely explanation for the embedded particles is the difference in the microstructure between the 800°C and 1100°C samples as discussed previously. This theory stems from the idea that titanium α-grains are hexagonally close packed (HCP) making them inherently anisotropic. For example, depending on the declination angle between an applied stress and the C-axis of the α-grain, the stiffness can range from around 145 Gpa for fully aligned to 100 Gpa for 90° as shown in Figure 151. (18)

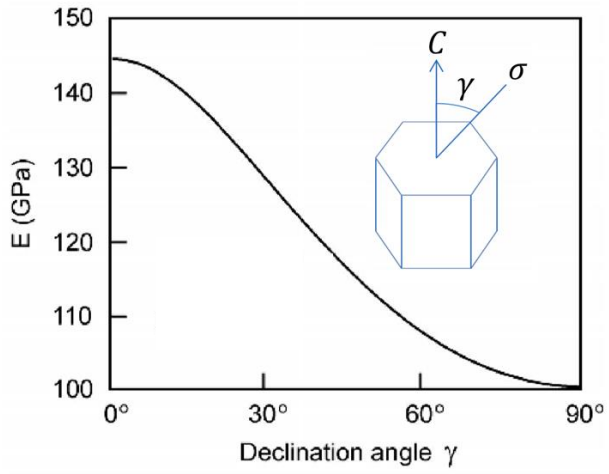

Figure 151. Stiffness vs declination angle on applied load for HCP α-phase Titanium. (18)

While exact values for other material properties, like strength, depend on factors like thermal history, a similar anisotropy exists for plastic deformation properties, as shearing in the c-axis direction is very difficult, but very easy in the a-direction on prism or basal planes (22) (63) As the SiC particles contact the surface, some α-colonies are considerably softer than other colonies, which may enable the SiC particle to be embedded in a soft orientation and then bet trapped adjacent to a hard orientation as depicted in Figure 152. For this to occur, large enough regions with the same crystal orientation that are significantly larger than the SiC particle size must be present on the surface to bring the hardness below some threshold to facilitate embedding. Figure 148 and Figure 149 show the embedded particles are approximately 10 μm in diameter which is smaller than many of the α-grain colonies found when examining the 1100°C microstructure, such as those found in sample 3-22 and in Figure 153.

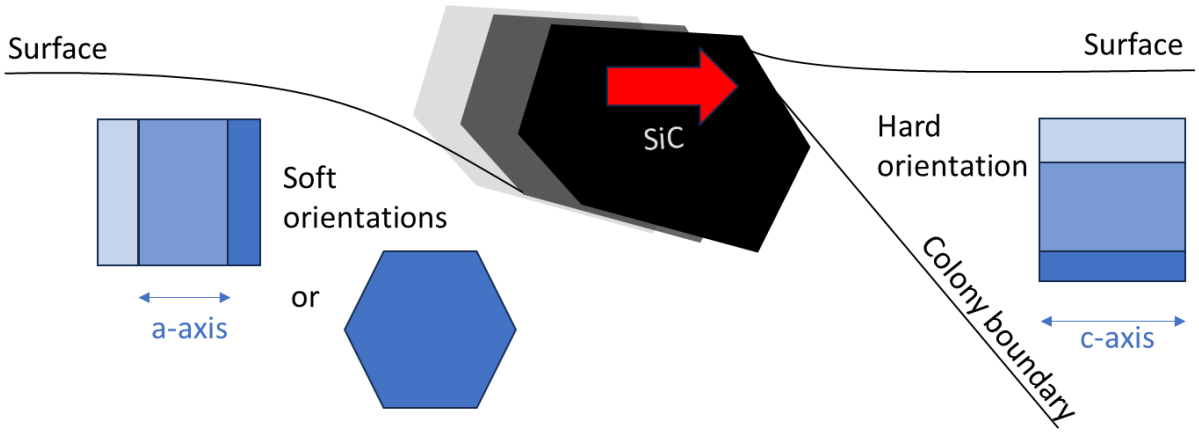

Figure 152. Depiction of SiC particle entrapment by a hard orientation downstream of a soft orientation. As illustrated by Dr. Thomas Bieler.

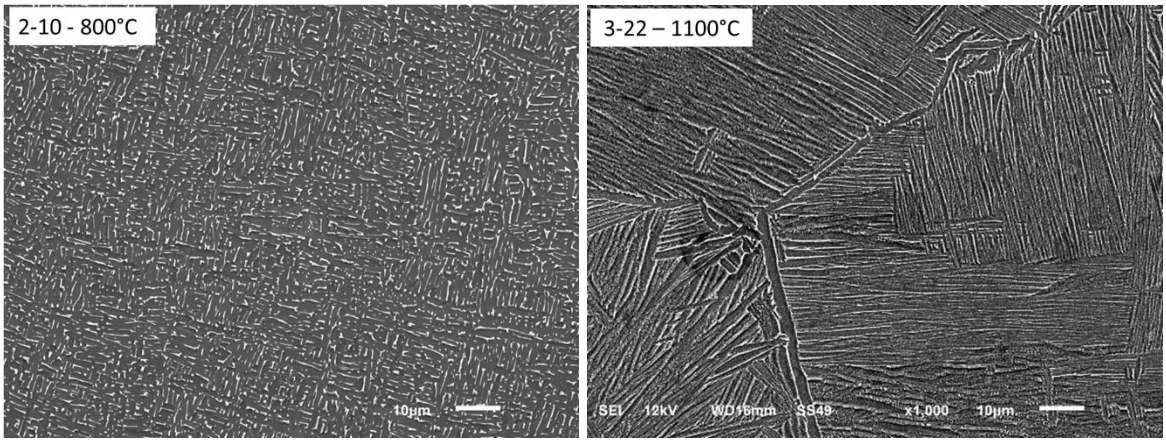

Figure 153. Micrographs of Ti-6Al-4V fatigue samples etched with Kroll's Reagent. Left) Sample 2-10 having 800°C HIP condition. Right) Sample 3-22 having 1100°C HIP condition.

Although there are the regions of aligned α-grains in the 800°C samples, as seen in sample 2-10 and again in Figure 153, most of these regions are smaller than 10 µm, making it likely that a particle interacting with the surface of the 800°C samples encountered two or more different grain orientations, providing the surface a more homogenous hardness. This theory is supported by a study published by Weaver et al. (63) who used nanoindentation testing to estimate the strength of β-annealed Ti-6Al-4V, featuring large α-β colonies (165 µm). They found that that when comparing the effects of indenter size on measured strength, that the variation in strength measurements decreased as the indenter size increased. This is due to the large indenter sampling a large number of colonies, homogenizing the effect of individual colonies on the overall measurement. It was also reported that higher variation in strength measurements occurred with smaller indicators, the highest being 1834 ± 324 MPa for the 16-micron indicator as compared to 1832 ± 197 for the largest 6350 µm indenter. Assuming the silicon carbide particle as the indenter, it reasonable to conclude that particles are more likely to interact and embed in a region on the surface of the 1100°C HIPed sample that is considerably softer than the overall bulk properties, as compared to the surface of the 800°C HIPed sample, which, at the particle scale,

are more likely to interact with multiple grain, homogenizing the impact of individual grains and more accurately representing the bulk material properties.

3.3.1 The 1100°C fatigue sample surface rework

As the source of these embedded particles was being determined, the fatigue results for the first few unpolished 1100°C samples were completed, which showed a significant drop in fatigue performance compared to the 800°C samples. Under the assumption that the reduced fatigue life was caused by the embedded silicon carbide particles acting as crack initiation sites, several attempts were made to rework the surface to remove any such particles. First, a set of 3 samples was returned to Element Materials Technology (EMT) who did the original machining. The samples were reground using the emery cloth sander shown in Figure 150. After regrinding, the samples were returned for inspection and the standard 1-hour MAF treatment was applied to remove machining marks to identify any remaining particles. An image of this inspection is provided in Figure 154.

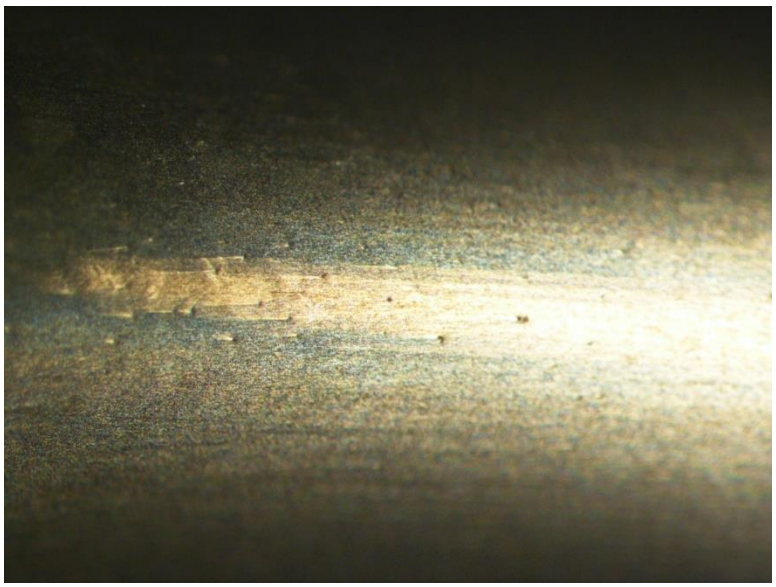

Figure 154. Embedded surface particles still present on surface of 1100°C sample reground by Element Materials Technology.

As seen in Figure 154, the embedded surface particles are still present. Next, these samples were again returned to EMT to turn down the gauge diameter until it was completely resurfaced, resulting in a final diameter of 2.5 mm from the original 3 mm diameter. EMT was also instructed not to use the emery cloth grinding step after this machine. Unfortunately, the amount of material removed was more than anticipated which influenced the samples ability to resonate in the fatigue tester as the sample now significantly deviated from the original design. In addition, significant surface defects from the machining were found that would have normally been removed by the emery cloth. These defects and considerable higher overall surface roughness could not be eliminated by the standard MAF polishing in a reasonable amount of time. Additional sets of three samples were sent to three other machine shops for reworking. After receiving the samples, a description of work to be done, and informed of the value of these samples, two of the shops did not think they could perform the machining as requested and returned the samples. Similar feedback was given by both shops, being the low stiffness of the sample making it difficult to machine the sample surface, as well as unfamiliarity with machining Ti-6Al-4V. The last machine shop attempted to rework a single sample using a file and scotch-brite. While they were successful in removing the particles, upon returning the sample for inspection, large dents and scrapes were found on the surface, as shown in Figure 155.

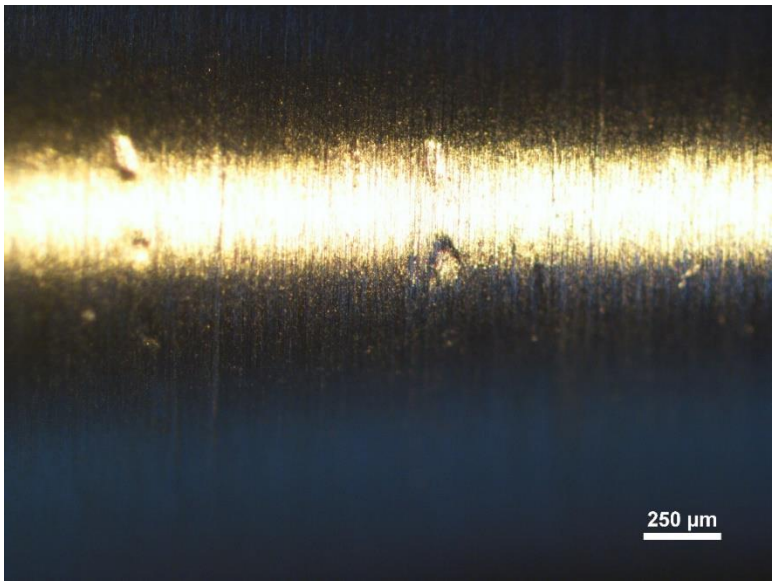

Figure 155. As-received surface condition of sample 4-27 after being sent out for reworked to remove embedded surface particles.

These defects are likely the result of the file unintentionally digging into the sample while reworking. The hourglass shape of these samples would make avoiding these dents almost impossible without a custom file that perfectly matched the sample geometry. This method of rework was not pursued any further as these defects were too deep to be polished out in an reasonable amount of time and were likely to be more detrimental to the fatigue life than the original embedded particles.

Using the information gained from these rework attempts and new strategy was formulated. Since turning and filing removed too much material and/or damaged the sample, a 3-step scotch-brite approach was attempted. This process used course, ultra fine, and light duty 3M branded scuff pads with grit size of 360-400, 2000-2500, and 2500, respectively. To start, a MAF polished sample was mounted between centers on a lathe set to 800 rpm and polished by hand for approximately 3 minutes per grit. Finally, the sample was further polished with an additional 15-minute MAF to help with identification of any embedded particles or defects by removing

any remaining sanding marks. Optical images of the surface throughout this process can be found in Figure 156.

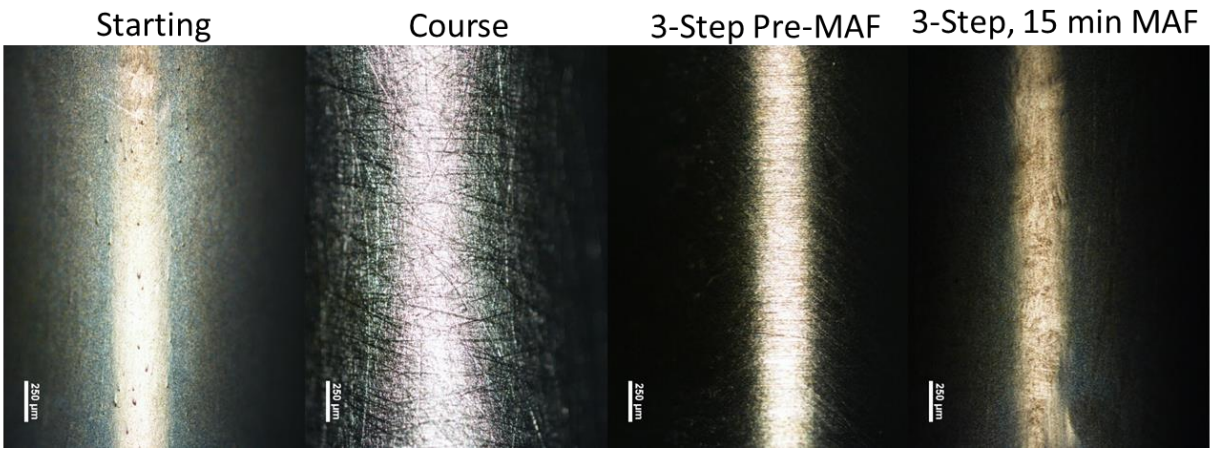

Figure 156. Progress of stepwise scotch-brite treatment aimed at removing silicon carbide particles embedded in the surface of a 1100°C fatigue sample.

Upon further examination, a majority of the particles were removed from the surface. However, some particles and defects left from the particles remained even after multiple treatments as illustrated in Figure 157.

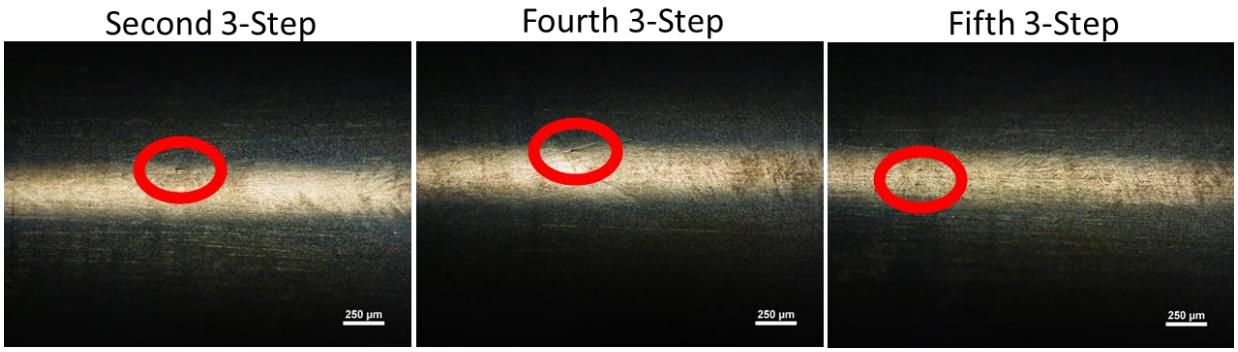

Figure 157. Remaining embedded particles or surface defects on the surface of an 1100°C fatigue sample after multiple 3-step scotch-brite and MAF treatments.

Concurrent investigation on the fracture surfaces of the first three tested 1100°C samples, revealed no evidence of surface defects near the crack initiation points. Instead, a majority of cracks were initiated by facet crack initiation stemming from the extensive prior β-grain coarsening caused by super-transus HIPing, as discussed previously. These results indicated the

surface defects may not be responsible for the poor performance after all. To confirm this, samples 5-13, 3-30, and 5-30 were polished using the 3-step scotch-brite and sent for fatigue testing. The cycles until failure for these samples were 3.52E+04 9.34E+03, and 1.64E+04, respectively. With no meaningful improvement in fatigue life even after extensive reworking, it was concluded that the primary cause of the poor fatigue life of the 1100°C samples was extensive prior β-grain coarsening and resulting α-colony size and not from the embedded surface particles. Thus, the remaining samples were polished using the standard 1-hour MAF treatment and sent out for fatigue testing.

3.4 Conclusion

MAF was shown to be an effective and low-cost method of polishing the Ti-6Al-4V hourglass fatigue samples featured in this dissertation. MAF was effective at not only reducing the overall surface roughness of the as-machined samples but also nearly eliminating any radial variability. Looking at the 800°C samples, MAF reduced the average surface roughness from 0.197 μm to 0.106 μm and reduced the standard deviation between samples by nearly half from 0.035 μm to 0.018 μm. Although the treatment was less effective for the 1100°C samples, this was the result of embedded silicon carbide (SiC) particles on the surface by emery cloth used to grind the surface after bulk machining. These particles were only found on the 1100°C sample and most likely caused by a combination of the anisotropic behavior of the α-phase and presence of large α-colonies found only in the 1100°C samples. Even with the extensive effort put into reworking these samples, not all traces of these particles could be removed without causing considerable damage to the samples. Simultaneous analysis of microstructure and fracture surfaces of the 1100°C samples as well as fatigue testing of reworked indicated that the poor

fatigue performance was not caused by the embedded surface particles, but rather by extensive prior β-grain coarsening and resulting large α-colonies.

4.0 PRODUCTION OF 4340 FATIGUE SAMPLES USING SCALABLE AND EXPEDITIOUS ADDITIVE MANUFACTURING (SEAM)

4.1 Project Scope

The objective of this study was to demonstrate the feasibility of producing full density 4340 steel fatigue samples using the Scalable and Expeditious Additive Manufacturing (SEAM) process invented by the advanced manufacturing group at Michigan State University (MSU). 4340 steel is a popular alloy that can be easily heat treated to achieve a wide range of mechanical properties. It is primarily used for power transmission gears and shafts, aircraft landing gear, and other structural components. (64) SEAM was selected over Electron Beam Melting (EBM) for this alloy as the high iron content and low alloying elements in 4340 leave it highly susceptible to magnetization, making it incompatible with electron beam controls of the Arcam A2X. The chemical composition of 4340 steel, given in weight percent (wt%), is provided in Table 23.

Table 23. 4340 Steel chemical composition. (64)

	4340 Steel (wt%)
Iron, Fe	95.195 – 96.33
Nickel, Ni	1.65 – 2.0
Chromium, Cr	0.7 – 0.9
Manganese, Mn	0.6 – 0.8
Carbon, C	0.37 – 0.43
Molybdenum, Mo	0.2 – 0.3
Silicon, Si	0.15 – 0.3
Sulfur, S	0.04
Phosphorous, P	0.035

Material development of Ti-6Al-4V with EBM and 4340 steel with SEAM were part of the same project funded by Eaton corporation and were conducted simultaneously.

4.2 Scalable and Expeditious Additive Manufacturing (SEAM)

Scalable and Expeditious Additive Manufacturing or SEAM is a new and innovative AM process developed at Michigan State University, and as the name suggests, is designed with the focus of fast printing times, scalability, and low cost. SEAM is similar to Binder Jet Printing (BJP) in that it utilizes a powder bed and binder phase to glue metal powders together into a low-density green part before consolidating it into a final full density part through a series of post processing steps. Unlike BJP, SEAM rakes a layer of metal powder pre-mixed with a photo curable resin into the build area, and then cures the layer in one step using a UV projector, significantly reducing layer time and machine complexity. This process is repeated layer-by-layer until the desired height is reached. A simple diagram of the SEAM process is provided in Figure 158.

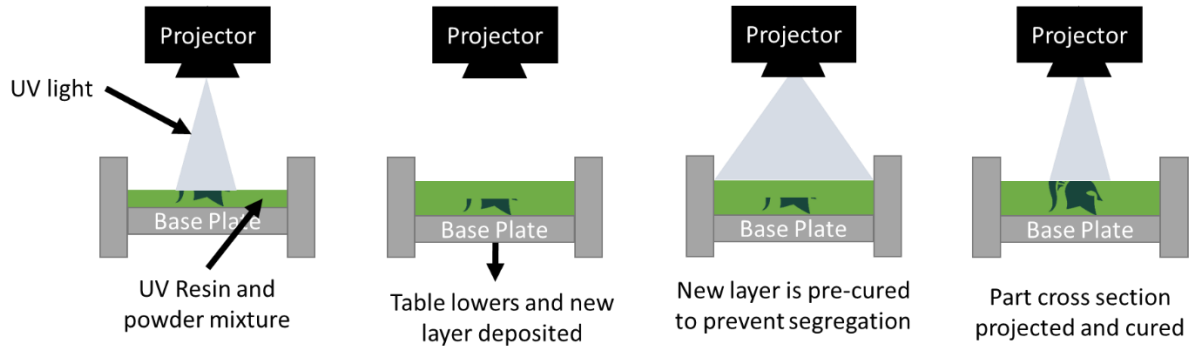

Figure 158. Diagram of Scalable Expedient Additive Manufacturing (SEAM) process.

After printing, the sample is typically de-bound in an air furnace at 430ºC for 2 hours and 1ºC/min ramp rate. During de-binding, the binder thermally decomposes, reacts with air, and is removed from the part. At the same time, the elevated temperature causes necking among the powders, holding the part together even after the binder is removed. Finally, the sample is placed

in a vacuum furnace and heated to around 90% of the material's melting point, sintering the powders together into a full density part while maintaining its overall shape.

4.3 Powder Tapping

Since room temperature processes like BJP and SEAM do not melt powders at the time of printing, green part density, and by extension the final sintered part, are more sensitive to the powder bed density than the complete melting processes like EBM and Laser Powder Bed Fusion (LPBF). Voids left by insufficient molten material can be filled with extra powder supplied by the subsequent rake pass. However, no additional material is introduced during standard sintering, meaning sufficient material must already be present to close all the remaining interstitial space among the powders if full density is to be achieved without excessive shrinkage or part deformation. Higher sintering temperatures can be used to fill in the interstitial space but only to a certain extent. If too much of the printed powder melts, the overall shape is lost. This relationship between initial powder bed density and final sintered density suggests the latter can be increased by increasing the former or can at least reduce sintering temperature and risk of losing the intended shape.

One way to increase the powder bed density is by combining two or more different sized powders in specific ratios. Optimal mix ratios can be estimated using a linear packing model for grain mixtures first developed by Stovall et al. (65). This model uses the individual tapped powder densities and mix ratios of selected constituent powders, as defined by ASTM B527-15 (66), to predict the tapped powder density of the final mixture. Maximizing bed density using this packing model has become a standard practice for the advanced manufacturing group when developing new materials for BJP or, for this project, SEAM.

The tapped powder density of candidate powders is measured using the custom-made device presented in Figure 160, which was designed and constructed based on the ASTM specifications and diagram depicted in Figure 159.

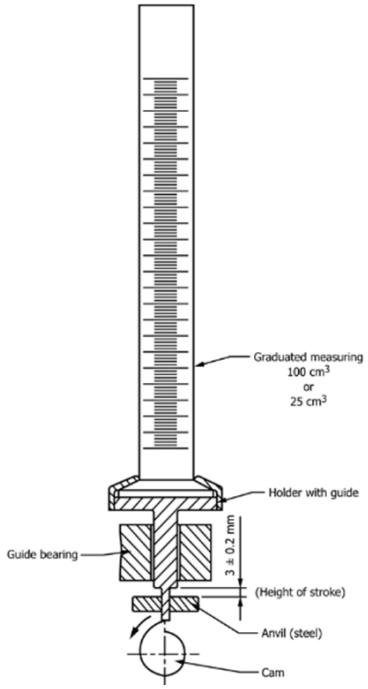

Figure 159. Representation of tapping device to be used for measuring tapped powder density of metal powders in accordance to ASTM B527-15. (66)

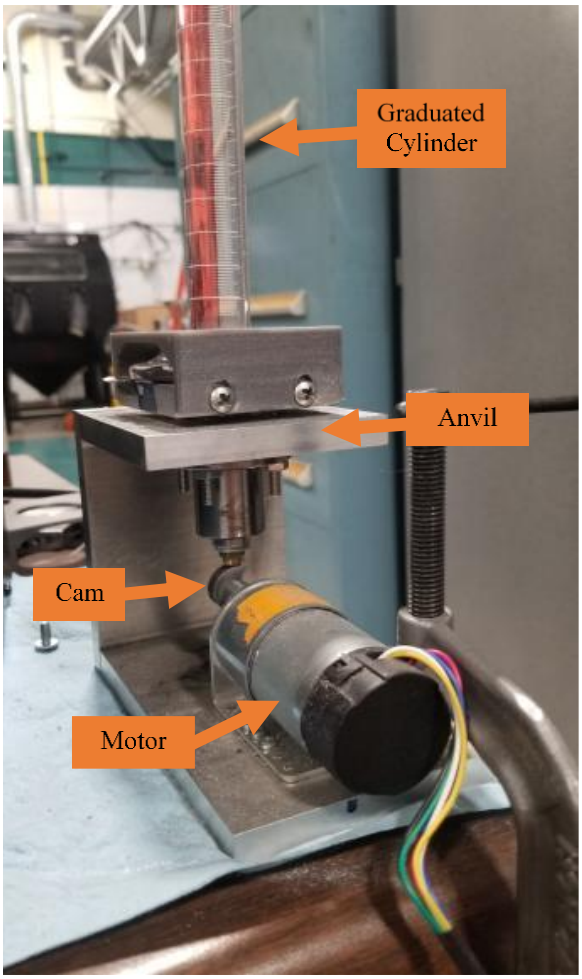

Figure 160. Custom powder tapping device made in accordance with ASTM B527-15 specifications.

The device uses gravity to tamp down 100 grams of powder, held in the graduated cylinder, by repeatedly raising it approximately three millimeters, via a cam and follower, before dropping it against an anvil. This is repeated until there is no change in powder level, 15 minutes at 60 rpm, recommended by the ASTM standard, was found to be more than sufficient. After tamping, the final height of the powder is measured and used along with the starting weight to determine the tapped powder density. Once each constituent powder is measured in this way, the predicted packing density of any give mix ratio is calculated using equations derived by Stovall et al. (65) given as

$$\gamma = \min(\gamma_1, \gamma_1, \cdots, \gamma_n). \tag{5}$$

Where γ is the final predicted packing density, n is the number of constituent powders listed in descending order in terms of diameter(d_i or d_j), i is an iterator, defined from 1 to n, during itteration the i^{th} powder is assumed to have the largest effect on final packing density and "dominates" the mixture, y_i is the volumetric fraction and γ_i, given by Eq. (6), is packing density of the i^{th} powder. (65)

$$\gamma_i = \frac{\beta_i}{1 - \sum_{j=1}^{i-1}\left[1 - \beta_i + b_{i,j}\beta_i\left(1 - \frac{1}{\beta_j}\right)\right]y_i - \sum_{j=i+1}^{n}\left[1 - a_{i,j}\frac{\beta_i}{\beta_j}\right]y_j} \tag{6}$$

Where another iterator, j is defined as $j = i + n$. β_i and β_j are the tapped powder density of the i^{th} or j^{th} powders and $a_{i,j}$ and $b_{i,j}$ are interaction factors defined as the loosening and wall effect parameters and are given in Eq. (7).

$$a_{i,j} = \sqrt{1 - \left(1 - d_j/d_i\right)^{1.02}}$$
$$b_{i,j} = 1 - \left(1 - d_i/d_j\right)^{1.50} \tag{7}$$

To calculate the predicted packing density γ, Eq. (6) must be solved n number of times while assuming a different powder as "dominating" the mixture each time, effectively iterating i from 1 to n. According to Eq. (5), the minimum γ of the n calculated is the actual predicted packing density, as there can only be one "dominant" powder for any given mixture (67) (65). Using this method, the mix ratio resulting in the highest possible tapped powder density can be determined by sweeping through all possible ratios, calculating the predicted tapped powder density, and plotting the results. This method was automated for a 2 particle size mixture using MATLAB, see Appendix B for the script specifics.

Although 4340 is a common steel alloy, it proved difficult to procure it in a powder form except with one company (GKN Powder Metallurgy, Auburn Hills, MI) who had only two sizes of 45-150 μm and 15-35 μm. As discussed previously, the tapped powder density for each powder was first measured. For calculations, the diameter of each powder was approximated as the average diameter of the distribution, being 25 μm and 97 μm. Tapping results for each constituent powder are provided in Table 24. The predicted packing density for all possible mix ratios was calculated and plotted using MATLAB. As presented in Figure 161, the optimal mixing ratio was calculated to be 67.4 wt% 45-150 μm powder and 32.6 wt% 15-35 μm powder and achieved a theoretical tapped powder density of 72.5%.

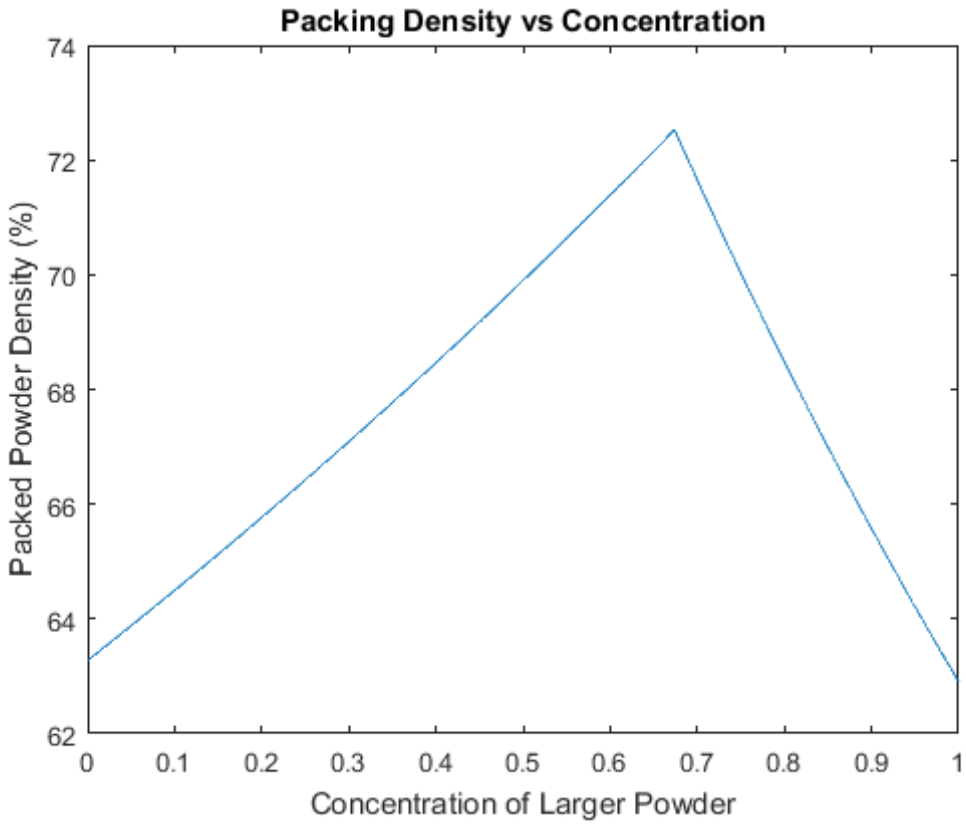

Figure 161. Calculated predicted packed powder density for mixture of 15-53 (smaller) and 45-150 (larger) 4340 powders.

100 grams of this optimal powder were then mixed and tapped to confirm the actual tapped density. These results are recorded at the bottom of Table 24.

Table 24. Tapped powder density measurement, calculation, and confirmation data for 4340 steel powder.

15-53 Micron											
Run	mass powder (g)	Start Top	Start Bot	Start Average	Start Density	% Packing	End Top	End Bot	End Average	End Density	% Packing
1	100	21.8	21.6	21.7	4.608	58.701	20.3	19.8	20.05	4.988	63.541
2	100	22	22	22	4.545	57.898	20.4	20.1	20.25	4.938	62.904
3	100	22.2	22.1	22.15	4.515	57.516	20.2	20	20.1	4.975	63.376
											63.274
45-150 Micron											
Run	mass powder (g)	Start Top	Start Bot	Start Average	Start Density	% Packing	End Top	End Bot	End Average	End Density	% Packing
1	100	21.8	21.8	21.8	4.587	58.433	20.3	20.2	20.25	4.938	62.904
2	100	21.9	21.6	21.75	4.598	58.573	20.4	20.2	20.3	4.926	62.752
3	100	21.6	21.6	21.6	4.63	58.981	20.2	20.2	20.2	4.95	63.057
											62.904
15-53 Micron	32.60%										
45-150 Micron	67.40%										
Run	mass powder (g)	Start Top	Start Bot	Start Average	Start Density	% Packing	End Top	End Bot	End Average	End Density	% Packing
1	100	20.8	20.8	20.8	4.808	61.248	19	18.9	18.95	5.277	67.223
2	100	21.6	21.6	21.6	4.63	58.981	19.2	19.3	19.25	5.195	66.178
3	100	21.2	21	21.1	4.739	60.369	19	19.1	19.05	5.249	66.866
											66.756

The actual measured value fell short of the predicted 72.5%, only achieving a packing density of 66.8 %. Although several factors could contribute to the lower actual density, it is believed that approximating the entire powder distribution as a single average diameter is responsible for the majority of error. Regardless, the mixture achieved an improvement of almost 3% over both individual powders. Stovall et al. did outline a method for better calculating optimal packing for continuous powder distributions (65). However, to this author's knowledge this would require measuring the tapped density for each size powder in the distribution. Requiring multiple sieve screens of fine step sizes to isolate specific diameter powders for testing before recombining them back together. Due to limited powder supplies and time, the approximation was decided as sufficient for our purposes.

4.4 Preliminary Testing Cubes

After determining the optimal powder mixture, a preliminary SEAM build was run to provide a large number of cubes for burnout and sintering tests. One hundred 10x10x10 mm

cubes were printed, taking up as much of the build area as possible and minimizing waste as the partially cured powder between each part that cannot be recovered. Images of the build in progress can be found in Figure 162 and Figure 163.

Figure 162. SEAM setup in the process of printing set of 100 preliminary 4340 steel cubes. Each cube has a green part size of 10 x 10 x 10 mm after printing.

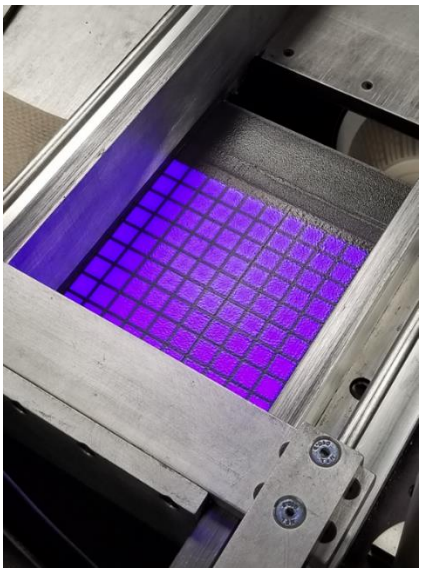

Figure 163. Build bed of SEAM machine during curing phase of printing set of 100 preliminary 4340 cubes. Each cube has a green part size of 10 x 10 x 10 mm after printing.

One kilogram of the mixed powder was combined with 44% vol% or 11.5 wt% photo curable resin. A standard pre-scan time of 5 seconds and layer cure time of 60 seconds and 150 μm layer thickness. These values were based on the previous experience of printing similar material and produced excellent quality samples as shown in Figure 164.

Figure 164. Set of 100 4340 cubes printed using SEAM.

4.4.1 Burn Out

A constant concern associated with the binder burnout process is oxidation, especially for corrosion-prone materials like 4340 compared to other commonly processed materials like stainless steels or nickel-based super alloys. To begin, three samples set on an alumina base plate were placed in an air furnace, heated to the resin manufacture's specified burnout temperature of 430ºC at a rate of 5ºC/min and held for 10 hours. Before and after images of these samples are provided in Figure 165.

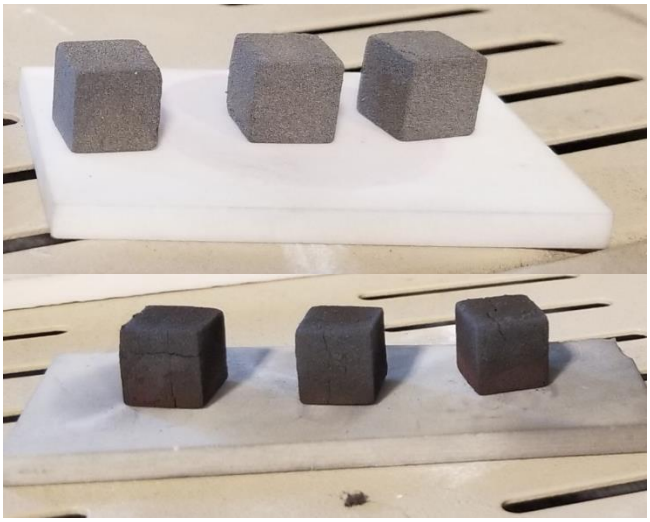

Figure 165. Pre and post burnout images of 3 4340 cubes. Burnout process was performed in an air furnace at 430°C for 10 hours with a 5°C/min ramp.

Sample masses were recorded before and after burnout in an attempt to track the amount of binder removed from the sample. These measurements have been recorded in Table 25.

Table 25. Weight change of 4340 steel cubes before and after burnout.

	Sample 1	Sample 2	Sample 3
Pre-Burnout (g)	4.7040	4.363	4.706
Post Burnout (g)	4.303	3.947	4.322
Change (g)	-.401	-.4161	-.384

These mass changes correspond to a weight change of 9.5, 9.5, and 8.2 percent, respectively. Although the weight change is less than the 11.5 wt% of resin added to the powder, it is difficult to differentiate how much of the weight loss is masked by the weight gained from obvious oxidation on the part surface. Later, the cross-sectional analysis of sintered parts would reveal only a minor layer of oxidation on the surface with little to no penetration into the part interior, but it still remains difficult to decouple the simultaneous weight loss and gain. Oddly, when Sample 1 was again measured after sintering an additional weight loss was measured for the overall weight change of -0.5045 grams, or 11.7 %. An additional un-burned-out sample included alongside Sample 1 in the sintering run had a measured weight change of -11.3 %. Although this may indicate most of the binder is removed from the sample, it is not clear at this time why similar weight changes are observed after sintering for both burned out and non-burned-out samples. However, this phenomenon is outside the scope of this project and may be the subject of another study.

4.4.2 Sample Cracking

In addition to surface oxidation, significant cracking was observed in samples after the binder burnout process as depicted in Figure 166.

Figure 166. Cracked 10 x 10 x 10 mm 4340 steel cube printed using SEAM and burned out at 430°C for 10 hours with 5°C/min ramp.

At first, cracking was suspected to be caused by the accumulation of thermal stresses during the 5ºC/min ramp to 430ºC. This theory was tested by reducing the ramp rate to 1ºC/min resulting in the sample presented in Figure 167.

Figure 167. Un-cracked 10 x 10 x 10 mm 4340 steel cube printed using SEAM and burned out at 430°C for 10 hours with 1°C/min ramp.

With the cracking problem expected to be solved, this slow ramp was repeated for six additional samples found in Figure 168.

Figure 168. Additional 10 x 10 x 10 mm 4340 steel cubes printed using SEAM and burned out at 430°C for 10 hours with 1°C/min ramp. Samples feature extensive cracking even after using the same burnout treatment as previous uncracked sample.

While cracking was still present, the majority was horizontal with respect to the build direction rather than erratic multi-layer cracking observed previously. Based on these results, it appears that the slower ramping may have prevented thermal stress cracking but could not prevent print defects, present prior to burnout, from opening. The consistent horizontal cracks seem to be the result of insufficient bonding between print layers, known as delamination. Unfortunately, with the current machine set up too much powder is required to troubleshoot curing times as each build requires the entire build area be filled with the powder binder mixture. While the majority of UV light emitted by the projector is concentrated in the desired part curing area, it also emits a small amount of UV light throughout its entire projection area. This effect can be seen in Figure 170. The UV bleed partially cures the surrounding bed, still allowing the final desired green parts to be removed but preventing the partially cured material from being reused. This means that printing even a single cube would require the same amount of powder and resin be used as to print the 100 cubes shown earlier, significantly limiting the number of builds that can be

performed while investigating different machine parameters. To reduce the amount of powder required for printing, a drop in elevator device was designed, fabricated, and installed into the SEAM machine. This device significantly reduces the build area of the machine by covering the original build area with a flat stationary plate and connecting a much smaller circular build plate directly to the existing elevator mechanism. A tube welded to the stationary top plate acts as the new walls of the build chamber, reducing the 130x130 mm build area to just a 25 mm diameter circle, without significantly compromising Z-axis travel. Installing this device reduces the volume of powder to create a 10 mm tall build to just 2.9 % of the original volume of 169000 mm^3. This miniature build area has just enough room to print four 10x10x10 mm cubes as shown in Figure 169 and Figure 170, perfect for testing various curing times, rake settings, or sintering additives without excessive powder consumption.

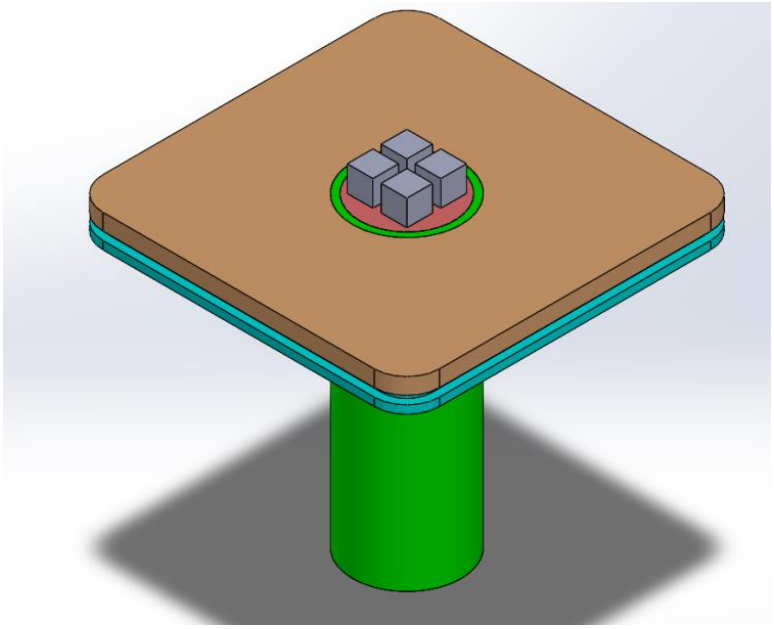

Figure 169. Drop in Elevator for SEAM machine. This device is meant to reduce the SEAM machine build bed allowing for printing of small batches of cubes.

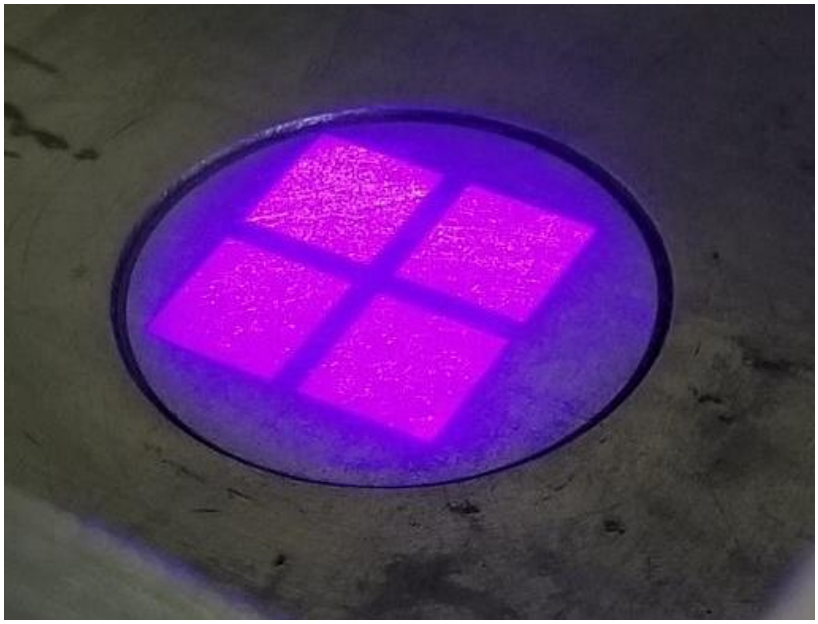

Figure 170. Installed drop in build elevator for SEAM machine. Featuring 25 mm diameter build area capable of printing 4 cubes while minimizing required material.

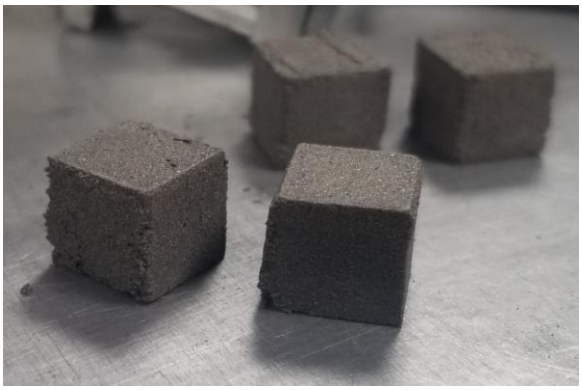

Figure 171. SEAM produced 4340 steel cubes using the installed mini elevator.

4.4.3 Sintering: First Attempts

Although most parts showed significant signs of cracking, sintering was still performed to begin work on determining the optimal sintering conditions for maximum density. First, samples were sintered at 1300ºC with a 5ºC/min ramp rate and 6-hour dwell time. Due to a mistake, these samples were sintered in an Argon environment rather than vacuum which has been shown to achieve higher densities for similar SS420 and SS316L alloys. (68) (69) Images

of sample before and after the first sintering attempt can be found in Figure 172 and Figure 173, respectively.

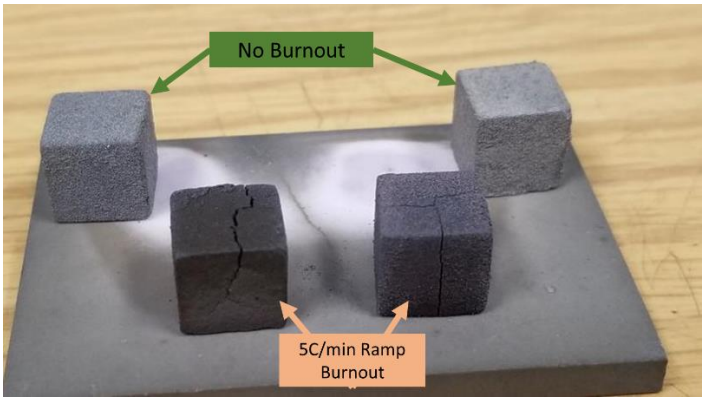

Figure 172. 4340 steel cubes from the original 100 cubes printed using SEAM prior to sintering. Top two samples did not undergo any burnout treatment while bottom two samples were burned out in air furnace at 430°C with 5°C/min and a dwell time of 10-hours.

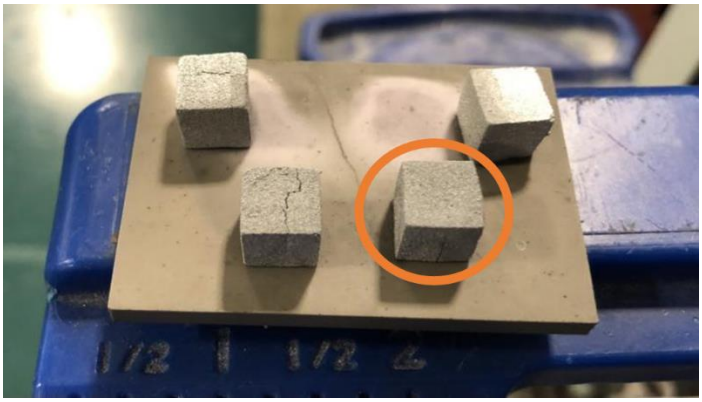

Figure 173. 4340 steel cubes from the original 100 cubes printed using SEAM after sintering at 1300°C with 5°C/min and 6-hour dwell.

Of the four samples, only one (circled above) showed enough evidence of densification to warrant further investigation by sectioning and cross-sectional imaging. Images of the polished cross-section, provided in Figure 174, were taken using an optical microscope. A custom MATLAB script was used to calculate the final density of 83.5%, far lower than expected. The final processed image with traced porosity is also provided in Figure 174 alongside the original image. A copy of the script used for this analysis is provided in Appendix B.

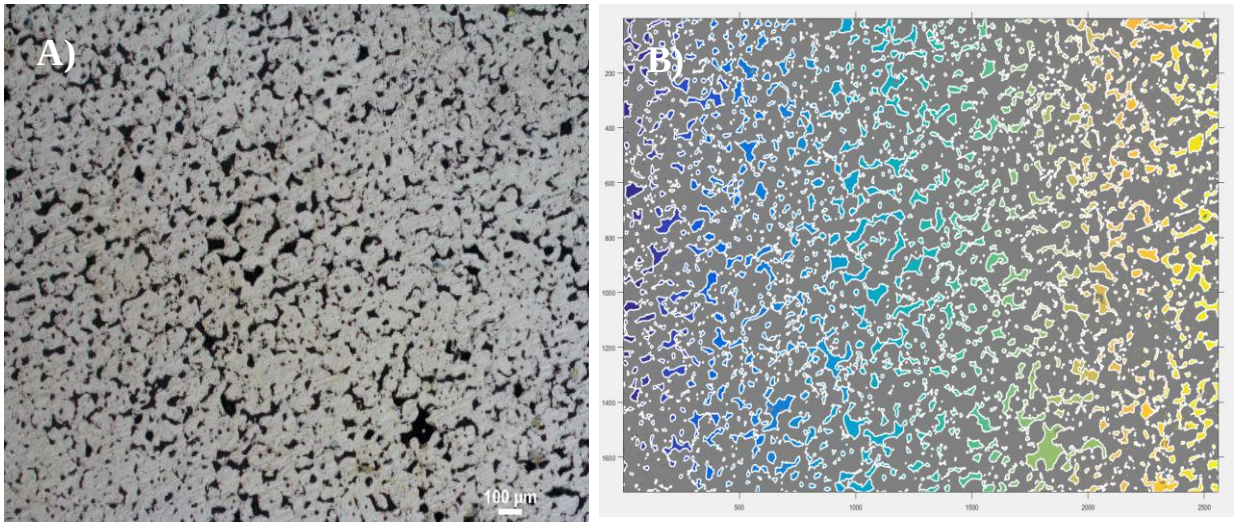

Figure 174. A) 5x optimal image of polished cross sectional of a 4340 cube printed using SEAM. B) Same cross-sectional image after processing using custom porosity measuring script, with identify pores filled with color gradient. The sample was burned out in an air furnace at 430°C with 5°C/min ramp and dwell time of 10 hours. The sample was then sintered at 1300°C with 5°C/min ramp and 6-hour dwell. Software measured a pore volume fraction of 83.5%.

The remaining three samples from the first build are expected to have even lower density as indicated by reduced shrinkage and were not examined further. In addition to low sintering temperature and incorrect environment, another explanation for the poor sintering performance is the samples welding to the Alumina plate. Some materials tend to weld or stick to the alumina base plate early in the furnace cycle. As the part shrinks, the welded portions prevent the perimeter from consolidating along with the bulk of the sample, resulting in large cracks or voids inside the part as the bulk of the sample was pulled away from the fixed sections. Welding was prevented in subsequent tests by floating samples on top a thin layer of loose Zirconia powder spread across the alumina plate, as shown in Figure 175.

Figure 175. 4340 steel cubes from the original 100 cubes printed using SEAM. Bottom right two samples were not burned out. The remaining samples were burned out in air furnace at 430°C with 5°C/min ramp and dwell time of 10 hours. All samples were then sintered in vacuum furnace at 1350°C with 5°C/min ramp and 6-hour dwell time.

Sintering tests were repeated for 1300°C and 1350°C with 5°C/min ramp rate and the 6-hour dwell time in vacuum environment. However, there was no significant increase in density for any sample, making it clear more than just traditional sintering would be required to achieve full density.

4.5 Liquid Phase Sintering

Liquid phase sintering is typically characterized by the addition of a lower melting point material to a partially sintered part to fill any remaining gap, promote further densification via surface tension, and braze the remaining solid particles together. Although the final overall density is improved, the overall properties are significantly inferior to that of a full density part. A diagram of this process is provided in Figure 176. (70)

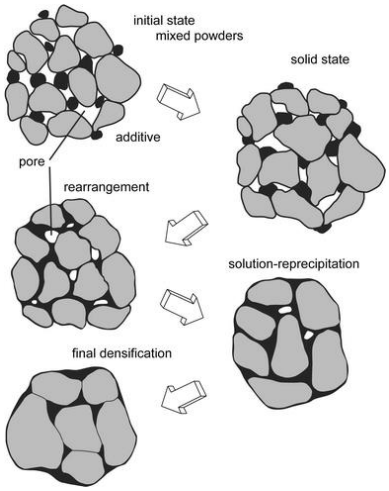

Figure 176. Diagram of traditional liquid phase sintering. (70)

In order to achieve near full density properties, Do et al. (68) (69) developed another version of liquid phase sintering for stainless steels printed by binder jet printing. A diagram of the process is provided in Figure 177.

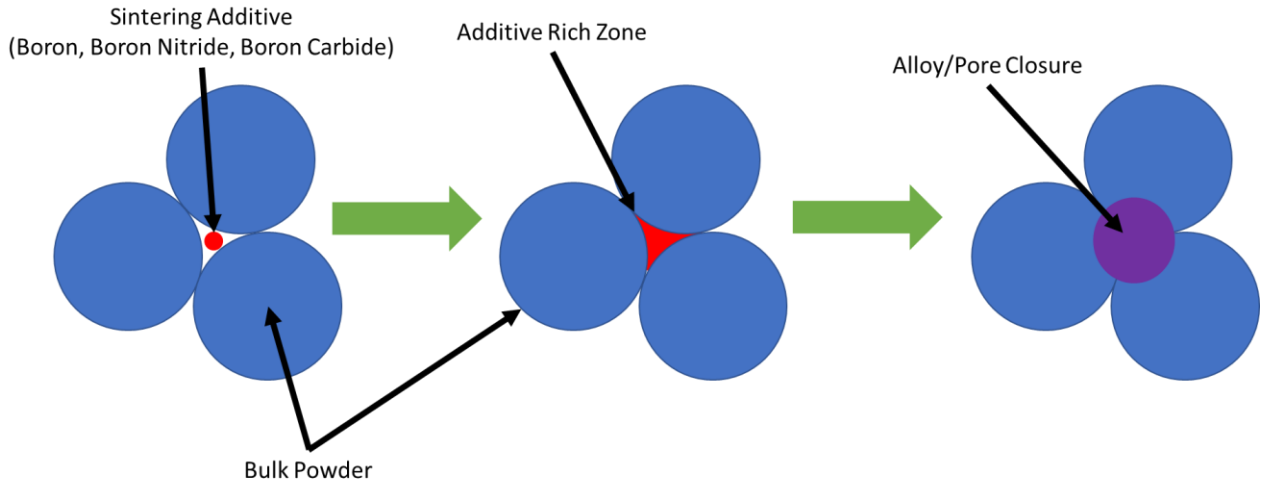

Figure 177. Diagram of liquid phase sintering process developed at MSU.

Rather than infiltrating a part with molten material, a small amount of solid sintering additive is mixed in with the powder before printing. The chemistry of the additive is determined by examining the phase diagrams of the major bulk powder constituents, to identify a particular additive that can significantly reduce the melting point of the bulk material, even at low concentrations. In the case of stainless steels, pure boron (B) and boron compounds were used.

These small powders settle into the interstitial spaces among the larger powders and diffuse into the surrounding surface during sintering, creating an additive rich zone around the pore, reducing the melting point of the material and promoting pore closure. Using this method, they were able reach near 100 percent density with the addition of just 0.5 wt% boron nitride (BN), without significantly impacting the SS420 mechanical properties. Examples of the optimization process are provided in Figure 178, where B, BN, and BC stand for boron, boron nitride, and boron carbide, respectively.

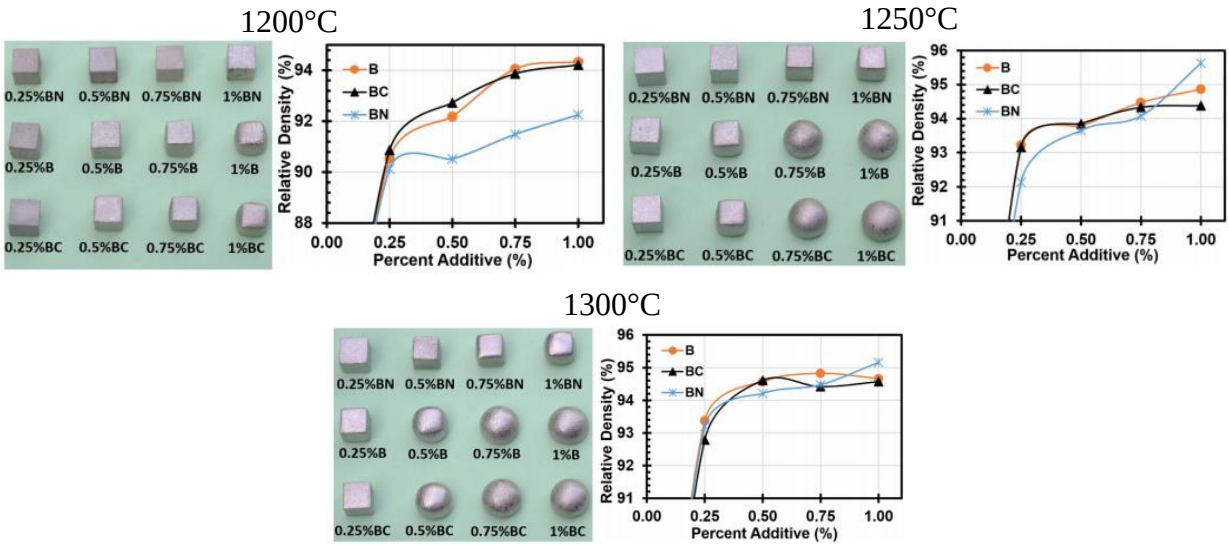

Figure 178. Comparison of burnout temperature with relative density results of SS420 powder mixed with various concentrations of BN, B, or BC sintering aids. Each set of samples were sintered at different temperatures of 1200°C (top left) 1250°C (top right), and 1300°C (bottom center). All samples were printed using binder jet printing and sintered with Argon shielding gas. (69)

Although some samples had high relative densities, such as 1.0 wt% BN sintered at 1300°C, excessive liquid phase was produced during sintering causing the original cube shape to deform into a sphere. It is critical that as much of the original shape be retained as possible to allow for printing of more complex geometries. Do et al. (69) concluded that BN provided the highest densities with minimal distortion. According to Heaney (71), higher densities can be achieved

with vacuum sintering, as furnace shielding gases can become trapped inside the part as it sinters, preventing full densification. Do et al. then repeated their experiment using the same concentrations of BN for vacuum and argon sintering environment. The results of this comparison test are presented in Figure 179.

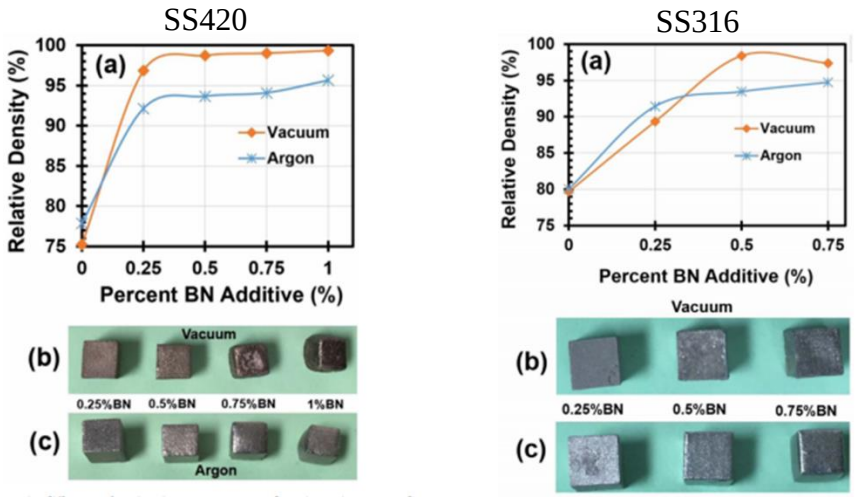

Figure 179. Comparison between vacuum and Argon shield gas sintering at 1250°C for SS420 (left) and SS316 (Right) mixed with various concentrations of BN sintering aids. (69)

For SS420, vacuum sintering resulted in higher densities at every BN concentration. The best combination of density and shape retention was determined to be 0.5 wt% BN with a relative density of 99.6%. Addition of BN and vacuum sintering was also shown to be effective at improving the density of SS316, proving that this technique could be applied to other materials.

4.5.1 Preliminary Liquid Phase Sintering Testing

With traditional sintering alone being insufficient to fully sinter, the SEAM produced 4340 steel, the same liquid phase sintering technique developed by Do et al. (69) was utilized to improve final density. To avoid having to repeat the sintering aid optimization, the composition of 4340 steel and SS420 were compared in order to estimate the appropriate amount of BN that should be added to the 4340 steel. A comparison of these compositions is provided in Table 26.

Table 26. Composition comparison between 4340 steel and SS420 stainless steel. (64) (72)

	4340 Steel	SS420
Iron, Fe	95.195 – 96.33	≈ 84
Nickel, Ni	1.65 – 2.0	-
Chromium, Cr	0.7 – 0.9	12.0 – 13.0
Manganese, Mn	0.6 – 0.8	0 – 1
Carbon, C	0.37 – 0.43	> 0.15
Molybdenum, Mo	0.2 – 0.3	-
Silicon, Si	0.15 – 0.3	0 – 1
Sulfur, S	0.04	0 – 0.03
Phosphorous, P	0.035	-

The largest difference between 4340 steel and SS420 is the chromium concentration, which is approximately 10 wt% higher in SS420 and corresponds to a 10 wt% higher iron concentration for 4340 steel. A rough estimation of the effect of boron on the melting point of iron and chromium as a function of wt% was estimated using an iron – boron and chromium – boron phase diagram, as seen in Figures 180 and 181.

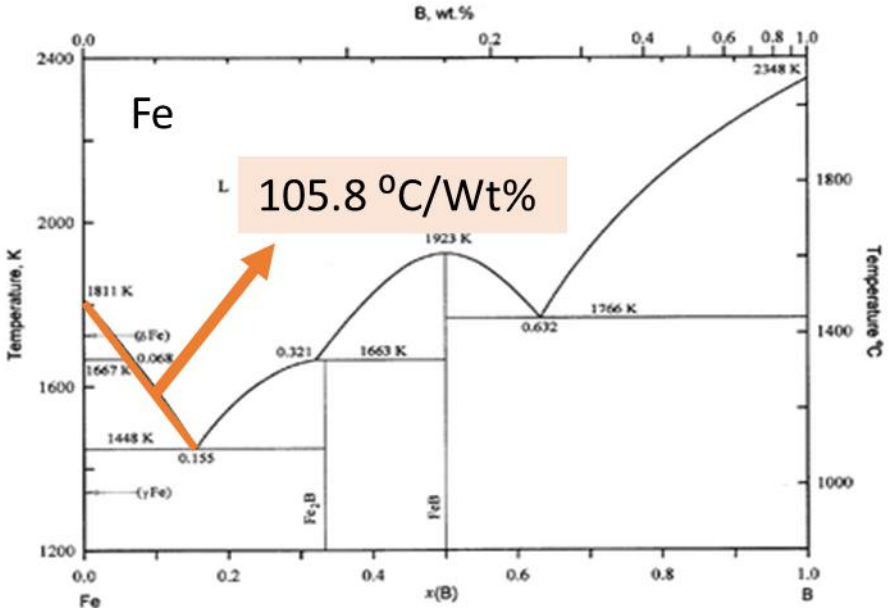

Figure 180. Boron - iron phase diagram, with approximate measure of reduction in melting point based on weight percent boron added. (73)

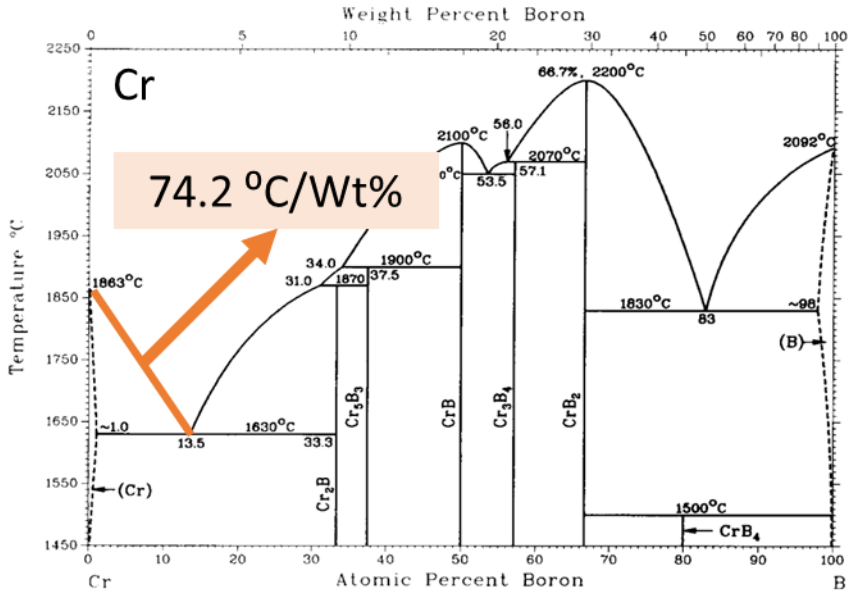

Figure 181. Boron - chrome phase diagram, with approximate measure of reduction in melting point based on weight percent boron added. (74)

Using these slopes and composition of each material the melting point of 4340 steel and SS420 was estimated to decrease by 101.7°C/B wt% and 98.2°C/B wt%, respectively. Therefore, these two materials should be similarly affected by boron concentration and the optimal boron

concentration of 0.5 wt% BN, determined by Do et at., can be directly applied to the 4340 steel. It should be noted that attempts were made at using pure boron to avoid the formation of nitrides. However, during printing, it was found that adding pure boron powder to the mixture would prevent the UV curable photo-resin from curing. No such problems occurred when boron nitride was used instead. Since SEAM takes place at room temperature, it is assumed this was caused by optical scattering and not a chemical reaction between boron and the resin.

4.6 Sintering: Final Optimization

A new batch of 4340 steel power was mixed using the same proportions of large and small powders. 0.5 wt% BN, with the average powder size of 1 μm was also added. To ensure that BN was uniformly distributed, powders were dry mixed for fifteen minutes by ball-milling with 0.5" (12.7 mm) diameter alumina grinding media. Since this was only a short mixing process no alumina contamination was expected. Just before printing, the powder mixture was combined with 44% vol% or 11.5 wt% photo curable resin. Print settings were also refined to improve removal of the part from surrounding partially cured material, improve dimensional accuracy, and speed up printing. It was found that a certain amount of the projected UV light would bleed into the bed during extended pre-scan and cure times, causing the material in the bed surrounding the desired part to begin curing. This curing made it difficult to separate the parts from the surrounding material, often resulting in the parts being damaged. The process was optimized by printing multiple sets of 4 cubes using the mini build elevator, then adjusting settings by trial and error. With the reduced build volume, new print settings could be tested using only a fraction of the material used to print the original 100 test cubes. The final optimized settings were found to be 1 second pre-scan time, 45 second layer cure time, and 150 μm layer thickness. By reducing the pre-scan and cure time, the amount of bleed was limited allowing the

parts to be more easily separated from the surrounding material after printing. However, this resulted in rounding for some of the cube's sharp corners, creating uneven samples. Therefore, the sample geometry was changed to a cylinder to maintain uniformity of the cross section. Using these new settings, additional 10 mm tall cylinders with 10 mm diameter were printed and used for sintering testing. An example of these new cylindrical sample geometry is provided in Figure 182.

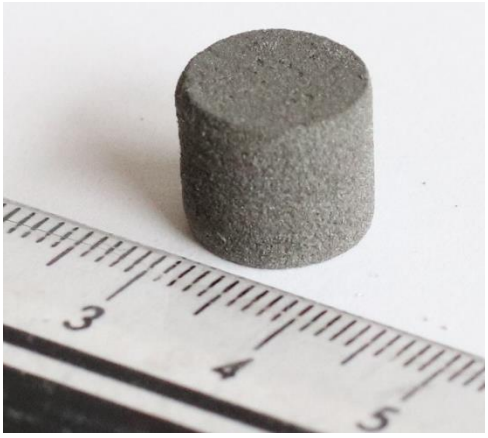

Figure 182. 4340 steel cylindrical green part produced with SEAM. The Sample is 10 mm in diameter and 10 mm tall.

During sintering samples were placed on top of a thin layer of zirconia powder spread across an alumina base plate. As discussed earlier, this powder layer prevents the part from welding to the alumina plate which would result in non-uniform shrinking. Also, the burnout process was also no longer performed on any sample, for two reasons. The first concern was about how to remove the oxide layer for more complex geometries. The simple cubes used in this study could be easily polished to remove the oxide layer. However, it would not be feasible to remove the oxide from internal pathways and cavities, defeating the purpose developing this material on such a versatile and flexible process like SEAM. Therefore, it was decided to try and develop a sintering process that did not require a burnout process. The residual binder is not expected to have a significant impact on the steel apart from slightly elevated carbon levels that

could theoretically be corrected with a decarbonization treatment, if required. The second concern stems from previous BJP experience, where samples with thick oxide layers were found to be difficult to full sinter. During sintering, the un-oxidized internal material consolidates more than the ceramic outer shell (oxide layer), causing it to pull away and form large internal void, much like shrinkage porosity in castings. This had yet to be observed with burned out and sintered 4340 steel thus far, possibly due to the poor sintering results. With the incorporation of BN sintering aid, the density and thus total consolidation and shrinkage of a part were expected to increase, making it likely this oxide layer interaction would occur.

The first sintering test performed was a 1-step sintering process in vacuum at 1350°C with a 1°C/min ramp rate and 10-hour hold time. After the hold, the furnace was turned off and allowed to cool naturally at an estimated rate of around 1°C/min. This shut-off procedure was done for each additional sintering test. After sintering, the sample was sectioned, polished, and imaged to measure density. An image of this cross-section is included in Figure 183.

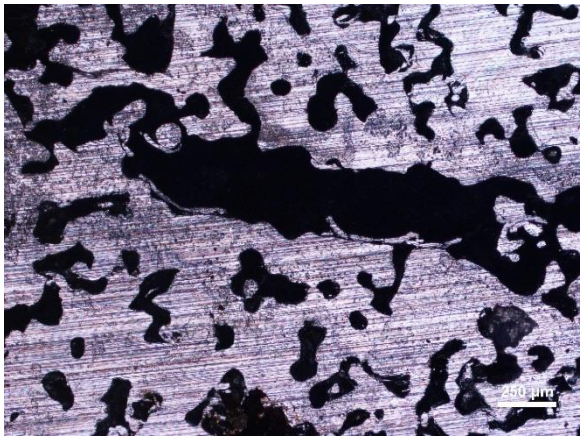

Figure 183. SEAM produced 4340 steel with 0.5 wt% boron nitride. 1-step sintering process in vacuum: 1°C/min 0 to 1350°C 10-hour hold.

Surprisingly, even with the high temperature and sintering additive, a large amount of porosity was still found. Therefore, the sintering temperature was increased to 1375°C with the same

1°C/min ramp rate and the shorter hold time of 6-hours. A cross-section of a sample treated with this condition is presented in Figure 184.

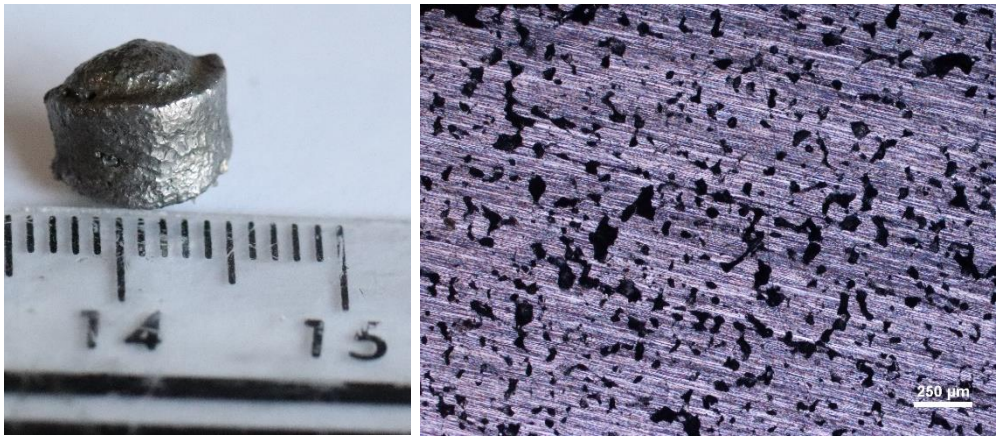

Figure 184. SEAM produced 4340 steel with 0.5 wt% boron nitride, 44vol% binder. 1-step sintering process in vacuum: 1°C/min 0 to 1375°C 6-hour hold. Left: Overall optical image with 1 cm scale bar. Right: 10x optical microscope image of cross section.

Even with the higher temperature, a large amount of porosity was still present in the cross-section, as well as significant geometric distortion. Another sintering treatment was repeated with the same 1375°C and 1°C/min ramp with a 10-hour hold time to hopefully reduce the porosity. A cross-section image of the sample treated with this condition is presented in Figure 185.

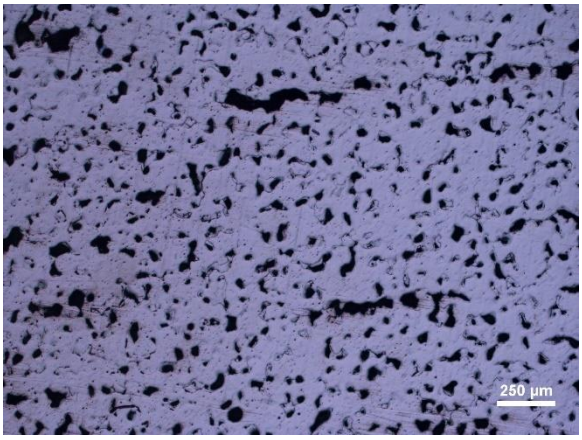

Figure 185. SEAM produced 4340 steel with 0.5 wt% boron nitride, 44vol% binder. 1-step sintering process in vacuum: 1°C/min 0 to 1375°C 10-hour hold.

Even with the high temperature and extended hold time, a large amount of porosity was still present. At this time, it was determined the sintering approach used must be fundamentally different. After re-examining the cross-sectional images of the two previous samples, the porosity was found to be near-spherical, much like a large-scale version of the trapped gas porosity, commonly found in the other additive process, making it less likely that the observed porosity was the result of insufficient temperature or dwell time. It was theorized that the outer surface of the sample was being heated much faster than anticipated and completely consolidated before the bulk of the sample could reach similar temperatures, effectively sealing the part. As the interior temperature rose, gases of some kind, most likely from the decomposing binder phase, formed and were trapped throughout the interior by the consolidated shell and preventing the part from consolidating. To test this theory, a 2-step sintering process was developed. First the part would be heated to 800°C at a rate of 5°C/min and held for one hour. 800°C was selected since the exact composition of the UV-curable photo-resin is unknown, but after reviewing literature it was found that most polymers undergo pyrolysis, or thermal decomposition in an inert atmosphere, between 500°C and 800°C. (75) Holding the sample at 800°C would hopefully allow the binder to decompose and be extracted by the vacuum before the sample's outer layer had a chance to consolidate. After this intermediate hold, the sample would then be heated to 1375°C with the 1°C/min ramp rate and 10-hour hold time, to finish the densification process. Results of this 2-step sintering process are presented in Figure 186.

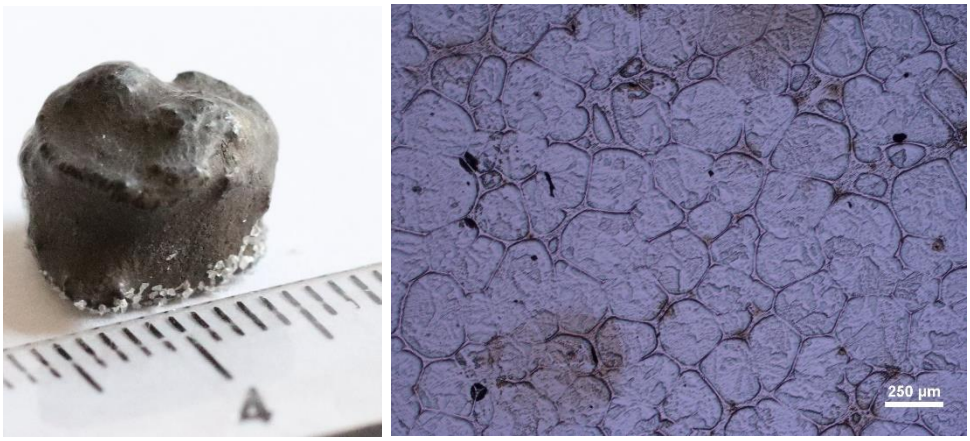

Figure 186. SEAM produced 4340 steel with 0.5 wt% boron nitride. 2-step sintering process in vacuum: 5°C/min 0 to 800°C 1-hour hold, 5°C/min 800 to 1375°C 10-hour hold. Left: Photo of deformed sample. Right: 10x optical microscope image of cross section.

It is clear that the 2-step sintering process resulted in significantly reduced porosity, confirming the trapped gas hypothesis. Close examination of the dark or discolored regions will reveal they are not pores, but most likely damage caused by polishing. To illustrate the effect of even a small amount of sintering additive on the overall shape, an additional sample with no sintering additive was included in the 1375°C run and is provided in Figure 187.

Figure 187. SEAM produced 4340 steel with no sintering additive. 2-step sintering process in vacuum: 5°C/min 0 to 800°C 1-hour hold, 5°C/min 800 to 1375°C 10-hour hold.

Although porosity was almost completely eliminated, the 1375°C samples still had significant geometric distortion from the high sintering temperature. Therefore, the maximum hold

temperature was reduced for the next test. To ensure as much binder was removed as possible, another intermediate 1200°C step was added. Dwell times at each intermediate step were also increased. The sample had sufficient time to equilibrate at a higher temperature before reaching the sintering temperatures. This new 3-step process consisted of 5°C/min ramp to 800°C with 2-hour hold, then 5°C/min ramp to 1200°C with another 2-hour hold, before a final 1°C/min ramp to 1350°C with 10-hour hold. Results of this treatment are presented in Figure 188. The left image in Figure 188 is a top down image of the sample after being sectioned, mounted in epoxy resin, and polished.

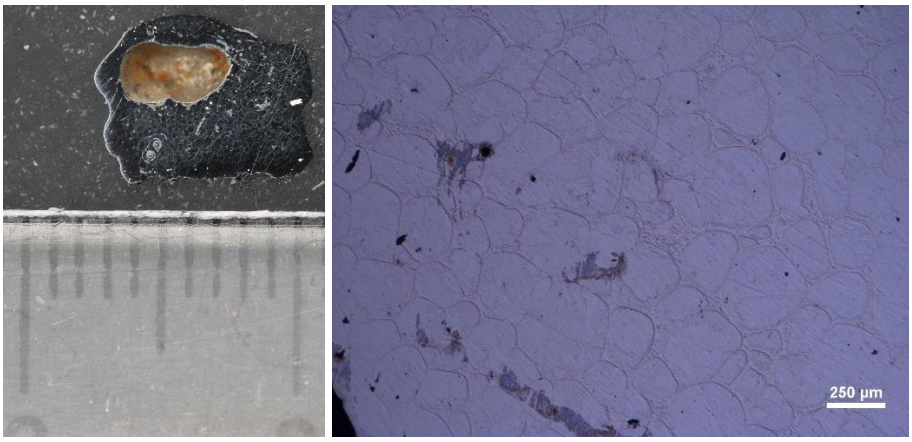

Figure 188. SEAM produced 4340 steel with 0.5 wt% boron nitride. 3-step sintering process: 5°C/min 0 to 800°C 2-hour hold, 5°C/min 800 to 1200°C 2-hour hold, 1°C/min 1200 to 1350°C 10-hour hold. Left: Overall optical image with 1 cm scale bar. Right: 10x optical microscope image of cross section.

Here again a majority of the dark spots and discoloration are the result of polishing damage. However, the highly circular defects are in fact pores. Porosity from the previous figure is highlighted in Figure 189.

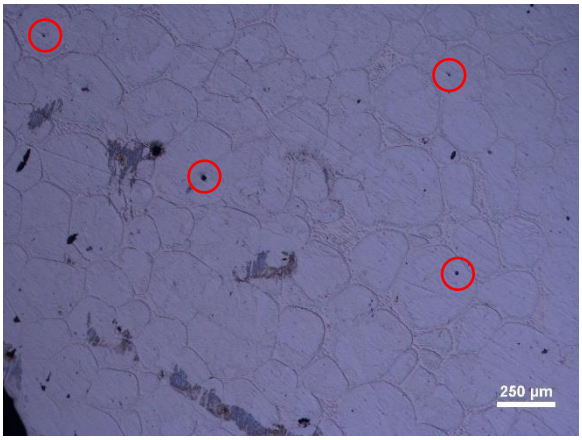

Figure 189.Copy of Figure 178 with porosity circled in red.

Although more pores were present, the geometric distortion was still too large, so the maximum temperature was reduced further to 1310°C. Intermediate hold times were also increased to see if these small pores could be eliminated. The next 3-step process consisted of a 5°C/min ramp to 800°C with a 4-hour hold, then 5°C/min ramp to 1200°C with another 4-hour hold, before a final 1°C/min ramp to 1330°C with 10-hour hold. Results of this treatment are presented in Figure 190.

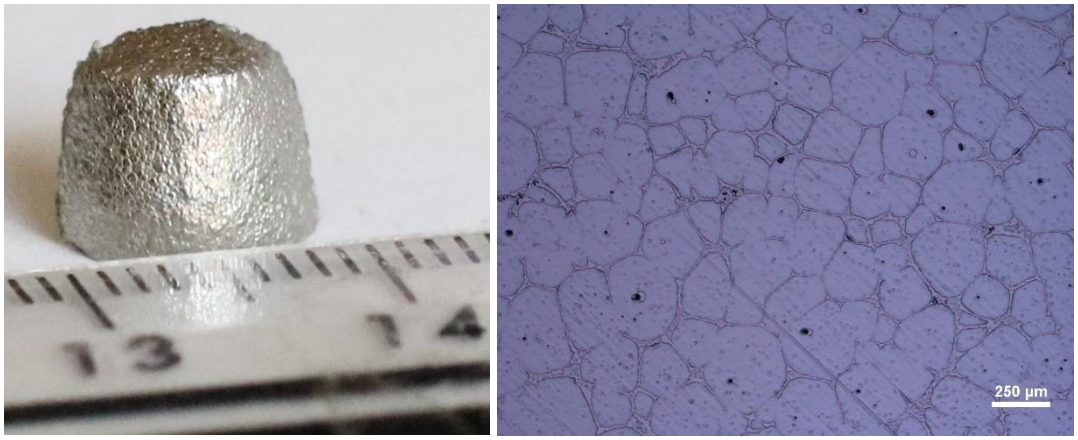

Figure 190. SEAM produced 4340 steel with 0.5 wt% boron nitride. 3-step sintering process: 5°C/min 0 to 800°C 4-hour hold, 5°C/min 800 to 1200°C 4-hour hold, 1°C/min 1200 to 1330°C 10-hour hold. Left: Photo of deformed sample. Right: 10x optical microscope image of cross section.

As expected, the decreased maximum sintering temperature corresponded to the increase in porosity. However, the geometric distortion was still too high, with the sample appearing to be

melted with a wider bottom than the top. As such, the maximum temperature was reduced further to 1310°C. For this test, the intermediate steps were left unchanged. Results of this test are provided in Figure 191.

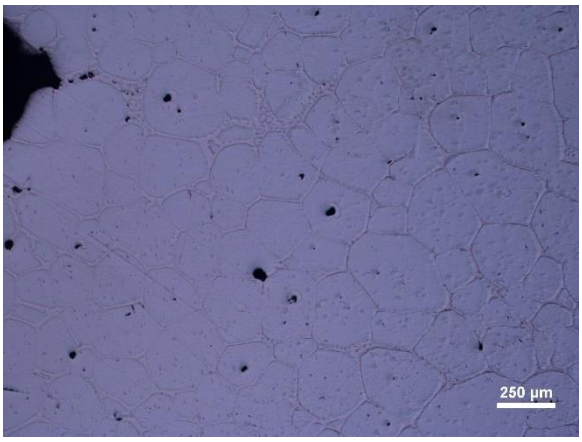

Figure 191. SEAM produced 4340 steel with 0.5 wt% boron nitride. 3-step sintering process: 5°C/min 0 to 800°C 4-hour hold, 5°C/min 800 to 1200°C 4-hour hold, 1°C/min 1200 to 1310°C 10-hour hold.

Again, even more porosity is evident. This test marks the first time that the sample did not exhibit significant geometric distortion following the sintering process. However, unlike the previous attempts a single large pore, measured approximately 500 µm in diameter, can be seen just out of frame in the top left corner of the previous figure. The origin of this defect is unclear, the most likely cause is a print defect or large trapped gas bubble. The final hold time was reduced down to three hours to determine if the excessively long 10-hour hold was necessary. Each intermediate step was also reduced to 3.5 hours to reduce overall processing time. Results of this sintering test are provided in Figure 183.

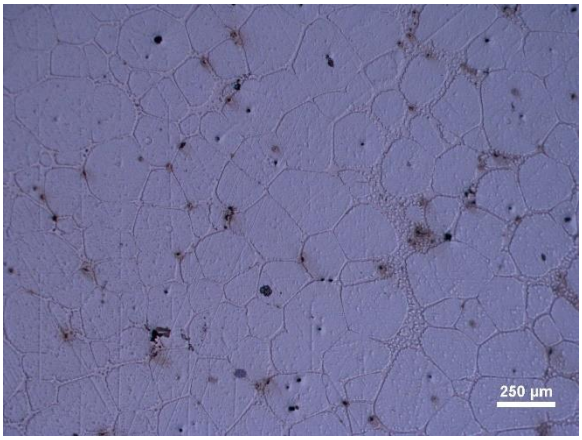

Figure 192. SEAM produced 4340 steel with 0.5 wt% boron nitride. 3-step sintering process in vacuum: 5°C/min 0 to 800°C 3.5-hour hold, 5°C/min 800 to 1200°C 3.5-hour hold, 1°C/min 1200 to 1310°C 3.5-hour hold.

No pores on the scale seen in Figure 191 was found, indicating it was most likely caused by a print defect. In addition, reducing each step time did not appear to be detrimental to final density, in fact the size of the pores, other than the massive center pore, appear to be reduced. Each hold time was then reduced to three hours in order to test if the final density will be further improved as well as reduced the overall processing time. The next sintering schedule was 5°C/min ramp to 800°C with 3-hour hold, then 5°C/min ramp to 1200°C with another 3-hour hold, and finally a 1°C/min ramp to 1310°C with a final 3-hour hold. Results of this sintering test are provided in Figure 193.

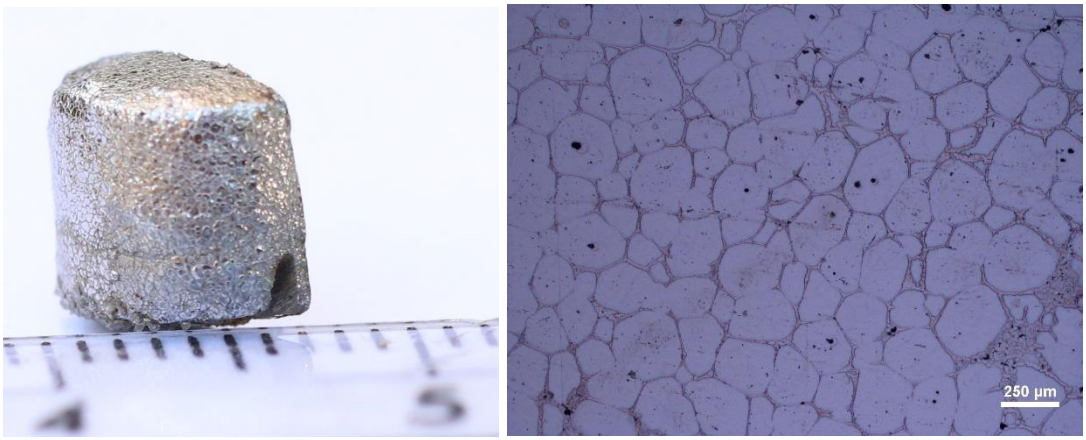

Figure 193. SEAM produced 4340 steel with 0.5 wt% boron nitride. 3-step sintering process in vacuum: 5°C/min 0 to 800°C 3-hour hold, 5°C/min 800 to 1200°C 3-hour hold, 1°C/min 1200 to 1310°C 3-hour hold. Left: Photo of sample with small cut mark from wafering saw on bottom face. Right: 10x optical microscope image of cross section.

This sintering schedule was found to produce the best results of any other tests performed, having a high density and minimal geometric distortion. Pore volume fraction was estimated to be 0.23%, giving a final density of 99.77%. This estimation was done using the same custom MATLAB script used for estimating the Ti-6Al-4V sample density. The code used can be found in Appendix B. In addition to the high final density, this sample had the least geometric distortion compared to any other previous test. Further tests with reduced hold time were attempted but were found to have lower relative densities. Attempts were made to combine the sintering process with a HIP by sintering the part inside the HIP chamber. Results of one attempt are provided in Figure 194.

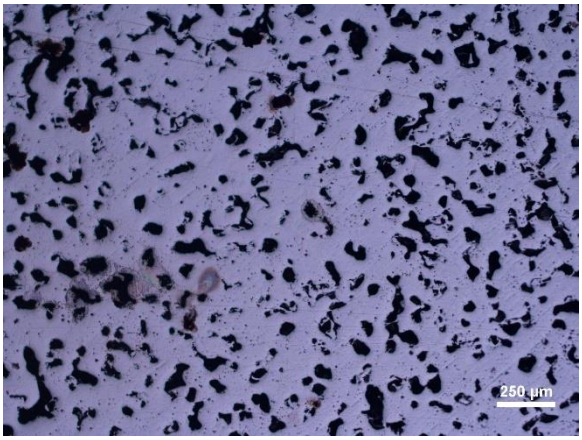

Figure 194. SEAM produced 4340 steel with 0.5 wt% boron nitride. 3-step sintering process in HIP with 30 Ksi Argon: 5°C/min 0 to 800°C 2-hour hold, 5°C/min 800 to 1200°C 2-hour hold, 1°C/min 1200 to 1310°C 3-hour hold.

It is clear that combining the processes in this manner is less effective than conventional sintering. The lack of consolidation caused by the large amount of interconnected porosity allowed the high-pressure argon to infiltrate the green part, equalizing the pressure, and preventing pore consolidation. In addition, one of the key steps needed for full consolidation was sintering in a vacuum environment. While these results were not unexpected, confirming the sintering and HIP treatments could not be combined in this way, made it an worthwhile endeavor.

4.7 Conclusion

This work demonstrated the ability to produce full density 4340 steel using SEAM. Full density was achieved using a combination of a linear packing model and liquid phase sintering using 0.5 wt% boron nitride. 4340 steel powders 15-53 μm and 45-150 μm were mixed at a ratio of 23.6 wt% and 67.4 wt% to produce a mixture with a tapped powder density of 66.8% (relative to solid 4340), approximately only 3% higher than the tapped powder density of either constituent. The sintering additive of 0.5 wt% boron nitride was used to significantly increase the final sintered density. The concentration used was based on Do et al.'s (69) previous work on

BJP printing of SS420, as well as chemical comparison between SS420 and 4340 steel. A 3-step sintering schedule of 5°C/min 0 to 800°C 3-hour hold, 5°C/min 800 to 1200°C 3-hour hold, 1°C/min 1200 to 1310°C 3-hour hold was used to achieve a relative density of 99.77%. Sintering during simultaneous HIP treatment was also attempted but was found to be ineffective. Unfortunately, due to time constraints, full fatigue samples could not be produced and tested.

BIBLIOGRAPHY

1. Ebay. *MAKERBOT MP05825 Replicator Desktop 3D Printer.* [Online] https://www.ebay.com/p/8003306299.

2. *History of additive manufacturing.* Wohlers, T and Gornet, T. 2014, Wohlers Report, Vol. 24, p. 118.

3. Hanson, Kip. SME. *Metal Milestones in 3D Printing.* [Online] https://www.sme.org/technologies/articles/2020/march/metal-milestones-in-3d-printing/.

4. Exone. *Our Story.* [Online] https://www.exone.com/en-US/About/Our-Story.

5. Jackson, Beau. 3D printing Industry. *GE ADDITIVE CHAMPIONS LEAN MANUFACTURING IN NEW ARCAM EBM CENTER OF EXCELLENCE.* [Online] https://3dprintingindustry.com/news/ge-additive-champions-lean-manufacturing-in-new-arcam-ebm-center-of-excellence-160550/.

6. GE Additive. GE Additive. [Online] November 2021. https://www.ge.com/additive/additive-manufacturing/machines/ebm-machines/arcam-ebm-a2x?gclid=CjwKCAjwm7mEBhBsEiwA_of-TDNcFX-JwnnLgDbH4h9a_bTM-UdLBTX_xrXOgXyVFmJ7BwvaCA9mDRoC82IQAvD_BwE.

7. Electron gun. *Wikipedia.* [Online] https://en.wikipedia.org/wiki/Electron_gun.

8. *XCT analysis of the influence of melt strategies on defect population in Ti–6Al–4V components manufactured by Selective Electron Beam Melting, Materials Characterization.* S. Tammas-Williams, H. Zhao, F. Léonard, F. Derguti, I. Todd, P.B. Prangnell. 2015, Vol. 102, pp. 47-61.

9. *Influence of the focus offset on the defects, microstructure, and mechanical properties of an Inconel 718 superalloy,.* Hae-Jin Lee, Han-Kyu Kim, Hyun-Uk Hong, Byoung-Soo Lee,. 2018, Journal of Alloys and Compounds.

10. *Electron Beam—Specimen Interactions: Interaction Volume. In: Scanning Electron Microscopy and X-Ray Microanalysis.* J.I., Goldstein, et al. New York, NY : Springer, 2018, Scanning Electron Microscopy and X-Ray Microanalysis.

11. . *State of the Art in Directed Energy Deposition: From Additive Manufacturing to Materials Design.* Dass, Adrita & Moridi, Atieh. (2019), Coatings, p. 9. 418.

12. *Keyhole-induced porosities in Laser-based Powder Bed Fusion (L-PBF) of Ti6Al4V: High-fidelity modelling and experimental validation.* Bayat, Mohamad, et al. 2019, Additive Manufacturing, Vol. 30, p. 100835.

13. *Gas Atomization of Amorphous Aluminum Powder: Part II. Experimental Investigation.* Zheng, Baolong, et al. 2009, Metallurgical and Materials Transactions, pp. 995-1004.

14. ***Distribution of porosity in electron beam melting additive manufactured Ti-6Al-4V component.*** **. He, Chaoyi & Wang, Pan & Nai, Mui Ling Sharon & Wei, J. 2016.**

15. ***Improvement of Mechanical and Physical Properties in Powder Metallurgy.*** **Torralba, J.M. [ed.] Gilmar Ferreira Batalha, Chester J. Van Tyne, Bekir Yilbas Saleem Hashmi. s.l. : Elsevier, 2014, Comprehensive Materials Processing, pp. 281 - 294.**

16. ***The Effectiveness of Hot Isostatic Pressing for Closing Porosity in Titanium Parts Manufactured by Selective Electron Beam Melting.*** **Tammas-Williams, S., Withers, P.J. and Todd, I. 2016, Metall Mater Trans A 47, pp. 1939–1946.**

17. ***Fatigue life of additively manufactured Ti–6Al–4V in the very high cycle fatigue regime.*** **Günther, J, et al. 2017, International Journal of Fatigue, Vol. 94 Part 2, pp. 236-245.**

18. **Lutjering, Gerd, and James C. Williams.** ***Titanium. 2nd ed.*** **s.l. : Springer, 2007.**

19. **Greenwood, N. N. and Earnshaw, A.** ***Chemistry of the Elements (2nd ed.).*** **s.l. : Oxford: Butterworth-Heinemann., 1997.**

20. **International Titanium Association. Stanley Abkowitz, 90; Titanium Industry Pioneer. [Online] 2017. https://titanium.org/news/373100/Stanley-Abkowitz-90-Titanium-Industry-Pioneer.htm.**

21. **ASTM. Standard Specification for Wrought Titanium-6Aluminum-4Vanadium Alloy for Surgical Implant Applications (UNS R56400)1. 2014. Vol. 13.01.**

22. **Donachie, Matthew J. Jr.** ***Titanium: A technical Guide.*** **2ed Edition. s.l. : ASM International, 2000.**

23. ***Comparative study of fatigue properties of Ti-6Al-4V specimens built by electron beam melting (EBM) and selective laser melting (SLM).*** **Chastand, Victor, et al. 2018, Materials Characterization, Vol. 143, pp. 76-81.**

24. ***The Effects of Processing Parameters on Defect Regularity in Ti-6Al-4V Parts Fabricated By Selective Laser Melting and Electron Beam Melting.*** **Gong, Haijun & Rafi, H. & Starr, Thomas & Stucker, Brent. 2013. 24th International SFF Symposium - An Additive Manufacturing Conference.**

25. ***Chad E. Duty, A review on the fatigue behavior of Ti-6Al-4V fabricated by electron beam melting additive manufacturing.*** **Chern, Anddrew H., et al. 2019, International Journal of Fatigue, Vol. Volume 119, pp. 173-184.**

26. ***Critical assessment of the fatigue performance of additively manufactured Ti–6Al–4V and perspective for future research,.*** **Li, P., et al. 2016, International Journal of Fatigue,, Vol. 85, pp. 130-143.**

27. ***Effect of microstructure on the fatigue properties of Ti-6Al-4V titanium alloys.*** **Wu, G.Q., et al. 2013, Materials & Design,, Vol. 46, pp. p. 668-674.**

28. ***Microstructures and Mechanical Properties of Ti6Al4V Parts Fabricated by Selective Laser Melting and Electron Beam Melting.*** **Rafi, H. K., et al. 2013, J. of Materi Eng and Perform, Vol. 22, pp. 3872–3883.**

29. ***Fatigue Crack Initiation and Facet Formation in Ti-6Al-4V Wires.*** **Everaerts, J. 2017.**

30. ***Effect of HIP post-processing at 850 °C/200 MPa in the fatigue behavior of Ti-6Al-4V alloy fabricated by Selective Laser Melting.*** **Alegre, J.M., et al. 2022, International Journal of Fatigue, Vol. 163.**

31. ***Hot isostatic pressing (HIP) to achieve isotropic microstructure and retain as-built strength in an additive manufacturing titanium alloy (Ti-6Al-4V).*** **Benzing, Jake, et al. 2019, Materials Letters,, Vol. 257.**

32. ***Defect distribution and microstructure heterogeneity effects on fracture resistance and fatigue behavior of EBM Ti–6Al–4V.*** **Seifi, Mohsen, et al. 2, 2017, International Journal of Fatigue, Vol. 94, pp. 263-287.**

33. ***A Review of the Fatigue Properties of Additively Manufactured Ti-6Al-4V.*** **F., Cao, et al. 2018, JOM, Vol. 70, pp. 349–357.**

34. ***Ti-6Al-4V Additively Manufactured by Selective Laser Melting with Superior Mechanical Properties.*** **Xu, W., Sun, S. and Elambasseril, J. . 2015, JOM, Vol. 67, pp. 668–673 .**

35. ***The Kinetics of Phase Transformations During Continuous Cooling of the Ti6Al4V Alloy from the Single-Phase β Range.*** **Dabrowski, Robert. 2011, Archives of Metallurgy and Materials , Vol. 56, pp. 703-707.**

36. ***Metallurgy of Additive Manufacturing: Examples from Electron Beam Melting.*** **Murr, Lawrence. 2014, Additive Manufacturing , Vol. 5.**

37. Woolf, Peter and al., et. Engineering LibreTexts. ***Design of Experiments via Taguchi Methods - Orthogonal Arrays.*** **[Online] University of Michigan, March 5, 2021. https://eng.libretexts.org/@go/page/22674.**

38. ***Tiferet E, Ganor M, Zolotaryov D, et al. Mapping the Tray of Electron Beam Melting of Ti-6Al-4V: Properties and Microstructure. Materials (Basel). 2019;12(9):1470. Published 2019 May 7. doi:10.3390/ma12091470.*** **Tiferet, E., et al. 2019, Materials (Basel)., Vol. 12.**

39. ***Influence of build layout and orientation on microstructural characteristics of electron beam melted Alloy 718.*** **Karimi, P., Sadeghi, E., Deng, D. et al. 2018, Int J Adv Manuf Technol, Vol. 99, pp. 2903–2913.**

40. Institute of Physics and Materials Science, BOKU, Vienna. Ultrasonic Fatigue Testing Equipment. 2009.

41. MatWeb. Titanium Ti-6Al-4V (Grade 5), Annealed. ***ASM Aeropace Specification Metals, inc.*** **[Online] https://asm.matweb.com/search/SpecificMaterial.asp?bassnum=mtp641.**

42. Bureau, U.S. Census. Statistical Quality Standards. 2013.

43. ASTM. *ASTM E8/E8M-22: Standard Test Methods for Tension Testing of Metallic Materials.* Vol. 03.01.

44. Wikipedia. Deformation (engineering). [Online] https://en.wikipedia.org/wiki/Deformation_%28engineering%29.

45. National Institute of Standards and Technology. Grubbs' Test for Outliers. *Engineering Statistics.* [Online] https://www.itl.nist.gov/div898/handbook/eda/section3/eda35h1.htm.

46. *Microstructure and Mechanical Properties of Ti-6Al-4V Additively Manufactured by Electron Beam Melting with 3D Part Nesting and Powder Reuse Influences.* Wanjara, P., et al. 21, 2022, Journal of Manufacturing and Materials Processing, Vol. 6.

47. *Effects of processing on microstructure and mechanical properties of a titanium alloy (Ti–6Al–4V) fabricated using electron beam melting (EBM), part 1: Distance from build plate and part size.* Hrabe, Nikolas and Quinn, Timothy. 2013, Materials Science and Engineering: A, Vol. 573, pp. 264-270.

48. *Effects of the microstructure and porosity on properties of Ti-6Al-4V ELI alloy fabricated by electron beam melting (EBM).* Galarraga, Haize, et al. 2016, Additive Manufacturing, Vol. 10, pp. 47-57.

49. *Microstructures and mechanical properties of electron beam-rapid manufactured Ti–6Al–4V biomedical prototypes compared to wrought Ti–6Al–4V.* Murr, L.E., et al. 2, 2009, Materials Characterization, Vol. 60, pp. 96-105.

50. *Graded microstructure and mechanical properties of additive manufactured Ti–6Al–4V via electron beam melting.* Tan, Xipeng, et al. 2015, Acta Materialia, Vol. 97, pp. 1-16.

51. *Microstructure and Mechanical Properties of Long Ti-6Al-4V Rods Additively Manufactured by Selective Electron Beam Melting Out of a Deep Powder Bed and the Effect of Subsequent Hot Isostatic Pressing.* Lu, S. L., et al. 2015, Metallurgical and Materials Transactions A, Vol. 46, pp. 3824–3834.

52. *A critical evaluation of the microstructural gradient along the build direction in electron beam melted Ti-6Al-4V alloy.* Sharma, H., et al. 2019, Materials Science and Engineering: A, Vol. 744, pp. 182-194.

53. *Titanium Science and Technology.* Lucas, J.J. 1973, Plenum Press, New York, Vol. 3, p. 2081.

54. *Fatigue crack initiation in as forged Ti–6Al–4V bars with macrozones present.* K. Zhang, K.V. Yang, A. Huang, X. Wu, C.H.J. Davies. 2015, International Journal of Fatigue, Vol. 80, pp. 288-297.

55. ***Characterization of fatigue crack-initiation facets in relation to lifetime.*** **S.K. Jha, C.J. Szczepanski, P.J. Golden, W.J. Porter, and R. John. 2012, International Journal of Fatigue, Vol. 42, pp. 248-257.**

56. ***Effects of stress ratio on high-cycle and very-high-cycle fatigue behavior of a Ti-6Al-4V alloy.*** **Liu, X., Sun, C. and Hong, Y. 2015, Materials Science and Engineering A, Vol. 622, pp. 228-235.**

57. Lambrighs, K. Fatigue properties of heavily drawn steel wires. ***Ph.D. Thesis. Leuven, Katholieke Universiteit Leuven.*** **2010.**

58. University of Cambridge. Slip geometry: the critical resolved shear stress. ***Dissemination of IT for the Promotion of Materials Science (DoITPoMS).*** **[Online] https://www.doitpoms.ac.uk/tlplib/slip/slip_geometry.php#:~:text=The%20quantity%20cos%20%CF%86%20cos,y%20cos%20%CF%86%20cos%20%CE%BB.**

59. Lubliner, Jacob. ***Plasticity theory.*** **s.l. : Dover, 2008. ISBN 978-0-486-46290-5..**

60. ***Very high cycle fatigue of engineering materials: A literature review.*** **Kazymyrovych, V. s.l. : Karlstad University Studies, 2009.**

61. ***Analysis of fatigue properties and failure mechanisms of Ti6Al4V in the very high cycle fatigue regime using ultrasonic technology and 3D laser scanning vibrometry.*** **Heinz, Stefan, et al. 8, 2013, Ultrasonics, Vol. 53, pp. 1433-1440.**

62. ***Distribution of Internal Crack Initiation Sites in High-cycle Fatigue for Titanium Alloys.*** **Yokoyama, Hisanaga, et al. 12, 1997, ISIJ International, Vol. 37, pp. 1237-1244.**

63. ***Mechanical characterization of Ti-6Al-4V titanium alloy at multiple length scales using spherical indentation stress-strain measurements.*** **Weaver, Jordan S. and Kalidindi, Surya R. 2016, Materials & Design, Vol. 111, pp. 463-472.**

64. AZO Materials. AISI 4340 Alloy Steel (UNS G43400). ***AZO Materials.*** **[Online] 2012. https://www.azom.com/article.aspx?ArticleID=6772.**

65. ***Linear packing density model of grain mixtures.*** **Stovall, T., Larrard, F. de and Buil, M. 1, 1986, Powder Technology, Vol. 48, pp. 1-12.**

66. ASTM. ASTM B527-15, Standard Test Method for Tap Density of Metal Powders and Compounds,. ***ASTM International.*** **West Conshohocken, PA, 2015, www.astm.org : s.n., 2015.**

67. ***"Model Guided Mixing of Ceramic Powders With Graded Particle Sizes in Binder Jetting Additive Manufacturing."*****. Du, W, et al. College Station, Texas, USA. June 18–22 : s.n., 2018. ASME 2018 13th International Manufacturing Science and Engineering Conference. Vol. 1.**

68. ***Process development toward full-density stainless steel parts with binder jetting printing.*** **Truong Do, Patrick Kwon, Chang Seop Shin. 2017, International Journal of Machine Tools and Manufacture, Vol. 121, pp. 50-60.**

69. ***Additively Manufactured Full-Density Stainless Steel 316L With Binder Jet Printing.*** **Do, T, et al. College Station, Texas : s.n., 2018. Proceedings of the ASME 2018 13th International Manufacturing Science and Engineering Conference. Vol. 1.**

70. ***Review: liquid phase sintering.*** **German, R.M., Suri, P. & Park, S.J. 2009, J Mater Sci, Vol. 44, pp. 1-39.**

71. Heaney, D.F. 8 - Vacuum sintering. [ed.] Z.Z. Fang. ***Sintering of Advanced Materials: Fundamentals and Processes.*** **s.l. : Woodhead Publishing, 2010, pp. 189-221.**

72. AZO Materials. Stainless Steel - Grade 420. [Online] https://www.azom.com/article.aspx?ArticleID=972.

73. ***Thermodynamic properties and phase equilibria in the iron–boron system. Transition of the Fe–B melt into the amorphous state.*** **Alexander, Zaitsev, Natal'ya, Zaitsevaa and Alexander, Kodentsovb. 2003, Journal of Materials Chemestry, Vol. 13, pp. 943-950.**

74. ***The B−Cr (Boron-Chromium) system.*** **Liao, P.K. and Spear, K.E. s.l. : Bulletin of Alloy Phase Diagrams, 1986, Vol. 7, pp. 232–237.**

75. Elsevier. Chapter 2 Thermal decomposition of polymers. [ed.] Serban C. Moldoveanu. ***Techniques and Instrumentation in Analytical Chemistry.*** **s.l. : Elsevier, 2005, pp. 31-107.**

76. ***A. Microstructural porosity in additive manufacturing: The formation and detection of pores in metal parts fabricated by powder bed fusion.*** **Sola, A, Nouri. 2019, J Adv Manuf Process., p. 1:e10021.**

77. ***Metallurgy and Design of Alloys with Hierarchical Microstructures.*** **Mishra, Rajiv S. and Sankaran, Krishnan S. 2017, Elsevier, pp. Pages 177-288.**

78. Wikipedia. Stress–strain curve. ***Wikipedia.*** **[Online] 2013. https://en.wikipedia.org/wiki/Stress%E2%80%93strain_curve.**

79. ***Processing window and evaporation phenomena for Ti–6Al–4V,produced by selective electron beam melting.*** **Juechter, V., et al. 2014, Acta Materialia, Vol. 76, pp. 252-258.**

APPENDIX A: FATIGUE RESULTS

Table 27. Complete fatigue data for all samples tested. Samples for build 2 were eliminated from the main study and used for various preliminary testing. Samples labeled "No Resonance" were machined during attempts to remove surface embedded silicon carbide particles. Removal of material shifted the natural frequency outside the fatigue testing machine's excitation range and could not be tested. An "" is used to designate samples that were misplaced and not tested.*

Build	Sample	Speed Function	Line Offset (mA)	Focus Offset (mA)	HIP (°C)	Rough-ness (µm)	Load (MPa)	Cycles
1	1	30	0.1	0	800	0.1	500	3.47E+07
3	1	30	0.1	0	800	0.1	550	8.10E+05
4	1	30	0.1	0	800	0.1	500	1.00E+08
5	1	30	0.1	0	800	0.1	550	2.60E+05
6	1	30	0.1	0	800	0.1	500	1.00E+08
7	1	30	0.1	0	800	0.1	550	1.91E+05
8	1	30	0.1	0	800	0.1	500	7.47E+07
1	2	30	0.11	7	800	0.1	550	3.69E+05
3	2	30	0.11	7	800	0.1	500	1.00E+08
4	2	30	0.11	7	800	0.1	550	5.43E+05
5	2	30	0.11	7	800	0.1	500	1.00E+08
6	2	30	0.11	7	800	0.1	550	9.86E+05
7	2	30	0.11	7	800	0.1	500	2.08E+06
8	2	30	0.11	7	800	0.1	550	*
1	3	30	0.12	13	1100	0.2	500	4.49E+05
3	3	30	0.12	13	1100	0.2	550	2.73E+04
4	3	30	0.12	13	1100	0.2	500	6.43E+05
5	3	30	0.12	13	1100	0.2	550	1.43E+05
6	3	30	0.12	13	1100	0.2	500	1.48E+05
7	3	30	0.12	13	1100	0.2	550	22166
8	3	30	0.12	13	1100	0.2	500	7.06E+05
1	4	30	0.13	20	1100	0.2	550	4.44E+04
3	4	30	0.13	20	1100	0.2	500	1.30E+06
4	4	30	0.13	20	1100	0.2	550	3.72E+04
5	4	30	0.13	20	1100	0.2	500	7.37E+05
6	4	30	0.13	20	1100	0.2	550	1.65E+05
7	4	30	0.13	20	1100	0.2	500	63898
8	4	30	0.13	20	1100	0.2	550	6.84E+04
1	5	33	0.1	7	1100	0.2	500	1.57E+06
3	5	33	0.1	7	1100	0.2	550	3.21E+05
4	5	33	0.1	7	1100	0.2	500	655656
5	5	33	0.1	7	1100	0.2	550	1.33E+05

Table 27. (cont'd)

6	5	33	0.1	7	1100	0.2	500	1.25E+06
7	5	33	0.1	7	1100	0.2	550	1.32E+05
8	5	33	0.1	7	1100	0.2	500	1.57E+06
1	6	33	0.11	0	1100	0.2	550	1.03E+04
3	6	33	0.11	0	1100	0.2	500	1.62E+06
4	6	33	0.11	0	1100	0.2	550	70702
5	6	33	0.11	0	1100	0.2	500	1.80E+04
6	6	33	0.11	0	1100	0.2	550	1.12E+05
7	6	33	0.11	0	1100	0.2	500	4.88E+05
8	6	33	0.11	0	1100	0.2	550	1.11E+05
1	7	33	0.12	20	800	0.1	500	*
3	7	33	0.12	20	800	0.1	550	4.14E+06
4	7	33	0.12	20	800	0.1	500	1.00E+08
5	7	33	0.12	20	800	0.1	550	1.28E+05
6	7	33	0.12	20	800	0.1	500	1.00E+08
7	7	33	0.12	20	800	0.1	550	5.10E+06
8	7	33	0.12	20	800	0.1	500	1.00E+08
1	8	33	0.13	13	800	0.1	550	*
3	8	33	0.13	13	800	0.1	500	9.96E+07
4	8	33	0.13	13	800	0.1	550	1.31E+05
5	8	33	0.13	13	800	0.1	500	9.96E+07
6	8	33	0.13	13	800	0.1	550	8.27E+06
7	8	33	0.13	13	800	0.1	500	1.00E+08
8	8	33	0.13	13	800	0.1	550	6.99E+06
1	9	37	0.1	13	800	0.2	500	*
3	9	37	0.1	13	800	0.2	550	2.26E+05
4	9	37	0.1	13	800	0.2	500	3.39E+07
5	9	37	0.1	13	800	0.2	550	1.27E+05
6	9	37	0.1	13	800	0.2	500	9.96E+07
7	9	37	0.1	13	800	0.2	550	1.23E+05
8	9	37	0.1	13	800	0.2	500	9.96E+07
1	10	37	0.11	20	800	0.2	550	*
3	10	37	0.11	20	800	0.2	500	1.00E+08
4	10	37	0.11	20	800	0.2	550	7.60E+07
5	10	37	0.11	20	800	0.2	500	1.00E+08
6	10	37	0.11	20	800	0.2	550	3.29E+05
7	10	37	0.11	20	800	0.2	500	3.97E+06
8	10	37	0.11	20	800	0.2	550	2.56E+05
1	11	37	0.12	0	1100	0.1	500	*
3	11	37	0.12	0	1100	0.1	550	1.2E+05

Table 27. (cont'd)

4	11	37	0.12	0	1100	0.1	500	8.05E+05
5	11	37	0.12	0	1100	0.1	550	1.31E+05
6	11	37	0.12	0	1100	0.1	500	*
7	11	37	0.12	0	1100	0.1	550	3.37E+04
8	11	37	0.12	0	1100	0.1	500	*
1	12	37	0.13	7	1100	0.1	550	5.84E+05
3	12	37	0.13	7	1100	0.1	500	73600
4	12	37	0.13	7	1100	0.1	550	6.69E+04
5	12	37	0.13	7	1100	0.1	500	1.40E+06
6	12	37	0.13	7	1100	0.1	550	3.15E+05
7	12	37	0.13	7	1100	0.1	500	2.11E+06
8	12	37	0.13	7	1100	0.1	550	1.40E+05
1	13	40	0.1	20	1100	0.1	500	4.28E+05
3	13	40	0.1	20	1100	0.1	550	1.22E+05
4	13	40	0.1	20	1100	0.1	500	6.93E+05
5	13	40	0.1	20	1100	0.1	550	3.52E+04
6	13	40	0.1	20	1100	0.1	500	*
7	13	40	0.1	20	1100	0.1	550	2.99E+04
8	13	40	0.1	20	1100	0.1	500	No Resonance
1	14	40	0.11	13	1100	0.1	550	4.80E+04
3	14	40	0.11	13	1100	0.1	500	*
4	14	40	0.11	13	1100	0.1	550	2.64E+05
5	14	40	0.11	13	1100	0.1	500	5.96E+04
6	14	40	0.11	13	1100	0.1	550	5.40E+05
7	14	40	0.11	13	1100	0.1	500	4.95E+05
8	14	40	0.11	13	1100	0.1	550	6.02E+05
1	15	40	0.12	7	800	0.2	500	1.00E+08
3	15	40	0.12	7	800	0.2	550	9.59E+04
4	15	40	0.12	7	800	0.2	500	9.96E+07
5	15	40	0.12	7	800	0.2	550	2.25E+07
6	15	40	0.12	7	800	0.2	500	9.96E+07
7	15	40	0.12	7	800	0.2	550	1.37E+05
8	15	40	0.12	7	800	0.2	500	1.00E+08
1	16	40	0.13	0	800	0.2	550	2.40E+05
3	16	40	0.13	0	800	0.2	500	9.96E+07
4	16	40	0.13	0	800	0.2	550	2.25E+05
5	16	40	0.13	0	800	0.2	500	1.00E+08
6	16	40	0.13	0	800	0.2	550	1.53E+05
7	16	40	0.13	0	800	0.2	500	9.96E+07

Table 27. (cont'd)

8	16	40	0.13	0	800	0.2	550	1.08E+05
1	17	30	0.1	0	800	0.1	550	2.94E+05
3	17	30	0.1	0	800	0.1	500	6.58E+07
4	17	30	0.1	0	800	0.1	550	4.28E+05
5	17	30	0.1	0	800	0.1	500	3.21E+07
6	17	30	0.1	0	800	0.1	550	4.72E+05
7	17	30	0.1	0	800	0.1	500	9.96E+07
8	17	30	0.1	0	800	0.1	550	9.47E+05
1	18	30	0.11	7	800	0.1	500	9.95E+07
3	18	30	0.11	7	800	0.1	550	1.63E+05
4	18	30	0.11	7	800	0.1	500	9.95E+07
5	18	30	0.11	7	800	0.1	550	6.72E+05
6	18	30	0.11	7	800	0.1	500	9.96E+07
7	18	30	0.11	7	800	0.1	550	6.27E+05
8	18	30	0.11	7	800	0.1	500	1.00E+08
1	19	30	0.12	13	1100	0.2	550	1.93E+05
3	19	30	0.12	13	1100	0.2	500	*
4	19	30	0.12	13	1100	0.2	550	7.62E+04
5	19	30	0.12	13	1100	0.2	500	642668
6	19	30	0.12	13	1100	0.2	550	No Resonance
7	19	30	0.12	13	1100	0.2	500	9.09E+05
8	19	30	0.12	13	1100	0.2	550	2.12E+05
1	20	30	0.13	20	1100	0.2	500	7.06E+05
3	20	30	0.13	20	1100	0.2	550	No Resonance
4	20	30	0.13	20	1100	0.2	500	3.87E+04
5	20	30	0.13	20	1100	0.2	550	8.72E+04
6	20	30	0.13	20	1100	0.2	500	*
7	20	30	0.13	20	1100	0.2	550	No Resonance
8	20	30	0.13	20	1100	0.2	500	4.83E+05
1	21	33	0.1	7	1100	0.2	550	5.44E+04
3	21	33	0.1	7	1100	0.2	500	2.36E+06
4	21	33	0.1	7	1100	0.2	550	1.71E+04
5	21	33	0.1	7	1100	0.2	500	6.18E+05
6	21	33	0.1	7	1100	0.2	550	1.92E+05
7	21	33	0.1	7	1100	0.2	500	9.43E+05
8	21	33	0.1	7	1100	0.2	550	*
1	22	33	0.11	0	1100	0.2	500	6.36E+05

Table 27. (cont'd)

3	22	33	0.11	0	1100	0.2	550	1.03E+06
4	22	33	0.11	0	1100	0.2	500	1.89E+06
5	22	33	0.11	0	1100	0.2	550	2.39E+04
6	22	33	0.11	0	1100	0.2	500	2.03E+06
7	22	33	0.11	0	1100	0.2	550	2.92E+04
8	22	33	0.11	0	1100	0.2	500	3.09E+05
1	23	33	0.12	20	800	0.1	550	4.30E+06
3	23	33	0.12	20	800	0.1	500	9.96E+07
4	23	33	0.12	20	800	0.1	550	9.87E+06
5	23	33	0.12	20	800	0.1	500	1.00E+08
6	23	33	0.12	20	800	0.1	550	1.02E+07
7	23	33	0.12	20	800	0.1	500	1.00E+08
8	23	33	0.12	20	800	0.1	550	6.84E+06
1	24	33	0.13	13	800	0.1	500	5.38E+05
3	24	33	0.13	13	800	0.1	550	6.92E+06
4	24	33	0.13	13	800	0.1	500	1.00E+08
5	24	33	0.13	13	800	0.1	550	8.97E+03
6	24	33	0.13	13	800	0.1	500	2.59E+07
7	24	33	0.13	13	800	0.1	550	1.26E+06
8	24	33	0.13	13	800	0.1	500	4.44E+06
1	25	37	0.1	13	800	0.2	550	1.70E+05
3	25	37	0.1	13	800	0.2	500	1.00E+08
4	25	37	0.1	13	800	0.2	550	4.56E+05
5	25	37	0.1	13	800	0.2	500	*
6	25	37	0.1	13	800	0.2	550	1.89E+05
7	25	37	0.1	13	800	0.2	500	9.95E+07
8	25	37	0.1	13	800	0.2	550	1.93E+05
1	26	37	0.11	20	800	0.2	500	1.00E+08
3	26	37	0.11	20	800	0.2	550	5.31E+05
4	26	37	0.11	20	800	0.2	500	7.85E+06
5	26	37	0.11	20	800	0.2	550	1.49E+05
6	26	37	0.11	20	800	0.2	500	1.54E+06
7	26	37	0.11	20	800	0.2	550	4.59E+06
8	26	37	0.11	20	800	0.2	500	9.96E+07
1	27	37	0.12	0	1100	0.1	550	*
3	27	37	0.12	0	1100	0.1	500	1.85E+05
4	27	37	0.12	0	1100	0.1	550	3.89E+04
5	27	37	0.12	0	1100	0.1	500	1.21E+05
6	27	37	0.12	0	1100	0.1	550	1.28E+05

Table 27. (cont'd)

7	27	37	0.12	0	1100	0.1	500	6.6E+05
8	27	37	0.12	0	1100	0.1	550	6.99E+04
1	28	37	0.13	7	1100	0.1	500	1.10E+03
3	28	37	0.13	7	1100	0.1	550	5.15E+05
4	28	37	0.13	7	1100	0.1	500	9.38E+05
5	28	37	0.13	7	1100	0.1	550	No Resonance
6	28	37	0.13	7	1100	0.1	500	4.16E+05
7	28	37	0.13	7	1100	0.1	550	1.16E+05
8	28	37	0.13	7	1100	0.1	500	1.57E+06
1	29	40	0.1	20	1100	0.1	550	9.55E+05
3	29	40	0.1	20	1100	0.1	500	1.3E+05
4	29	40	0.1	20	1100	0.1	550	40764
5	29	40	0.1	20	1100	0.1	500	1.31E+06
6	29	40	0.1	20	1100	0.1	550	5.50E+05
7	29	40	0.1	20	1100	0.1	500	6.18E+05
8	29	40	0.1	20	1100	0.1	550	*
1	30	40	0.11	13	1100	0.1	500	1.31E+06
3	30	40	0.11	13	1100	0.1	550	9336
4	30	40	0.11	13	1100	0.1	500	1.03E+06
5	30	40	0.11	13	1100	0.1	550	16367
6	30	40	0.11	13	1100	0.1	500	1.37E+06
7	30	40	0.11	13	1100	0.1	550	5.31E+04
8	30	40	0.11	13	1100	0.1	500	1.24E+06
1	31	40	0.12	7	800	0.2	550	1.07E+05
3	31	40	0.12	7	800	0.2	500	1.00E+08
4	31	40	0.12	7	800	0.2	550	2.32E+05
5	31	40	0.12	7	800	0.2	500	1.00E+08
6	31	40	0.12	7	800	0.2	550	2.54E+06
7	31	40	0.12	7	800	0.2	500	9.96E+07
8	31	40	0.12	7	800	0.2	550	2.61E+06
1	32	40	0.13	0	800	0.2	500	9.96E+07
3	32	40	0.13	0	800	0.2	550	1.27E+07
4	32	40	0.13	0	800	0.2	500	1.00E+08
5	32	40	0.13	0	800	0.2	550	1.73E+05
6	32	40	0.13	0	800	0.2	500	1.00E+08
7	32	40	0.13	0	800	0.2	550	1.89E+05
8	32	40	0.13	0	800	0.2	500	2.62E+06

APPENDIX B: MATLAB CODE

Script for calculating the optimal mixing ratios of a 2 powder size mixture using Stovall et al.'s linear packing model for grain mixtures.

```
close all
clear all

VolVal=0:.001:1;

X=0:.001:1;
Y=0:.001:1;
Z=0:.001:1;

Beta=[0.629043 0.6327367];    % Packing Density
Gammai=[];
Sum1=0;
Sum2=0;
d=[97 34]*10^(-6);       % Diamater microns
dsize=size(d);
n=dsize(1,2);
Sol=zeros(1*10^8,4);
s=1;
for Xx=1:size(X,2)
    Xx
    for Yy=1:size(Y,2)
%         Zz=abs(1-X(Xx)-Y(Yy));
        Zz=0;
        sumXYZ=X(Xx)+Y(Yy)+Zz;
          if sumXYZ==1
             y=[X(Xx) Y(Yy) Zz];       % Volumetric Fraction
             Gammai=zeros(1,n);
            for i=1:n
                    for j=1:(i-1)
                        b=1-(1-d(i)/d(j))^(1.5);
                        Sum1=Sum1+(1-Beta(i)+b*Beta(i)*(1-
Beta(j)^(-1)))*y(j);
                        clear b
                    end
                    for j=(i+1):n
                        a=(1-(1-d(j)/d(i))^1.02)^0.5;
                        Sum2=Sum2+(1-a*Beta(i)/Beta(j))*y(j);
                        clear a
                    end

                    Gammai(i)=Beta(i)/(1-Sum1-Sum2)*100;
```

```
                    Sum1=0;
                    Sum2=0;
            end
            GammaMin=min(Gammai,[],2);
            temp=[y GammaMin];
            Sol(s,:)=temp;
            s=s+1;
          end
    end
end
ZeroRows=find(all(Sol==0,2));   % Finds row numbers for any zero
rows
Sol(ZeroRows,:)=[];             % Removes all the zero rows
MaxPack=max(Sol(:,4));
[val,index]=max(Sol(:,4));      % Finds the largest packing
density
Sol(index,:)                    % Displays the largest packing
density and concentrations in the window
plot(Sol(:,1),Sol(:,4))
title('Packing Density vs Concentration');
ylabel('Packed Powder Density (%)')
xlabel('Concentration of Larger Powder')
```

Script for automatic scale calculation and calculation of pore volume fraction of cross section images.

```
clear all
close all

% Adjustable Values
ScaleBarCropPercent=.1;     % Percent of bottom of image removed
to get rid of scale bar
AdaptiveThreshValue=0.4;   % Value for removing the background
shading of image
ScaleMicron=250;    % Micron label on rthe sacale bart
ScalePixel=24;     % Length of scale bar in pixels, can measure
with something like paint
GrayConnectedThresh=1;  % Intensity threshhold for isolating
scalebar.

% Flags (used to determine which parts of codwe shoulsd be run)
AutoScaleBar=1;     % Automatic scale bar detection flag.  1=Use
auto detecrt 0=Use input values
```

```
AdaptiveThreshFlag=1; % This is for testing the program with
binary images since they do not need the threshold. 1= Use
Adaptave thresh 0= Do not use adaptave thresh
ExcelOutputFlag=1;  % Flag for asking if you want to save the
data as an excel file at the end. 1= Yes 0= No

%%%%%%%%%%%%%%%% INPUT FILE PATH
HERE%%%%%%%%%%%%%%%%%%%%%%%%%%%%
CPath = 'D:\19-09-13_Thin Wall Porosity\5';
addpath( CPath )
%%%%%%%%%%%%%%%% INPUT FILE PATH
HERE%%%%%%%%%%%%%%%%%%%%%%%%%%%%

d = dir(CPath);              % For selecting the file you want
to read
fn = {d.name};
[indx,tf] = listdlg('PromptString','Select a file:',...
                            'SelectionMode','single',...
                            'ListString',fn);

ImageName = strcat( CPath, filesep, d(indx,1).name);

ImageNameShort=split(d(indx,1).name,'.'); % Gives just the name
of the image, none of the path or file type.

ImOOG = imread( ImageName, 'tif' );
isu8=isa(ImOOG,'uint8');    % Checks to see if the image is
already in unit 8
if isu8 ~= 1
    ImOG = uint8( ImOOG(:,:,1:3) );  % converting the image to
double precision
    Im=rgb2gray(ImOG);
else
    if size(ImOOG,3)==4
        ImOG=ImOOG(:,:,1:3);
        Im=rgb2gray(ImOG);
    elseif size(ImOOG,3)==3
        ImOG=ImOOG(:,:,1:3);
        Im=rgb2gray(ImOG);
    else
        ImOG=ImOOG;
        Im=ImOG;
    end
end

% Im=Im(100:end,100:1500);
```

```
figure
imshow(Im)

RerunRect=0;
RerunPoint=0;
if AutoScaleBar==1
    ScaleMicron = inputdlg('Input Scalebar Length (micron)');
    ScaleMicron=str2double(ScaleMicron);
%     ImScale=Im==255;
    while RerunRect==0  % Loop for selecting the genereal area
of the scale bar for identifying the scale bar
        title('Draw a square around the scale bar')
        rect=getrect;   % Returens upper lefdt corner column,
row, width, height
        if (rect(1)+rect(3))>=size(Im,2)   % Ensures the wundow
is not larger than to image
            rect(3)=size(Im,2)-rect(1);
        end
        if (rect(2)+rect(4))>=size(Im,1)
            rect(4)=size(Im,1)-rect(2);
        end


Imrect=Im(rect(2):(rect(2)+rect(4)),rect(1):(rect(1)+rect(3)));
        figure
        imshow(Imrect);

        RerunRect=choosedialogRect;

        if RerunRect==0
            close
            clear Imrect
        end


    end
    while RerunPoint==0  % Loop for selecting the genereal area
of the scale bar for identifying the scale bar
        title('Right click inside scalebar')
        [x,y]=getpts;
        point(:,1)=x;
        point(:,2)=y;
        if size(point,1)>1
            f = warndlg(' Select only 1 Point');
            uiwait(f);
            clear point
            continue
```

```
        end
        if point(1,1)<0 || point(1,1)>rect(3)
            f = warndlg(' Select point inside the image');
            uiwait(f);
            clear point
            continue
        end
        if point(1,2)<0 || point(1,2)>rect(4)
            f = warndlg(' Select point inside the image');
            uiwait(f);
            clear point
            continue
        end

        point=floor(point);

SB=grayconnected(Imrect,point(1,2),point(1,1),GrayConnectedThres
h); % Returns logical for all values equal to the intensity of
the scalebar
%         SBI=~SB;    % Inverts the logical matrix

        figure
        imshow(SB);

        SBLength=sum(SB,2); % sums number of 1s giving length
ofn scalebar
        [M,I]=max(SBLength);  % finds row with maXIMUM values
        numrows=sum(SBLength==M,1); % Finds number of rows with
that value. should equal for the scalebar
        centerSB=I+floor(numrows/2);% calculates center ofd
scalebar but not very robust
        [R C]=find(SB(I,:),1);  % finds fdirst non zero column
in center row for drawing line. not robust, if not clean edge
this wont work
        line([C C+M],[centerSB centerSB]);

        RerunPoint=choosedialogPoints;
        if RerunPoint==0
            close
        else
            close
            close
            MicronPerPixel=ScaleMicron/M;
        end

    end
```

```
else
    MicronPerPixel=ScaleMicron/ScalePixel;
end

crop=size(Im,1)*ScaleBarCropPercent;
Im=Im([1:size(Im,1)-crop],:,:);

if AdaptiveThreshFlag==1    % Used to bypass the adaptive thresh
for testing with binary images.

[J,AdaptiveThreshValueNew]=AdaptiveThresh(Im,AdaptiveThreshValue
);
else
    J=Im;
end

figure
[B,L,n,A] = bwboundaries(J,'noholes');
imshow(label2rgb(L, @parula, [.5 .5 .5]))
hold on
for k = 1:length(B)
   boundary = B{k};
   plot(boundary(:,2), boundary(:,1), 'w', 'LineWidth', 2)
end

i=1;
area=zeros(size(B,1),size(B,2));
for i=1:size(B,1)
    area(i,1)=polyarea(B{i,1}(:,1), B{i,1}(:,2));
end

area=area*(MicronPerPixel)^2;   % Changes areas from pixel to
microns

RerunAreaThresh=0;
while RerunAreaThresh==0
    areathresh = inputdlg('Minimum Area (micron)');
    areathresh=str2double(areathresh);

    toosmall=area<areathresh;

    i=1;
    j=1;
    for i=1:size(B,1)
        if toosmall(i)~=1
            NewB{j,:}=B{i,1};
            Newarea(j,1)=area(i,1);
```

```
            j=j+1;
        end
    end

PercentPore=sum(Newarea)/(size(J,1)*size(J,2)*(MicronPerPixel^2)
)*100;

%     Data string for Dialog box
    Data(1)=mean(Newarea);              % 1 Average area of
thresholded pore
    Data(2)=size(Newarea,1);            % 2 Number of pixels in
thresholded pore
    Data(3)=max(Newarea);               % 3 Maximum pore Area
    Data(4)=min(Newarea);               % 4 Minimum pore Area
    SpeckDia=((Newarea./pi()).^.5)*2;   % Calculates Diamater
    Data(5)=mean(SpeckDia);             % 5 Average pore
Diamater
    Data(6)=max(SpeckDia);              % 6 Maximum pore
Diamater
    Data(7)=min(SpeckDia);              % 7 Minimum pore
Diamater
    Data(8)=PercentPore;                % 8 Percent of the
thresholded image that is porosity

    figure
    ImFin=imshow(label2rgb(L, @parula, [.5 .5 .5]));
    hold on
    for k = 1:length(NewB)
       boundary = NewB{k};
       plot(boundary(:,2), boundary(:,1), 'w', 'LineWidth', 2)
    end

%     RerunAreaThresh = choosedialog(Data);   % Runs the dialog
box function
    RerunAreaThresh = choosedialog2(Data);   % Runs the dialog
box function
    if RerunAreaThresh==0
        close
        clear Data Newarea NewB
    end
end

  for i = 1:length(NewB)

pore=J(min(NewB{i,1}(:,1)):max(NewB{i,1}(:,1)),min(NewB{i,1}(:,2
)):max(NewB{i,1}(:,2))); % Gets the part of the matrix that has
the pore in it
```

```
        Rowmin=min(NewB{i,1}(:,1));
        Colmin=min(NewB{i,1}(:,2));
        COM(i,:)=CenterOfMass(pore,Rowmin,Colmin,NewB{i});
        Feret(i,1)=max(NewB{i,1}(:,1))-min(NewB{i,1}(:,1));
        Feret(i,2)=max(NewB{i,1}(:,2))-min(NewB{i,1}(:,2));
  end

Feret_Micron=Feret*MicronPerPixel;

Centroids=zeros(size(J,1),size(J,2));
linearInd = sub2ind(size(Centroids),COM(:,1),COM(:,2));
Centroids(linearInd)=1;

red=cat(3, ones(size(J)),zeros(size(J)), zeros(size(J)));
hold on
Color=imshow(red);
hold off
set(Color, 'AlphaData', Centroids)

Image = getframe(gcf);
SaveString=strcat(ImageNameShort{1,1},'_Final','.tiff');
imwrite(Image.cdata, SaveString);


figure
[N,edges] = histcounts(Newarea);
histogram(Newarea,edges)
title('Histogram of Pore areas');
xlabel('Pore Area (Micron)');
ylabel('Counts');

TextOutput=RunSettingsText(ImageNameShort,ScaleBarCropPercent,Sc
aleMicron,M,GrayConnectedThresh,AutoScaleBar,MicronPerPixel,Adap
tiveThreshValueNew,areathresh);

if ExcelOutputFlag==1
    T=ExcelOutput(Newarea,Feret,COM,Data,TextOutput);
end

f = msgbox('Finished');

% RerunAreaThresh = choosedialog2(Data);   % Runs the dialog box
function

function
[J,AdaptiveThreshValue]=AdaptiveThresh(Im,AdaptiveThreshValue)
    RerunThresh=0;
```

```
    RunCounter=0;   % Counter to see if the loop has run once
    while RerunThresh==0
        if RunCounter==1
            AdaptiveThreshValueNew = inputdlg('Adaptive
Threshold');

AdaptiveThreshValueNew=str2double(AdaptiveThreshValueNew);
            if size(AdaptiveThreshValueNew,1)~=0
                AdaptiveThreshValue=AdaptiveThreshValueNew;
            end
        end
        T =
adaptthresh(Im,AdaptiveThreshValue,'ForegroundPolarity','dark');
        BW = imbinarize(Im,T);
        temp=ones(size(BW,1),size(BW,2));
        temp(BW)=0;

        figure
        Imtemp=Im;
        Imtemp(temp>0)=255;
        imshow(Imtemp)
    %     imshow(BW)

        if RunCounter==0
            RunCounter=1;
        end

        RerunThresh = choosedialog1;
        if RerunThresh==0
            close
            clear T BW temp
        end
    end

    figure
    imshow(temp)
%
%     % SE = strel('disk',5);
%     % J = imclose(temp,SE);
% %     J = imfill(temp,8);
%     % imfill
%     se = strel('disk',3);
%     Im_CL=imclose(temp,se);
%     J=imclose(temp,se);
    se = strel('disk',5);
    ImGL_di = imdilate(temp,se);
```

```
    ImGL_dir =
imreconstruct(imcomplement(ImGL_di),imcomplement(temp));
    ImGL_direr = imerode(ImGL_dir,se);    % reconstruction by
closing
    ImGL_direrr = imreconstruct(ImGL_direr,ImGL_dir);   %
reconstruction by opening
    ImGL_direrr=imcomplement(ImGL_direrr);

    se=strel('disk',2);
    J=imclose(ImGL_direrr,se);

    figure
    imshow(J)

    Closed=abs(temp-J);

    figure
    imshow(Closed);

    figure
    Im(J>0)=255;
    imshow(Im)
end
function COM=CenterOfMass(pore,Rowmin,Colmin,outline)
    [R C]=size(pore);
    Rowind=1:1:R;
    Colind=1:1:C;
    % What I am trying to do here is to get the x and y
coridinates of all
    % the points inside the pore matrix so that I can get all
the pixels
    % inside the current boundry in case other pixels make it
inside the
    % window. Neec to keep the values from big matrix associated
with small
    % window so that inpolygon works. Once I find the center can
add the
    % indicis to the top left corner and associate a center
point with a
    % given area.
    Row=zeros(1,length(pore(:)));
    Col=zeros(1,length(pore(:)));
    for i=1:length(pore(:)) % Now the matrix is a column vector
        [Row(i), Col(i)]=ind2sub(size(pore),i);
    end
    Row=Row+Rowmin-1;   % Converts the rows from inside the pore
matrix to the real index from the overall image
```

```
    Col=Col+Colmin-1;
    [in, on]=inpolygon(Row,Col,outline(:,1),outline(:,2));   %
In also includeds the on
    CurrentPoreOnly=vec2mat(in,R);
    CurrentPoreOnly=CurrentPoreOnly';   % Has to be done becasue
of how the vec2mat or the in works.

COMrow=floor(sum((sum(CurrentPoreOnly,2).*Rowind'))/sum((sum(Cur
rentPoreOnly,2)))); % Sums the rows, multiplys each row by the
indicy aka distance from top to row, then divide by the sum of
areas.

COMcol=floor(sum((sum(CurrentPoreOnly,1).*Colind))/sum((sum(Curr
entPoreOnly,1))));
    COMrow=COMrow+Rowmin;
    COMcol=COMcol+Colmin;
    COM=[COMrow COMcol];
end
function choice = choosedialogRect
    d = dialog('Position',[100 400 220 100],'Name','Rectangle
Select');
    txt = uicontrol('Parent',d,...
           'Style','text',...
           'Position',[10 40 210 40],...
           'String','Redo Rectangle?');

    btn = uicontrol('Parent',d,...
           'Position',[30 20 70 25],...
           'String','Yes',...
           'Callback',@pushbutton1_Callback);

    btn = uicontrol('Parent',d,...
           'Position',[120 20 70 25],...
           'String','No',...
           'Callback',@pushbutton2_Callback);

    % Wait for d to close before running to completion
    uiwait(d);

      function pushbutton1_Callback(hObject, eventdata, handles)
        % hObject    handle to pushbutton1 (see GCBO)
        % eventdata  reserved - to be defined in a future
version of MATLAB
        % handles    structure with handles and user data (see
GUIDATA)
        choice=0;
        close(gcf);
```

```
      end

      function pushbutton2_Callback(hObject, eventdata, handles)
        % hObject    handle to pushbutton1 (see GCBO)
        % eventdata  reserved - to be defined in a future
version of MATLAB
        % handles    structure with handles and user data (see
GUIDATA)
        choice=1;
        close(gcf);
      end
end
function choice = choosedialogPoints
    d = dialog('Position',[100 400 220 100],'Name','Point
Select');
    txt = uicontrol('Parent',d,...
           'Style','text',...
           'Position',[10 40 210 40],...
           'String','Reselect point?');

    btn = uicontrol('Parent',d,...
           'Position',[30 20 70 25],...
           'String','Yes',...
           'Callback',@pushbutton1_Callback);

    btn = uicontrol('Parent',d,...
           'Position',[120 20 70 25],...
           'String','No',...
           'Callback',@pushbutton2_Callback);

    % Wait for d to close before running to completion
    uiwait(d);

      function pushbutton1_Callback(hObject, eventdata, handles)
        % hObject    handle to pushbutton1 (see GCBO)
        % eventdata  reserved - to be defined in a future
version of MATLAB
        % handles    structure with handles and user data (see
GUIDATA)
        choice=0;
        close(gcf);
      end

      function pushbutton2_Callback(hObject, eventdata, handles)
        % hObject    handle to pushbutton1 (see GCBO)
        % eventdata  reserved - to be defined in a future
version of MATLAB
```

```
        % handles    structure with handles and user data (see
GUIDATA)
        choice=1;
        close(gcf);
      end
end
function choice = choosedialog1
    d = dialog('Position',[100 400 220 100],'Name','Pore Data');
    txt = uicontrol('Parent',d,...
           'Style','text',...
           'Position',[10 40 210 40],...
           'String','Rerun with new Adaptive Threshold?');

    btn = uicontrol('Parent',d,...
           'Position',[30 20 70 25],...
           'String','Yes',...
           'Callback',@pushbutton1_Callback);

    btn = uicontrol('Parent',d,...
           'Position',[120 20 70 25],...
           'String','No',...
           'Callback',@pushbutton2_Callback);

    % Wait for d to close before running to completion
    uiwait(d);

      function pushbutton1_Callback(hObject, eventdata, handles)
        % hObject    handle to pushbutton1 (see GCBO)
        % eventdata  reserved - to be defined in a future
version of MATLAB
        % handles    structure with handles and user data (see
GUIDATA)
        choice=0;
        close(gcf);
      end

      function pushbutton2_Callback(hObject, eventdata, handles)
        % hObject    handle to pushbutton1 (see GCBO)
        % eventdata  reserved - to be defined in a future
version of MATLAB
        % handles    structure with handles and user data (see
GUIDATA)
        choice=1;
        close(gcf);
      end
end
function choice = choosedialog2(Data)
```

```
    % What each value of the Data vector are equal to:
        % 1 Average area of thresholded speckles
        % 2 Number of pixels in thresholded speckles
        % 3 Maximum speckle Area
        % 4 Minimum speckle Area
        % 5 Average Speckle Diamater
        % 6 Maximum speckle Diamater
        % 7 Minimum speckle Diamater

    d = dialog('Position',[100 300 220 500],'Name','Pore Data');
    txt = uicontrol('Parent',d,...
           'Style','text',...
           'Position',[10 450 210 40],...
           'String',strcat('Average Area:',{'
'},num2str(Data(1))));

    txt = uicontrol('Parent',d,...
           'Style','text',...
           'Position',[10 400 210 40],...
           'String',strcat('Number of Pores:',{'
'},num2str(Data(2))));

    txt = uicontrol('Parent',d,...
           'Style','text',...
           'Position',[10 350 210 40],...
           'String',strcat('Maximum Pore Area:',{'
'},num2str(Data(3))));

    txt = uicontrol('Parent',d,...
           'Style','text',...
           'Position',[10 300 210 40],...
           'String',strcat('Minimum Speckle Area:',{'
'},num2str(Data(4))));

    txt = uicontrol('Parent',d,...
           'Style','text',...
           'Position',[10 250 210 40],...
           'String',strcat('Average Speckle Diamater:',{'
'},num2str(Data(5))));

    txt = uicontrol('Parent',d,...
           'Style','text',...
           'Position',[10 200 210 40],...
           'String',strcat('Maximum Speckle Diamater:',{'
'},num2str(Data(6))));

    txt = uicontrol('Parent',d,...
```

```
           'Style','text',...
           'Position',[10 150 210 40],...
           'String',strcat('Minimum Speckle Diamater:',{'
'},num2str(Data(7))));

    txt = uicontrol('Parent',d,...
           'Style','text',...
           'Position',[10 100 210 40],...
           'String',strcat('Percent Porostity:',{'
'},num2str(Data(8))));

    txt = uicontrol('Parent',d,...
           'Style','text',...
           'Position',[10 40 210 40],...
           'String','Rerun with new Area Threshold?');

    btn = uicontrol('Parent',d,...
           'Position',[30 20 70 25],...
           'String','Yes',...
           'Callback',@pushbutton1_Callback);

    btn = uicontrol('Parent',d,...
           'Position',[120 20 70 25],...
           'String','No',...
           'Callback',@pushbutton2_Callback);

    % Wait for d to close before running to completion
    uiwait(d);

      function pushbutton1_Callback(hObject, eventdata, handles)
        % hObject    handle to pushbutton1 (see GCBO)
        % eventdata  reserved - to be defined in a future
version of MATLAB
        % handles    structure with handles and user data (see
GUIDATA)
        choice=0;
        close(gcf);
      end

      function pushbutton2_Callback(hObject, eventdata, handles)
        % hObject    handle to pushbutton1 (see GCBO)
        % eventdata  reserved - to be defined in a future
version of MATLAB
        % handles    structure with handles and user data (see
GUIDATA)
        choice=1;
        close(gcf);
```

```
      end
end
function T=ExcelOutput(Newarea,Feret,COM,Data,TextOutput)

Filename=inputdlg('Input File Name');
Filename=strcat(Filename,'.xlsx');
Filename=char(Filename);

Average_Area=Data(1);
Number_of_Pores=Data(2);
Max_Pore_Pore_Area=Data(3);
Min_Pore_Pore_Area=Data(4);
Average_Pore_Diamater=Data(5);
Max_Pore_Diamater=Data(6);
Min_Pore_Diamater=Data(7);
Percentage_Porosity=Data(8);

Pore_Area_Micron=Newarea;
Feret_Row_Micron=Feret(:,1);
Feret_Col_Micron=Feret(:,2);
Center_Of_Mass_Row_Pix=COM(:,1);
Center_Of_Mass_Col_Pix=COM(:,2);

T=table(Pore_Area_Micron,Feret_Row_Micron,Feret_Col_Micron,Cente
r_Of_Mass_Row_Pix,Center_Of_Mass_Col_Pix);
writetable(T,Filename,'Sheet',1);

xlswrite(Filename,{'Average_Area'},'Sheet1','F3')
xlswrite(Filename,Average_Area,'Sheet1','F4')
xlswrite(Filename,{'Number_of_Pores'},'Sheet1','G3');
xlswrite(Filename,Number_of_Pores,'Sheet1','G4');
xlswrite(Filename,{'Max_Pore_Pore_Area'},'Sheet1','H3');
xlswrite(Filename,Max_Pore_Pore_Area,'Sheet1','H4');
xlswrite(Filename,{'Min_Pore_Pore_Area'},'Sheet1','I3');
xlswrite(Filename,Min_Pore_Pore_Area,'Sheet1','I4');
xlswrite(Filename,{'Average_Pore_Diamater'},'Sheet1','J3');
xlswrite(Filename,Average_Pore_Diamater,'Sheet1','J4');
xlswrite(Filename,{'Max_Pore_Diamater'},'Sheet1','K3');
xlswrite(Filename,Max_Pore_Diamater,'Sheet1','K4');
xlswrite(Filename,{'Min_Pore_Diamater'},'Sheet1','L3');
xlswrite(Filename,Min_Pore_Diamater,'Sheet1','L4');
xlswrite(Filename,{'Percentage_Porosity'},'Sheet1','M3');
xlswrite(Filename,Percentage_Porosity,'Sheet1','M4');

xlswrite(Filename,{TextOutput{1,1}},'Sheet1','F1')
xlswrite(Filename,{TextOutput{1,2}},'Sheet1','F2')
xlswrite(Filename,{TextOutput{2,1}},'Sheet1','G1')
```

```
xlswrite(Filename,{TextOutput{2,2}},'Sheet1','G2')
xlswrite(Filename,{TextOutput{3,1}},'Sheet1','H1')
xlswrite(Filename,{TextOutput{3,2}},'Sheet1','H2')
xlswrite(Filename,{TextOutput{4,1}},'Sheet1','I1')
xlswrite(Filename,{TextOutput{4,2}},'Sheet1','I2')
xlswrite(Filename,{TextOutput{5,1}},'Sheet1','J1')
xlswrite(Filename,{TextOutput{5,2}},'Sheet1','J2')
xlswrite(Filename,{TextOutput{6,1}},'Sheet1','K1')
xlswrite(Filename,{TextOutput{6,2}},'Sheet1','K2')
xlswrite(Filename,{TextOutput{7,1}},'Sheet1','L1')
xlswrite(Filename,{TextOutput{7,2}},'Sheet1','L2')
xlswrite(Filename,{TextOutput{8,1}},'Sheet1','M1')
xlswrite(Filename,{TextOutput{8,2}},'Sheet1','M2')
xlswrite(Filename,{TextOutput{9,1}},'Sheet1','N1')
xlswrite(Filename,{TextOutput{9,2}},'Sheet1','N2')

% FinalData=[Newarea,Feret,COM];
% writematrix(FinalData,Filename)
end
function
TextOutput=RunSettingsText(ImageNameShort,ScaleBarCropPercent,Sc
aleMicron,ScalePixel,GrayConnectedThresh,AutoScaleBar,MicronPerP
ixel,AdaptiveThreshValueNew,areathresh)

TextOutput{1,1}='File Name';
TextOutput{2,1}='ScaleBarCropPercent';
TextOutput{3,1}='ScaleMicron';
TextOutput{4,1}='ScalePixel';
TextOutput{5,1}='GrayConnectedThresh';
TextOutput{6,1}='AutoScaleBar';
TextOutput{7,1}='MicronPerPixel';
TextOutput{8,1}='AdaptiveThreshValueNew';
TextOutput{9,1}='Areathresh';

TextOutput{1,2}=ImageNameShort{1};
TextOutput{2,2}=ScaleBarCropPercent;
TextOutput{3,2}=ScaleMicron;
TextOutput{4,2}=ScalePixel;
TextOutput{5,2}=GrayConnectedThresh;
TextOutput{6,2}=AutoScaleBar;
TextOutput{7,2}=MicronPerPixel;
TextOutput{8,2}=AdaptiveThreshValueNew;
TextOutput{9,2}=areathresh;
end
function [ H, H_norm, H_cumu ] = Hists( Im )
% this function determines the histograms of image Im
```

```
if strcmp( class( Im ) , 'uint8' ) == 1
    Bins = 2^8;  % number of Bins (256 for uint8)
    Mn = uint16( min( Im(:) ) );
    Mx = uint16( max( Im(:) ) );

elseif strcmp( class( Im ) , 'uint16' ) == 1
    Bins = 2^16;  % number of Bins (65536 for uint16)
    Mn = uint32( min( Im(:) ) );
    Mx = uint32( max( Im(:) ) );

end

Edges = Mn : Mx + 1;  % defining bin edges based on the minimum
and maximum intensity values in the image
                      % this is important when the image does
not span the whole dynamic range

Im = double( Im );  % converting image to double precision

H = histcounts( Im(:), Edges );   % generating the unnormalized
histogram based on
                                  % the vector of Edges

%zero-padding the histogram
H = [ zeros( 1, min( Im(:) ) ), H, zeros( 1, ( Bins - 1 ) - max(
Im(:) ) ) ];

H_norm = H / sum( H ); % normalizing the histogram
H_cumu = cumsum( H_norm ); %determining the cumulative frequency
histogram

End
```

Script for calculating the average α-lath thickness using combination of image processing and manual line selection.

```
close all
clear all
% Adjustable Values
LeftRightCropPercent=.13;    % Percent of left or right of image to be
removed
ScaleBarCropPercent=0;     % Percent of bottom of image removed to get
rid of scale bar
```

```
AdaptiveThreshValue=100;   % Value for removing the background shading
of image
GrayConnectedThresh=1;  % Intensity threshhold for isolating scalebar.
FigureNum=0;

% Flags (used to determine which parts of codwe shoulsd be run)
AutoScaleBar=0;     % Automatic scale bar detection flag.  1=Use auto
detecrt 0=Use input values
AdaptiveThreshFlag=1; % This is for testing the program with binary
images since they do not need the threshold. 1= Use Adaptave thresh 0=
Do not use adaptave thresh
ExcelOutputFlag=0;  % Flag for asking if you want to save the data as
an excel file at the end. 1= Yes 0= No
LeftFlag=0;         % Crops out left side of image when analysing left
end of wall
RightFlag=0;
FinalImageSaveFlag=1; % Flag for final image with the red lines
ManualFileSelect=0; % 1- Use manual file selection 0- Process all tif
files in folder
RerunThreshFlag=0;      % 0- Would like to be able to specify other
Thresh 1- Do not want to specify just use preset
ShowFigureFlag=0;     % 0- Dont show figures 1- Show figures
%%%%%%%%%%%%%%%%%% INPUT FILE PATH HERE%%%%%%%%%%%%%%%%%%%%%%%%%%%%
% CPath = 'D:\Eaton Etched\4_11_22';
% addpath( CPath )
%%%%%%%%%%%%%%%%%% INPUT FILE PATH HERE%%%%%%%%%%%%%%%%%%%%%%%%%%%%

% d = dir(CPath);              % For selecting the file you want to
read


[file,path] = uigetfile('*.tif');
if isequal(file,0)
   disp('User selected Cancel');
else
   disp(['User selected ', fullfile(path,file)]);
end

%% Test
if file(1:4)=='Test'
    x = [0,100;0,100;0,100;0,50];
    y = [0,100;50,50;33,66;0,102];
    BW=padarray(BW(:,:,1),[1,1]);
    ScaleUmPerPix = 1;
end
%% 1-31
```

```
if file(1:4)=='1-31'
    Cutoff = 0.63;
    x =
[860,923;2237,2232;1838,2074;187,241;1453,1377;2093,2040;1145,795;419,
328];
    y =
[1452,1317;1148,952;228,88;687,585;317,25;1655,1460;958,876;1539,1833]
;
end
%% 2-10
if file(1:4)=='2-10'
    Cutoff = 0.6;
    x =
[1985,1843;2471,2116;1527,1533;307,448;587,318;1602,1353;1223,1299;230
4,2125;1770,1702;762,520;2540,2479;69,96;171,200;];
    y =
[804,778;1370,1240;1720,1539;1692,1272;542,550;417,324;1481,1294;189,1
26;1577,1729;119,36;100,20;1807,1752;1812,1753];
end
%% 2-16
if file(1:4)=='2-16'
    Cutoff = 0.55;
    x =
[340,395;1283,1352;2206,2288;454,322;1749,1628;913,753;451,602;1614,17
82];
    y =
[346,232;537,404;480,347;1051,957;1731,1556;1086,967;832,636;958,1137]
;
end
%% 2-25
if file(1:4)=='2-25'
    Cutoff = 0.6;
    x =
[332,271;422,367;785,708;1358,1349;1931,1897;2352,2381;895,1264;1137,1
147;1501,1617;139,12];
    y =
[429,280;1593,1111;1658,1381;1067,865;623,331;744,875;644,541;1473,132
2;778,762;852,830];
end
%% 2-31
if file(1:4)=='2-31'
    Cutoff = 0.55;
    x =
[2024,2059;1664,1775;2548,2367;564,654;1012,905;1321,1115;2467,2280;84
8,720;240,22;334,483];
```

```
    y =
[343,231;1439,1307;1745,1675;1224,1102;473,447;1629,1504;1056,923;810,
748;1178,1047;1645,1502];
end
%% 2-33
if file(1:4)=='2-33'
    Cutoff = 0.5;
    x =
[1372,1307;1265,1128;1039,927;2108,1976;444,517;2393,2359;1131,1238;48
2,423;824,815;1896,1931];
    y =
[1327,1217;1714,1535;1637,1499;708,749;895,803;688,619;702,660;231,136
;808,724;1525,1322];
end
%% 3-34
if file(1:4)=='3-34'
    Cutoff = 0.55;
    x =
[722,578;196,333;1079,1026;1030,971;2538,2449;2401,2555;1294,1164;1236
,1130;636,804;2189,2248;];
    y =
[981,915;1155,1126;1292,1278;1251,1235;1731,1699;663,513;1313,1273;139
4,1350;1498,1457;372,186;];
end
%% 4-01
if file(1:4)=='4-01'
    Cutoff = 0.75;
    x =
[754,718;694,648;1004,849;795,720;574,539;1506,1266;1638,1707;1871,201
6;2168,2106;2507,2323;150,326;354,778;258,404;1389,1693;1683,1610;1509
,1674];
    y =
[835,822;843,826;705,649;721,694;850,837;1394,1243;1150,1104;1500,1345
;718,640;732,369;1694,1480;1037,879;221,37;1572,1726;367,274;847,721;]
;
end
%% 5-15
if file(1:4)=='5-15'
    Cutoff = 0.55;
    x =
[2113,2248;993,1058;495,537;482,515;507,549;232,279;236,280;2259,2273;
964,979;2328,2174;1811,1818;1375,1412;];
    y =
[465,525;1320,1101;251,188;294,250;136,74;352,251;452,378;1454,1384;15
51,1470;1140,1030;906,724;1908,1815;];
end
```

```
%% 5-33
if file(1:4)=='5-33'
    Cutoff = 0.5;
    x =
[1895,1862;1807,1801;212,214;1370,1264;2382,2313;796,791;854,845;2048,
2018;388,444;470,458;2308,2289;306,243;2398,2397;2421,2371;1841,1829;1
785,1776];
    y =
[1153,1022;1153,1070;261,204;986,1009;196,194;1537,1495;1581,1540;874,
792;1864,1842;1395,1338;714,683;927,960;844,804;1233,1226;1686,1605;16
97,1621;];
    x = [x;1731,1706;799,804;1964,1957;1603,1599;1507,1504;];
    y = [y;1541,1421;483,344;310,258;703,644;1044,980];
end
%% 5-34
if file(1:4)=='5-34'
    Cutoff = 0.5;
    x =
[1268,1444;1298,1364;1246,1321;1097,1176;1243,1296;681,755;1238,1322;1
209,1323;2219,2175;2237,2210;2514,2443;788,726;793,932;];
    y =
[1393,1251;1076,1004;1585,1534;1767,1691;1156,1114;865,931;1748,1668;1
875,1772;1646,1566;1351,1297;215,129;390,328;211,125;];
    x = [x;190,77;1497,1686;];
    y = [y;714,563;844,610;];

end
%% 6-07
if file(1:4)=='6-07'
    Cutoff = 0.55;
    x =
[2476,2143;1950,2023;951,793;479,446;633,499;1313,1364;839,794];
    y = [1521,1335;220,59;22,20;661,552;1770,1748;1762,1570;409,126];
end
%% 6-10
if file(1:4)=='6-10'
    Cutoff = 0.6;
    x =
[2463,2259;1942,2007;445,299;312,300;169,118;178,84;1555,1613];
    y = [16,34;801,717;968,775;530,348;1449,1281;1445,1231;379,212];
end
%% 6-24
if file(1:4)=='6-24'
    Cutoff = 0.4;
```

```
    x =
[2309,2514;232,184;1873,1724;1132,1064;1720,1847;871,640;1720,1850;170
6,1630];
    y =
[1432,1001;1227,1092;1430,1275;304,192;708,647;1826,1878;708,651;1855,
1718];
end
%% 6-26
if file(1:4)=='6-26'
    Cutoff = 0.5;
    x = [2445,2320;1731,1717;854,863;600,457;995,826;1266,1365];
    y = [117,102;1072,858;722,509;1033,674;1733,1748;1819,1803];
end
%% 7-09
if file(1:4)=='7-09'
    Cutoff = 0.5;
    x =
[2366,2417;1111,1120;2452,2473;653,649;1416,1244;2324,2327;382,332];
    y =
[643,523;297,208;1389,1242;729,636;1668,1603;1034,918;1357,1283];
end
%% 8-16
if file(1:4)=='8-16'
    Cutoff = 0.6;
    x =
[1515,1388;620,735;445,366;2092,1978;1716,1618;1143,922;970,981];
    y =
[526,472;287,131;1207,1173;1506,1480;1744,1672;669,610;1835,1697];
end
%% Plotting/figures
addpath(path);
I=imread(file);
if file(1:4)=='6-24'
    T = adaptthresh(I,Cutoff,'ForegroundPolarity','bright');
    BW = imbinarize(I,T);
else
    BW = imbinarize(I(:,:,1),Cutoff);
end

Image = figure(1);
% imshow(I(:,:,1:3)); % For test image only
imshow(I)
BWImage = figure(2);
imshow(BW(:,:,1));

ScalePix=199;
```

```
Scaleum=10;
ScaleUmPerPix= 10/199;


figure(Image)
for n=1:size(x,1)
    line(x(n,:),y(n,:),'Color','red','LineWidth',5);
end

figure(BWImage)
for n=1:size(x,1)
    line(x(n,:),y(n,:),'Color','red','LineWidth',5);
end

for n=1:size(x,1)
    LineProfile{1,n}(:,1)=x(n,:);
    LineProfile{1,n}(:,2)=y(n,:);
    LineProfile{2,n} = improfile(BW,x(n,:),y(n,:));
    bw=LineProfile{2,n}(:,1)';

    gap.start_indices = find( diff([0,bw])<0 );
    gap.start_indices(end)=[];
    gap.end_indices = find( diff([bw,0])>0 );
    gap.end_indices(1)=[];
    gap.length = gap.end_indices-gap.start_indices+1;

    DeltaX=abs(x(n,1)-x(n,2));
    DeltaY=abs(y(n,1)-y(n,2));
    LineProfile{3,n}=[DeltaX,DeltaY];
    LineProfile{3,n}(2,1)=sqrt(DeltaX^2+DeltaY^2);

    PathagScale=LineProfile{3,n}(2,1)/(length(LineProfile{2,n})-1);
    LineProfile{4,n}=gap.length;
    LineProfile{5,n}=gap.length*PathagScale;

    figure
    plot(LineProfile{2,n}(:,1))
end

gaps=[];

for n=1:size(x,1)
    gaps=[gaps LineProfile{5,n}];
end
```

```
gaps=gaps*ScaleUmPerPix;
GapZ=zscore(gaps);
GapZ(abs(GapZ)>=3)=[]; % Eliminating anything larger than 3 deviations
from data
gaps(abs(GapZ)>=3)=[];
GapMean=mean(gaps)
GapSTD=std(gaps)
figure
histfit(gaps)
title('5-33')
xlabel('Alpha Thickness (um)')
ylabel('Counts')
```